José Nuno Varandas da Silva Ferreira
Mestre em Engenharia de Estruturas

LONG-TERM BEHAVIOUR OF RAILWAY TRANSITIONS UNDER DYNAMIC LOADING

APPLICATION TO SOFT SOIL SITES

Dissertação para obtenção do Grau de Doutor em Engenharia Civil

Orientador:	Manuel Américo Gonçalves da Silva, Professor Catedrático, FCT/UNL
Co-orientador:	Paul Hölscher, Senior advisor, Deltares

Júri:

Presidente:	Professora Doutora Ana Maria Félix Trindade Lobo
Arguentes:	Professor Doutor Rui Artur Bártolo Calçada
	Professor Doutor Eduardo Manuel Cabrita Fortunato
Vogais:	Professor Doutor Raimundo Moreno Delgado
	Professora Doutora Zuzana Dimitrovová

FACULDADE DE CIÊNCIAS E TECNOLOGIA
UNIVERSIDADE NOVA DE LISBOA

Fevereiro 2013

Long-Term Behaviour of Railway Transitions under Dynamic Loading
Application to Soft Soil Sites

To my wife Filipa and our daughter Alice

In memory of José Augusto Varandas

Acknowledgments

The work described in this thesis was developed with guidance, help, and support of people and institutions to which I wish to endorse my sincere gratitude.

I am deeply grateful to Prof. Manuel Gonçalves da Silva, my supervisor, for the wise guidance, for the rigorous sharing of knowledge, for the excellent conditions of work and cooperation with other institutions that has provided, and for all the priceless reviews.

I thank from the bottom of my heart to Dr. Paul Hölscher, my co-supervisor, for all the invaluable scientific discussions, for the availability and patience in sharing knowledge, for the support and friendship, and for the dedication and scientific rigor, which constitutes an example that I will keep forever.

I am grateful to Bruno Coelho for the fruitful discussions from which I have learned so much, and for having facilitated my integration in the course of the field measurements.

I am indebted to Prof. Stefan van Bars for the excellent lessons on soil mechanics, and for all the logistical support concerning my stays in Delft.

I also thank Arno Mulder for help in preparing and processing the samples of ballast, and I thank Ad Verweij and Piet Meijers, from Deltares, for the support and care in Delft.

I thank the members of IDMEC participants in project SMARTRACK. In particular, I thank the project leader Prof. Jorge Ambrósio for the enthusiastic lessons on railway topics, and I thank Dr. João Pombo, for his invaluable support and for his kind friendship.

I thank the members of REFER participants in project SMARTRACK. In particular, I thank Eng. José Carlos Clemente for the sympathy and interest that has revealed, I thank Eng. Marco Baldeiras for his insightful explanations about railway maintenance procedures, and I thank Eng. Nuno Lopes for the excellent cooperation and discussions on wheel-rail interaction topics.

I kindly thank Dr. João Marcelino, for the cooperation and sharing of information in the

field of numerical modelling.

I am indebted to Prof. Zuzana Dimitrovová, to whom I deeply thank the teachings and cooperation in the development of analytical solutions for railways.

I thank Prof. Armando Antão for the instructive discussions in soil mechanics, and for the interest revealed in my work.

I thank Prof. Corneliu Cismaşiu and Prof. Ildi Cismaşiu, for the knowledge shared in the area of finite elements, and for the kind friendship.

I thank Eduardo Cavaco for his kind interest and for the very useful discussions on non-linear numerical solutions, which helped me during one of the hardest periods of my work.

I thank Prof. Luís Neves for the interest, for the help with Latex, and for the wise counsels and friendship.

I am deeply grateful to Prof. João Rocha de Almeida for the unconditional support always provided in logistical and administrative issues.

I deeply thank Dr. João Paulo Bilé Serra for having lead so brightly my initiation in scientific research in the area of soil dynamics.

I thank Filipe Santos and Mario Silva for having shared so many waves and laughs with me.

At the end, a special thank, from the bottom of my heart, for all the support and care of my family. I specially thank my wife Filipa, my mother, my sister, e aos meus queridos avós.

I acknowledge the financial support of Fundação para a Ciência e Tecnologia, through a Ph.D grant (SFRH/BD/25297/2005), through the project "Interacção solo-via férrea para comboios de alta velocidade" (POCI/ECM/61114/2004), and through the project SMARTRACK (PTDC/EME-PME/101419/2008).

Abstract

Transition zones in railway tracks are built to mitigate damage and wear to tracks and trains, and discomfort to passengers, caused by structural and foundation discontinuities, such as those introduced by bridge approaches or culverts. However, additional strains are still generated that cause changes of track geometry, that lead to more frequent maintenance operations and sometimes speed restrictions, that raise costs, and need to be minimized.

This thesis addresses those questions and describes research undertaken to model the dynamic response of the railway tracks, taking into account the behaviour of ballast at the aforementioned railway transition zones, where the long-term settlements are amplified by dynamical loading on the ballast due to the discontinuities.

Novel numerical models for the simulation of the dynamic response of the system soil-ballast-track-vehicle and accounting for those phenomena are presented. The models are validated by field measurements performed at a passage over a culvert, located in a soft soil site. The models include the unloaded level of the track, the possibility of voids under the sleepers, and the non-linear constitutive behaviour of the ballast, as well as representation, albeit simplified, of the vehicles.

The forces transmitted to the ballast at transition areas vary considerably, both in time and space: loading of ballast reaches higher values than in regular tracks, and the additional vibrations cause larger differences between loads transmitted to consecutive sleepers. This causes higher densification of ballast at transition zones.

Transition zones solely composed of approach slabs are not effective in soft soil sites. The soil and ballast at approach regions settle more than the segment on top of the much stiffer structure, leading to the appearance of hanging sleepers. The subsequent combined effect of lower load on part of the ballast and motion of the approach slabs results on increased settlement of the ballast and sub-ballast, increasing the voids under the sleepers, and causing more severe actions on the track.

Possible improvement measures were modeled and tested computationally at the later stages of the thesis. The numerical simulations showed that the use of soft railpads on the stiff side of the transition is beneficial, provided the problem is mostly caused by stiffness variation of the track support. Slab track solution was also tested and showed advantages over the ballasted track by showing much smaller differential rail displacements, for identical change of the track support stiffness.

Resumo

As zonas de transição de vias férreas são construídas para mitigar danos e desgaste de vias e comboios, e desconforto para passageiros, causado por descontinuidades estruturais e da fundação, tais como aquelas introduzidas por entradas em pontes ou passagens hidráulicas. No entanto, deformações adicionais são ainda assim geradas que causam alterações da geometria da via, que conduzem a operações de manutenção mais frequentes e por vezes a restrições de velocidade, que aumentam custos, e precisam de ser minimizadas.

Esta tese aborda estas questões e descreve trabalho de investigação empreendido para modelar a resposta dinâmica de vias férreas, considerando o comportamento do balastro nas supracitadas zonas de transição ferroviárias, onde os assentamentos de longo-prazo são amplificados pelo carregamento dinâmico no balastro devido às descontinuidades.

Nesta tese são desenvolvidos e apresentados modelos numéricos para a simulação do comportamento dinâmico e de longo-prazo do sistema solo-balastro-via-veículo. Os modelos são validados com medições de campo efectuadas numa passagem hidráulica, localizada numa zona de solos moles. Os modelos incluem o perfil longitudinal da via, a possibilidade de existirem vazios sob as travessas, o comportamento constitutivo não-linear do balastro, assim como uma representação, ainda que simplificada, dos veículos.

As forças transmitidas ao balastro em zonas de transição variam consideravelmente, tanto no tempo como no espaço: o carregamento do balastro é geralmente maior do que em zonas de via regular, e com maiores diferenças entre a carga máxima transmitida em travessas consecutivas. Isto provoca uma maior densificação do balastro em zonas de transição.

Zonas de transição compostas somente por lajes de transição não são efectivas em zonas de solos moles. O solo e o balastro na secção de aproximação têm maiores assentamentos do que a secção sobre a estrutura rígida, conduzindo ao aparecimento de travessas flutuantes. O subsequente menor pré-carregamento do balastro combinado com o movimento dinâmico das lajes de transição, resulta em maiores assentamentos do balastro e sub-balastro, aumentando os correspondentes vazios sob as travessas e causando acções

ainda mais severas na via.

No final da tese são modeladas e testadas computacionalmente possíveis medidas de melhoramento das zonas de transição. As simulações numéricas mostram que o uso de elementos de ligação carril-travessas com baixa rigidez vertical na zona sobre a estrutura rígida é benéfico, desde que o problema seja essencialmente causado pela variação da rigidez de suporte da via. A solução de via em laje é também testada e mostra-se que apresenta vantagens sobre a solução balastrada, por apresentar deslocamentos diferenciais do carril muito inferiores, para mudanças idênticas da rigidez de suporte da via.

Contents

List of Figures

List of Tables

List of Symbols

Convention

a, A, α	Scalar
$\mathbf{a}$	Vector
$\mathbf{A}$	Matrix

Subscript

$\mathrm{a_a}$	Quantity referred to wheel-rail interaction
$\mathrm{a_d}$	Quantity referred to damping
$\mathrm{a_e}$	Quantity referred to deformation
$\mathrm{a_g}$	Quantity referred to gravity
$\mathrm{a_i}$	Quantity referred to inertia
$\mathrm{a_{rd}}$	Quantity referred to the damper
$\mathrm{a_{sp}}$	Quantity referred to the spring
$\mathrm{a_s}$	Quantity referred to the ballast-soil system
$\mathrm{a_t}$	Quantity referred to the track system
$\mathrm{a_v}$	Quantity referred to the vehicle system

Latin Symbols

a and $\mathbf{a}$	Accelerations
$\mathbf{C}$	Damping matrix
c_{rd}	Visco-elastic damper constant
$\mathbf{D}$	Constitutive stiffness matrix
E	Young's modulus
E_{r}	Resilient modulus
EI	Bending stiffness

F and $\mathbf{f}$	Force
G	Shear modulus
h	height of the void (also called gap) under the hanging sleepers
I	Moment of inertia
$\mathbf{K}$	Stiffness matrix
K	Bulk modulus
K_0	Coefficient of lateral earth pressure
L	Length
$\mathbf{M}$	Mass matrix
M	Oedometer modulus
m	Mass per unit length
M_f	Inclination angle of failure line
N	Number of applied load cycles
p	Mean normal stress
q	Deviatoric stress
ΔS	Maximum accumulated settlement between dynamic analyses
S_N	Settlement after N load cycles
S_b	Settlement due to changes in the ballast and sub-ballast layers
S_r	Settlement of the rail
S_sg	Settlement due to changes in the subgrade
TR	Transmissibility
t	Time
u and $\mathbf{u}$	Displacements
u_c	Displacement at which the sleeper contacts the ballast
u_p	Permanent deformation of the ballast
v and $\mathbf{v}$	Velocities
v_p	Velocity of primary body wave
v_s	Velocity of secondary body wave
x	Coordinate position, in longitudinal direction of the track

y	Coordinate position, in transverse direction of the track
z	Coordinate position, in vertical direction - depth

Greek Symbols

δ	Indentation
$\epsilon_{\mathrm{s,r}}$	Recoverable shear strain
$\epsilon_{\mathrm{v,r}}$	Recoverable volumetric strain
ϵ_i	Principal strains (1 - major, 2 - intermediate, 3 - minor)
ϵ_N	Total permanent strain after load cycle N
$\epsilon_{i,\mathrm{r}}$	Recoverable strain in direction i
ϵ_{ij}	Strain tensor
γ	Shear strain
γ_{oct}	Octahedral shear strain
ν	Poisson's ratio
ϕ_c	Critical state friction angle
ρ	Volumetric mass
σ_i	Principal stresses (1 - major, 2 - intermediate, 3 - minor)
σ_{ij}	Stress tensor
τ	Shear stress
θ	Sum of the principal stresses
θ_0	Reference stress (100 kPa)
ϵ	Vector form of the strain tensor
σ	Vector form of the stress tensor

Abbreviations

1-D	One-dimensional
2-D	Two-dimensional
3-D	Three-dimensional
BEM	Boundary Element Method
CCP	Triaxial test with constant confining pressure
CPT	Cone Penetration Test

DD	Railway vehicle - Doubledecker Inter-Regional trainunit
DOF	Degree-of-freedom
FDM	Finite Difference Method
FEM	Finite Element Method
GPR	Ground Penetration Radar
GPS	Global positioning system
ICM	Railway vehicle - Intercity trainunit
ICR	Railway vehicle - Intercity carriage
IEM	Infinite Element Method
LOC	Railway vehicle - Locomotive Class 1700
VCP	Triaxial test with variable confining pressure
VSPT	Vertical Seismic Penetration Test

Chapter 1

Introduction

1.1 Background to the study

Railways are recognized as the most reliable, safe and energy efficient means of transport for passengers and goods. In an era of increasing environmental concern, railway transport is also the most sustainable choice, with the lowest CO_2 emissions per km.ton transported. With this in mind, the railway sector has been the subject of renewed interest and rapid development in the last few decades. The expansion of the railway network is taking place mainly in China, Europe and Japan (Okada, 2007; EU, 2001; Takatsu, 2007).

One of the main disadvantages of railway transport is the high cost of construction and maintenance, when compared to other modes of transport. Furthermore, the increase in speed, axle-loads and traffic has led to higher-rates of degradation of the ballasted railway tracks (Schmitt, 2006; López-Pita et al., 2007). As so, a considerable effort is necessary for maintenance of the tracks, with corresponding increase in costs for the infrastructure managers. According to Schmitt (2006), 40-50% of these costs are spent to maintain the quality of the track geometry. The main cause for the loss of track geometry is deformation and densification of the ballast layer, representing 75% of the total track position maintenance (Selig and Waters, 1994; Esveld, 2001; Zhai et al., 2004). The seek for improved design solutions for railway tracks, keeping the maintenance costs at reasonable and competitive level, is thus the essential objective of the ongoing research on railways.

Transition zones in railway tracks are built to mitigate the impact caused by structural discontinuities existing along the track. These discontinuities may be bridge approaches, road crossings, culverts or transitions from slab tracks to ballasted tracks. The rate at

which the track geometry degrades on these transition zones is frequently higher than on the normal free track, leading to higher maintenance frequency and sometimes speed restrictions (Dahlberg, 2003; Li and Davis, 2005; Sasaoka and Davis, 2005; López-Pita et al., 2007). According to López-Pita et al. (2007) the frequency of maintenance at transitions in the Spanish railway line is three times that of normal plain track. In the Netherlands, where this problem is aggravated by the existence of soft soil conditions, it was found that the incidence is 4-8 times higher (Hölscher and Meijers, 2007). Therefore, additional research on railway transitions will allow the development of optimized maintenance procedures, and improved transition zones solutions for new railway lines or for the up-grade of existing ones.

1.2 Aim of the research

According to an extensive monitoring campaign performed in the US (Li and Davis, 2005), the poor performance of transition zones is significantly dictated by degradation mechanisms occurring in the ballast. The principal aim of this research is thus to improve knowledge on the ballast behaviour at transition zones, seeking a clarification of the causes responsible for the change of geometry of ballasted tracks on these areas, and to answer the question which mechanisms are responsible for the observed increased degradation.

At transitions, the dynamic loading on the ballast is highly influenced by the inhomogeneous nature of the support, which includes changes of the support stiffness and, possibly, voids under the sleepers. These aspects may evolve in time, with the accumulation of settlement at transitions, and therefore their influence on the long-term response of the track will also change in time. This study pursuits the development of a novel method suitable to predict the long-term behaviour of transition zones, considering the coupling between the dynamic response and the long-term behaviour.

This work also seeks the development of novel computer models adequate to analyze the dynamic behaviour of transition zones. The dynamic response of the track at transition zones is particularly affected by non-linear aspects. These non-linear aspects include the loss of contact between the sleepers and the ballast, and the non-linear constitutive behaviour of the ballast (Dahlberg, 2003). Another aim of this research is thus to analyze the importance of the consideration of these non-linear aspects in representative models, and how these non-linear aspects influence the obtained numerical response.

A final aim of this research is to provide methods and (numerical) tools adequate to analyze possible measures to improve the behaviour of railway tracks at transition zones.

1.3 Outline of the thesis

This thesis is composed of eight Chapters. In Chapter 2 of the thesis, the study starts by describing the usual problems associated with transition zones, and by presenting field measurements performed at one typical railway transition. The data collected in the field yielded a better understanding of frequent problems occurring in transition zones, and also allowed for a comprehensive quantification of its dynamic and long-term response. For this reason, the case described in this Chapter is the central case-study of this work. At the end of Chapter 2, a series of research questions concerning this case-study are formulated.

In Chapter 3, the mathematical models for railway tracks and ballast behaviour are reviewed, and important aspects to be considered in the models used within this work are identified.

Chapter 4 presents a one-dimensional train-track dynamic numerical model, incorporating non-linear aspects. This model is validated with the measurements given in Chapter 2, and some of the research questions formulated at the end of Chapter 2 are answered based on the numerical simulations.

Chapter 5 presents a methodology to estimate the loss of the vertical geometry of the track with time. For this, the dynamic model developed in Chapter 4 is coupled with a newly developed mathematical model to estimate the vertical settlement of the ballast, also presented in Chapter 5. The validation of the method and the settlement model is made with the long-term measurements given in Chapter 2. With the presented methodology, the importance of the coupling between the dynamic loading from the trains and the long-term response of the track is analyzed.

Results from Chapter 5 point to the need for additional dynamic simulations using three-dimensional models. Accordingly, a three-dimensional numerical model for the dynamic response of transition zones is developed and presented in Chapter 6. In this Chapter, the importance of the non-linear constitutive behaviour of the ballast on its dynamic response is also investigated, and the 3-D model is applied to study the standard transition case of the field measurements.

At the end of this thesis, in Chapter 7, the adequacy and effectiveness of possible measures to improve the behaviour of railway tracks at transition zones is analyzed. The tested measures are (i) the inclusion of soft railpads on the stiff part of the transition, and (ii) the replacement of the ballasted track solution by a slab track solution. To this effect, an additional model to determine the dynamic response of slab tracks to moving loads is here presented. This model considers the existence of an abrupt change in the stiffness of

the support, therefore representing the case of a railway transition, and the corresponding solution is obtained with analytical methods.

Chapter 8 summarizes the main conclusions from this work.

Chapter 2

Railway Transition Zones. Problem Description

2.1 Overview

Transition zones in railway tracks are built to mitigate the impact caused by structural discontinuities along the track. These discontinuities may be bridge approaches, passages over culverts, at road and rail crossings, ends of tunnels, or passages from slab tracks to ballasted tracks. Such places frequently show accelerated track geometry degradation and increased wear and tear on track and vehicle components. This leads to poor ride quality and sometimes speed restrictions. As a consequence, the maintenance incidence on track discontinuities may be three to eight times higher than that in normal plain track, increasing costs and decreasing the availability of the track (Kerr and Moroney, 1993; Kerr and Bathurst, 2001; Li and Davis, 2005; Read and Li, 2006; López-Pita et al., 2007; Hölscher and Meijers, 2007).

Two main causes are generally referred for the observed increased degradation at track discontinuities (Shenton, 1985; Hunt, 1997; Kerr and Bathurst, 2001; Li and Davis, 2005; Lundqvist et al., 2006):

(i) A change in the track supporting structure usually represents also a large change in the stiffness of the track and foundation. If the stiffness of the track changes abruptly, the train-track and the sleeper-ballast interaction forces increase, leading to localized increased settlement of the track. This, by turns, will lead to even higher forces, making it a feedback process.

(ii) On transitions, the ballasted approach section may inherently settles more than the section on top of the stiff structure, as the former is frequently built over embankments and the stiff structure is usually free of settlements. This, again, leads to differential settlements.

The uneven settlements occurring at these locations frequently lead to unsupported sleepers (also called hanging sleepers). These are sleepers suspended by the rails in the unloaded condition and thus with a gap between the sleeper and the ballast bed. Figure 2.1 shows the existence of hanging sleepers, which may appear in the vicinity of stiffer structures supporting the track. The existence of unsupported sleepers lead to impact loading on the track and thus to accelerated track damage, making it another cause for the observed increased degradation (Hunt, 1997; Augustin et al., 2003; Lundqvist and Dahlberg, 2005; Zhang et al., 2008).

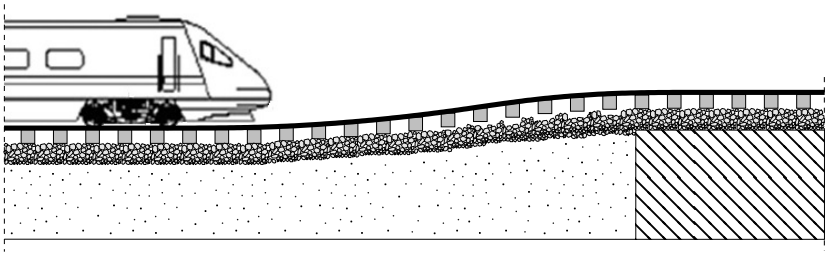

Figure 2.1: Structural discontinuity in the track

Briaud et al. (1997) refers to other causes for the differential settlements at bridge approaches, which include geotechnical defects, such as insufficient compaction and consolidation of the fill and embankment, poor drainage conditions, compression of natural soil due to embankment load, among others.

The experimental work in transitions is rather scarce (Coelho, 2011). Li and Davis (2005) and Li et al. (2010) have presented a study based on observations made at four ballasted railway bridge-approach transitions. This study has shown that the settlement on the approach zone is significantly higher than that of the free track or the track on the bridge. Other experimental findings on transitions may be found in (Kerr and Bathurst, 2001; Plotkin and Davis, 2008; Adif-Cedex, 2009). In these studies, no evaluation on the long-term behaviour of the transitions, before and after the implementation of mitigation techniques, were reported. Recent comprehensive experimental investigation over the behaviour of a culvert box transition was made in the Netherlands (Hölscher and Meijers, 2009; Coelho, 2011). Findings from this programme will be presented in the next Section.

A number of different solutions for transition zones have been proposed or used. These transitions are built to smooth the stiffness variation between the "soft" approach section and the "stiff" section on top of the structure. Transitions based on smoothing the stiffness variation on the "soft" side (Kerr and Moroney, 1993; Li and Davis, 2005; Read and Li, 2006) include the use of oversized sleepers, variable spaced sleepers, underlayments of hot-mix-asphalt or of geotextiles or of soil-cement, additional rails, approach slabs, among others. Transitions based on lowering the stiffness on the "stiff" section (Kerr and Moroney, 1993; Kerr and Bathurst, 2001; Sasaoka and Davis, 2005; Read and Li, 2006; Li et al., 2010) include the use of soft railpads, under sleeper pads, plastic sleepers or ballast mats. According to Li and Davis (2005), transition zones must address the specific stiffness issues of the correspondent track discontinuities in order to be effectives.

2.2 Field measurements on a railway transition

Experimental investigations on the behaviour of structures are important, not only because they allow for a good understanding of the physical phenomena under study, but also because they give data for the validation of representative models. As mentioned above, field measurements in transitions of railways are scarce. In the Netherlands, a monitoring programme was defined in order to improve knowledge on the behaviour of transition zones, comprising both short-term and long-term measurements. The field measurements were performed between 2008 and 2009, in a culvert box transition, located in a region with soft soils. The author had the opportunity to closely follow these field measurements, with a small contribution in the field. The collected data played an important role in the development and validation of the models presented in this work. Therefore, the data needed in Chapters 4 to 6, for validation of the models, will be presented next. These field measurements are extensively described in (Hölscher and Meijers, 2009; Coelho, 2011).

2.2.1 Case description

The case corresponds to a passage over a culvert that serves for water flow between both sides of the line. The selected culvert is located in the railway line between Utrecht and Gouda, close to the railway station of Gouda Goverwelle. The railway line is here composed of four parallel ballasted tracks, with wooden sleepers. Two of the tracks were built in 1855 and the other two in 1995. The culvert itself consists on a square concrete box 2 m by 2 m, approximately 60 m long. The culvert is founded on piles, thus settlement free. At each side, approach slabs of 4 m length and 30 cm thickness form the transition zones. These slabs are simply supported on the culvert. Figure 2.2 shows a transversal

and a longitudinal view of the culvert. Figure 2.2-a shows only the two newer tracks. The measurements were concentrated on the outer track (right-hand side in figure 2.2-a). In these two tracks, the trains travel from East to West.

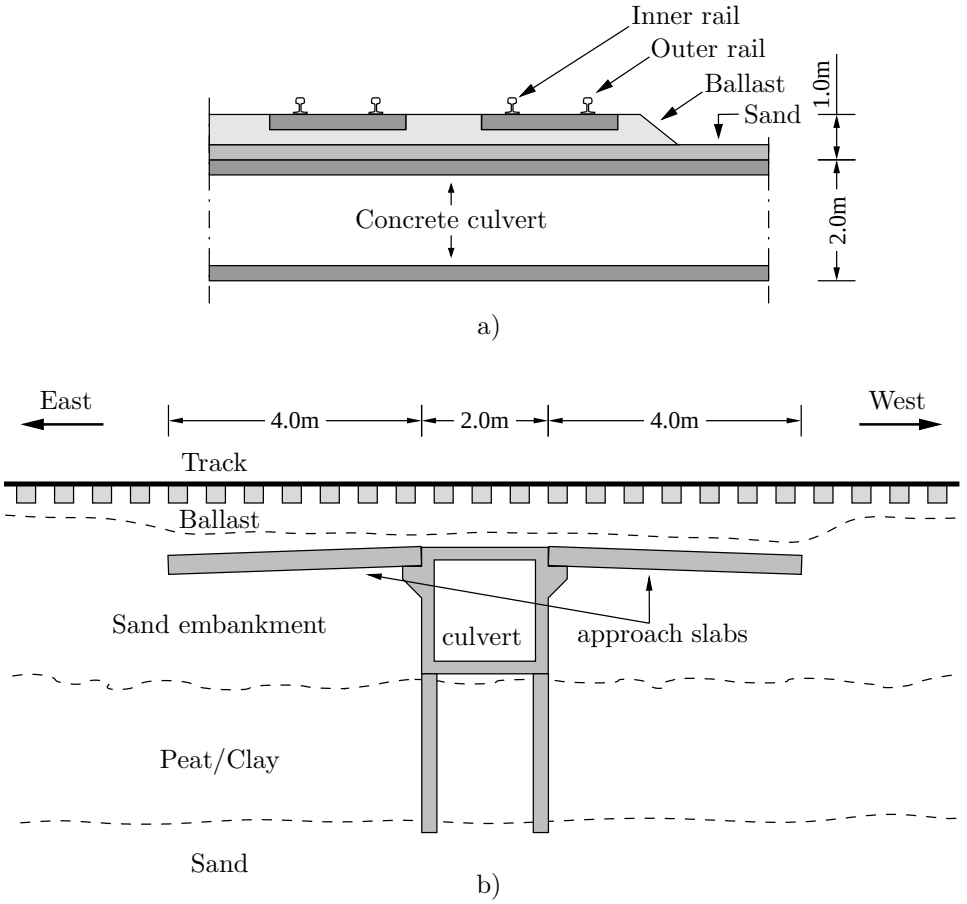

Figure 2.2: Transverse view (a) and longitudinal view (b) of the track passing over the culvert (not to scale)

Figure 2.3 shows the soil profile at the culvert. This profile was obtained based on CPT's, VSPT's and Ground Penetration Radar (GPR) measurements (Hölscher and Meijers, 2009). The reference for the vertical axis is placed at the top surface of the ballast.

The natural ground at this site mainly consists of soft soils, particularly peat. The thickness of this peat layer is around 6 m, with some variations. Inside this layer, a sand layer is present with thickness between 1 m and 2 m. These layers are laid on top of the Pleistocene sand which is located at around $z = -12$ m. The piles of the culvert are founded on this Pleistocene sand. On top of the soft layers, a sand embankment was built to support the railway line. The lower boundary of this sand embankment varies between -5 m and -6.5 m.

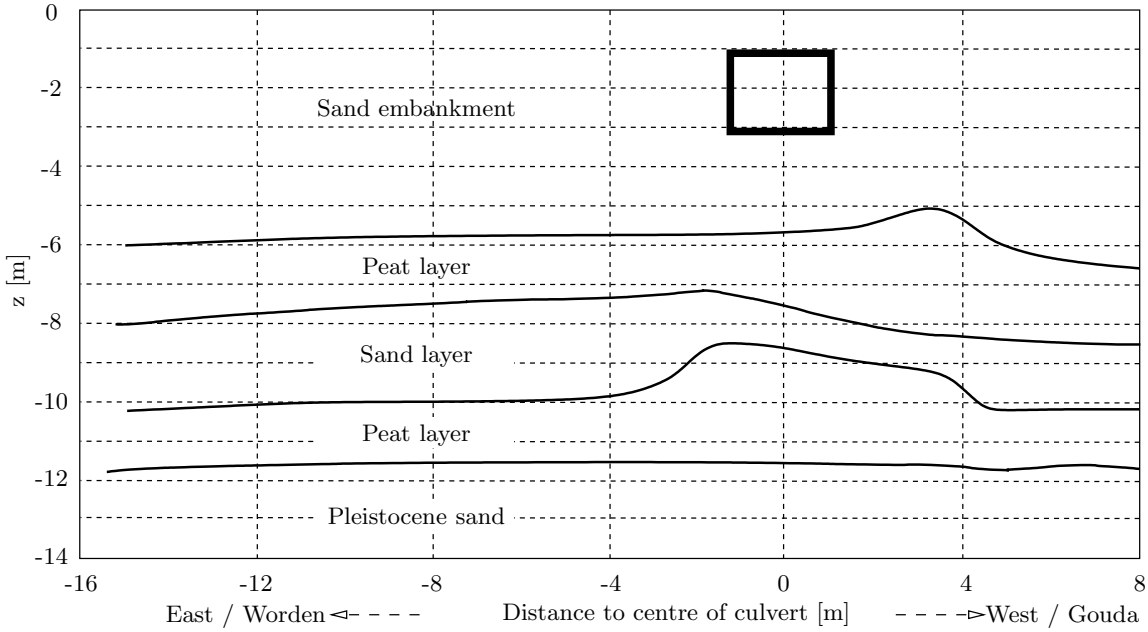

Figure 2.3: Soil profile at the culvert. The position of the culvert is represented with a square. Modified from (Hölscher and Meijers, 2009)

According to the VSPT's (Hölscher and Meijers, 2009), the shear wave velocity of the peat is around 50 m/s for the layer above the intermediate sand layer and around 80 m/s for the layer under this sand layer. The shear wave velocity of the intermediate sand layer is about 150 m/s and that of the pleistocene sand can be estimated to be slightly higher. At the embankment, the shear wave velocity could not be reliably measured and the CPT's showed significant variations in terms of tip resistance. This indicates a heterogeneous nature of the embankment.

The ballast layer was originally designed with 0.30 m thickness and the approach slabs were placed with 2.5% inclination. GPR measurements and trial pit excavations have shown that the ballast thickness now varies between around 0.40 m, on top of the culvert, to around 0.80 m, on top of the approach slabs. This is due to repeated maintenance operations along the years, comprising tamping and re-ballasting. Comparison between the GPR readings and the trial pit excavations has indicated that there might exist interpenetration of ballast into the sand layer and that a mixed zone of about 20 cm seems possible (Hölscher and Meijers, 2009). The GPR and the trial pit excavations have also shown that the inclination of the approach slabs has now increased to a value close to 18.5%. This is caused by rotation of the approach slabs due to progressive settlement of its free edges. Figure 2.4 shows the results from the GPR measurements, where again the origin of the vertical axis corresponds to the surface level of the ballast.

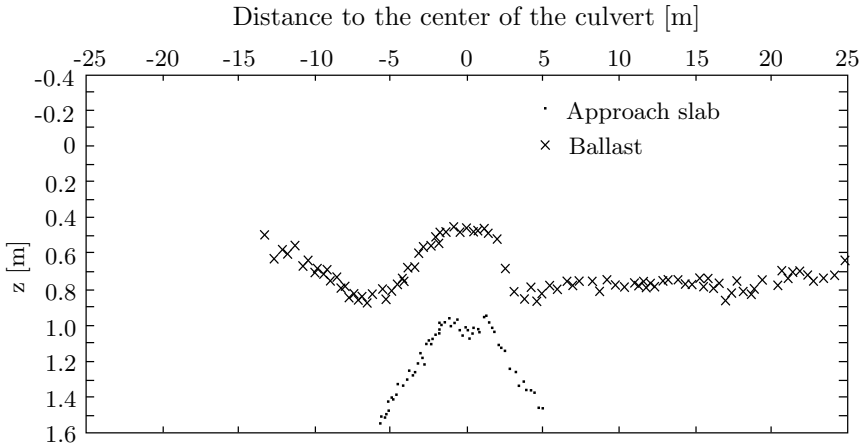

Figure 2.4: Height of ballast and position of the approach slabs from the GPR measurements. Modified from (Coelho et al., 2011)

2.2.2 Long-term behaviour

The long-term behaviour of the track was measured during one maintenance period (nine months). The measurements here presented include the periodic levelling of the track and the measurements of the voids under the sleepers.

Settlement of subgrade and approach slabs

The settlement of the free track embankment was estimated from the periodic measurement of the level of four concrete pylons, founded on the embankment and supporting the catenaries at this site (Hölscher and Meijers, 2009). It was found that the settlement of these pylons can be approximately represented by a linear function of time, with an average settlement rate of 1mm/month, relative to the culvert. This settlement may be considered as an indication of the settlement of the subsoil, supporting the embankment. This settlement is mainly due to consolidation of the peat layer (Coelho, 2011).

The settlement of the approach slabs was estimated based on the GPR measurements and on direct level measurements performed (through hand-dug holes) at one point of each slab, one located to the East and the other to the West of the culvert. At the free ends of the slabs, the settlement rate was estimated to be around 2.5 mm/month (Hölscher and Meijers, 2009). This settlement rate is therefore 2.5 times higher than the settlement rate of the subgrade. As the approach slabs are simply supported at the box culvert, which is founded on piles, this settlement of the “free” end causes a rotation of the approach slabs. The inclination of the approach slabs has thus raised from an initial value of 2.5%, to a

present value of 18.5% (Hölscher and Meijers, 2009).

Vertical motion of the track

The long-term vertical motion of the track was measured on top of each rail along one maintenance period. These levelling operations were made with high-precision topographical equipment, based on the Global Positioning System (GPS). The precision of the equipment was 0.5 mm. The level was measured above each sleeper, spaced 0.6 m. Figure 2.5 shows the spatial evolution of the level of the inner rail (as defined in Figure 2.2-a). The first levelling on 7^{th} October 2008 was performed a few hours after the maintenance operation. The figure also shows the position of the culvert and approach slabs. Figure 2.6 shows the time evolution of the inner and outer rail level in three different locations: on top of the culvert, on the free track to the East ($x = -12.6$m) and on the free track to the West ($x = +12.6$m). In this figure, the vertical position is relative to the initial position, measured on 7^{th} October.

Several observations are made looking at Figures 2.5 and 2.6:

- The track presents an up-and-down profile when passing over the culvert. The length of this bump is 10 to 20 m;
- The settlement is faster initially, right after the maintenance operation;
- After day 51 (27^{th} of November), the settlement is negligible on top of the culvert and evolves approximately linearly with time at the embankment areas;
- The initial settlement is higher on the outer rail compared to the inner rail;
- The initial settlement is higher on the embankment areas compared to the initial settlement on top of the culvert;
- The initial settlement is higher on the West side of the culvert compared to the East side.

Voids under the sleepers

The height of the voids under 15 sleepers were measured using a specific void indicator by Vortok. The precision of these devices is 3 mm. The indicators were placed close to the inner rail. Several readings were made between April and May 2009. Figure 2.7 shows the average measured height of the voids (indicated with circles) and the scatter of measured

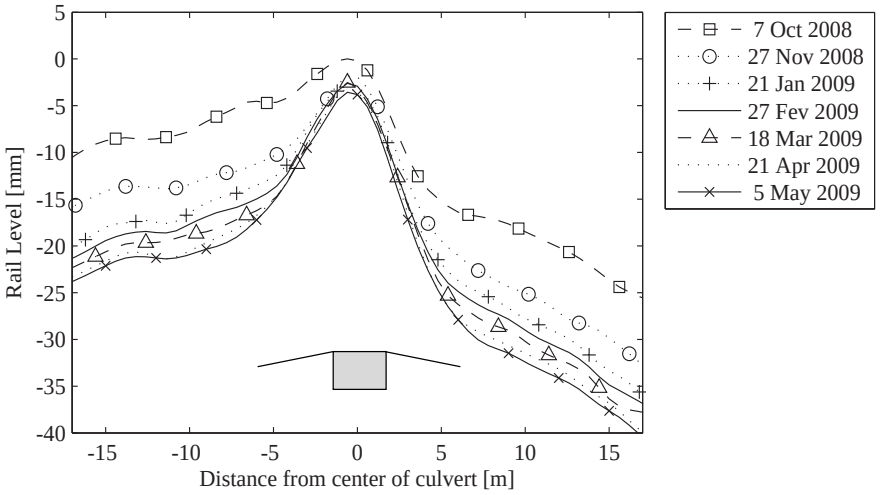

Figure 2.5: Rail level measured during one maintenance period. Modified from (Coelho et al., 2011)

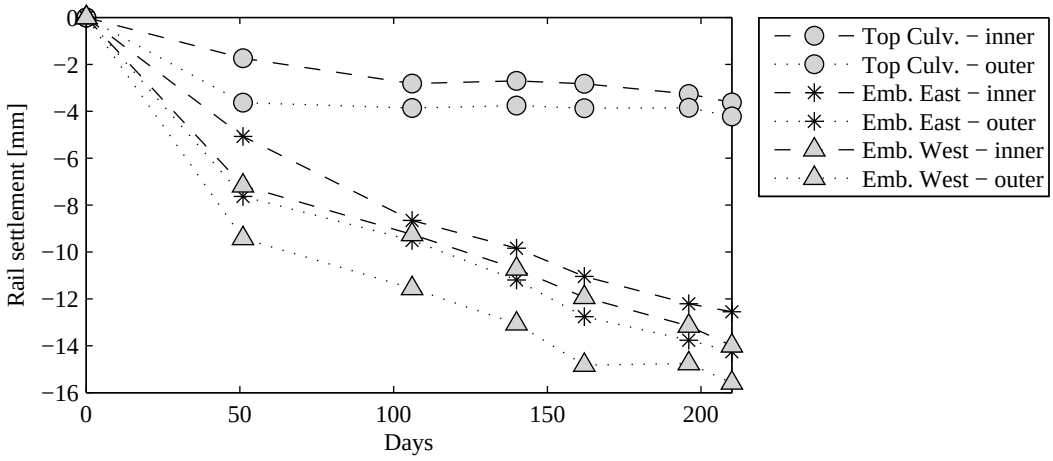

Figure 2.6: Evolution of settlement with days of the inner and outer rail at three different locations

values (vertical lines). The scatter is significant during the one month survey. From the figure, it can be seen that there is a significant amount of voids under the sleepers located above the approach slabs (between -5m to -1m and 1m to 5m) and that on top of the culvert, as expected, the sleeper soffit is in contact with the ballast.

Ballast behaviour

During the course of the field measurements two ballast samples were collected from the culvert site and examined in the laboratory facilities of TUDelft. One of the ballast samples was taken from under a sleeper located above the culvert and the other from a location preceding the culvert transition. The tests included petrographical examination of the

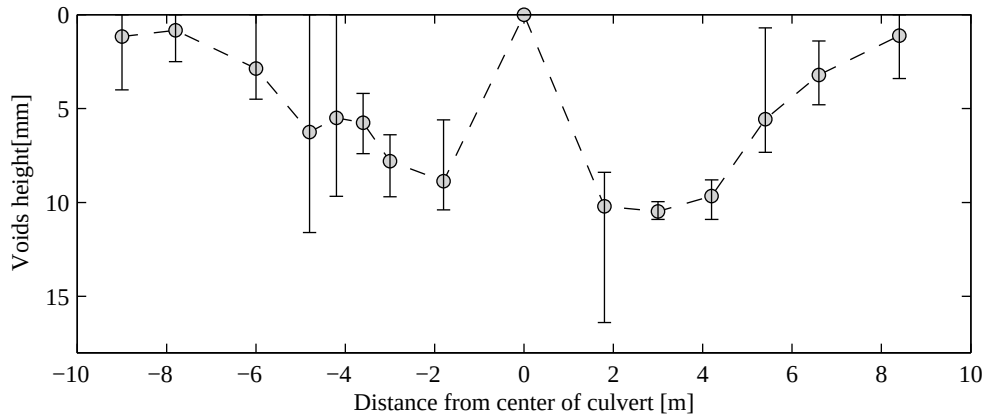

Figure 2.7: Voids measured under the sleepers. Modified from Hölscher and Meijers (2009)

Figure 2.8: Photo of ballast sample taken from the track on top of the culvert

ballast particles, particle size determination and Los Angeles abrasion tests. Figure 2.8 shows one photo of part of a ballast sample.

The petrographical examination, including microscopic analysis, concluded that the ballast is composed, at least, by three different types of rocks: basalt, gneiss and rhyolites. These rocks have different mechanical properties in terms of strength. The fact that most ballast in the Netherlands is imported and that several re-ballast operations were done since initial construction can explain the existence of three types of rocks in the ballast.

Figure 2.9 shows the particle size distribution of the two ballast samples (solid and dashed line in the figure). These curves were determined according to EN 933-1 (1997). The figure also shows the admissible limits for the particle size distribution of railway ballast according to EN 13450 (2002).

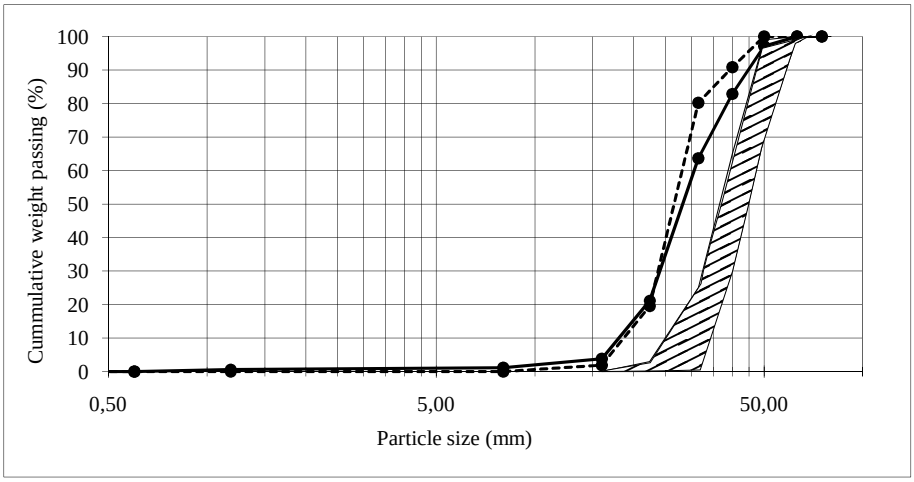

Figure 2.9: Particle size distribution of two samples collected from the culvert site

It can be seen in Figure 2.9 that the particle size distribution of the collected ballast lies outside the admissible limits imposed by the norm. The ballast particles sizes are generally smaller than they should be. Disregarding the hypothesis that the ballast was placed in the track with inadequate granulometry, it may be stated that the particle breakage at the culvert site is significant. Visual inspection of the collected ballast has also identified fresh cuts in some ballast particles confirming this assumption. This particles breakage alter the mechanical properties of the ballast, worsen its drainage capacity and contribute to the track geometry degradation.

2.2.3 Short-term behaviour

Train-induced track vibrations were measured using geophones, accelerometers and one high-speed camera. These measurements were done in May 2008 and May 2009, during regular train passages. Figure 2.10 shows a photo of the short-term measurements apparatus. The complete set up for the dynamic measurements is described in (Hölscher and Meijers, 2009; Coelho et al., 2011). Here only part of the track motion measurements in May 2008 are briefly presented.

Seven geophones measuring vertical motion were connected to the wooden sleepers in locations shown in Figure 2.11. All geophones were placed close to the outer rail, except geophone G4, which was placed on the opposite side. The displacements were obtained from the velocity signal acquired with the geophones, by filtering and integration, and were then validated by cross comparison with the displacements directly measured with the high-speed camera (Bowness et al., 2007).

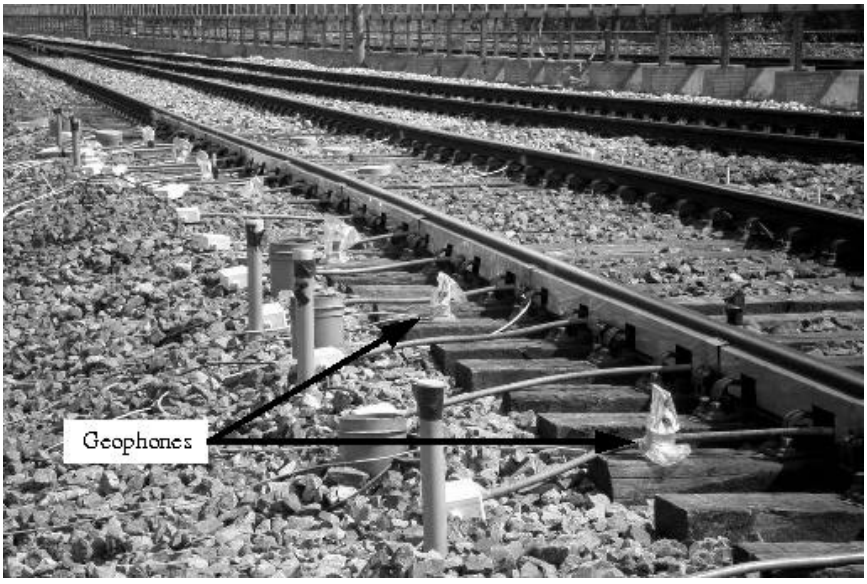

Figure 2.10: Photo of the monitored track section (May 2009)

The displacements measured by geophones G7, G3 and G1 during one train passage at 114km/h are shown in Figure 2.12. From this figure, it appears that the upward motion has about the same magnitude as the downward motion. However, this is in fact a consequence of the filter and integration procedure, necessary to transform velocities to displacements (Bowness et al., 2007). From comparison with the displacements directly measured with the high-speed camera, it was concluded that a downward drift of the displacements obtained with the geophones is necessary, in order to represent the real upward and downward motion of the sleepers (Coelho et al., 2009).

Comparing the displacements above the free track (G7) and above the culvert (G1), it can be seen that the peak-to-peak displacements differ by a factor of 2. The stiffness on top of the culvert is higher, as expected. Over the approach slab, there should be a gradual transition, in terms of displacements and stiffness, between the free track and the culvert (Kerr and Moroney, 1993; Esveld, 2001). However, the measured displacement amplitudes on location G3 were much higher than at G7 and G1.

Figure 2.13 shows the displacements measured at G7, G6, G5 and G3, for the same case presented in Figure 2.12. The origin of the vertical axis coincides (approximately) with the initial position of the sleepers before the train passage. It can be seen that the downward displacements tend to increase from G7 to G3 and that an upward spike is visible for the measurements performed at G5 and G3.

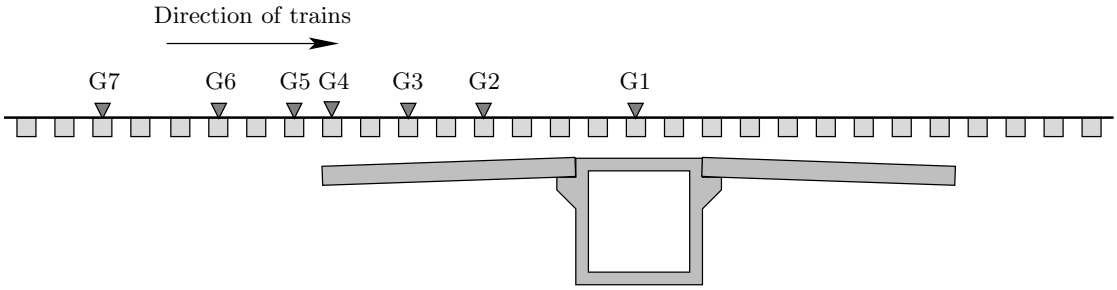

Figure 2.11: Position of geophones

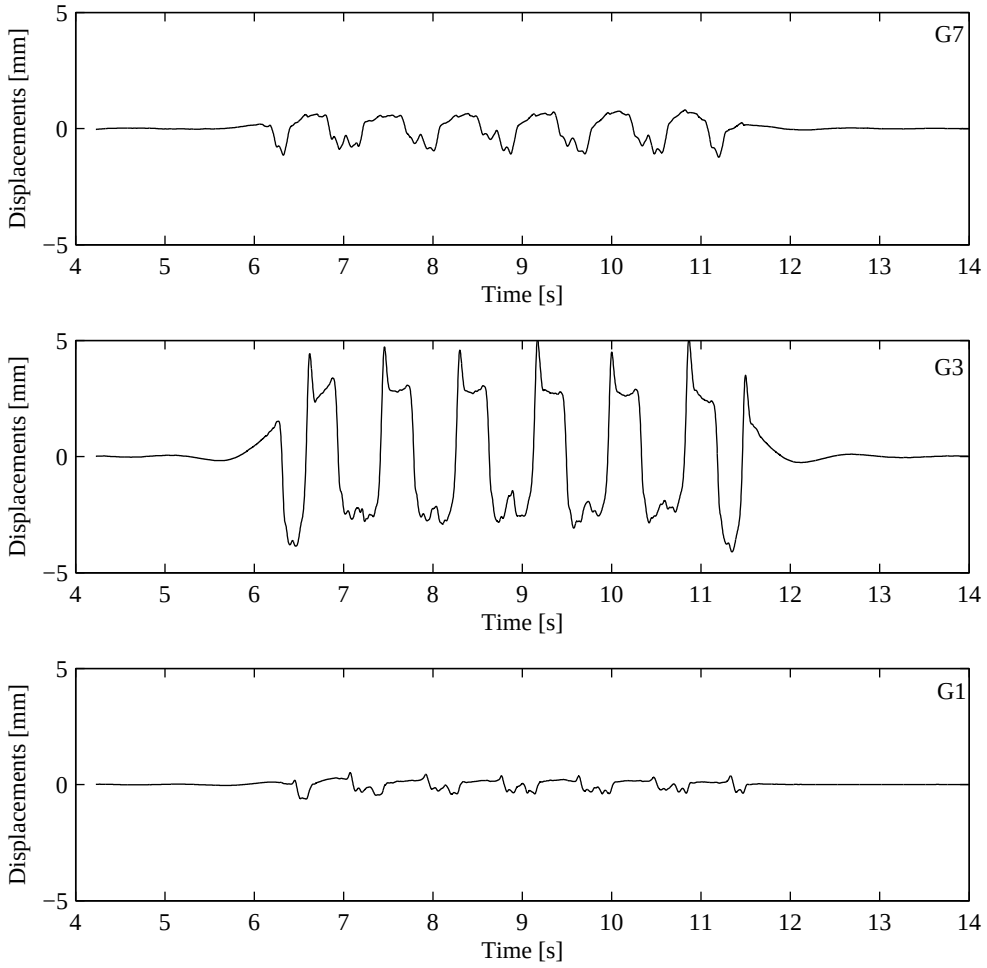

Figure 2.12: Vertical sleeper displacements during passage of an intercity doubledecker train at 114km/h on the free track (G7), on top of the approach slab (G3) and on top of the culvert (G1). Modified from (Coelho et al., 2009)

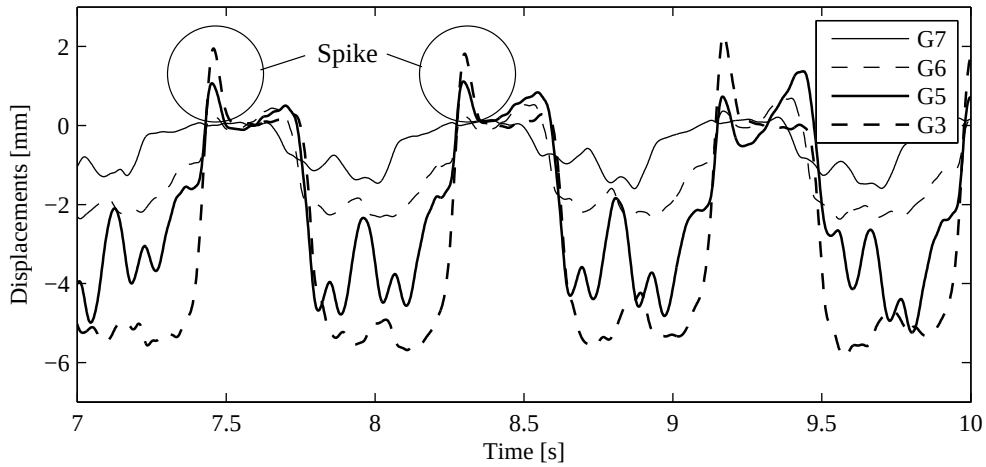

Figure 2.13: Vertical sleeper displacements at G7, G6, G5 and G3

2.2.4 Interpretation and discussion

The settlement of the embankment was found to evolve approximately linearly with time. The settlement of the embankment results from permanent deformations in the soft layers of peat and in the sand layer forming the embankment itself. These settlements evolve non-linearly from the time the track was built. However, between two successive maintenance operations, after some years of service operation, the settlement of the subgrade can be approximated by a linear function of time (Shenton, 1985; Sato, 1995).

The measurements have shown that the tips of the approach slabs are settling at an higher rate, relative to the settlement of the embankment. The mechanism causing the higher settlement rate of the approach slabs may be a flow of sand from under the slab to under the culvert, combined with higher densification caused by a concentration of stresses at the free ends of the slabs, motivated by the existence of a voided region under the approach slabs, close to the culvert vertical wall (Hölscher and Meijers, 2009).

The settlement rate observed at the free track (away from the culvert) after day 51 was estimated to be approximately constant and slightly above 1mm/month. This value is approximately the same as the value estimated for the settlement rate of the embankment, referred in Section 2.2.2. Therefore, it can be concluded that the settlement observed at the rail level in the free track, after the first period of rapid initial settlement, is mainly due to settlement of the subgrade, under the ballast layer. This mostly explains the bump observed in Figure 2.5: progressive settlement of the subgrade is not followed by the culvert, which is founded on piles. The culvert, therefore, stands in a relatively higher position. As so, the ballast thickness tends to increase on the long-term, due to

re-ballasting operations required for the upkeep of the track.

According to literature, the rapid settlement measured at the rail level during the first period after maintenance is mainly caused by densification of the ballast (Sato, 1995; Dahlberg, 2001). The lift of the track is performed with tamping operations which basically consists on lifting the sleepers to a prescribed level, after which steel tines are inserted in the ballast, vibrating and squeezing the underlying ballast particles to fill the voids under the sleepers (Suiker et al., 2005). This operation destroys the previous stable particle arrangement of the ballast, loosens the ballast, decreases its strength and stiffness and causes particle breakage (Esveld, 2001; Indraratna et al., 1998; Anderson and Key, 2000; Suiker et al., 2005). Therefore, as soon as traffic is reestablished, the densification of ballast restarts, by means of particle rearrangements, reducing its void ratio and augmenting its stiffness, until the ballast particles find a new stable configuration.

The higher initial settlement at the outer rail, compared to the inner rail, may be explained by the fact that the outer rail is closer to the ballast slope. This implies lower confinement of the ballast located under the outer rail, compared to the ballast under the inner rail, leading to higher rates of densification of the ballast (Lackenby et al., 2007). Moreover, it was visually observed that the inclination of the ballast slope, initially high after the maintenance, rapidly flattens as ballast reestablishes a stable configuration. This indicates a flow of ballast in the lateral horizontal direction, which also contributes for a global lateral rotation of the track towards the outside.

The initial settlement of ballast is smaller on top of the culvert than at the embankment areas. This is explained by the existence of a rigid surface under the ballast on top of the culvert. According to Saussine et al. (2006), who performed numerical simulations using the discrete element method, high stiffness of the underlayers implies a strong contact force network, more compactness of the pack, and less movement of particles under the sleepers, whereas in case of more flexible underlayers, the force intensity between particles is lower, which facilitates the circulation of particles under the sleepers. Furthermore, the initial lower settlement of ballast on top of the culvert can also be attributable to the fact that the existence of a rigid surface under the ballast, as is the culvert, will yield an higher efficiency during the compaction of the ballast layer, performed during the maintenance operation, immediately after the lift and tamping of the track (Faure, 1982).

The settlement of the top surface of the ballast is equal to the rail settlement plus the height of the voids existent under the sleepers. This settlement of the top surface of the ballast is due to the settlement of the embankment plus the settlement of the ballast and

sub-ballast layers. Therefore, an expression as

$$S_{\mathrm{r}.i} + h_i = S_{\mathrm{b}.i} + S_{\mathrm{sg}.i} \tag{2.1}$$

is possible for sleeper i, where S_{r} represents the settlement of the rail, h the height of the void under the sleeper, S_{b} represents the settlement due to changes in the ballast and sub-ballast layers, and S_{sg} the settlement of the subgrade. Using Equation (2.1), the settlement due to changes in the ballast and sub-ballast layer, S_{b}, at the culvert site can be estimated. For this, the quantity h_i is estimated for all sleepers, interpolating from the average results shown in Figure 2.7, and assuming no voids under the sleepers above the culvert, and no voids under the sleepers away from the transition zones.

Figure 2.14 shows the estimated settlement, after 7 months of service operation. The figure presents the assumed subgrade settlement, S_{sg}, which includes the effect caused by the rotation of the approach slabs, and the settlement of the ballast, S_{b}, determined with Equation (2.1), under the inner rail and under the outer rail. From Figure 2.14, it can be seen that the ballast settlement (S_{b}) presents significant fluctuations on the transition zones. This settlement is maximum on locations -1.8 m and 1.8 m, which are locations on top of the approach slabs but close to the culvert. Figure 2.14 shows that the settlement on the transition zones (equal to $S_{\mathrm{b}} + S_{\mathrm{sg}}$) is caused by two factors: a rotation of the approach slabs, motivated by the subgrade settlement, which is dominant between 3 m to 6.6 m away from the culvert center, and increased localized permanent deformations of the ballast layer, which is dominant between 1.2 m to 3.0 m away from the culvert center.

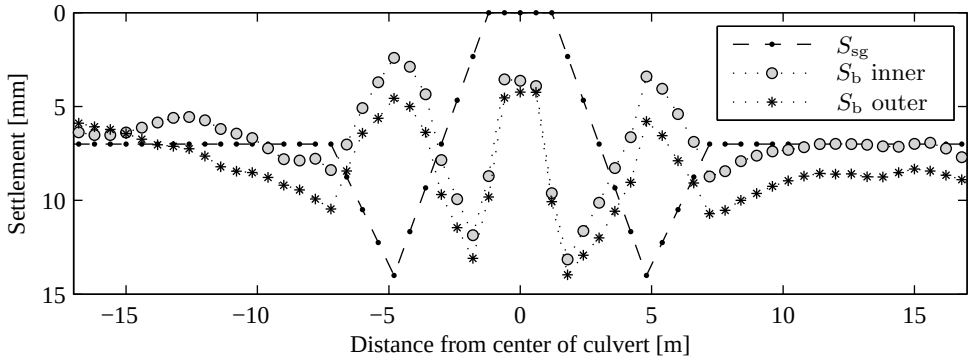

Figure 2.14: Estimated settlement 7 months after the maintenance operation: (i) autonomous settlement due to subgrade, (ii) ballast settlement under the inner rail and (iii) ballast settlement under the outer rail

The short-term measurements have shown that the dynamic displacement amplitudes are higher at the transition zones, above the approach slabs, than at the free track, away from

the transition, or above the culvert. The reason for these higher displacements seems to be the existence of consecutive hanging sleepers on both sides of the culvert. Figure 2.5 shows that the track level, starting from the culvert centre to each side, is similar to that of a uniformly loaded cantilever beam: this is a preliminary indication for the existence of consecutive hanging sleepers. Furthermore, the increase in downward displacements evidenced in Figure 2.13, follows approximately the void profile shown in Figure 2.7.

2.2.5 Research questions

The monitoring campaign has given valuable data that allowed for a comprehensive understanding of the short-term and long-term behaviour of a culvert transition. However, there are still some aspects requiring further analyses and clarification. Some of these aspects are:

(i) how many consecutive sleepers are hanging, and what is the amount of void under each hanging sleeper?

(ii) what is the reason for the upward displacement spike of the sleepers located at the transition zones?

(iii) what is the force transmitted through each sleeper to the underlying ballast in the transition area?

(iv) what are the causes for the observed increased settlement of the ballast above the approach slabs, as evidenced in Figure 2.14?

These aspects will be investigated in Chapters 4 to 6. For this, mathematical models, adequate to represent the short-term and long-term behaviour of transition zones, will be used. These models will be validated with the data collected from the field measurements described in this Chapter. The next Chapter 3 summarizes existing models for railway tracks and ballast behaviour.

Chapter 3

State-of-the-Art on Modelling of Ballast and Railway Tracks

The existing technical literature is reviewed with emphasis on two main topics: the behaviour of ballast under dynamic loading, and mathematical models representative of railway tracks loaded by moving trains. Recent reviews describing comprehensively these issues can be found in Ionescu (2004); Lim (2004); Indraratna and Salim (2005) for the mechanics of ballast, and in Beskou and Theodorakopoulos (2011) for models representing railway tracks.

3.1 The mechanical behaviour of ballast

Ballast is used as a load-bearing drainage material in railway tracks. It consists on medium to coarse sized aggregates (10-60 mm), free from dust and not prone to cementing action (Esveld, 2001; Ionescu, 2004; Indraratna et al., 2006). Ballasted track is the most common railway structure thanks to its relatively low cost of construction and possibility of rapid repositioning of the track geometry. The main function of ballast is to distribute the train loads to the underlying subsoil, to damp dynamic loading and to provide lateral resistance and rapid drainage (Esveld, 2001; Suiker, 2002; Burrow et al., 2007). The material may be granite, limestone, basalt, diorite, gravel, among others (Selig and Waters, 1994). The thickness of the ballast layer must assure a uniform distribution of loads to the underlying subgrade and its optimum value is usually 250-300 mm, measured from the bottom surface of the sleepers (Esveld, 2001).

3.1.1 Resilient behaviour

The deformation of ballast produced during one cycle of railway-type loading can be separated in a resilient (recoverable) part and a permanent part, as depicted in Figure 3.1 (a). Except for the initial phase of loading, while ballast is in a loose state, the deformation of ballast during train loading is essentially recoverable (Uzan, 1985; Fortunato, 2005). Due to this, the non-elastic behaviour of ballast is frequently neglected on constitutive models, assuming the material presents an elastic response, as shown in Figure 3.1 (b).

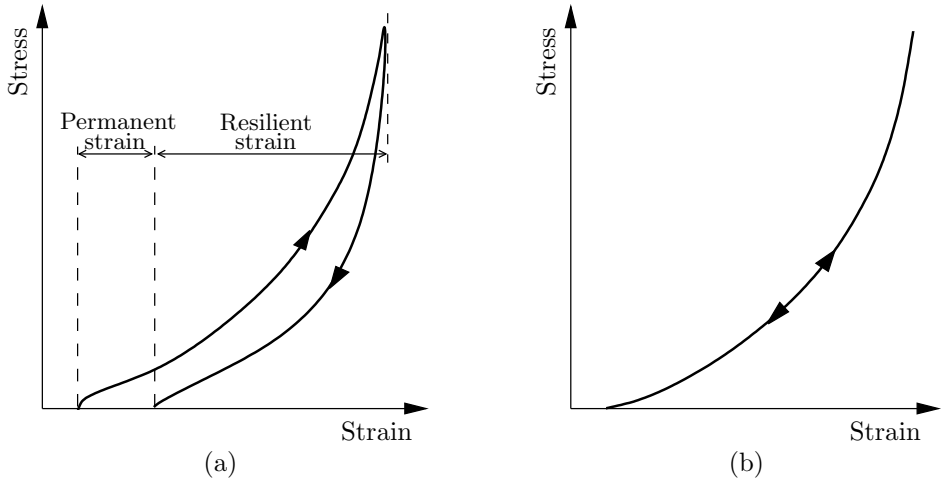

Figure 3.1: Strains during one cycle of compression load application. (a) - separation between permanent and resilient strains; (b) - non-linear elastic model

The resilient behaviour of ballast is highly governed by deformation of the ballast particles under compression loads. At a microscopic level, when two (sphere) particles are gradually pressed against each other, the contact surface increases, and the rate of change of the contact stress decreases, leading to higher stiffness at higher level of applied pressure (Timoshenko, 1915). This partly explains the non-linear stress-strain path of ballast under compression loads, with the stiffness increasing with the stress level, as can be seen in Figure 3.1 (b).

The resilient nature of ballast is commonly quantified by the resilient modulus, E_r and the Poisson's ratio, ν, which for repeated load triaxial tests with constant confining pressure (CCP) are defined as,

$$E_\mathrm{r} = \frac{\Delta(\sigma_1 - \sigma_3)}{\epsilon_{1,\mathrm{r}}} \tag{3.1}$$

$$\nu = -\frac{\epsilon_{3,\mathrm{r}}}{\epsilon_{1,\mathrm{r}}} \tag{3.2}$$

where σ_1 and σ_3 are the major and minor principal stresses, and $\epsilon_{1,\mathrm{r}}$ and $\epsilon_{3,\mathrm{r}}$ are the major and minor recoverable strains, respectively. The resilient modulus is the (non-linear) equivalent to the Young's modulus of the traditional theory of linear elasticity.

The resilient modulus E_r increases considerably with the stress level, mainly with the confining pressure and the sum of principal stresses (Hicks, 1970; Uzan, 1985; Sweere, 1990; Kolisoja, 1997). The modulus E_r also increases with the number of applied load cycles, N, mainly during the first cycles (Allen, 1973; Kedhr, 1985). After the completion of a small number of cycles (typically less than 1000 cycles), the value of E_r still increases with N, but at a very small rate (Lackenby et al., 2007). Figure 3.2 represents a typical stress-strain diagram of a granular material under repeated loading. The resilient modulus at the first load cycle, at the 26^{th} cycle, and at the final stage of the test, is the inclination of the corresponding dashed lines in the figure. The figure also shows the stiffening of the material with the increase in stress and the stabilization of the stress-strain path for increasing N.

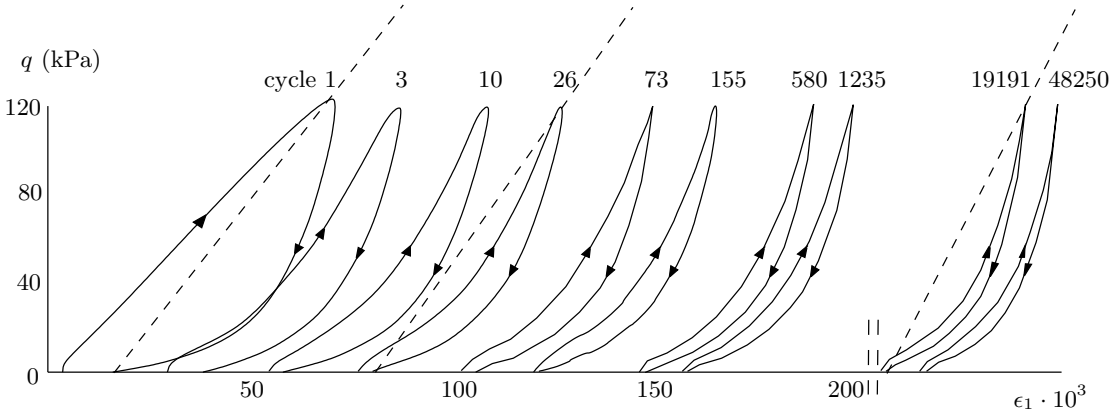

Figure 3.2: Stress-strain diagram of a granular material under repeated loading (Allaart, 1992)

The most widely used model to describe the non-linear resilient nature of unbound granular materials is the $K-\theta$ model (Brown and Pell, 1967; Hicks, 1970; Hicks and Monismith, 1972). This model was developed to describe the results of CCP tests and expresses the dependency of the resilient modulus on the sum of the principal stresses, according to:

$$E_\mathrm{r} = K_1 \left(\frac{\theta}{\theta_0} \right)^{K_2} \tag{3.3}$$

where θ is the sum of the principal stresses, defined positive for compression, which is the first stress invariant, θ_0 is a reference stress usually equal to 100kPa, and K_1 and K_2 are material parameters. In this model the Poisson's ratio is the third material parameter and is assumed constant.

According to Correia et al. (1999), when, in the end of the 70's, more evolved triaxial tests with variable confining pressure (VCP) were performed to better represent the *in situ* loading conditions, it was seen that the resilient modulus depends not only on the sum of the principal stresses, θ, but also on the stress path, or the stress ratio (p/q) and that the Poisson's ratio is not a constant and varies with the applied stresses (Brown and Hyde, 1975; Boyce, 1980; Sweere, 1990; Lackenby et al., 2007).

For that reason, Boyce (1980) proposed a different non-linear elastic model to describe the behaviour of granular materials under repeated loading. Instead of using the resilient modulus and the Poisson's ratio to characterize the stress-strain relationship, Boyce uses a different approach, based on the bulk and shear moduli:

$$p = K\ \epsilon_{\mathrm{v,r}} \tag{3.4}$$

$$q = 3\ G\ \epsilon_{\mathrm{s,r}} \tag{3.5}$$

where K is the bulk modulus, G is the shear modulus, p is the mean normal stress, q is the shear or deviatoric stress, $\epsilon_{\mathrm{v,r}}$ is the recoverable volumetric strain and $\epsilon_{\mathrm{s,r}}$ is the recoverable shear strain. According to Brown and Hyde (1975), the separation of stresses and strains into volumetric and shear components gives a better description of the elastic behaviour of granular materials. In triaxial tests, where $\sigma_2 = \sigma_3$ and $\epsilon_2 = \epsilon_3$, these stress and strain quantities are defined according to:

$$\begin{aligned} p &= 1/3\,(\sigma_1 + 2\sigma_3) \\ q &= \sigma_1 - \sigma_3 \\ \epsilon_{\mathrm{v,r}} &= \epsilon_{1,\mathrm{r}} + 2\epsilon_{3,\mathrm{r}} \\ \epsilon_{\mathrm{s,r}} &= 2/3\,(\epsilon_{1,\mathrm{r}} - \epsilon_{3,\mathrm{r}}) \end{aligned}$$

In the model of Boyce, the stress dependent values of K and G are determined according to:

$$K = K_1 \left(\frac{p}{p_0}\right)^{1-n} \cdot \frac{1}{1 - \frac{q^2}{p^2}\beta} \tag{3.6}$$

$$G = G_1 \left(\frac{p}{p_0}\right)^{1-n} \tag{3.7}$$

with

$$\beta = \frac{K_1\,(1-n)}{6G_1}$$

where K_1, G_1 and n are the material parameters of the model and p_0 is again a reference

stress value. The term $1 - \frac{q^2}{p^2}\beta$, included in Equation (3.6), was derived so that the model preserves elasticity, which also means that no strain energy disappears for any chosen stress-strain path (Timoshenko and Goodier, 1970; Allaart, 1992). According to Correia et al. (1999), the Boyce model is superior to the K-θ model in predicting the non-linear behaviour of granular materials in VCP tests, with coefficients of correlation ranging between 0.6 and 0.9.

Other models derived from the Boyce model are available in the literature. For example, the contour model presented by Brown and Pappin (1981) extends the three-parameter model of Boyce to a five or even six parameter model. This model is able to predict test results very well, but it can be shown that this model is no longer entirely elastic (Allaart, 1992).

3.1.2 Settlement of ballast

The degradation of the track geometry is due to settlements on the supporting layers of ballast, sub-ballast and subgrade. In regular tracks founded on good subgrade, the main contribution to track settlement is from the ballast, as can be seen in Figure 3.3, whereas the subgrade settlement is only significant during the early life of the track (Shenton, 1985).

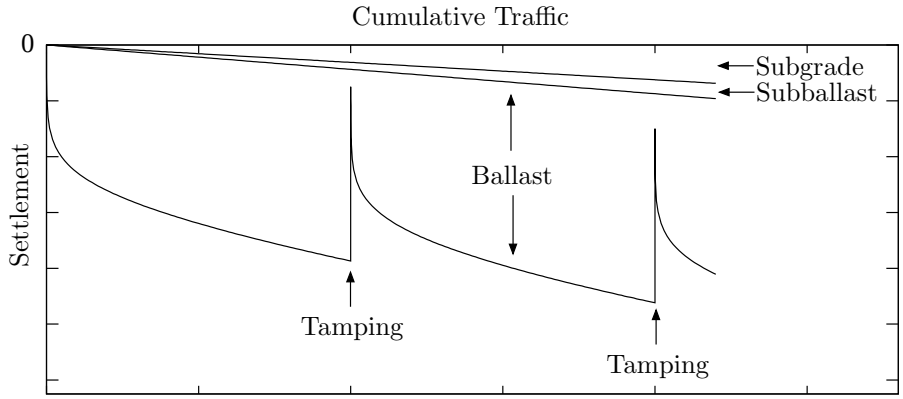

Figure 3.3: Relative contributions of substructure to the settlement of the track (from (Selig and Waters, 1994)).

The settlement of ballast, with given material properties and density, strongly depends on the loading amplitude and history (Stewart, 1986; Diyaljee, 1987). The accumulation of axial permanent strain in granular materials, as ballast, is known to be directly related to deviator (shear) stress and inversely related to confining pressure (Lekarp et al., 2000).

Figure 3.4 shows results of cyclic triaxial tests on ballast performed by Stewart (1986). Four stress paths are shown where the loading amplitude changes at every 1000 load cycles. The loading was applied at 1Hz frequency varying from a constant minimum of 21kPa (coincident with the horizontal confining stress) to the following vertical amplitudes: 42kPa (A), 64kPa (B), 86kPa (C) or 107kPa (D). The stress paths are defined in the figure. It can be seen that when the loading amplitude increases above any previously applied value, the permanent deformation increases immediately, approaching asymptotically a new value with increasing number of cycles. According to these tests, the final permanent deformation does not depend on the sequence of loading. It can also be seen that the settlement rate decreases with an increasing number of load cycles, if the loading amplitude remains constant.

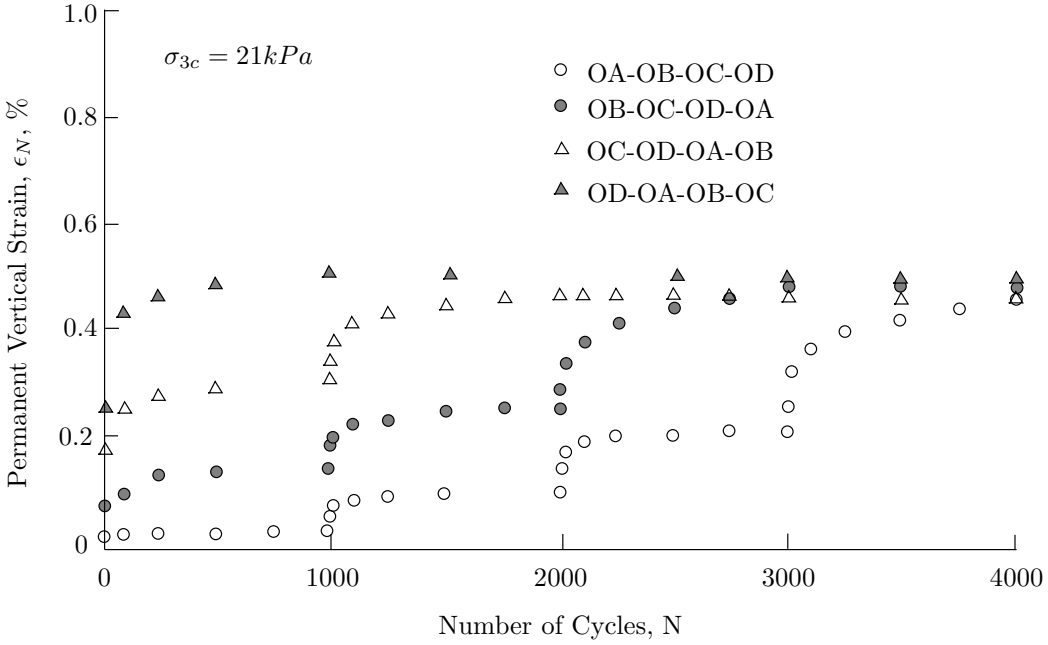

Figure 3.4: Permanent strains in ballast from four triaxial tests with variable cyclic amplitudes of loading (from Stewart (1986)).
σ_1 - (variable) vertical stress; σ_3 - (constant) horizontal stress

Other factors influencing ballast behaviour are the minimum load caused by the unloaded track weight and impact loads on the ballast. The former is beneficial regarding the permanent deformation, by preventing dilatant behaviour and flow of ballast under cyclic loading (Baessler and Ruecker, 2003; Augustin et al., 2003; Lackenby et al., 2007). Impact loads, on the other hand, will increase permanent deformation on the ballast (Baessler and Ruecker, 2003).

The factors described above activate several degradation mechanisms in the ballast. Prob-

ably the most important mechanism is compaction, where the packing assembly of ballast is compressed due to gradual particle rearrangements (Sato, 1995; Dahlberg, 2003). This mechanism is dominant when ballast is first loaded, after the tamping operations. The second mechanism is the flow of ballast particles on lateral and longitudinal direction, especially from under the sleepers. Sato (Sato, 1995) considers this to develop linearly with the accumulation of traffic. The flow of ballast occurs in cases where the ballast is poorly confined, when suspended sleepers impact the ballast (Baessler and Ruecker, 2003) or when high lateral loads are transmitted by the trains to the sleepers. Other degradation mechanisms include breakage and abrasion of ballast particles (Lim, 2004; Sekine et al., 2005; Lackenby et al., 2007), the penetration of finer particles belonging to sub-layers on the ballast layer or the jumping of ballast particles caused by high dynamic action (Sato, 1995; Baessler and Ruecker, 2003).

Existing models

Available railway settlement models include the logarithmic model (ORE, 1970; Alva-Hurtado and Selig, 1981), the Shenton model (Shenton, 1985), the Sato model (Sato, 1995) and the Hettler model (Mauer, 1995). Dahlberg (2001) presents a critical review of some of the most important models, including these ones. Common features are:

(i) the models are empirically based;

(ii) the track settlement is characterized by two phases: an initial phase of rapid settlement after tamping followed by a phase where the settlement rate is more or less constant with time (or number of cycles);

(iii) the loading of the track is determined by the number of loading cycles and/or passed tonnage;

(iv) the loading characteristics are assumed to be constant in time.

The logarithmic model states that

$$\epsilon_N = \epsilon_1(1 + C\ log(N)) \tag{3.8}$$

where ϵ_N is the total permanent strain after load cycle N, ϵ_1 is the permanent strain after the first load cycle and C is a parameter of the model. This model was derived from triaxial experiments on ballast. The accumulated settlement after load cycle N may be estimated from $S_N = \epsilon_N \cdot H$, where S_N is the accumulated settlement and H is the thickness of ballast.

Through experiments and experience in Japan, Sato states that the accumulated settlement of the ballast may be determined from:

$$S_N = \gamma(1 - \mathrm{e}^{-\alpha N}) + \beta N \tag{3.9}$$

where N is the number of load cycles, and α, β and γ are parameters. In these two models, no distinction is made between loadings of varying magnitudes. Their application is therefore limited to cases where the loading magnitudes are approximately constant in time.

Based on available field data from world wide sources, Shenton stated that the logarithmic model may underestimate the settlement for a large number of cycles and that a preferable model is:

$$S_N = K_s \frac{A_{\mathrm{eq}}}{20} \left(K_1 N^{0.2} + K_2 N\right) \tag{3.10}$$

where S_N is the total settlement, A_{eq} the equivalent axle load, K_s a factor function of the sleeper type and size, ballast type and thickness, and the subgrade, K_1 a factor function of the lift given to the track during maintenance and K_2 a constant value. According to Shenton, the first part represents the ballast settlement immediately after tamping, predominating up to one million load cycles, and the second part the residual settlement which occurs in the deeper ballast and foundation. The proposed formula to determine the equivalent axle load is:

$$A_{\mathrm{eq}} = \sqrt[5]{\frac{\sum_{n=1}^{N} A_n^5}{N}} \tag{3.11}$$

where A_n is the axle load passing at load cycle n.

Hettler presents a model, based on the logarithmic model (Eq. (3.8)):

$$S_N = s \; F_{\mathrm{eq}}^{1.6} \; (1 + C \; log(N)) \tag{3.12}$$

where F_{eq} is the equivalent sleeper-ballast force and s and C are model parameters. Hettler defined the equivalent sleeper-ballast force as the mean value of the applied loads:

$$F_{\mathrm{eq}} = \frac{1}{N} \sum_{n=1}^{N} F_n \tag{3.13}$$

Although able to handle cases of varying loading amplitudes, the equivalent load concept, present in Equations (3.11) and (3.13), is not able to reproduce the behaviour presented in Figure 3.4. This figure shows that the settlement rate may strongly increase if the loading is raised above any previously applied value. Using the models above, the settlement rate

is much less influenced by changes in F_n.

Mathematical schemes for the logarithmic based models, (3.8) and (3.12), with variable loading amplitudes can be found in (Stewart, 1986; Ford, 1995; Mauer, 1995). These methods are only practical for cases with a limited number of load changes, between phases of constant loading amplitudes.

The loading history is not treated accurately with the models presented above. Therefore, they are hardly suited to study cases where the amplitudes of loading may continuously change. This is the case in transition zones founded on soft soils. In Chapter 5, a novel settlement model to address this problem will be presented.

3.2 Mathematical models for railway tracks

3.2.1 Overview

The first mathematical models developed to determine the dynamic response of railtrack-like structures were one-dimensional. These models were generally composed of a beam, representing the rail, laid on an elastic or visco-elastic foundation, of the Winkler type, representing the ground (Timoshenko, 1915; Kenney, 1954; Mathews, 1958; Achenbach and Sun, 1965; Choros and Adams, 1979; Jezequel, 1980; Vestnitskii and Metrikine, 1993; Zhai and Cai, 1997; Bitzenbauer and Dinkel, 2002; Shamalta and Metrikine, 2003; Nielsen and Oscarsson, 2004; Zhang et al., 2008; Lei and Zhang, 2010). Most of these models are linear except (a few) for the conditions at the wheel-rail contact. The work of Nielsen and Oscarsson (2004) introduces the state-dependent properties of railpads and ballast/subgrade and it shows that the influence of these non-linear aspects is significant, for example, in the calculation of rail and sleeper bending moments.

These one-dimensional models do not include the three-dimensional wave field generated in the ground by the moving train. These models are therefore restricted to cases where the analyst is solely interested in the dynamic response at the rail/sleepers level. Furthermore, if the velocity of the train approaches the Rayleigh wave speed of the track (critical velocity effect (Krylov, 1995)), the waves in the ground, not contemplated in these models, will play a decisive role in the dynamic response of the track/ground system. For trains approaching the critical velocity of the track, the use of one-dimensional models should therefore be avoided (Vostroukhov, 2002).

The first three-dimensional model representing a railway track was derived by Fillipov (1961) and Labra (1975), to determine the steady-state response of a moving constant

force on an Euler-Bernoulli beam, resting on an homogeneous elastic half-space. This model was extended by Krylov (1995) and Dieterman and Metrikine (1996), for the case of train speeds above the critical velocity, and further elaborated by many authors to include moving harmonic forces (Dieterman and Metrikine, 1997), discrete support by the sleepers (Metrikine and Popp, 1999; Vostroukhov, 2002), homogeneous multilayering (Sheng et al., 1999; Kaynia et al., 2000; Vostroukhov, 2002), rail irregularities (Sheng et al., 2004), moving vehicle represented by a set of masses (Metrikine et al., 2005; Lombaert et al., 2006) or poroelastic behaviour of the soil (Cai et al., 2008; Sun et al., 2010). The models developed by these authors in these works assume invariant properties of the track in its longitudinal direction, and are therefore not adequate for the study of transition zones.

3.2.2 Methods of solution

Initially, the methods to solve the governing equations of the problems were analytic. Analytical methods mainly use the Fourier or the Laplace transform with respect to time and to the space variables, transforming the equations into the frequency and wave-number domain, and contour integration for the inversion process. Many times, the resolution starts with a change of coordinates to moving ones, and the transformations are applied to all variables but one, so that the problem is reduced from partial to an ordinary differential equation. The main difficulty with this analytic process is the inversion of the solution of the transformed equations. Closed-form solutions are only presented for some special and simplified cases. Otherwise, the inversion of the transformed solution is only possible using numerical methods. A recent review paper on mathematical models for railroads and railways by Beskou and Theodorakopoulos (2011) summarizes analytical methods and corresponding original papers.

Solutions based on analytical methods give reliable results, providing a better insight into the physics of the problem, and are useful to verify other models, not based on analytical methods. However, the development of solutions based on analytical methods have important limitations. For example, the geometry of the track-soil model must be sufficiently simple in order to have a treatable mathematical solution. Also, these methods are generally founded on the principle of linear behaviour of the dynamic system under study.

Non-linear aspects which are present on the dynamic behaviour of railway tracks are: (i) the possibility of loss of contact between the sleepers and the ballast (Lundqvist and Dahlberg, 2005), (ii) the non-linear contact between the wheels and the rails and (iii) the non-linear constitutive behaviour of the ballast and underlying soils, as discussed in

Section 3.1.

With the strong increase of processing capacity and speed of calculation of computers, numerical methods have been broadly used to determine solutions for the governing equations of the problems. These numerical methods usually operate in the time domain, whereas the above referred analytical methods usually operate in the frequency domain. The governing differential equations are discretized in the space domain, and the solution is calculated by numerical integration methods in the time domain (Clough and Penzien, 2003; Hughes, 1987). The available methods for discretization of the continuum field are the Finite Element Method (FEM) (Hughes, 1987), the Boundary Element Method (BEM) (Banerjee and Butterfield, 1981), the Infinite Element Method (IEM) (Bettess, 1980), and the Finite Difference Method (FDM). These methods may be applied in combination, as BEM and IEM are many times applied with FEM.

Numerical one-dimensional Winkler type models using the FEM may be found in (Zhai and Cai, 1997; Nielsen and Oscarsson, 2004; Zhang et al., 2008; Lei and Zhang, 2010). Two or three-dimensional numerical models using the FEM may be found in (Hall, 2003; Lundqvist and Dahlberg, 2005; Lane et al., 2007; Yang et al., 2009; Priest et al., 2010), using the BEM combined with the FEM in (Auersch, 2005; Sheng et al., 2006; Galvín and Domínguez, 2007; Chebli et al., 2008; Galvín et al., 2010), using the IEM combined with the FEM in (Costa et al., 2010; Kouroussis et al., 2011), or using the FDM in (Fortunato, 2005). These models are generally able to represent complex track geometries, e.g. with embankment/ballast slopes, railway vehicles represented by rigid-bodies systems moving at constant or variable speed, or rail and wheels imperfections.

The incorporation of non-linear aspects is possible using numerical integration methods in the time domain (Clough and Penzien, 2003). However, with exception made to some limited number of works, the constitutive model for the ballast/subgrade is generally assumed linear in most of the available dynamic numerical work on railways. The main reason for this is the computational time (still) required to numerically solve a non-linear dynamic system of equations, having possibly a large number of degrees-of-freedom. Among the few exceptions, Fortunato (2005) studies the behaviour of the railway infrastructure using a 3-D FDM model, considering the non-linear constitutive response of the ballast and sub-ballast layers. The numerical model used by Fortunato (2005) considered the static equilibrium of forces, only. Costa et al. (2010) uses a model in which the degradation of the stiffness/damping with strain is accounted for through an (iterative) equivalent linear analysis. The model uses 2.5D finite elements and is therefore restricted to structures which can be assumed to have invariant properties in one direction.

3.2.3 Models for transitions

There are only a few analytical solutions that study the case of tracks running over inhomogeneous foundations. One-dimensional Winkler type models, where a discontinuity is introduced by changing the stiffness values of the supporting springs, can be found in (Vesnitskii and Metrikine, 1993; Metrikine et al., 1998; Dimitrovová and Varandas, 2009). A two-dimensional model where a point load crosses the interface of two elastic half-planes can be found in (van Dalen and Metrikine, 2008). Results from these models show that the passage of a point load over an abrupt change of foundation stiffness may lead to the appearance of waves radiating from the discontinuity, if the velocity of the load approaches, or exceeds, the critical velocity of the track.

In this work, in Chapter 7, a novel model based on analytical methods for transition zones is presented. The model consists on two superposed Euler-Bernoulli beams, interconnected by visco-elastic elements, and supported on a visco-elastic foundation, where the stiffness of the (upper and lower) visco-elastic elements may change abruptly at a given section of the track. Being one-dimensional, the model has the corresponding limitations, referred above.

Numerical models to study transition zones can be found in (Schooleman, 1996; Gardien, 2005; Lundqvist et al., 2006; Ribeiro et al., 2007; Alves Ribeiro et al., 2007; Banimahd and Woodward, 2007; Galvín et al., 2010). Schooleman (1996) has performed numerical analyses on transition zones using three decoupled numerical models: a 2-D model for the subsurface layers, a 1-D discrete Winkler model for the rail and a three dof lumped mass model for the vehicle. The study focused on the influence of varying stiffness and/or unlevelled track on the forces in the track and on the accelerations in the carriage. The maximum allowed differential settlements for different velocities were determined. As an example, for the high-speed line (300km/h), a maximum differential settlement of 6 mm over 20 m is permitted. Gardien (2005) studied transition zones from a slab track (of the Rheda type) to ballasted track. He used a 2-D model which included a 10 dof model for each train carriage interacting with the track, and more detailed 3-D finite element models, to determine the characteristics of the springs and dampers of the track model. Gardien (2005) proposed several improvements on the design of these transitions, recommending that the differential sleeper load (on consecutive sleepers) be not greater than 45%, in order to limit differential ballast degradation. Lundqvist et al. (2006) performed dynamic finite element analyses to study the influence of railway track stiffness variations on the wheel/rail contact forces. He concluded that the wheel/rail contact forces variations can be reduced with an optimized stiffness variation in the transition zone, which can be built with under-sleeper pads and/or ballast mats. In all these works, the constitutive relations

of materials and springs were assumed linear.

From the literature (see Section 3.1), it was seen that the resilient behaviour of ballast in railway tracks is non-linear, with stiffness increasing with the stress level. However, most numerical models representing railway tracks assume the linear elastic model for the track bed layers, including the ballast. Furthermore, and as seen in Chapter 2, in transition zones, another important non-linear aspect is the existence of voids under the sleepers, determining an on/off contact between these hanging sleepers and the ballast. This work seeks the development of computer models adequate to analyze the dynamic and the long-term behaviour of transition zones, incorporating these non-linearities. To incorporate the non-linear track behaviour on a transition, a time dependent numerical model is required. This model will be developed in this work. As so, Chapter 4 presents a one-dimensional numerical non-linear model, considering the train-track interaction, and Chapter 6 presents a three-dimensional non-linear dynamic finite element program. Both models allow the consideration of the non-linear material behaviour of the granular layers of ballast and sub-ballast, and the non-linear contact between the sleepers and the ballast.

Chapter 4

Modelling of Train-Track Dynamic Response*

4.1 Introduction

In this Chapter, a numerical non-linear model for the calculation of the dynamic forces exerted by the sleepers on the ballast due to a train passage is presented.

As discussed in previous Chapter 3, the non-linear behaviour of the track-soil system should be represented to evaluate its dynamic response to moving loads. Important non-linear aspects include the loss of contact between the sleepers and the ballast, and the non-linear constitutive behaviour of the ballast. If hanging sleepers appear, and/or the track support stiffness changes, and/or the vertical level is not horizontal, the pre-load on the ballast, due to the track weight, may differ strongly per sleeper. Due to the non-linear response, this variation implies a different receptance of each sleeper felt by the train passing over. Also, hanging sleepers and the track unevenness, typical above transition zones, may lead to high impact stresses during a train passage at some sleepers, and low (or even zero) stresses at other adjacent sleepers. This influences the long-term behaviour of the track (Baessler and Ruecker, 2003; Augustin et al., 2003).

The key parameters of the model are selected from the field tests, presented in Chapter 2. The aim is to interpret some of the characteristics of the measured dynamic response of the culvert case-study, as referred at the end of Chapter 2, as well as to discuss implications of the numerical results on the long-term behaviour of transition zones.

* This Chapter is based on (Varandas et al., 2011)

4.2 Numerical model

The presented model is non-linear, taking into account the unloaded position of the track and the ballast (including the hanging distances), and the speed and dynamic properties of the train. The calculations are divided in two phases: a first phase where the initial state of the track is determined and a second phase corresponding to the train passage over the track.

Figure 4.1 shows a schematic representation of the train-track model. The main assumptions of the model are:

- Symmetry along the longitudinal axis of the track. The lateral motions of the vehicle and differences between (the supports of) the two rails are neglected;
- The stiffness of the support (ballast/soil) of the sleeper is non-linear and increases with increasing displacement of the sleeper contacting the ballast;
- Initially, some sleepers may be hanging;
- The contact between the sleeper soffit and the ballast may be lost and/or re-established during dynamic loading;
- The ballast around the sleeper generates friction damping and the vibration of the sleeper contacting the underlying ballast generates radiation damping. These are assumed to be proportional to the vertical velocity of the sleeper;
- The influence of the motion of the hanging sleeper (which may decrease the contact surface) on the friction damping is neglected.
- The stiffness of the railpad, between the rail and the sleeper, is sufficiently high, so that it can be neglected from studies limited to the low frequency range (Ilias, 1999).

The track model is one-dimensional. The continuous rail is assumed to follow the Euler-Bernoulli conditions of engineering beam theory. This seemed adequate since the analyses focused on the low-frequency components of the response (Dahlberg, 2003). The sleepers are represented by their masses; their support is represented by a discrete spring-damper system representing the behaviour of the foundation, ballast, embankment and soil included. The rail is modelled by using finite elements. The nodal distance in the mesh is an integer fraction of the sleeper distance. This makes it possible to concentrate each sleeper mass and support response in a node.

Each carriage of the train is modelled as an assembly of rigid bodies connected by springs and dampers forming a 10 dof system (Zhai and Cai, 1997). The mass of the car, bogies

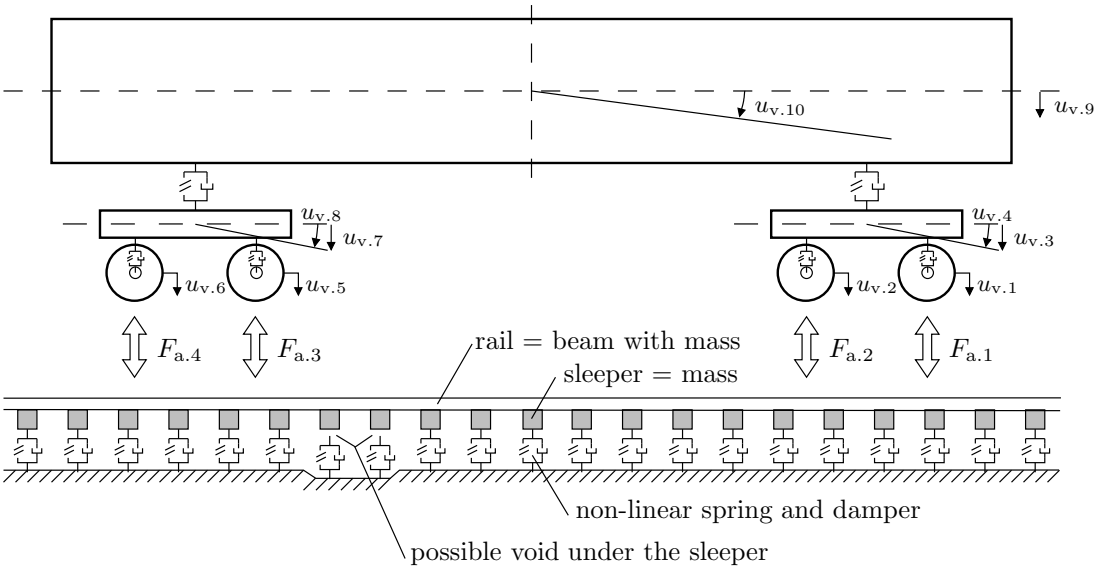

Figure 4.1: Train-track interaction model - $u_{v.i}$ is the ith dof of the vehicle and $F_{a.j}$ is the interaction force between wheel j and the rail

and wheels, as well as the longitudinal rotation inertia of car and bogies, are included. Figure 4.1 identifies the 10 dof, $u_{v.i}$. The subscript v refers to vehicle. The two systems, the track and the vehicle, are linked together by the interaction forces between the wheels and the rail, represented in Figure 4.1 as $F_{a.j}$.

4.2.1 Initial state of the track

The geometric configuration of the track prior to the passage of the trains is designated, here and in the sequel, as initial state of the track. Its calculation requires knowledge of the dead-weight forces exerted by the sleepers on the supporting ballast, considering the level of the track (supposedly known from measurements) and the stiffness of the track's support. In general, the stiffness is non-linear and, on a transition, it varies in space.

The determination of these forces seems to be a standard inverse finite element problem, consisting in calculating the forces on the track using the available data from the levelling. However, the levelling data contains errors due to its limited accuracy (0.50mm on the case of the levelling shown in Figure 2.5), introducing significant errors on the solution. Instead, an iterative calculation method is used. The general procedure will be described hereafter.

Sleeper support

The displacement of each sleeper i on the vertical direction will be called $u_{\mathrm{t}.i}$, defined positive downwards. The subscript t refers to track. Each sleeper has a spring under it (see Figure 4.1). The spring reaction against the sleeper is zero in a non-contact situation and increases non-linearly with increasing downward displacement in the contact situation. Figure 4.2 illustrates the spring behaviour on a one dof system. The system on the left hand side is unloaded and the system on the right hand side is the final position after loading. The value of the loading force is F_{eq} and the corresponding equilibrium position is u_{eq}. The displacement at which the sleeper contacts the ballast is designated by u_{c}. The properties of the force-displacement paths of the springs, as will be described on the next sub-section, are assumed known, except the contact positions. The level of the track is known from the measurement.

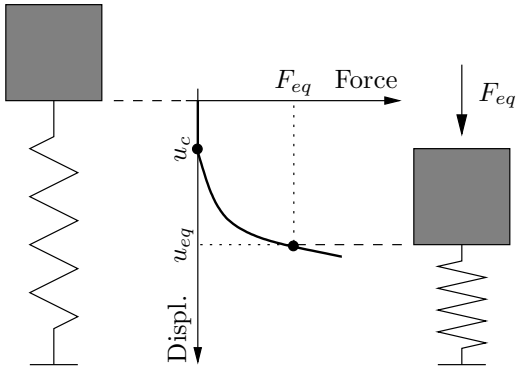

Figure 4.2: General force-displacement behaviour of the springs

Iterative procedure

(i) The rail/sleeper system is initially on a horizontal position ($u_{\mathrm{t}.i} = 0$). The contact position of each spring is defined according to:

$$u_{\mathrm{c1}.i} = u_{\mathrm{level}.i} \tag{4.1}$$

where $u_{\mathrm{c1}.i}$ is the contact position of sleeper i and $u_{\mathrm{level}.i}$ is the position of sleeper i known from the levelling. Figure 4.3 shows this initial phase of the calculations.

Then, the equilibrium position of the rail/sleeper system under the gravity loads is found (the track moves down due to gravity). The resultant equilibrium position of each sleeper i is here called $u_{\mathrm{eq1}.i}$. Having in mind that the weight is imposed downward, it is expected that this equilibrium position be generally somewhat lower than the track level, $u_{\mathrm{level}.i}$.

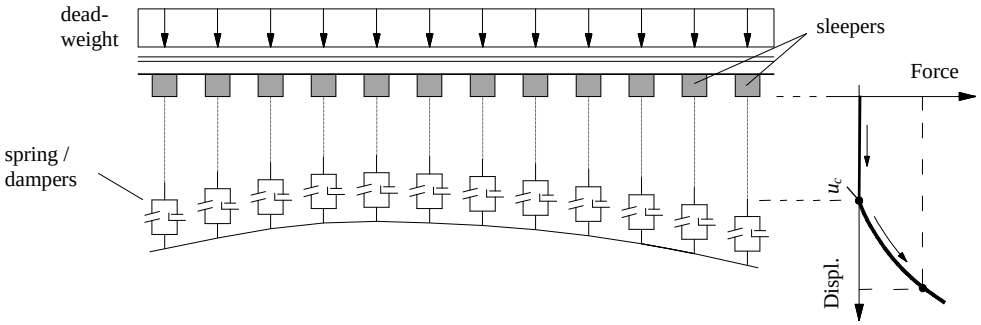

Figure 4.3: Rail/sleeper system on iteration one of calculations

(ii) The contact position of each spring is now repositioned according to:

$$u_{c2.i} = \begin{cases} u_{c1.i} - (u_{eq1.i} - u_{c1.i}) & \text{, if } u_{eq1.i} > u_{level.i}, \\ u_{c1.i} & \text{, if } u_{eq1.i} \leq u_{level.i}. \end{cases} \tag{4.2}$$

where $u_{c2.i}$ is the new contact position of the sleeper i. According to Eq. (4.2), if the equilibrium position found in the previous step (i) is lower than the track level, then the contact position of the corresponding sleepers are lift by an amount equal to the difference between the previous equilibrium position and the track level. The rail/sleeper system is again positioned at the horizontal origin, and a new equilibrium position of the rail/sleeper system with the gravity loads, $u_{eq2.i}$, is found. This equilibrium position is very close to the levelling: $u_{eq2.i} \approx u_{level.i}$. The differences should be lower, on absolute value, than half the value of the levelling accuracy. In this case the obtained solution is acceptable since the error is within the measuring accuracy. Higher differences may occur due to differences between reality and the model in the weight of the track, the bending stiffness of the rail or the sleeper spacing.

(iii) When the level of the track is significantly uneven, as on the culvert case, some sleepers will not reach the contact position previously defined for that sleeper. These sleepers are hanging and the equilibrium position $u_{eq2.i}$ is at higher level than the contact position $u_{c2.i}$ for these sleepers. On these cases these contact positions are repositioned according to $u_{c2.i} = u_{eq2.i}$. These sleepers are again in contact with the ballast although no force is transmitted through it.

(iv) Finally, the hanging distances, when existent, are introduced at the corresponding sleepers. For this, the contact positions of these sleepers are repositioned according to:

$$u_{c3.i} = u_{c2.i} + h_i \tag{4.3}$$

where $u_{c3.i}$ is the new contact position of sleeper i, $u_{c2.i}$ is its previous contact position

and h_i is its hanging distance. When the hanging distances are introduced only in the group of sleepers referred to in step (iii), then this final step does not alter the equilibrium position of the rail/sleeper system. Otherwise, a new calculation step must be performed in order to obtain the final force distribution in equilibrium with the dead-weight of the track.

The hanging distances can be estimated by engineering judgment, measured directly by special void indicators or estimated from dynamic measurements of the motion of sleepers and ballast during train passage.

On the end of the iterative procedure, the final equilibrium position of the rail/sleeper system is approximately equal to its given vertical profile and the equilibrium forces, which support the rail-sleepers system in that position, are approximately known. This force distribution corresponds to the pre-load on the ballast before the train passage.

4.2.2 Equations of motion and time integration

According to Newton's second law of motion and d'Alembert's Principle, the equations of motion in vector form for vehicle and track are, respectively:

$$\begin{cases} \mathbf{f}_{\mathrm{v.e}} + \mathbf{f}_{\mathrm{v.d}} + \mathbf{f}_{\mathrm{v.i}} = \mathbf{f}_{\mathrm{v.g}} + \mathbf{f}_{\mathrm{a}} \\ \mathbf{f}_{\mathrm{t.e}} + \mathbf{f}_{\mathrm{t.d}} + \mathbf{f}_{\mathrm{t.i}} = \mathbf{f}_{\mathrm{t.g}} - \mathbf{f}_{\mathrm{a}} \end{cases} \tag{4.4}$$

where the resisting forces due to deformation ($\mathbf{f}_{\mathrm{e}}$), damping ($\mathbf{f}_{\mathrm{d}}$) and inertia ($\mathbf{f}_{\mathrm{i}}$) are in equilibrium with the applied loads, in this case, the gravity load ($\mathbf{f}_{\mathrm{g}}$) and the interaction force between the vehicle and the track ($\mathbf{f}_{\mathrm{a}}$). Again, the subscripts v and t relate to vehicle and track, respectively.

The behaviour of the vehicle system is assumed to be linear. It can be written in matrix form as:

$$\mathbf{K}_{\mathrm{v}}\mathbf{u}_{\mathrm{v}} + \mathbf{C}_{\mathrm{v}}\mathbf{v}_{\mathrm{v}} + \mathbf{M}_{\mathrm{v}}\mathbf{a}_{\mathrm{v}} = \mathbf{f}_{\mathrm{v.g}} + \mathbf{f}_{\mathrm{a}} \tag{4.5}$$

where $\mathbf{K}_{\mathrm{v}}$, $\mathbf{C}_{\mathrm{v}}$ and $\mathbf{M}_{\mathrm{v}}$ are the stiffness, damping and mass matrices of the vehicle, as may be derived from (Zhai and Cai, 1997), and $\mathbf{u}_{\mathrm{v}}$, $\mathbf{v}_{\mathrm{v}}$ and $\mathbf{a}_{\mathrm{v}}$ are, respectively, the vectors of generalized displacements, velocities and accelerations.

The track itself behaves linearly, but the springs and dampers which support the sleepers introduce corresponding non-linearities. Since the springs and dampers are support elements, the equations of motion can be written:

$$\mathbf{K}_{\mathrm{t}}\mathbf{u}_{\mathrm{t}} + \mathbf{C}_{\mathrm{t}}\mathbf{v}_{\mathrm{t}} + \mathbf{M}_{\mathrm{t}}\mathbf{a}_{\mathrm{t}} = -\mathbf{f}_{\mathrm{t.sp}} - \mathbf{f}_{\mathrm{t.rd}} + \mathbf{f}_{\mathrm{t.g}} - \mathbf{f}_{\mathrm{a}} \tag{4.6}$$

where $\mathbf{K}_\mathrm{t}$, $\mathbf{C}_\mathrm{t}$ and $\mathbf{M}_\mathrm{t}$ are, respectively, the stiffness, damping and mass matrices of the beam representing the rail and $\mathbf{f}_\mathrm{t.sp}$ and $\mathbf{f}_\mathrm{t.rd}$ the stiffness and damping force vectors of the foundation. These still depend on $\mathbf{u}_\mathrm{t}$ and $\mathbf{v}_\mathrm{t}$. This representation is detailed further into the text.

All matrices were obtained by traditional finite element assembling procedure. $\mathbf{M}_\mathrm{t}$ contains the mass contributions from the rail and the sleepers. $\mathbf{K}_\mathrm{t}$ was assembled using the 4x4 element stiffness matrix of the Euler-Bernoulli beam, as can be found in, e.g. (Clough and Penzien, 2003). The rotational degrees-of-freedom were condensed after the global assembling.

The damping matrix $\mathbf{C}_\mathrm{t}$ represents the material damping of the track system due to rail and sleeper internal damping and the lateral friction between sleepers and the confining ballast. All these terms are assumed to be linear. Matrix $\mathbf{C}_\mathrm{t}$ corresponds to the assumption of Rayleigh damping (Clough and Penzien, 2003):

$$\mathbf{C}_\mathrm{t} = a_0\mathbf{M}_\mathrm{t} + a_1(\mathbf{K}_\mathrm{t} + \mathbf{K}_\mathrm{sp}) \tag{4.7}$$

where $\mathbf{K}_\mathrm{sp}$ is the support stiffness below the sleeper, accounted solely with its linear part (the terms $k_{1.i}$ presented below). The parameters a_0 and a_1 were determined according to:

$$\begin{bmatrix} a_0 \\ a_1 \end{bmatrix} = \frac{2\xi}{\omega_1 + \omega_2} \begin{bmatrix} \omega_1 \ \omega_2 \\ 1 \end{bmatrix} \tag{4.8}$$

where ξ is the damping ratio selected for two radial frequencies ω_1 and ω_2.

Definition of the sleeper support reaction

$\mathbf{f}_\mathrm{t.sp}$ and $\mathbf{f}_\mathrm{t.rd}$ are the support reactions at the sleeper's soffit. The force-displacement relation of the springs is shown in Figure 4.2. The behaviour of spring i is defined by:

$$F_{\mathrm{t.sp}.i} = \begin{cases} k_{1.i}(u_{\mathrm{t}.i} - u_{\mathrm{c}.i}) + k_{2.i}(u_{\mathrm{t}.i} - u_{\mathrm{c}.i})^{p_i} & \text{, if } u_{\mathrm{t}.i} \geq u_{\mathrm{c}.i}, \\ k_{3.i}(u_{\mathrm{t}.i} - u_{\mathrm{c}.i}) & \text{, if } u_{\mathrm{t}.i} < u_{\mathrm{c}.i}. \end{cases} \tag{4.9}$$

where $k_{1.i}$, $k_{2.i}$ and p_i are stiffness parameters on the contact situation (compression) and $k_{3.i}$ is the linear stiffness on the no-contact situation (tension). A non-zero (positive) value of $k_{3.i}$ may be defined to represent adhesion between the sleeper and the ballast. In this work, this value was assumed to be zero. The force-displacement relation of the springs for the compression case was derived from available field measurements. Some examples can be found in (Dahlberg, 2003) and (Nielsen and Oscarsson, 2004).

The radiation damping, accounted in $\mathbf{f}_{\mathrm{t.rd}}$, refers to the damping resulting from the contact between the base of the sleeper and the ballast. The damping due to the lateral friction with the confining ballast is included in the damping matrix $\mathbf{C}_{\mathrm{t}}$. Lysmer model was used to estimate the damper value, although originally defined for a homogeneous half-space. The visco-elastic damper constant, c_{rd}, is (Mylonakis et al., 2006):

$$c_{\mathrm{rd}} = \frac{3.4\ A}{(1-\nu)\pi}\sqrt{G\rho} \tag{4.10}$$

where A is the area of the footing, ν is the Poisson's ratio of the half-space, G is its shear stiffness and ρ is its volumetric mass. The force-velocity relation of the damper located at sleeper i is defined by:

$$F_{\mathrm{t.rd}.i} = \begin{cases} c_{\mathrm{rd}.i}\ v_{\mathrm{t}.i} & \text{, if } u_{\mathrm{t}.i} \geq u_{\mathrm{c}.i}, \\ 0 & \text{, if } u_{\mathrm{t}.i} < u_{\mathrm{c}.i}. \end{cases} \tag{4.11}$$

Wheel-rail interaction

The interaction forces between the wheels and the rail, F_{a}, are determined using the non-linear Hertzian contact theory for metals (Timoshenko and Goodier, 1970):

$$F_{\mathrm{a}.j} = k_{\mathrm{c}}\ \delta_j^{1.5} \tag{4.12}$$

where k_{c} is a stiffness coefficient and δ is the indentation for wheel j. The indentation δ is calculated from:

$$\delta_j = u_{\mathrm{v}.j} - u_{\mathrm{t}.j} \tag{4.13}$$

where $u_{\mathrm{v}.j}$ is the displacement of wheel j and $u_{\mathrm{t}.j}$ the displacement of the rail at the position of wheel j.

Time integration

The time integration procedure adopted to approximately solve the coupled equations of motion (4.5) and (4.6), was an explicit predictor-corrector integration scheme, presented in Zhai (1996). The method consists of pure vector operations, avoiding to solve any system of simultaneous equations as long as the mass matrix remains diagonal. Conditionally stable, the method requires much smaller time steps for convergence, compared with implicit methods. However, when solving large-scale non-linear problems, the vectorized form of the method proves to be efficient and competitive compared to the more stable implicit algorithms (Zhai, 1996).

The initial conditions are supposedly known:

$$\begin{aligned} \text{at } t = 0,\ \mathbf{u}_{\mathrm{v}} = \mathbf{u}_{\mathrm{v}}(0), \mathbf{v}_{\mathrm{v}} = \mathbf{v}_{\mathrm{v}}(0), \\ \mathbf{u}_{\mathrm{t}} = \mathbf{u}_{\mathrm{t}}(0), \mathbf{v}_{\mathrm{t}} = \mathbf{v}_{\mathrm{t}}(0). \end{aligned} \tag{4.14}$$

The steps of the method are:

(i) Predict the displacements and velocities using the known values of the two preceding time steps with:

$$\begin{aligned} \tilde{\mathbf{u}}_{\mathrm{v.n+1}} &= \mathbf{u}_{\mathrm{v.n}} + \mathbf{v}_{\mathrm{v.n}}\ \Delta t + \left(\frac{1}{2} + \psi\right)\ \mathbf{a}_{\mathrm{v.n}}\ \Delta t^2 - \psi\ \mathbf{a}_{\mathrm{v.n\text{-}1}}\ \Delta t^2 \\ \tilde{\mathbf{v}}_{\mathrm{v.n+1}} &= \mathbf{v}_{\mathrm{v.n}} + (1 + \varphi)\ \mathbf{a}_{\mathrm{v.n}}\ \Delta t - \varphi\ \mathbf{a}_{\mathrm{v.n\text{-}1}}\ \Delta t \\ \tilde{\mathbf{u}}_{\mathrm{t.n+1}} &= \mathbf{u}_{\mathrm{t.n}} + \mathbf{v}_{\mathrm{t.n}}\ \Delta t + \left(\frac{1}{2} + \psi\right)\ \mathbf{a}_{\mathrm{t.n}}\ \Delta t^2 - \psi\ \mathbf{a}_{\mathrm{t.n\text{-}1}}\ \Delta t^2 \\ \tilde{\mathbf{v}}_{\mathrm{t.n+1}} &= \mathbf{v}_{\mathrm{t.n}} + (1 + \varphi)\ \mathbf{a}_{\mathrm{t.n}}\ \Delta t - \varphi\ \mathbf{a}_{\mathrm{t.n\text{-}1}}\ \Delta t \end{aligned}$$

where the symbol ˜ indicates a predictor value, Δt is the time step and ψ and φ are parameters of the integration method. The subscript n represents the current time step of the integration.

(ii) Calculate the force vectors on the RHS of the equations of motion, including the interaction forces using equations (4.12) and (4.13), and the non-linear support reactions $\mathbf{f}_{\mathrm{t.sp}}$ and $\mathbf{f}_{\mathrm{t.rd}}$ using equations (4.9) and (4.11), with the predictors.

(iii) Calculate the acceleration vectors for both systems using equations (4.5) and (4.6) and the predictors obtained in (i) and (ii). This leads to:

$$\begin{aligned} \tilde{\mathbf{a}}_{\mathrm{v.n+1}} &= \mathbf{M}_{\mathrm{v}}^{-1}(\mathbf{f}_{\mathrm{v.g}} + \tilde{\mathbf{f}}_{\mathrm{a.n+1}} - \mathbf{K}_{\mathrm{v}}\tilde{\mathbf{u}}_{\mathrm{v.n+1}} - \mathbf{C}_{\mathrm{v}}\tilde{\mathbf{v}}_{\mathrm{v.n+1}}) \\ \tilde{\mathbf{a}}_{\mathrm{t.n+1}} &= \mathbf{M}_{\mathrm{t}}^{-1}(-\tilde{\mathbf{f}}_{\mathrm{t.sp.n+1}} - \tilde{\mathbf{f}}_{\mathrm{t.rd.n+1}} + \mathbf{f}_{\mathrm{t.g}} - \tilde{\mathbf{f}}_{\mathrm{a.n+1}} - \mathbf{K}_{\mathrm{t}}\tilde{\mathbf{u}}_{\mathrm{t.n+1}} - \mathbf{C}_{\mathrm{t}}\tilde{\mathbf{v}}_{\mathrm{t.n+1}}) \end{aligned}$$

(iv) Correct the displacements and velocities on both systems with the Newmark implicit method (Hughes, 2003):

$$\begin{aligned} \mathbf{u}_{\mathrm{v.n+1}} &= \mathbf{u}_{\mathrm{v.n}} + \mathbf{v}_{\mathrm{v.n}}\ \Delta t + \left(\frac{1}{2} - \beta\right)\ \mathbf{a}_{\mathrm{v.n}}\ \Delta t^2 + \beta\ \tilde{\mathbf{a}}_{\mathrm{v.n+1}}\ \Delta t^2 \\ \mathbf{v}_{\mathrm{v.n+1}} &= \mathbf{v}_{\mathrm{v.n}} + (1 - \gamma)\ \mathbf{a}_{\mathrm{v.n}}\ \Delta t + \gamma\ \tilde{\mathbf{a}}_{\mathrm{v.n+1}}\ \Delta t \\ \mathbf{u}_{\mathrm{t.n+1}} &= \mathbf{u}_{\mathrm{t.n}} + \mathbf{v}_{\mathrm{t.n}}\ \Delta t + \left(\frac{1}{2} - \beta\right)\ \mathbf{a}_{\mathrm{t.n}}\ \Delta t^2 + \beta\ \tilde{\mathbf{a}}_{\mathrm{t.n+1}}\ \Delta t^2 \\ \mathbf{v}_{\mathrm{t.n+1}} &= \mathbf{v}_{\mathrm{t.n}} + (1 - \gamma)\ \mathbf{a}_{\mathrm{t.n}}\ \Delta t + \gamma\ \tilde{\mathbf{a}}_{\mathrm{t.n+1}}\ \Delta t \end{aligned}$$

(v) Re-calculate the force vectors on the RHS of the equations of motion using the corrected values of displacements and velocities obtained on the previous step;

(vi) Calculate corrected values of accelerations for both systems with:

$$\mathbf{a}_{\mathrm{v.n+1}} = \mathbf{M}_{\mathrm{v}}^{-1}(\mathbf{f}_{\mathrm{v.g}} + \mathbf{f}_{\mathrm{a.n+1}} - \mathbf{K}_{\mathrm{v}}\mathbf{u}_{\mathrm{v.n+1}} - \mathbf{C}_{\mathrm{v}}\mathbf{v}_{\mathrm{v.n+1}})$$
$$\mathbf{a}_{\mathrm{t.n+1}} = \mathbf{M}_{\mathrm{t}}^{-1}(-\mathbf{f}_{\mathrm{t.sp.n+1}} - \mathbf{f}_{\mathrm{t.rd.n+1}} + \mathbf{f}_{\mathrm{t.g}} - \mathbf{f}_{\mathrm{a.n+1}} - \mathbf{K}_{\mathrm{t}}\mathbf{u}_{\mathrm{t.n+1}} - \mathbf{C}_{\mathrm{t}}\mathbf{v}_{\mathrm{t.n+1}})$$

(vii) proceed to the next time step.

The values selected for the parameters ψ and φ on the calculations here presented were, respectively, $\frac{1}{6}$ and $\frac{1}{2}$. This predictor scheme is made supposing that the acceleration line between n-1 and n continues with the same slope to n+1. The parameters β and γ were also $\frac{1}{6}$ and $\frac{1}{2}$, respectively, which corresponds to the Newmark linear acceleration method.

On the first integration step the parameters ψ and φ are zero and the accelerations are determined from the equations of motion, i.e.:

$$\mathbf{a}_{\mathrm{v.0}} = \mathbf{M}_{\mathrm{v}}^{-1}(\mathbf{f}_{\mathrm{v.g}} - \mathbf{K}_{\mathrm{v}}\mathbf{u}_{\mathrm{v.0}} - \mathbf{C}_{\mathrm{v}}\mathbf{v}_{\mathrm{v.0}})$$
$$\mathbf{a}_{\mathrm{t.0}} = \mathbf{M}_{\mathrm{t}}^{-1}(-\mathbf{f}_{\mathrm{t.sp.0}} - \mathbf{f}_{\mathrm{t.rd.0}} + \mathbf{f}_{\mathrm{t.g}} - \mathbf{K}_{\mathrm{t}}\mathbf{u}_{\mathrm{t.0}} - \mathbf{C}_{\mathrm{t}}\mathbf{v}_{\mathrm{t.0}}).$$

4.2.3 Calculation procedure

Initially, the track is at rest under its own weight on a certain vertical position, as described in section 4.2.1. The train is then placed in a start section, preceding the section of study, as depicted in Figure 4.4. The train is not moving, submitted to his own weight. Only when the vibrations of placing the train over the track are vanished, the train starts moving, crossing the section of study, until reaching the end section of the model.

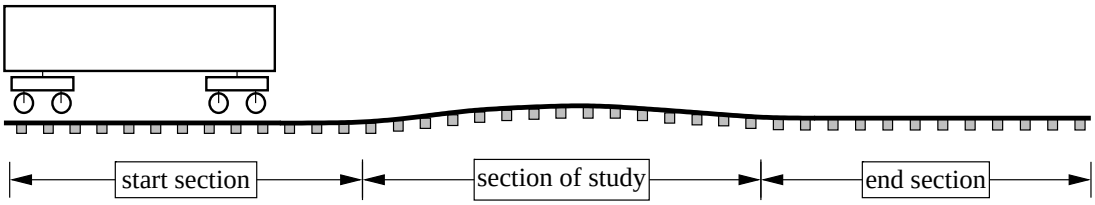

Figure 4.4: Schematic longitudinal view of the train-track model

4.3 1-D dynamic simulation of a railway transition

In this section, a model representing the culvert case-study, described in Chapter 2, is developed and applied to simulate its dynamic behaviour. The numerical model is vali-

dated with the corresponding experimental data, and the numerical results are analyzed to assess the structural behaviour of the transition zone.

4.3.1 Applicability of 1-D model

As discussed in previous Chapter 3, one-dimensional models of a beam on Winkler foundation have an important limitation: if the velocity of the train approaches the Rayleigh wave speed of the track, the waves in the ground will play an important role in the dynamic response of the track-soil system, and therefore the use of one-dimensional models should be avoided. It is thus important to determine the Rayleigh wave speed of the ground supporting the track in the region of the culvert case-study, in order to verify the applicability of a one-dimensional model to analyze its dynamic response.

Table 4.1 defines an approximate characterization of the soil profile at the culvert site, in terms of homogeneous horizontal layers. The wave velocity values shown for the ballast and sub-ballast layers were derived assuming an equivalent Young's modulus of 150 MPa and 100 MPa, respectively. The wave velocity values shown for the soil layers were based on the field survey, namely on the CPT's and VSPT's measurements, reported in Chapter 2. The Poisson's ratio, ν and the density, ρ, were estimated based on typical values for the correspondent soil types (Budhu, 2000). The values of the compressional wave for the peat layers, v_p, were derived assuming a Poisson's ratio close to 0.5 (the value 0.495 was used).

Layer	H [m]	ν	v_s [m/s]	v_p [m/s]	ρ [t/m^3]
Ballast	0.4	0.2	186	304	1.8
Sub-Ballast	0.4	0.2	150	248	1.8
Sand emb.	4.2	0.3	140	262	1.7
Peat 1	3.2	0.5	50	502	1.7
Sand int.	1.2	0.3	150	281	1.7
Peat 2	2.4	0.5	80	804	1.7
Sand pleist.	∞	0.3	180	337	1.7

Table 4.1: Parameters values of soil profile

Considering the soil layering presented in Table 4.1, Figure 4.5 shows the dispersion curve in terms of Rayleigh wave modes (marked with crosses) and the apparent dispersion curve associated with vertical motion at the surface (marked with circles). These curves were obtained using the thin layer method, given by Kausel and Rosset (1981), for the determination of the Rayleigh modes, and using the analytical solution for the Rayleigh wave field generated by an harmonic point load, given by Aki and Richards (1980), for the

determination of the apparent dispersion curve. The used methods and computational tools were described in (Varandas, 2005). In Figure 4.5, it can be seen that the minimum Rayleigh wave velocity of induced waves at the surface is around 90m/s, corresponding to 324km/h, occurring at a frequency of 5Hz. The maximum train speed at this site is 140km/h, which is thus significantly lower than the critical speed of the track. Therefore, no resonance phenomena associated with the critical speed effect is expected at this site.

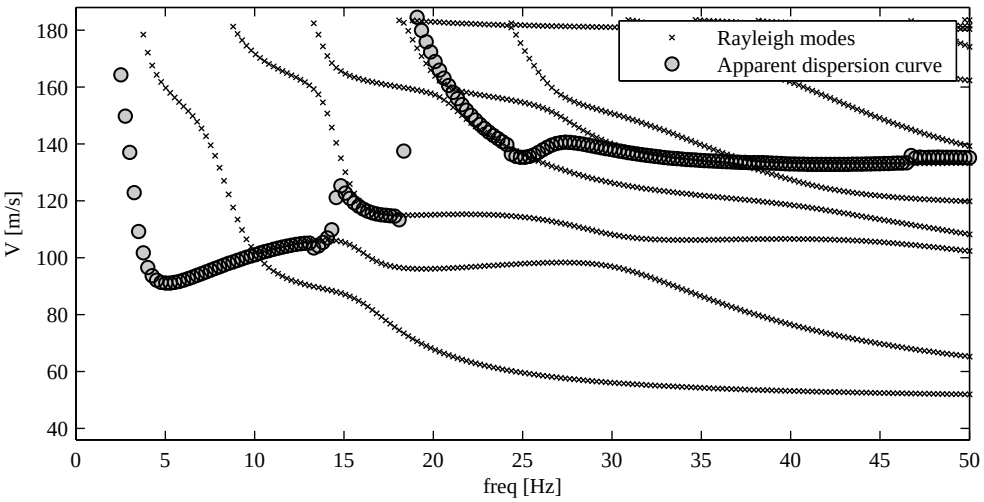

Figure 4.5: Apparent dispersion curve of vertical motion at the surface

4.3.2 Model parametrization

Table 4.2 list the values assumed for the vehicle parameters. The train data refer to a Koploper ICM trainset (motorcar and trailer) and to an ICR carriage, both of NS-reizigers (the Dutch national railway company). The track model was composed of one rail with the masses of half sleepers attached to it. In accordance, also the mass, damping and stiffness values presented in Table 4.2 for modeling the vehicle were reduced to half. The geometrical and some mechanical parameters of the vehicles are defined in Figure 4.6. The parameters values of the vehicles were provided by the Dutch Railway company in collective COB research (Esveld, 2000).

Table 4.3 list the values assumed for the track parameters. The justification for the selected values used to construct the damping matrix $\mathbf{C}_\mathrm{t}$, shown in Table 4.3, will be made further in the text.

According to equation (4.9), there are three parameters to be determined for each spring supporting the sleepers: k_1, k_2 and p. The values of these parameters were established

Vehicle	ICM motorcar	ICM trailer	ICR carriage
Mass of the car [kg]	39000	34500	60000
Mass of the bogie [kg]	6100	2600	3400
Mass of the wheel set [kg]	1500	875	750
Mass inertia of the car [kgm^2]	586620	518938	902500
Mass inertia of the bogie [kgm^2]	3176	1354	1857
Stiffness $k_{\text{v.1}}$ [N/m]	28.0×10^5	24.8×10^5	18.0×10^5
Stiffness $k_{\text{v.2}}$ [N/m]	17.2×10^5	14.4×10^5	8.0×10^5
Damping $c_{\text{v.1}}$ [Ns/m]	5.0×10^3	2.9×10^3	10.0×10^3
Damping $c_{\text{v.2}}$ [Ns/m]	39.7×10^3	31.1×10^3	35.4×10^3
L_{c} [m]	26.05	27.05	26.40
L_{b} [m]	19.0	19.0	19.0
L_{w} [m]	2.50	2.50	2.56
Contact stiffness coefficient (k_c)		91×10^9 N/m$^{1.5}$	

Table 4.2: Parameters of the ICM and ICR vehicles

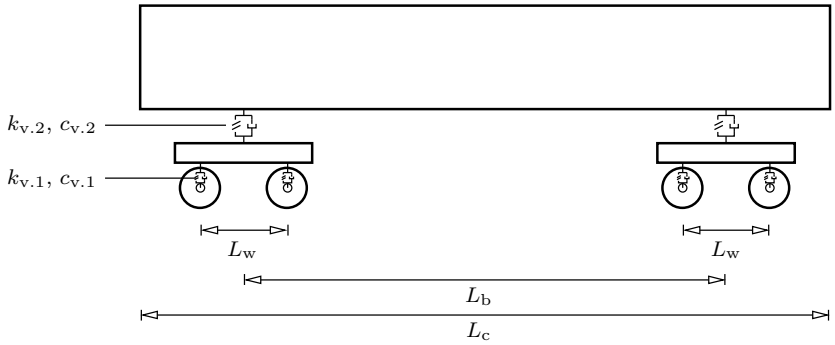

Figure 4.6: Geometrical and mechanical parameters of the vehicles

Mass of the rail (UIC 54)	54.7 kg/m
Bending stiffness (EI) of the rail	4.91×10^6 Nm^2
Mass of $\frac{1}{2}$ sleeper (including fixing system)	80kg
Contact area between $\frac{1}{2}$ sleeper and ballast (A)	0.8×0.28 m^2
Young Modulus of half-space (E)	200×10^6 N/m^2
Poisson's ratio of half-space (ν)	0.15
Volumetric mass of half-space (ρ)	1800 kg/m^3
Distance between center of sleepers	0.60m
Number of beam-elements between sleepers	3
Damping ratio (ξ) for frequencies ω_1 and ω_2	4%
ω_1 and ω_2	12.6 and 188.5 rad/s

Table 4.3: Track parameters

from the dynamic measurements performed during service trains operation. The use of dynamic loads from service trains operation allows the stiffness to be determined at magnitudes and frequencies of loading relevant to in-service conditions (Priest and Powrie, 2009). Moreover, since the calculations include the self-weight of the track, the forces and deflections of the springs will also include this component, which must then be accounted for additionally to the values obtained from the dynamic measurements.

Train	Static Load [kN]	Velocity [km/h]	Displacement G7 [mm]	Displacement G1 [mm]
ICM (motorcar)	72	120	1.00	0.38
ICM (trailer)	54	120	0.82	0.32
ICR	87	130	1.10	0.40

Table 4.4: Average wheel load, train velocity and corresponding maximum downward displacement on locations away from the transition zone (G7) and on top of the culvert (G1)

Around location G7 (see Figure 2.11), at the embankment area, the sleepers are not hanging and so the measured downward displacements are directly related to the stiffness of the track, ballast and subgrade. Table 4.4 lists the average static wheel loads for three different train types, and the corresponding average maximum displacements measured at G7. These average values were determined from several trains passages recorded during one day of service operation.

Previous (unpublished) research at Dutch Railways, showed that $p = 2$ is a reasonable value for this parameter. The values of k_1 and k_2 were then defined so that the force-displacement path obtained using Equation (4.9) would pass through, or as close as possible, the three points defined in Table 4.4 for location G7. The spring type supporting the sleepers at the embankment area is designated here by S1 and the corresponding selected values for the parameters are listed in Table 4.5. Figure 4.7 shows the force-displacement path of spring type S1, as well as the three points, represented with circles, corresponding to the measured values at location G7. The spring force values shown in Figure 4.7 do not coincide with the static wheel loads, since these are applied to the rail, and the spring forces also include the track weight, as aforementioned. It can be seen that the assumed value for parameter p is reasonable.

Spring	k_1 [MN/m]	k_2 [MN/m^p]	p [-]
S1	10	14000	2.0
S2	15	30000	2.0
S3	40	70000	2.0

Table 4.5: Springs parameters

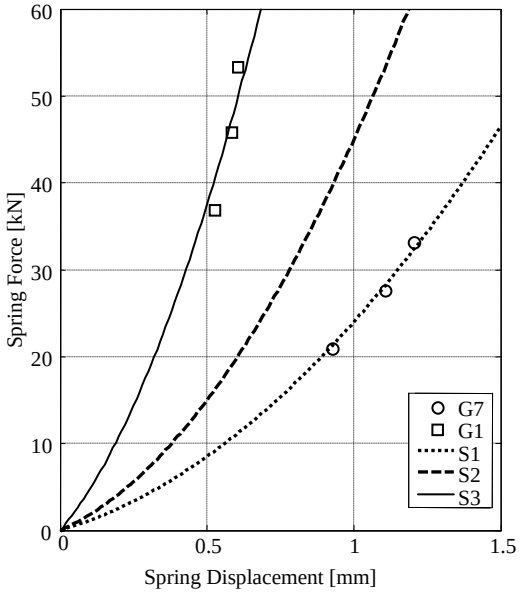

Figure 4.7: Force-displacement path of the springs

The properties of the springs supporting the central sleepers above the culvert centre were defined from spring type S1, based on the knowledge that the stiffness at this location is higher. Gradual increase of stiffness were tried for the central springs above the culvert until the dynamic calculations gave satisfactory agreement with the values presented in Table 4.4 for location G1. In fact, good agreement was obtained when the highest stiffness was located on G1 (corresponding to spring S3) and when the two adjacent springs, prior and after the central one, had intermediate properties (corresponding to spring S2). The properties of springs S3 and S2 are shown in Table 4.5. Figure 4.7 also shows the corresponding force-displacement path for spring S3 and S2 and the three points, represented with squares, derived from the measured displacement values at location G1. The secant stiffness values associated with the spring S3 are in the same range as those obtained in a field survey on Swedish high-speed railway tracks at constant 2Hz frequency (Nielsen and Oscarsson, 2004).

The locations G6 to G2, between G7 and G1, lie on the transition zone, before the culvert centre, where significant voids under the sleepers exist. Because of this, the dynamic measurements performed at these locations could not be used to estimate the stiffness parameters of the corresponding springs. It was thus assumed that the springs supporting the sleepers located on this region were of the type S1. Also, since there are no measurements available beyond the culvert, it was assumed that the springs supporting the sleepers after the culvert are also of the type S1.

4.3.3 Detection of hanging sleepers

The initial state of the track was determined using the method presented in section 4.2.1. The assumed vertical level of the inner and outer rails is depicted in Figure 4.8.

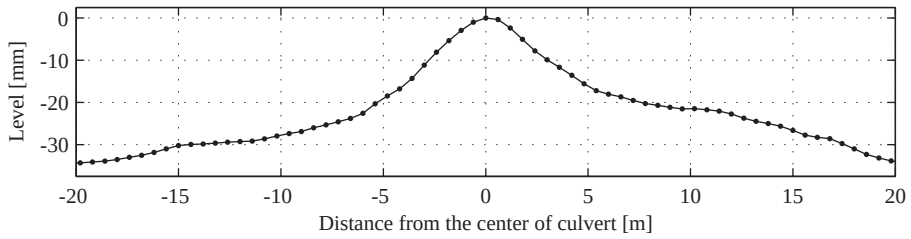

(a) inner rail

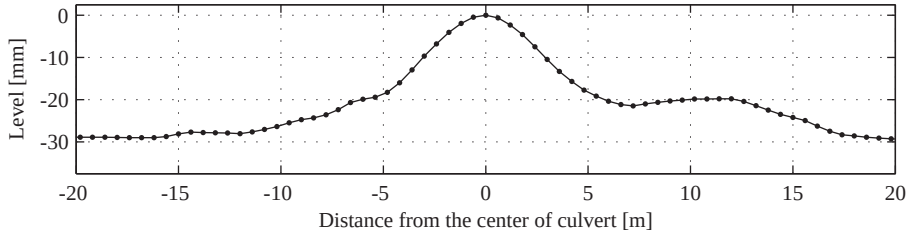

(b) outer rail

Figure 4.8: Vertical measured level of the: (a) inner rail, (b) outer rail

Figure 4.9 presents the corresponding forces that support the inner and the outer rail-sleeper system at rest. Each circle represents one sleeper. Figure 4.9 also includes a representation of the measured track level.

Due to the variation of the level, the forces on the sleepers vary significantly; especially at the center of the culvert where a high value is found. The support force on the extremities of the model, where the rail level is assumed to be horizontal, is 1.13kN, which equals the weight of 0.60 m (between sleepers) length of track (rail and half sleeper). On the central sleeper of the inner rail (point A in Figure 4.9), the absolute maximum is 16.3kN, which is 14.5 times the weight of 0.6 m length, and on the central sleeper of the outer rail (point B in Figure 4.9) the carried weight is 10.1kN, which equals 9 times the weight of 0.60 m length.

The sleepers with zero support force are marked in Figure 4.9 with black dots inside the corresponding circles. These sleepers are hanging. From the point of view of equilibrium, their weight is carried by the track to the adjacent supported sleepers. To each side of the culvert center it is visible that there are several consecutive hanging sleepers. The number of consecutive hanging sleepers varies from 8 to 9, in accordance with a preliminary

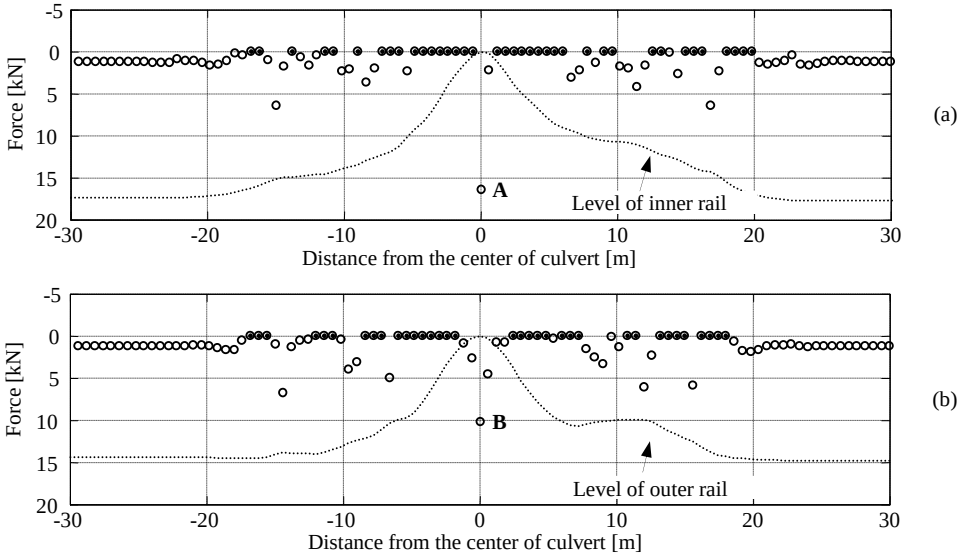

Figure 4.9: Force distribution at rest on the inner rail (a) and on the outer rail (b). Each circle corresponds to one sleeper. The dotted lines are scaled representations of the rail level

estimate based on the cantilever solution (Hölscher and Meijers, 2009).

4.3.4 Validation of the numerical model

Amount of voids under the sleepers

As mentioned before, the short-term measurements have shown the existence of voids under several sleepers located on the transition zones. Also, preliminary dynamic analyses have demonstrated that when a significant amount of void is introduced under the sleeper, the corresponding maximum downward displacement caused by a train passage is dominated by the amount of void introduced. The amount of void under the hanging sleepers were then estimated based on the known maximum downward displacements registered for several train's passages on four different sleepers located on the transition zone before the culvert center. The short-term measurements were performed on top of the sleepers, next to the outer rail (RHS rail in Figure 2.2a).

Figure 4.10 shows the voids introduced (each point on the figure represents one sleeper), as well as the location of the geophones placed on the sleepers. The short-term measurements were performed one month before the first measurement of the track level (the level used for these dynamic analyses). For this reason there is not a strict correspondence between the location of the hanging sleepers depicted in Figure 4.10 and that presented in Figure 4.9. Based on these results, it is estimated that the hanging distance is slightly higher than 6 mm before the culvert, on a location on top of the approach slab, and that, at rest, the

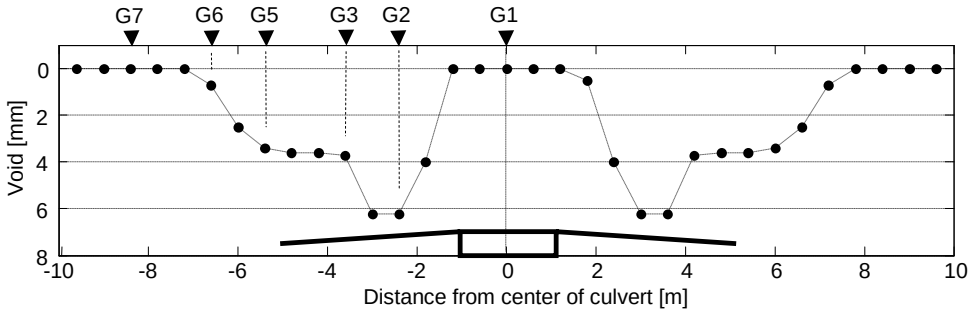

Figure 4.10: Introduced voids under the hanging sleepers

sleeper soffit is touching the ballast only on five sleepers above the culvert box. Due to the inexistence of short-term measurements beyond the culvert, the voids profile on this side of the culvert was made almost symmetrical. The only difference is a one sleeper shift (to the right), performed for better agreement with the G1 measurement.

Calculated displacements

The length of the track model was 108m (181 sleepers) and the time step was fixed at 4×10^{-5} s. The track level was as measured on the outer rail, depicted in Figure 4.8(b). The train model was composed of two consecutive ICR carriages. The introduced hanging distances were shown in Figure 4.10.

Figure 4.11 shows the calculated displacements on six sleepers (locations shown in Figure 4.10) compared with the measured ones for the passage of an ICR carriage. Figure 4.11 shows only the displacements of the four consecutive wheels, each pair belonging to a bogie of each carriage.

The numerical results show good agreement with the measured displacements. Also good agreement was achieved with other measurements related to different train's types and loads. The higher displacements registered on the transition zone are due to the existence of hanging sleepers and not because of a local soft-foundation situation, since the springs supporting the sleepers are all identical except the central three on top of the culvert.

The upward spikes visible on the displacements measured on the transition zone (G5, G3 and G2), around instants 8.3 s and 9.0 s, are also reproduced on the numerical results. This upward motion is initiated right after the wheels pass the 6 m trough formed by the consecutive voids under the sleepers, shown in Figure 4.10. When the wheels move onto the trough existing after the culvert, a lever effect lifts the rail/sleepers system before the culvert. Figure 4.12 gives a simplified representation of this vibration mode.

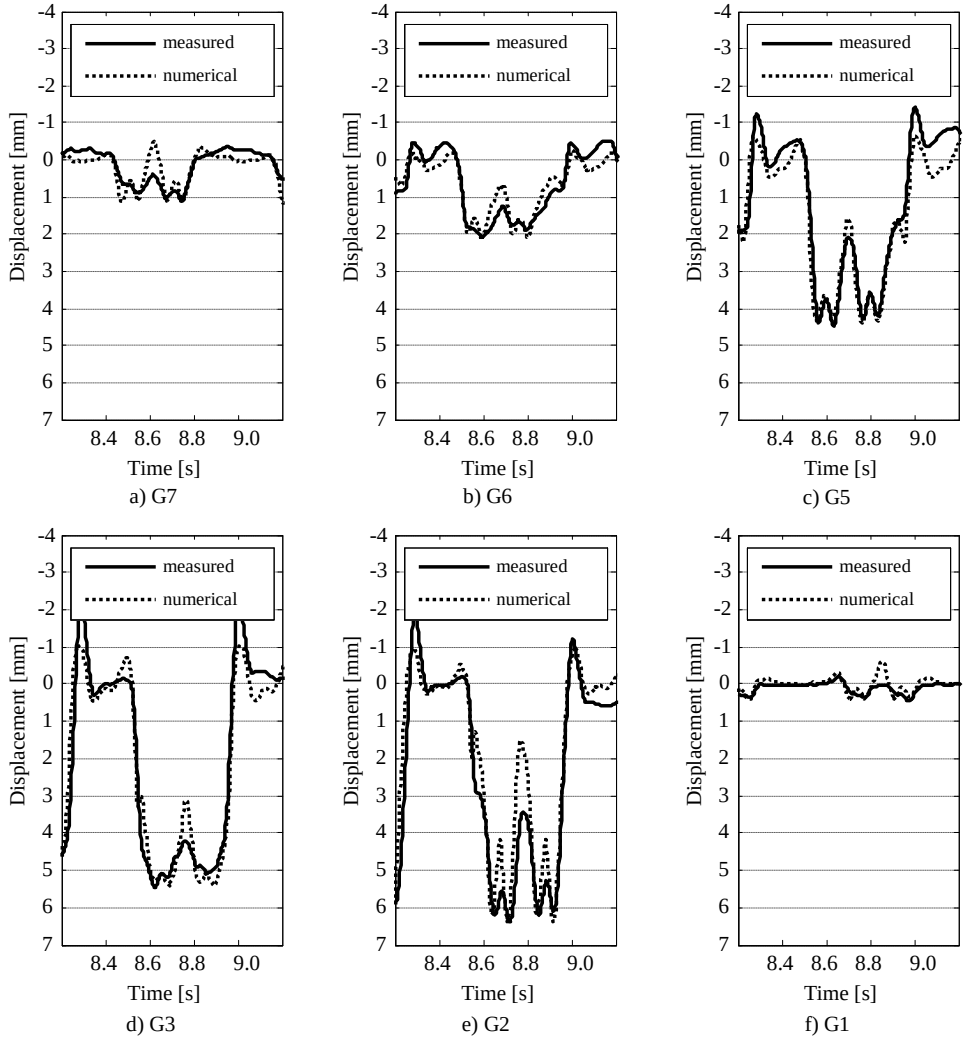

Figure 4.11: Displacements of sleepers G7 to G1 due to ICR passage

4.3.5 Parametric study of the friction damping value

The energy dissipation associated with the unloaded upward motion of the rail/sleepers system is low, given by internal material damping and by lateral friction between the sleepers and the ballast. The friction and material damping properties of the track system, as listed in Table 4.3, were then defined based on the amplitude of the measured upward peaks.

The two frequencies needed to define the Rayleigh damping matrix, presented in Table 4.3, 2 Hz and 30 Hz, were selected in order to encompass the natural frequency associated with the vibration mode shown in Figure 4.12, and the frequency range of interest for this study. For example, the frequency associated with the passage of the two consecutive wheels from the same bogie lies between 7Hz and 15Hz, depending on the velocity of the train and the

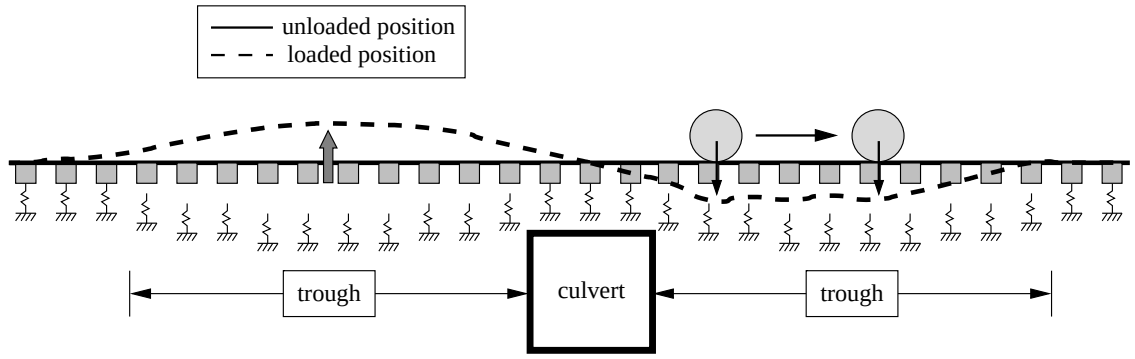

Figure 4.12: Upward motion of the track after the passage of the wheels over the first trough before the culvert

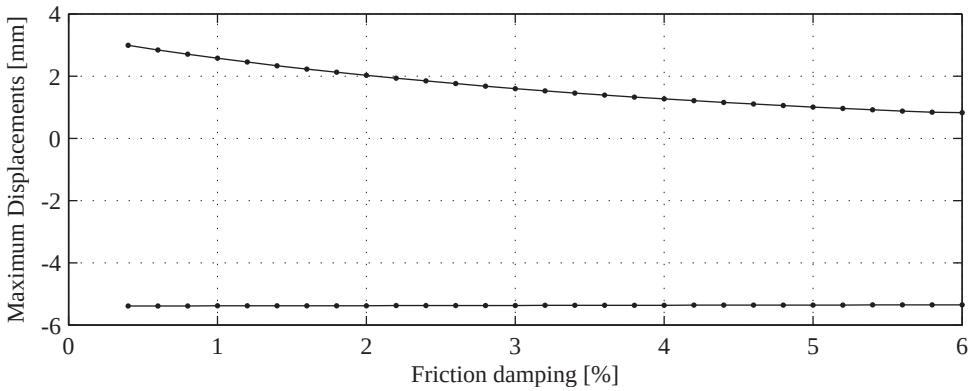

Figure 4.13: Maximum upward (top) and downward (bottom) displacements for sleeper located at G3 ($x = -3.6$m) depending on the friction damping

distance between the two wheels.

A parametric analysis was made varying the damping ratio fixed for the two mentioned frequencies. Figures 4.13 and 4.14 illustrate the results obtained during this process. In these figures the origin of the vertical axis corresponds to the initial position before the passage of the moving load. The load corresponds to a single wheel traveling at 130km/h.

It can be seen that the maximum downward displacements do not depend on the friction damping but the maximum upward displacement on the hanging zones does. This is due to the fact that the dissipation of energy in the downward motion is governed by the radiation damping ($\mathbf{f}_{\mathrm{t.rd}}$), but during the upward motion of the hanging sleepers, as mentioned above, the dissipation of energy is solely given by material and friction damping ($\mathbf{C}_{\mathrm{t}}$). Matching the numerical results with the measured displacements, as shown in Figure 4.11, yielded the 4% value for the material and friction damping ratio, presented in Table 4.3.

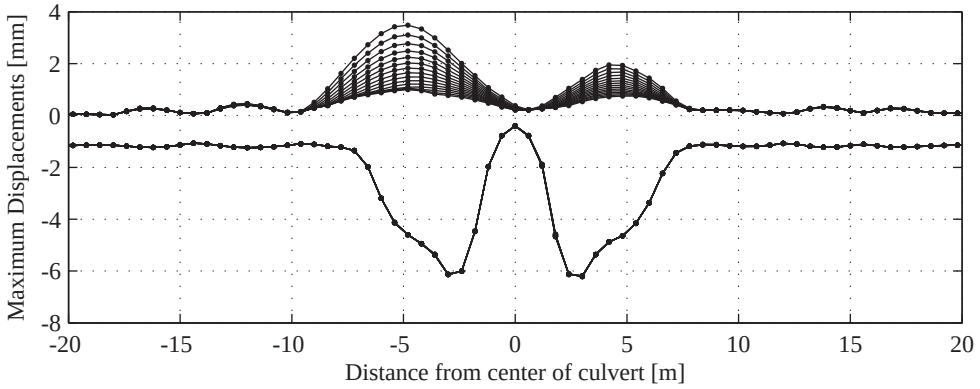

Figure 4.14: Maximum upward (top) and downward (bottom) displacements depending on the location and the friction damping

4.3.6 Assessment of the structural behaviour

The force transmitted through each sleeper to the ballast-soil foundation is the sum of the spring and the damper force:

$$F_{\mathrm{t.tr.}i}(t) = F_{\mathrm{t.sp.}i}(t) + F_{\mathrm{t.rd.}i}(t) \tag{4.15}$$

where $F_{\mathrm{t.tr.}i}$ is the force transmitted through sleeper i, or through half sleeper i, depending if the model considers the complete track, or only half track.

Figure 4.15 shows the variation of the transmitted force with time on two different sleepers when four consecutive wheels of the ICR carriage pass over. The first sleeper is located before the transition zone (dotted line) and the second is two sleepers before the culvert center (full line). The maximum absolute value of the first case is 34 kN which is less than half the maximum absolute value of the second case: 83 kN. Having in mind that the static wheel load of the ICR carriage is 87 kN, it may be stated that the maximum transmitted force on the first case is approximately 39% of the static train load and on the second case 95%.

These values may be referred to as the transmissibility, defined as:

$$\mathrm{TR}_i = \frac{\max|F_{\mathrm{t.tr.}i}(t)|}{F_{\mathrm{w}}} \tag{4.16}$$

where F_{w} is the static axle load, or the static wheel load, and TR_i the transmissibility of sleeper i. It should be noted that the numerator in Equation (4.16) includes the initial force due to the self-weight of the track. When the track is horizontal, this part represents less than 5% of the maximum transmitted force, depending on the train load and the weight of the track. However, on the central sleeper above the culvert, this part represents

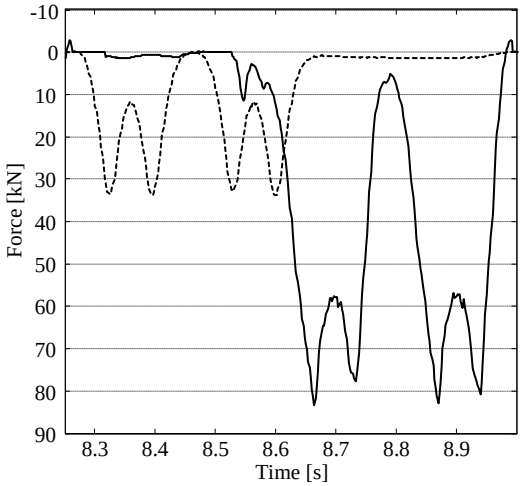

Figure 4.15: Force transmitted through half sleeper to the ballast, on a sleeper before the transition zone (dotted line) and on the sleeper located two sleepers before the culvert centre (full line)

approximately 20% of the maximum force.

Figure 4.16 shows the transmissibility profiles considering the track level shown in Figure 4.8(b) and the hanging distances depicted in Figure 4.10. This figure compares the results obtained for an ICR passage and for an ICM trainset passage. These transmissibility profiles are identical but some differences can be seen, especially on the transition zone where the sleepers are hanging.

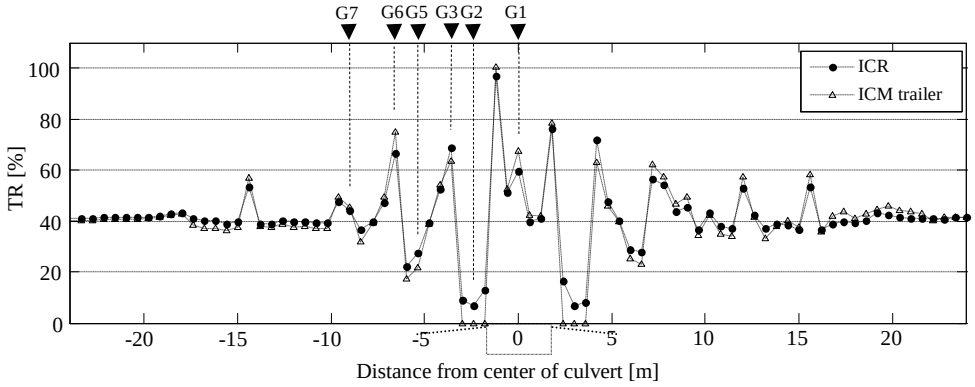

Figure 4.16: Transmissibility due to an ICR passage and an ICM passage considering the track level shown in Figure 4.8(b) and the hanging distances shown in Figure 4.10

It can be seen that the transmissibility strongly oscillates, mainly due to the existence of hanging sleepers. Some sleepers on the transition zone present high transmissibility while others have small or zero transmissibility. The highest transmissibility is observed at the first sleeper above the culvert, not at the very stiff center sleeper (location G1). Also, the transmissibility is not symmetric over the culvert, it depends on driving direction (which

is from left to right).

Looking again at Figure 4.11, it can be seen that the downward displacement profile observed on location G3 is different from the ones measured on locations G5 and G2. Namely, the downward spikes caused by the wheels passage are much less evident at G3 compared to G5 and G2. This fact was observed during other trains passages and the numerical results also show this behaviour. The explanation lies on the fact that the transmissibility at G3 is high and at G5 and G2, which are neighboring sleepers, is low. This means that the sleeper at G3 is being highly pushed against the ballast while in G5 and (specially at) G2 it barely touches the ballast.

Figure 4.17 shows the transmissibility profile obtained with the track level as measured a few hours after a maintenance operation. The differential level between the center of the culvert and the embankment is lower than on the previous case, but the same up and down profile can still be seen. No voids under the sleepers were introduced since it is expected that after a maintenance operation they do not exist. This figure shows also the transmissibility obtained considering a horizontal track.

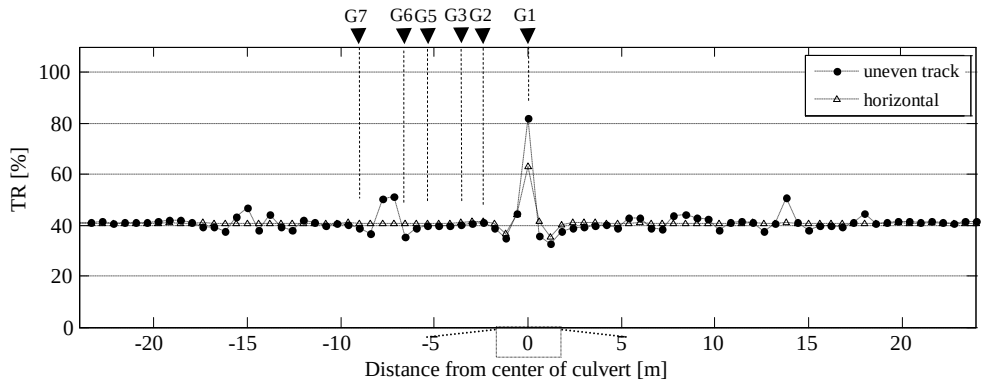

Figure 4.17: Transmissibility considering a track level measured after a maintenance operation and a horizontal track level, both for an ICR passage and no voids under the sleepers

It can be seen that without voids under the sleepers the transmissibility variation is much smaller. Also it is clear that the consideration of the initial track level on the model is important. The observed differences between the two cases presented in Figure 4.17 come mainly from the initial dead-weight force contribution. Also the oscillation of the train carriage travelling over an uneven track plays a role and contributes for the differences shown.

4.3.7 Discussion and consequences

The results show that the loading transferred through the sleeper to the ballast can significantly change on a transition zone, both in time and space, especially with the appearance of voids under the sleepers. As the long-term behaviour of ballast strongly depends on the loading amplitudes, it can be concluded that this evolution of the transmissibility will have consequences on the long-term behaviour of the transition zone.

High impact forces in the ballast produce higher densification (Baessler and Ruecker, 2003). Figure 4.16 shows that on transition zones there can be hanging sleepers with high transmissibility (e.g. on location G3). This means that not only these sleepers are impacting the ballast from an initial suspended position but also that the loading amplitude is high compared to the initial situation, after maintenance, without voids under the sleepers. This is a cause for higher settlement of the ballast. Figure 4.16 also shows that on the transition zones, neighboring the sleepers with the highest transmissibility there are sleepers with very low transmissibility. This may contribute to higher rates of settlement, due to lower horizontal confinement.

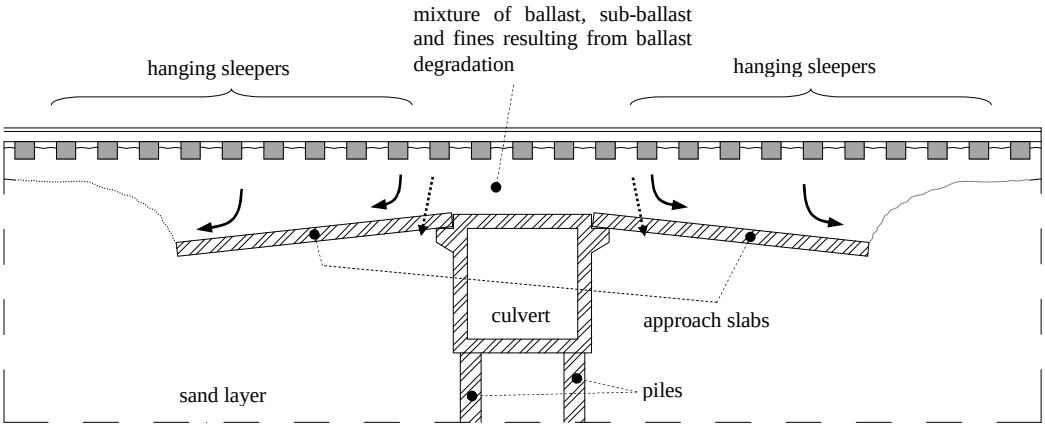

Figure 4.18: Longitudinal view of the track, showing the possible flow of ballast in the transition zone

The settlement of the ballast over the approach slab may not only be directly caused by loading from the sleepers, but also by a global (horizontal) flow of ballast. This possibility may explain the fact that some sleepers close to the culvert do not touch the ballast during some train passages, as can be found in Figure 4.16. Moreover, the significant inclination of the approach slabs may act as a ramp and strength this ballast flow. Figure 4.18 shows a schematic representation of this mechanism. These aspects will be further analyzed in the following Chapters.

4.4 Conclusions

This Chapter has presented a one-dimensional numerical model that proved to be adequate to describe the dynamic behaviour of the track on a transition during train passages. The field measurements on the culvert case-study played an important role in the development and in the determination of the parameters values. Important aspects to be considered in the modelling were the variable stiffness of the support, the possibility of voids under the sleepers, and the unloaded level of the track.

The applicability of the one-dimensional model on the culvert case-study was verified with the determination of the corresponding critical speed of the track. The critical speed at the culvert case-study is around 320 km/h, therefore well above the maximum allowed train speed at the site, of 140 km/h.

With the numerical model, it was seen that the levelling of the track gives essential information on the sleepers that are hanging and the initial position in the non-linear stiffness curve. On the culvert case-study, it was seen that, for the considered level, there are about 8-9 consecutive sleepers hanging at either side of the culvert, and that the transmission of the weight of the track to the ballast varies considerably, with the sleepers above the culvert transmitting more than 25 kN, whereas the considered weight of the track was 2.26 kN per sleeper.

The dynamic simulations have shown that the maximum downward displacements at the culvert transition zones are determined by the amount of void under the hanging sleepers. These amount of voids reach more than 6 mm, and the maximum void occur on locations above the middle of the approach slabs. The numerical analyses have also shown that the measured upward displacement spikes, shown in Figure 2.13, are due to two combined effects: the upward unloaded motion of the sleepers after the passage of two consecutive bogies, and a lever effect that lifts the rail/sleeper system on the opposite side of the position of the wheels, relative to the culvert box. Furthermore, it was also concluded that the damping due to lateral friction between the sleepers and the confining ballast is important for the determination of the motion of the sleepers while not in base contact with the ballast (during the upward motion).

From the numerical results, it was seen that the peak sleeper/ballast contact-forces are very variable in the transition zones. On the culvert area, the transmissibility of the track may vary between 0% and 100%, depending on the location of the sleeper and the considered vehicle. Therefore, it turns out that some sleepers are barely touching the ballast, even when the heavier trains are passing, and others are loading the ballast with very high pressures. Differential sleeper loads on consecutive sleepers of more than 45% occurs at

several locations, whereas Gardien (2005) stated that this value of 45% corresponds to a limit admissible value, in order to limit differential ballast degradation. This will have important consequences for the long-term ballast behaviour.

In the next Chapter 5, a non-elastic constitutive law for the ballast settlement will be derived. Together with the dynamic model, this will facilitate to perform a complete simulation of a period between two maintenance instances, taking into account the dynamic loading on the ballast, the long term deformations of the ballast under this loading, as well as the mutual interaction.

Chapter 5

Modelling of Track Settlement*

5.1 Introduction

This Chapter presents a methodology to estimate the loss of the vertical geometry of the track with time. For this, the dynamic train-track interaction model presented in the previous Chapter is coupled with a novel mathematical model to estimate the vertical settlement of the ballast. Justification for this new settlement model is the inadequacy of existing models for proper representation of the loading history, as mentioned in Section 3.1. The validation of the methodology is made with the measurements performed at the culvert transition described in Chapter 2. Special attention is paid to the magnitude of the forces transmitted to the ballast and to its evolution with time, caused by the appearance and development of differential settlements. The importance of several aspects, for example, the coupling between the dynamic loading from the trains and the long-term response of the track, is analyzed.

5.2 Methodology to determine the settlement of the track

Three different approaches to determine the track settlement evolution are described in literature:

(i) Determination of dynamic response of the track and of the deformation in ballast and subsoil by separate models (Mauer, 1995; Hunt, 1997; Kempfert and Hu, 1999);

(ii) Non-linear and non-elastic three-dimensional treatment of granular layers as con-

* This Chapter is based on (Varandas et al., 2013)

tinuum solids (Augustin et al., 2003; Suiker and de Borst, 2003; Lundqvist and Dahlberg, 2004); or

(iii) Numerical discrete models, where possibly each ballast particle is treated independently (Saussine et al., 2006; Gardien, 2005; Lu and McDowell, 2007).

The calculation of the track settlement at transition zones should take into account several aspects simultaneously. The rapid development of differential settlements significantly influences the wheel-rail contact forces and consequently the distribution of forces transmitted to the ballast. On the other hand, the weight of the track transmitted to the ballast through each sleeper depends on the track vertical level, with the result that the pre-load on the ballast will also be changing in time. Moreover, the development of voids under the sleepers, which are more likely to occur at transition zones, will not only influence the wheel-rail contact forces (Recuero et al., 2011), but also cause impact loads which may trigger unwanted degradation mechanisms. Therefore, successive calculations are necessary in order to determine the evolution of the loading conditions on transition zones.

The main limitation of the second and third approaches is the computational time still needed to run dynamic three-dimensional analysis with a large number of degrees of freedom representing a railway transition. This limitation is particularly severe if a large number of successive dynamic analyses is required. Using the first approach, it is possible to build a model that accounts for the particular inhomogeneous nature of transition zones and arbitrary loading schemes, and allows the determination of the accumulated settlement after millions of axle passages. For this reason, the methodology adopted in this work follows the first approach mentioned above.

Figure 5.1 presents the basic scheme of the methodology. The methodology avoids performing dynamic analysis for each vehicle passing the site, which would be computationally impractical. For this, the train-track model is loaded, at a given time, by selected railway vehicles. Based on the forces transmitted to the ballast, the settlement produced under each sleeper of the track by each vehicle's axle is determined. Considering the traffic defined for the corresponding period, these settlement values are then linearly accumulated under each sleeper, until the accumulated settlement at any given sleeper reaches a certain limit value (ΔS). At this moment, new dynamic analyses are performed, considering the updated track configuration, and the process continues. The maximum accumulated settlement between dynamic analyses, ΔS, must be a value small enough to have insignificant influence on the calculated final position of the track. A process of gradual decrease of ΔS was used for corresponding determination. This issue will be further elaborated in Section 5.4.

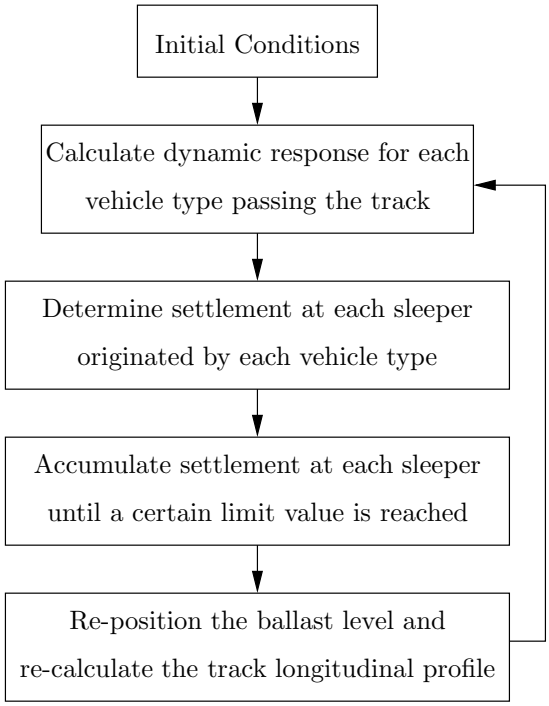

Figure 5.1: Methodology for calculation of track level degradation

Pre-required information includes the stiffness of the track and its foundation, the mechanical properties of the passing trains, the traffic at the site and the initial vertical level of the track, directly after a maintenance operation. A method to determine the stiffness of the track is described in Priest and Powrie (2009). The lighter railway vehicles can be neglected because they will have minimal influence on the total accumulated settlement of the track (Shenton, 1985). The vertical level can be acquired with high-precision topographical equipment or derived from the design or maintenance specifications.

5.3 Settlement model for ballast

The settlement model presented next was developed to determine the ballast settlement submitted to an arbitrary loading sequence, accounting for the loading history. The model is phenomenological, since it defines relationships from a macroscopic point of view, as the ones presented in (Shenton, 1985; Sato, 1995; Ford, 1995). The main aspects that sustained the development of this model are:

(i) the settlement of the ballast is proportional to the amplitude of the applied load;

(ii) the loading history plays a decisive role on the settlements;

(iii) the densification of ballast decreases with an increasing number of load cycles if the loading amplitude remains constant.

The settlement model determines the settlement at the surface of the ballast caused by the application of successive cycles according to:

$$u_{\mathrm{p}.n} = \frac{\gamma}{M_{\alpha\beta}} \int_0^{\bar{F}_n} F^{\alpha} \left(\frac{1}{h(F)+1} \right)^{\beta} \mathrm{d}F. \tag{5.1}$$

and

$$S_N = \sum_{n=1}^{N} u_{\mathrm{p}.n} \tag{5.2}$$

where $u_{\mathrm{p}.n}$ is the permanent deformation produced during load cycle n, S_N is the total settlement after N load cycles, $\bar{F}_n$ is the loading amplitude of the force passing through this sleeper to the ballast at load cycle n, $h(F)$ represents the loading history and α, β and γ are positive parameters. The meaning of these parameters, as well as of $h(F)$, will be explained further in the text. $M_{\alpha\beta}$ is a normalizing parameter defined by:

$$M_{\alpha\beta} = \frac{F_0^{(\alpha+1)}}{\alpha+1} \cdot \sum_{n=1}^{N_0} \left(\frac{1}{n} \right)^{\beta} \tag{5.3}$$

where F_0 is a reference loading amplitude and N_0 a reference number of cycles.

Constant loading case and determination of parameters

To discuss the meaning of the parameters, as well as of $M_{\alpha\beta}$, it is convenient to see how Equation (5.1) simplifies for the constant loading case. If $\bar{F}$ is the constant loading amplitude, then the function $h(F)$ can be replaced by the number of cycles passed and Equation (5.1) simplifies to

$$u_{\mathrm{p}.n} = \frac{\gamma}{M_{\alpha\beta}} \, \frac{\bar{F}^{\alpha+1}}{(\alpha+1)} \left(\frac{1}{n} \right)^{\beta} \tag{5.4}$$

and the corresponding accumulated settlement will be given by

$$S_N = \frac{\gamma}{M_{\alpha\beta}} \, \frac{\bar{F}^{\alpha+1}}{(\alpha+1)} \sum_{n=1}^{N} \left(\frac{1}{n} \right)^{\beta}, \tag{5.5}$$

which clearly shows that the parameter α expresses the dependence of settlement on the loading amplitude and the parameter β controls the progression of the settlement rate with the number of load cycles.

By comparing Equations (5.3) with (5.5), it can be seen that $M_{\alpha\beta}$ was derived so that parameter γ represents the total settlement after N_0 load cycles with a constant loading amplitude F_0. This way, γ has a clear physical meaning: it is the accumulated settlement in the reference test with loading amplitude F_0 and number of cycles N_0.

In the current work, the values $N_0 = 10^6$ and $F_0 = 50$ kN were used. The justification for the value chosen for N_0 is that many tests with ballast, available in literature, are performed with this total number of load cycles, e.g. (Anderson and Key, 2000; Suiker et al., 2005; Indraratna et al., 2006). The value fixed for F_0 (50 kN) was simply chosen in order to be representative of typical values of forces transmitted to the ballast through an half-sleeper. This value may therefore correspond to the force passing through half-sleeper due to a wheel load of 100 kN, assuming 50% of transmissibility (Indraratna and Salim, 2005). It should be mentioned that the force values in Equations (5.1) to (5.5) may either refer to the vertical force passing through a given sleeper, in correspondence with the axle load, or to the vertical force passing through half-sleeper, in correspondence with the wheel load. However, when the train-track interaction is accounted in the determination of these forces, and given the possibility of considering real (unequal) geometrical profiles, curves, irregularities, etc..., it is preferable to consider a separation between the left/right response. For this reason, the force values are here assumed to refer to the force passing through half-sleepers.

As referred above, the relation between the settlement and the loading amplitude is determined by the value chosen for parameter α. This relation is non-linear, as was demonstrated by Stewart (1986), using triaxial tests on ballast (see Figure 3.4) and Hettler (Mauer, 1995) by means of track models (scaled 1/3). Due to this, the settlement is many times expressed proportional to a power of the loading amplitude, as in (3.12). For the purpose of the current work, the value $\alpha = 0.6$ will be used, resulting from Hettler's law expressed in (3.12), and therefore $S_N \propto \bar{F}^{1.6}$ (see Eq. (5.5)).

According to Equation (5.5), the progression of the settlement rate with the number of load cycles is defined by a Riemann zeta function:

$$\zeta(\beta) = \sum_{n=1}^{\infty} \frac{1}{n^{\beta}}$$

This function is convergent if $\beta > 1$ and tends to infinity for $\beta \leq 1$. Test results from literature shows β values lower than one, which means that the models are applicable to a limited (but very high) number of load cycles only. The solid lines in Figure 5.2 show the progression of the settlement using three different values of β, leaving α and γ constants.

Figure 5.2 also depicts (dashed line) the settlement obtained with the first part of the

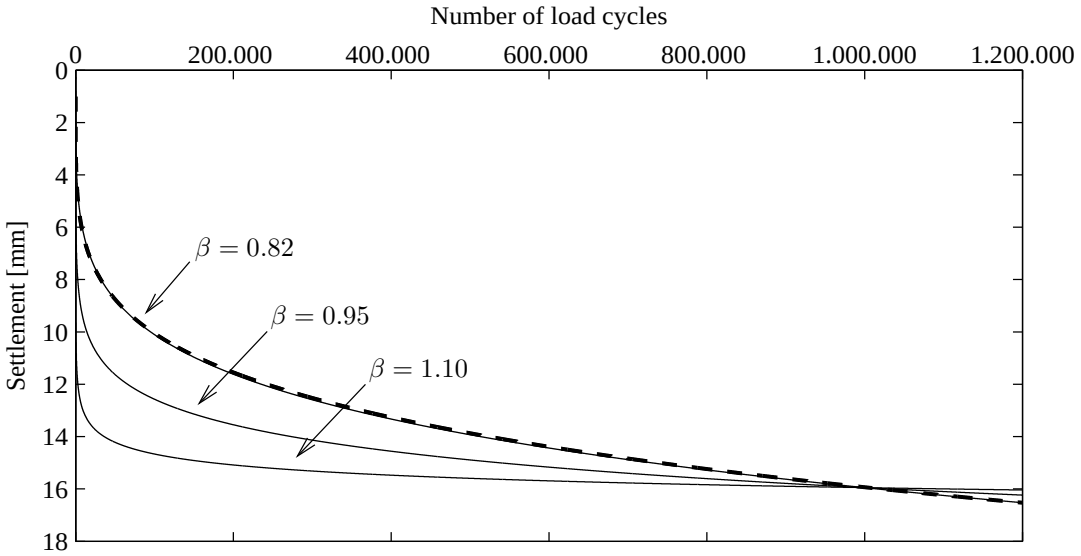

Figure 5.2: Progression of settlement for three different values of β for constant loading amplitude (thin solid lines). Comparison with the settlement model of Shenton (dashed line)

formula of Shenton, presented in Equation (3.10), referring to the ballast settlement after tamping. For this, it was considered an axle load of 200 kN, $K_s = 1.1$ and $K_1 = 0.914$, for A_{eq} expressed in tons (Shenton, 1985). The value of γ used to obtain the three solid lines with Equation (5.5) was $\gamma = 15.95$ mm, set in order to achieve coincidence with the settlement determined with the Shenton formula at cycle 10^6. The loading amplitude $\bar{F}$ was assumed to be 50 kN (transmissibility of 50%), the same value defined for the reference loading amplitude F_0. The main observation from Figure 5.2 is that the settlement curve obtained with $\beta = 0.82$ is almost coincident with the Shenton curve. So using $\beta = 0.82$ in Equations (5.1) and (5.4) leads to a progression of settlement with the number of load cycles similar to the Shenton formula. Therefore, this value will be used for parameter β.

The value of γ depends on the ballast intrinsic properties, the initial void ratio of ballast, the size and type of sleepers, the ballast height and the properties of the ballast underlayers, particularly the stiffness. The larger the flexibility of the underlayers, the larger the settlement in the ballast. According to Saussine et al. (2006), who performed numerical simulations using the discrete element method, high stiffness of the underlayer implies a strong network of contact forces, more compactness of the ballast assembly and less movement of particles under the sleepers. From compaction of sand it is known that soft subsoil hinders the compaction of thin sand layers. This might also hold for the tamping of ballast, meaning that the initial density of ballast on soft soil is lower and therefore, the possible additional compaction (and thus γ) is higher.

Variable loading case

The history of loading is stored and considered in the determination of the permanent vertical displacement of ballast due to each loading cycle by the function $h(F)$, presented in Equation (5.1). This function is an inverted cumulative histogram of the loading, storing the number of times the loading amplitude was higher than F. The term $+1$ inside the integral in Equation (5.1) is needed so that the function $h(F)$ is related only to the loading history prior to cycle N.

Table 5.1 shows an arbitrary example of a loading sequence composed of two periods. Periods 1 and 2 have the same duration, but a heavy vehicle type is added to the service during period 2. The Table shows the average loads transmitted through half-sleeper to the ballast, of each vehicle type and the corresponding minimum and maximum values, due to dynamic effects. The Table also shows the number of wheel passages belonging to each vehicle type that passed during each period. So, assuming all vehicles have four axles, a total of 90.000 cycles correspond to 22.500 vehicles passages.

Vehicle type	Average load [kN]	Minimum load [kN]	Maximum load [kN]	Num. cycles Period 1	Num. cycles Period 1 + 2
1	41	38	44	13.000	26.000
2	52	49	55	22.000	44.000
3	61	58	64	-	20.000
			total:	35.000	90.000

Table 5.1: Loading sequence with two periods

Figure 5.3 represents the function $h(F)$ at the end of the two periods presented in Table 5.1. As mentioned, for each force value the function gives the corresponding number of exceedences. For example, there are no exceedences above 65 kN and all cycles (90.000 total) were above 38 kN, as expected from Table 5.1.

Figure 5.4 shows the correspondent settlement determined with equations (5.1) and (5.2), with $\alpha = 0.6$ and $\beta = 0.82$, for the reasons given above, and $\gamma = 10$ mm, fixed arbitrarily. Within each period, the vehicles types sequence was mixed in time. The Figure shows a sudden increase in settlement in the beginning of period 2, caused by the heavier vehicle type added to the service.

The settlement model was also applied to reproduce the laboratory results obtained by Stewart, shown in Figure 3.4. As mentioned in Chapter 3, Stewart defined four stress-paths where the loading amplitude varied at each 1000 cycles. Figure 5.5 shows the results obtained by Stewart, represented with circles and triangles, and the settlement curves obtained with Equation (5.1), represented with lines. As can be seen, (i) the

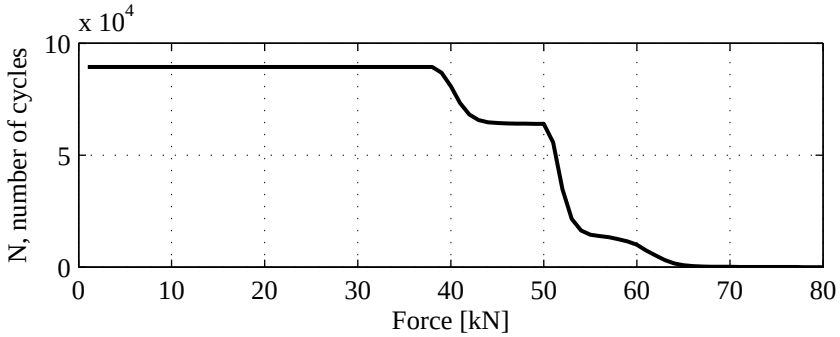

Figure 5.3: Example of an inverted cumulative histogram

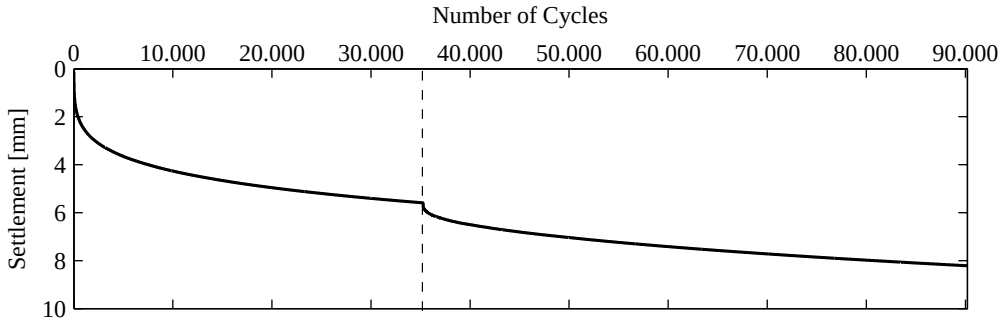

Figure 5.4: Settlement produced by load sequence presented in table 5.1. The vertical dashed line indicates the end of period 1

settlement model is able to follow the measured response, namely when the applied load suddenly increases, and (ii) the order of loading does not play a role in the calculated final settlement value, as is referred in literature concerning the ballast behaviour (Stewart, 1986; Indraratna and Salim, 2005).

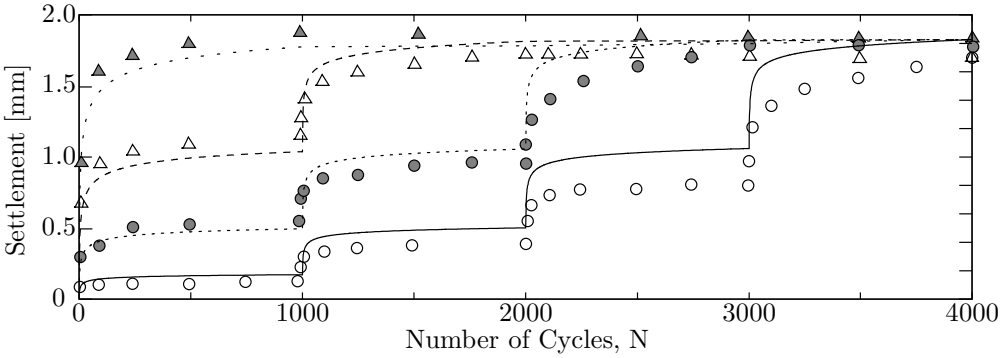

Figure 5.5: Settlement curves obtained with four different load paths (lines). Comparison with the results obtained by Stewart (circles and triangles) (Stewart, 1986).

The fitting of the calculated settlement curves to the results of Stewart was achieved with parameters $\alpha = 1.5$, $\beta = 1.1$ and $\gamma = 18$ mm. These values for parameters α and β differ from the above mentioned values of 0.6 and 0.82, respectively. The justification for this is the fact that the tests of Stewart were performed in a triaxial apparatus, with samples having 0.15m diameter and 0.38 m height. In this case, the sample size ratio, defined as the diameter of the specimen divided by the maximum particle dimension, is between two and three, for typical ballast gradation, which may be insufficient in order to avoid particle size effect (Indraratna et al., 1997). Also, the behaviour of ballast in relatively small samples actuated in triaxial tests may differ from its behaviour in real railway tracks actuated by moving trains, namely due to the rotation of the principal stresses directions, during loading by moving trains (Powrie et al., 2007).

5.4 Preliminary analysis

Importance of parameter ΔS

The influence of the value chosen for the maximum accumulated settlement between dynamic analyses, ΔS, on the calculated final position of the track is investigated here, using a simplified application of the train-track model presented in Chapter 4.

The example consists of an initially horizontal track with a single voided sleeper, as represented in Figure 5.6. The supporting stiffness is constant along the track, with the same properties as those defined for spring S1 in Table 4.5. Again, the sleeper spacing is 0.60m, an UIC54 rail profile is used and the mass of half sleeper, with the fixation system, was assumed to be 80kg.

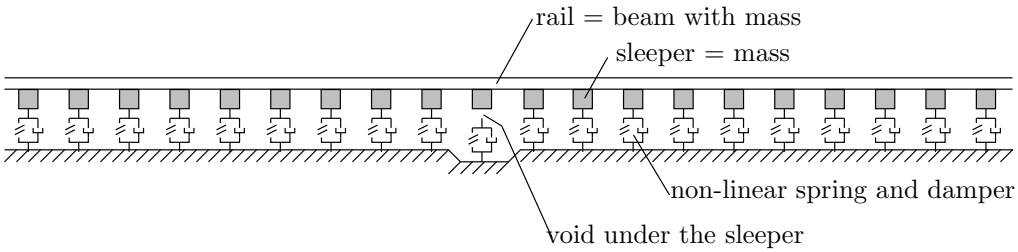

Figure 5.6: Track model

The settlement characteristics of the ballast are also assumed constant along the track. The parameter γ was chosen to be 20mm. As will be saw later, this value is in agreement with the track settlement measured during the monitoring campaign described in Chapter 2. The parameters $\alpha = 0.6$ and $\beta = 0.82$, for the reasons mentioned in Section 5.3.

Three different loading cases were defined, each case consisting on 7500 passages of a different vehicle type. This gives a total of 30.000 load cycles per simulation (four axles vehicles). The load model consisted on pairs of moving forces, representing two wheel loads belonging to the same bogie. The dynamics of the vehicles were here neglected. The vehicles represent: a locomotive class 1700 (LOC), an inter-city carriage (ICR) and an inter-city Koploper motorcar unit (ICM), in use in the Dutch railways. The corresponding static wheel loads are listed in Table 5.2. It was assumed that both ICR and ICM vehicles were evenly half-loaded.

Railway vehicle	Static wheel load
LOC	107.5kN
ICR	87.2kN
ICM	71.5kN

Table 5.2: Static wheel loads of the railway vehicles

Figure 5.7 presents the calculated position of the ballast surface using four different values of ΔS and for each loading case. The initial position of the ballast surface is represented on top, where it can be seen the position of the voided sleeper. The figure shows that the final position of the ballast surface obtained with ΔS=0.15mm and ΔS=0.30mm is identical and that the results obtained with ΔS=0.60mm or ΔS=0.90mm are significantly different. The potential impact of inadequate values chosen for ΔS is clearly demonstrated from these results.

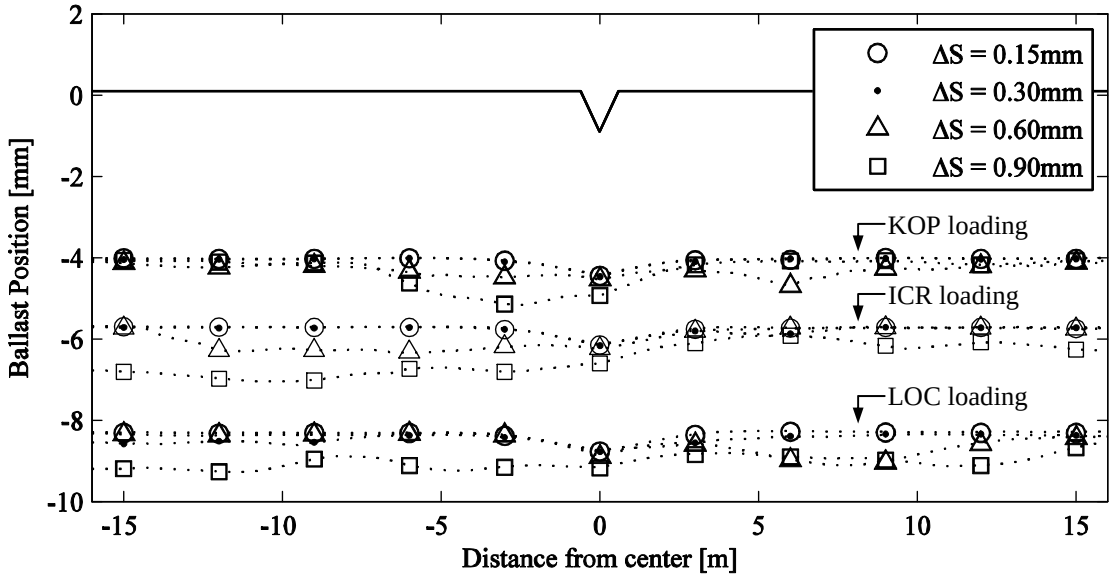

Figure 5.7: Ballast surface position after 30.000 load cycles

The justification for the numerical instability observed for high values of ΔS lies on the fact that the ballast settlement formula, presented in Equation (5.1), responds immediately when the loading increases above any previously applied value. Then, if the permanent deformation at any given sleeper is, eventually, over estimated and if this value is significantly accumulated before new dynamic analyses, because the value of ΔS is high, this will result in a permanent defect, with impact on the calculated final position of the track. If the value of ΔS is too high, a process of error accumulation may also occur, resulting on final results totally incorrect, as those obtained using ΔS higher than 0.3mm.

It can be seen in Figure 5.7 that there are some differences also between the results obtained with ΔS=0.15mm and ΔS=0.30mm. These are more evident on the LOC loading case, between locations -15m and -5m. The results obtained with values of ΔS lower than 0.15mm, not presented here, were the same as those found with $\Delta S = 0.15$mm. Therefore, it can be stated that for the track-model and the settlement properties under consideration, the value of 0.15mm for parameter ΔS is a good first estimate.

5.5 Long-term simulation of a railway transition

This section validates the methodology and the proposed settlement model with the long-term measurements performed at the culvert, presented in Chapter 2. The data used consists on the track settlement measured between October 7^{th} 2008 and May 5^{th} 2009, comprising 210 days, depicted in Figures 2.5 and 2.6.

5.5.1 Settlement due to ballast and subgrade

In Section 2.2.2 it was mentioned that the settlement of the soil layers under the ballast and the sub-ballast layers, referred to as the subgrade, is significant, with an average value of 1mm/month. It is thus necessary to consider the subgrade settlement, together with the ballast settlement model presented in Section 5.3, which leads to:

$$S_N = S_{\text{b}.N} + S_{\text{sg}.N} = \sum_{n=1}^{N} u_{\text{p}.n} + \delta S_{\text{sg}} \Delta t \tag{5.6}$$

where S_N represents the settlement of the surface of the ballast at load cycle N passed after maintenance, $S_{\text{b}.N}$ the corresponding settlement of the ballast layer, $S_{\text{sg}.N}$ the corresponding settlement of the subgrade, $u_{\text{p}.n}$ is the permanent deformation of ballast according to equation (5.1), δS_{sg} is the settlement rate of the subgrade and Δt is the time passed since maintenance.

The assumed settlement rate under the ballast layer in the culvert site is depicted in Figure 5.8. The position of the culvert and of the approach slabs are symbolically represented in the figure. This settlement rate profile reflects (i) the measured settlement of the subgrade on the embankment areas, (ii) the fact that the culvert is a settlement free structure and (iii) the rotation of the approach slabs, with maximum settlement at their free ends, as referred in Section 2.2.2.

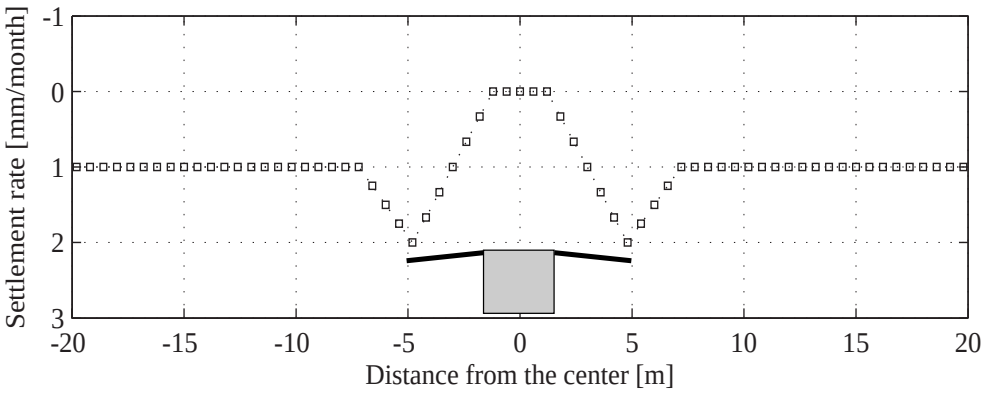

Figure 5.8: Setlement rate of the subgrade assumed for the track settlement calculations

5.5.2 Parametrization of the dynamic model

The dynamic model is 89.4 m long, comprising 150 sleepers spaced 0.60 m. A 'start' and 'end' section are needed in the model in order to minimize boundary effects on the results obtained at the section of study. These sections are depicted in Figure 4.4. The 'start' and 'end' section of the model have 26.4 m length, and the central section of study has 36.6 m length.

The values assumed for the parameters of the track were given in Table 4.3 and 4.5. The loading of the track represents four different vehicles of NS-reizigers (the Dutch national railway company) passing the site during the period of observation: a locomotive class 1700 (LOC), an intercity carriage (ICR), a motorcar unit belonging to a double deck vehicle (DD), and a motorcar unit belonging to an intercity train (ICM). The values assumed for the parameters of the ICR and the ICM vehicles were given in Table 4.2. The values for the parameters of the LOC and the DD vehicles are listed in Table 5.3.

Vehicle	LOC	DD
Mass of the car [kg]	40300	50850
Mass of the bogie [kg]	16800	3770
Mass of the wheel set [kg]	3030	1800
Mass inertia of the car [kgm^2]	157800	847460
Mass inertia of the bogie [kgm^2]	10974	1964
Stiffness $k_{\mathrm{v.1}}$ [N/m]	22.3×10^5	24.4×10^5
Stiffness $k_{\mathrm{v.2}}$ [N/m]	240.0×10^5	21.0×10^5
Damping $c_{\mathrm{v.1}}$ [Ns/m]	45.7×10^3	2.0×10^3
Damping $c_{\mathrm{v.2}}$ [Ns/m]	139.0×10^3	46.2×10^3
L_{c} [m]	17.9	28.2
L_{b} [m]	9.7	20.0
L_{w} [m]	2.8	2.5
Contact stiffness coefficient (k_c)	91×10^9 N/m$^{1.5}$	

Table 5.3: Parameters of the LOC and DD vehicles

5.5.3 Traffic

The traffic at this site varied along the day and also from week days to weekends. The traffic cases, defined in Table 5.4, attempt to represent the average situation. Two periods with different traffic scenarios were defined: one period between October and December 2008 and the other between January and May 2009. The four vehicles listed in Table 5.4 are the heavier vehicles passing the site. There are other lighter vehicles passing the site but their contribution to the accumulated settlement was considered negligible. Each day comprised 18 hours of train service. The validation of the calculations was made assuming six hours of train's passages from service operation, between the lift of the track and the first measurement of the track level.

Vehicle	Oct. to Dec. 2008	Jan. to May 2009	Static wheel load	Velocity
LOC	1 per hour	1 each 3 hours	107.5 kN	130 km/h
ICR	10 per hour	-	87.2 kN	130 km/h
DD	4 per hour	4 per hour	82.1 kN	120 km/h
ICM	9 per hour	12 per hour	71.5 kN	120 km/h

Table 5.4: Traffic defined in terms of number of vehicles per unit of time, static wheel loads and velocities of the railway vehicles

5.5.4 Parametrization of the ballast settlement model

The settlement of the ballast, calculated with Equation (5.1), requires three parameters: α, β and γ. The values $\alpha = 0.6$ and $\beta = 0.82$ were fixed, as explained in section 5.3.

The first values for parameter γ were chosen based on the total settlement measured at the embankment regions and on top of the culvert and accounted for the settlement resulting from compaction of the sublayers, described in 5.5.1. These values for γ were then gradually changed, following a trial and error procedure in order to obtain good agreement between the measured and calculated final levels of the track.

The final values fixed for parameter γ are listed in Table 5.5. As can be seen, there is one set of values for γ characterizing the ballast settlement under the inner rail and another set characterizing the ballast settlement under the outer rail. Under the outer rail, the settlement rate is approximately 30% higher than under the inner rail. For each set, there are four regions with corresponding values of γ. The value of γ is minimum on top of the culvert.

Distance to center [m]	-44.4 to -1.2	-0.6 to 0.6	1.2 to 9.6	10.2 to 45
Sleeper number	1 to 73	74 to 76	77 to 91	92 to 150
γ for inner rail [mm]	12.5	4.5	12.5	15.5
γ for outer rail [mm]	16.0	6.0	16.0	20.0

Table 5.5: Selected values for parameter γ, expressed in [mm]

5.5.5 Validation of the numerical simulation

Figure 5.9 shows the measured and calculated inner (a) and outer (b) rail level at three instants of time: at day 0 corresponding to the day when the maintenance operation and the first measurement of the track level were performed, at day 51 corresponding to the day of the second measurement of the track level and at day 210. The Figure shows the results obtained at the central section of study of the track, as defined in Figure 4.4. The calculated levels of the inner and outer rail follow closely the corresponding measured levels. These results demonstrate the suitability of the described methodology to calculate the evolution of the track settlement, even in cases of transition zones.

The calculation of the final level of the track, shown in Figure 5.9, required 126 dynamic analyses for the inner level and 135 dynamic analyses for the outer level, using $\Delta S = 0.15$ mm. Each dynamic analysis comprised the calculation of three or four vehicles passages, depending on the traffic period under consideration. A total of 447 and 482 vehicles passages calculations were therefore necessary to determine the final level of the tracks for the inner and outer rails, respectively. Using a personal computer with an i7 Intel processor, this required approximately 12 h of computation for each case, using the software MATLAB (MathWorks Inc., 2009).

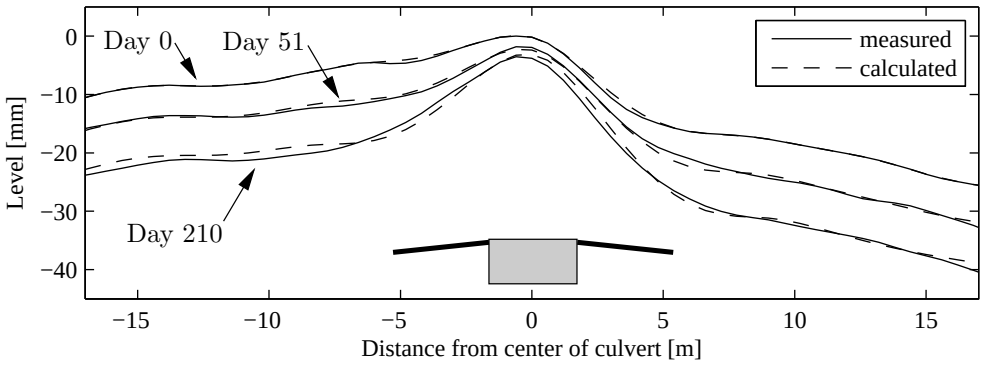

a) inner

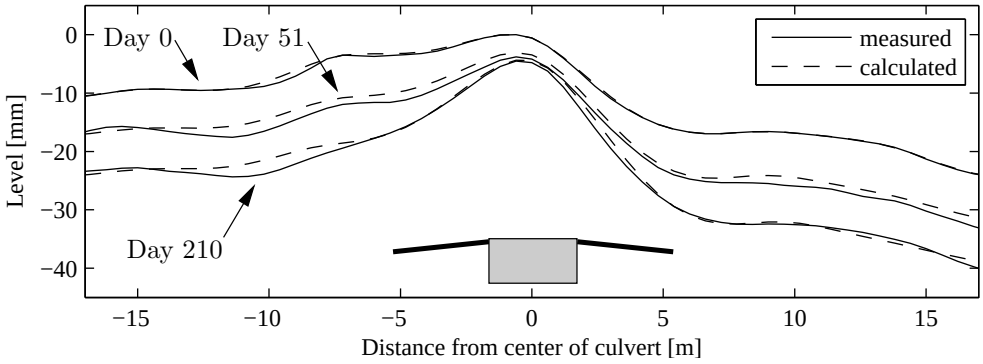

b) outer

Figure 5.9: Calculated and measured level of the inner (a) and outer (b) rail at three instants of time

The track levels shown in Figure 5.9 do not show the possible existence of hanging sleepers. Figure 5.10 shows the calculated level of the inner rail at day 210, with the corresponding position of the ballast surface, where each dot identifies one sleeper position. From this figure, it is clear that there are hanging sleepers to each side of the culvert. The vertical gap, which is the height of the void between the sleeper soffit and the ballast surface, can be calculated from the difference between the two sets of values presented in this figure.

Figure 5.11 shows the calculated vertical gaps under the inner rail for two instants of time together with the measured results. According to these calculations, the vertical gaps start developing right after the maintenance operation and at the final day 210 the vertical gaps reach 6 mm to the East of the culvert and 8 mm to the West of the culvert.

The field survey at this site included direct measurements of the voids under some sleepers around the culvert, mainly under the inner rail. These measurements were performed during the last two months of the total measurement period, using void indicator de-

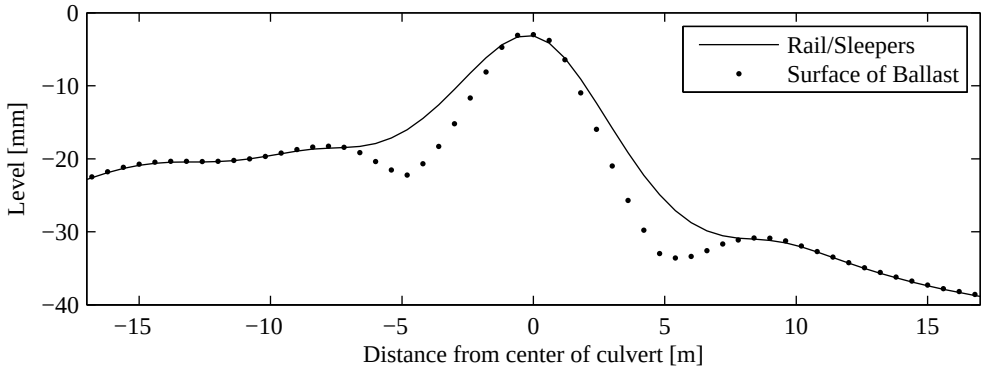

Figure 5.10: Level of the inner rail (solid line) and level of the top surface of the ballast (dots) calculated at day 210

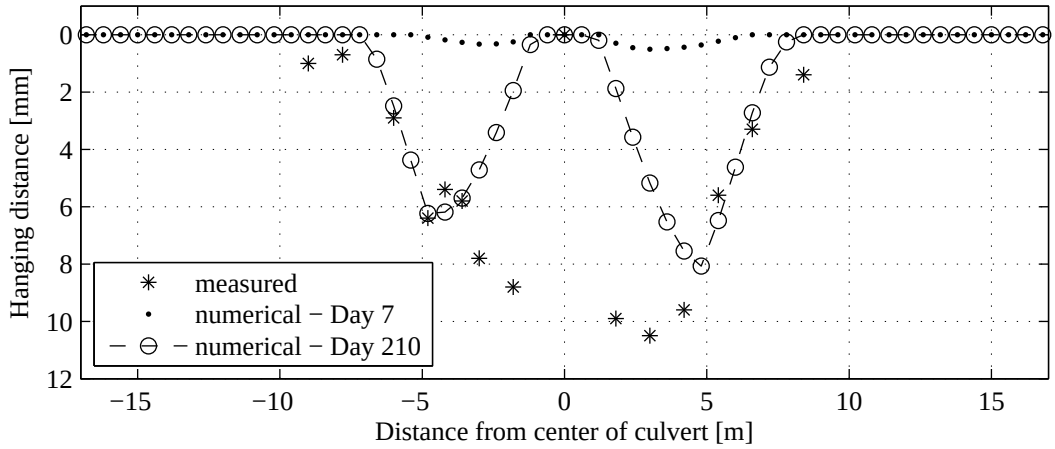

Figure 5.11: Measured and calculated voids under the sleepers. The measured voids correspond to an average of values measured between day 196 and 210.

vices (Vortok International, 2007). These measurements were shown in Figure 2.7. Figure 5.11 shows the average measured voids under the inner rail. It can be seen that the calculated vertical gaps are very close to the average measured values, except for locations distanced 1.8 m to 3.0 m from the center of the culvert, where the measured voids were considerably bigger.

5.5.6 Influence of the dynamic loading on the settlement of the ballast

The influence of the dynamic component of the train loading on the settlement of the ballast is investigated next. For this, the results of the model described above, which included inertia properties of the vehicles, are compared with those obtained with constant

moving forces. Therefore, the parametrization of the model is as given in Section 5.5.1 to 5.5.4.The dynamic part of the loading is caused by oscillations of the vehicle when passing the unleveled, and possibly suspended, track. The dynamic effects caused by interactions at the wheels-rail interface, due to rail corrugation or wheel out-of-roundness, were not accounted for in these calculations.

Figure 5.12 shows the amplitudes of the forces transmitted to the ballast under the wheel load, during the passage of a LOC vehicle at 130km/h. This figure compares the obtained result considering a moving mass-spring system for the vehicle, with that considering moving forces with a constant value equal to the static wheel load. The first observation is that the amplitudes of the applied forces to the ballast vary significantly on the transition zones, as already mentioned in Chapter 4. It can be seen that the transmission is minimum on locations coincident with the maximum hanging distances, around 5 m away from the culvert center.

According to this figure, the produced distribution of forces considering constant moving forces is approximately symmetrical around the culvert center, meaning that the direction of the passage of the train is almost irrelevant. This is not the case when accounting with the vehicle-track interaction, for which an asymmetrical distribution of forces is clear. Right before the culvert, the dynamic loading from the train increases the forces transmitted to the ballast, right after the culvert the effect is opposite, and from 5 m on past the culvert the force amplitudes are again larger.

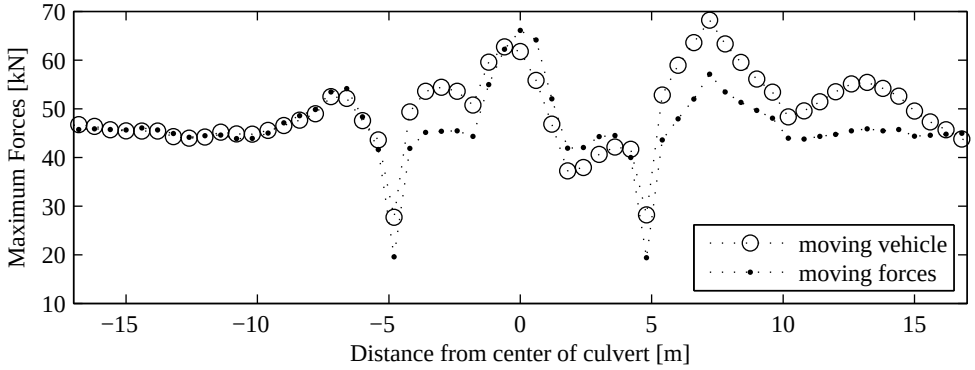

Figure 5.12: Amplitude of the forces passing to the ballast at each sleeper of the model caused by the passage of a LOC vehicle passing from left to right. Results obtained for the inner rail at day 210

The differences evident in Figure 5.12 have consequences on the settlement of the ballast layer. Figure 5.13 depicts the settlement of the ballast layer ($S_{\mathrm{b}.N}$ in Eq. (5.6)), which occurred during the 210 days of the analysis. The figure presents the result obtained with

the dynamic model for the vehicles and that obtained with moving constant forces. It can be seen that there are significant differences, which may reach 20%, and that the ballast settlement calculated with the moving vehicles systems is, generally, bigger, due to the vibration of the sprung wagon mass. Of course, differences are observed above and after the culvert only.

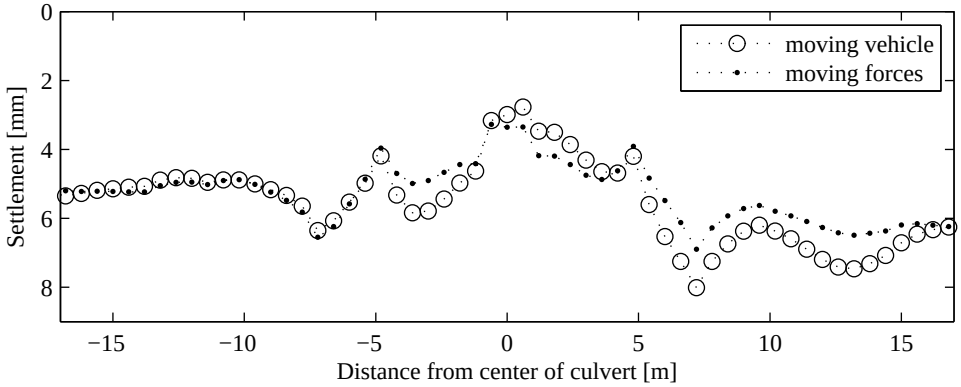

Figure 5.13: Total settlement of ballast during the 210 days of the analysis. Results with dynamic mass-spring model for the vehicles and with moving constant forces

The results shown confirm that the dynamic contribution of the train loading, frequently ignored in similar analyses, may significantly influence the settlement of the track. This influence will depend on the characteristics of the vehicles, which govern their natural frequencies, and on the speed of the trains, which govern the excitation frequencies and the excitation amplitudes, also influenced by the level of the track and the occurrence of hanging sleepers. Introducing the rail corrugation and wheels out-of-roundness will presumably augment the impact of the dynamic loading on the long-term deformation of the track, because the dynamic loading will be higher (Varandas et al., 2012).

5.5.7 Importance of the constitutive model

Ballast behaviour

Dynamic measurements of the track lead often to the conclusion that the soil response is non-linear (Nielsen and Oscarsson, 2004). This was also concluded from the dynamic measurements performed at the culvert, as explained in Chapter 4. Instead, is it possible to use a linearized constitutive model for the ballast and underlayers?

This section analyzes the importance of the non-linear soil response on the track settlement. The results presented in Section 5.5, determined with a model with springs

presenting a non-linear force-displacement path (see Eq. (4.9)), are compared with those obtained with an identical model, but with equivalent quasi-linear springs, with the force-displacement path defined as follows:

$$F_{\text{t.s.}i} = \begin{cases} k_{\text{lin.}i}(u_{\text{t.}i} - u_{\text{c.}i}) & \text{, if } u_{\text{t.}i} \geq u_{\text{c.}i}, \\ 0 & \text{, if } u_{\text{t.}i} < u_{\text{c.}i}. \end{cases} \tag{5.7}$$

where $F_{\text{t.s.}i}$ is the force acting on the spring i, $u_{\text{t.}i}$ is the downward displacement of the corresponding sleeper, $u_{\text{c.}i}$ is the position where the sleeper contacts the ballast, and $k_{\text{lin.}i}$ is the equivalent linear stiffness of the spring. This is in fact a bi-linear model because the spring only works during compression. Except for the parameters values of the supporting springs of the equivalent linear model, the parametrization of the models was the same as given in the previous sections.

The values for this equivalent stiffness were determined so that the maximum displacements calculated due to the passage of an ICR vehicle would be approximately the same as those previously obtained with the non-linear model. The choice of the ICR vehicle for the calibration of the equivalent linear springs was made because it presents an intermediate static weight among the considered types of vehicles. The values of k_{lin}, in correspondence with the non-linear equivalents given in Table 4.5, are given in Table 5.6.

Spring	k_{lin} [MN/m]
S1	26
S2	58
S3	90

Table 5.6: Equivalent stiffness of the linear springs

Figure 5.14 shows the results of the maximum track displacements when an ICR passes. These calculations were performed with the initial level of the track, at day 0 of the calculations (see Figure 5.9). The train is modeled with a mass-spring system. A good agreement between results obtained with the non-linear model and with the equivalent linear model can be seen. The differences between the two sets of results are due to fluctuations on the maximum displacements exhibited on the non-linear case only. These fluctuations are caused by the fact that the initial preload, due to the track weight, on this unlevelled track differs from sleeper to sleeper. In the case of non-linear force-displacement path of the springs, this implies that the receptance, defined as the ratio between the track deflection and the transmitted force (Dahlberg, 2003), will also differ from sleeper to sleeper.

The non-linear characteristic of the stiffness model brings significant implications for the

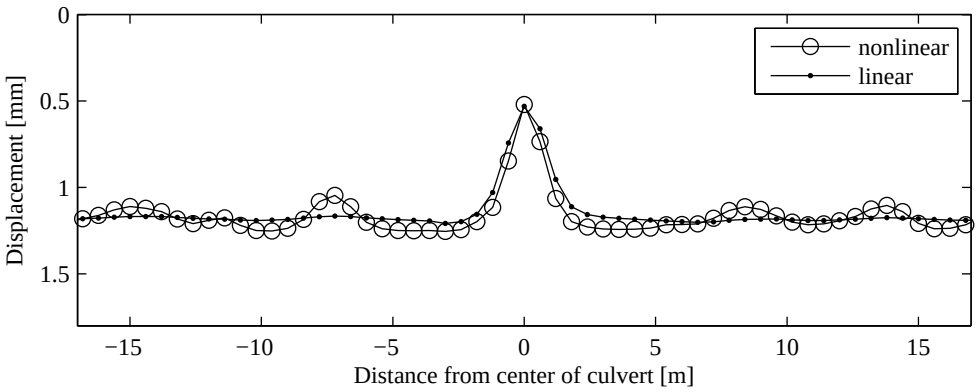

Figure 5.14: Maximum downward displacements caused by the passage of an ICR vehicle considering the initial level of the track, without voids under the sleepers. Results obtained with the non-linear model and with the linear model

transmitted forces to the ballast. Figure 5.15 presents the calculated maximum forces, where each dot or circle represents one sleeper location. These results were obtained with a passage of an ICR vehicle at day 85, the last day of circulation of this type of vehicle at this location.

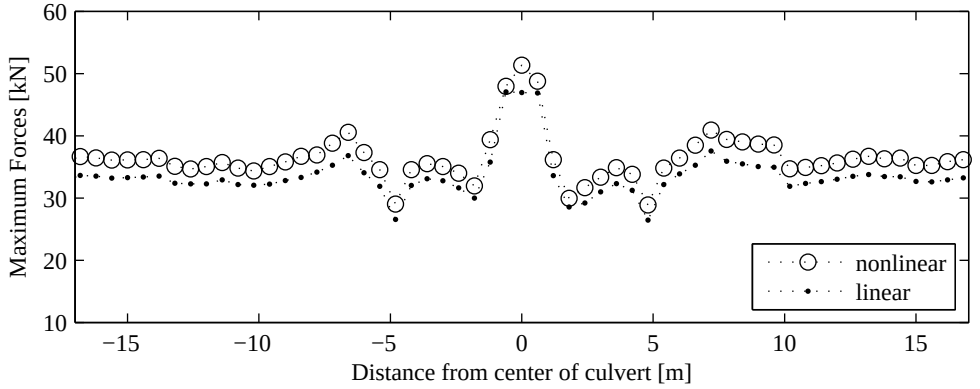

Figure 5.15: Amplitude of the forces passing to the ballast at each sleeper of the model caused by the passage of an ICR vehicle. Results obtained for the inner rail at day 85

The results presented in Figure 5.15 show that the maximum forces calculated with the non-linear stiffness model for the passage of an ICR vehicle are always higher than those obtained with the equivalent linear model. In fact, the same applies for the other types of vehicles. An explanation for this might be the fact that with the non-linear stiffness model, the stiffness under a sleeper directly loaded by an axle is locally higher than the stiffness under the neighbouring sleepers. This implies a higher transmissibility for the loaded sleeper, comparing with the case of uniform stiffness under the sleepers (the linear

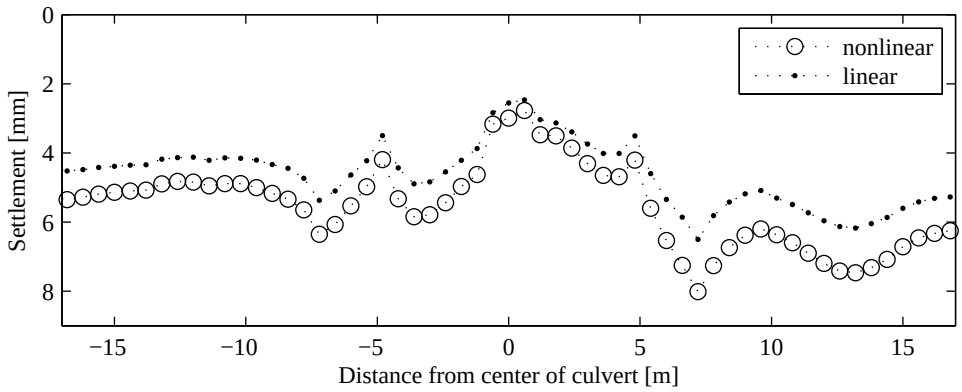

Figure 5.16: Total settlement of ballast during the 210 days of the analysis. Results with non-linear stiffness model and with quasi-linear stiffness model

model). As the settlement of ballast is assumed proportional to the maximum applied force, this leads to significant differences in terms of calculated settlement of the ballast when using one model or the other.

Figure 5.16 shows the corresponding total settlement of ballast, $S_{\mathrm{b}.N}$, determined at day 210. It can be seen that the differences in terms of ballast settlement varied between 10% and 25%, showing that the calculation of settlement based on force proportional models should take into consideration the non-linear stiffness behaviour of the layers forming the track bed. The importance of the considered constitutive model on the calculated dynamic response will be further analyzed in the following chapter.

Wheel-rail interaction

Since the forces passed to the ballast strongly differs on location, one might question on the influence of the non-linearity in the wheel-rail interaction. This is studied by replacing the non-linear Herzian contact spring (Eq. (4.12)) by an equivalent linearised spring, with (Esveld, 2001):

$$k_{\mathrm{H}} = \frac{3}{2}\, k_{\mathrm{c}}^{2/3}\; F_{\mathrm{st}}^{1/3}, \tag{5.8}$$

being the equivalent linearised spring stiffness, k_{c} [$\mathrm{Nm}^{-3/2}$] the stiffness parameter of the non-linear model, and F_{st} the static wheel load.

The results in terms of wheel-rail interaction forces only changed slightly (less than 1%), and therefore the calculated settlements are (approximately) the same. Ergo, the linearization of the Hertzian spring with Eq. (5.8) is possible for analyses considering the long-wave uneveness of the track.

5.6 Discussion

The results of the model show good agreement between the measured and calculated level of the track during the full measurement period of more than 7 months. The values fixed for parameter γ of the ballast settlement model were listed in Table 5.5. The justification for the variation of parameter γ is given next.

According to the measured changes of the level of the track, the outer rail settles more than the inner rail. The calculations have shown that a difference of 30% in the ballast settlement response, expressed by parameter γ, leads to the measured differences. This behaviour is explained by the fact that the outer rail is closer to the ballast slope, as can be seen in Figure 2.2. This implies lower confinement of the ballast located under the outer rail compared to the ballast under the inner rail, leading to higher rates of densification of the ballast (Lackenby et al., 2007). However, another influence might be the fact that the track is in a left curve, which might lead to a higher wheel load in the right rail. This aspect is not included in the dynamic model. The methodology here presented can still be applied to curved tracks, for which a 3D dynamic train-track model would then be necessary, for the corresponding determination of the loading transmitted to the ballast.

In order to get a good agreement between the measured and calculated track level, a relative small value for γ for the ballast on the top of the culvert must be chosen. This is explained by the fact that the ballast is on top of the stiff concrete culvert, so the stiffness under the ballast is higher. As already mentioned in Section 5.3, high stiffness of the underlayers implies less movements of ballast particles and thus less settlement of the assembly. During tamping the higher stiffness under the ballast leads to more efficient tamping. Since the culvert is locally the highest point of the track, the lift given to the track during maintenance is much smaller than on the rest of the track. According to Shenton (1985), smaller lift given during maintenance corresponds to smaller total settlement of ballast after maintenance. Since the parameter γ represents the total settlement after a reference number of cycles with a reference load, it is ergo understandable that the value of γ on top of the culvert must be smaller.

The application of the presented model for an independent prediction of settlement at transition zones, requires an adequate estimation of the parameter γ and still further verification of the model. In this study, the values of γ were defined based on available long-term measurements on a specific transition. For general application this parameter must be estimated before hand, based on or experience with the model from site measurements or based on properties of the problem at hand, e.g. the material properties of the ballast (preferably based on specific laboratory experiments), the initial state of the ballast in terms of void ratio and confinement, the size and type of sleepers, the ballast height

and the properties of the underlayers, particularly the stiffness. The predictions must be validated with additional long-term measurements at different sites.

The 1-D numerical simulations confirmed that the densification of ballast after tamping plays an important role on the loss of quality of a transition. However, the development of voids under the sleepers located above the approach slabs was underestimated compared to the measured values. This means that the permanent deformation of the ballast layer in this specific region cannot be explained only by densification proportional to the loading of the track. The degradation mechanism responsible for this increased settlement of the ballast may be horizontal flow of ballast (which was observed visually at the test site and is possibly caused by impact loads from suspended sleepers (Baessler and Ruecker, 2003)), rolling of soil over the inclined approach slabs, increased crushing of ballast particles, among others. The next chapter will address this issue.

5.7 Conclusions

The methodology presented in this chapter proved to be adequate to calculate the track level evolution at transition zones. The settlement of the track is decomposed into a part due to the ballast and a part due to the subgrade. The ballast settlement law is proportional to the loading amplitudes applied to the ballast and depends on the number of loading cycles. Application of the inverted cumulative histogram function offers the possibility to cover a wide range of maximum loading for each sleeper.

The distribution of the forces transmitted to the ballast varies considerably in transition zones. This force transmission depends on the location of the sleeper, the existence of a void under the sleeper, and the passing vehicle. It was also found that the development of voids under the sleepers leads to high differences between the maximum load under consecutive sleepers.

The differences in terms of forces transmitted to the ballast considering the inertia properties of the vehicles versus results with constant moving forces reach 20%. Consequently, the dynamic component of the train loading generally leads to an increase of the development of settlement of the ballast. In this study, the amplification from the vehicle dynamics is caused by long-wave uneveness of the track.

The linearization of the support stiffness model, representing the track foundation, leads to an underestimation of the accumulated settlement of the ballast.

Chapter 6

Three-Dimensional Non-Linear Modelling of Railway Tracks

6.1 Introduction

This Chapter presents a newly developed three-dimensional non-linear finite element program for the calculation of the dynamic loads on the ballast, imposed by trains passing a transition. As mentioned in Chapter 3, most numerical models representing railway tracks assume the linear elastic model for the track bed layers, including the ballast. However, not only the ballast has a non-linear response when loaded with passing trains, but also in Chapter 5 it was seen that the consideration of the non-linear response of the ballast is important for the determination of the loading transmitted to the ballast. The models used in Chapters 4 and 5 were one-dimensional, and as so they are not suited to study the dynamic stress-strain response of the ballast/soil layers. With the presented program, the importance of the consideration of the non-linear ballast response on the dynamic stress-strain field generated by the passage of railway vehicles will be analyzed.

The methodology from Chapter 5 gave good agreement in rail level, but did not calculate the voids close to the culvert correctly. Therefore, the results presented suggest that another mechanism, related with flow of ballast, plays an important role on the degradation of this transition zones. The three-dimensional dynamic response of the ballast is analyzed in terms of: (i) the influence of decreased initial load on the ballast (due to hanging sleepers) and (ii) the influence of the motion of the approach slabs, on the long-term response of the transition. At the end, the reasons for the magnitude of the voids existing under the sleepers located in the transition zones will be highlighted.

6.2 Numerical model

6.2.1 General description

A three-dimensional numerical program for the calculation of the dynamic response of railway tracks is presented. This program, hereafter called 'Pegasus', was fully coded in Matlab (MathWorks Inc., 2009). This Section describes the main features and assumptions of program Pegasus. The reason for the development of Pegasus was the intention to perform dynamic analyses incorporating the non-linear material behaviour of the granular layers of ballast and sub-ballast, and the non-linear contact between the sleepers and the ballast, executed with models representing transitions zones in railway tracks, having possibly more than 1 million dof. Initial attempts with available finite element programs failed due to difficulties with memory handling and required computational time.

Figure 6.1 shows a perspective of the main elements considered in the finite element models built with Pegasus. The railtrack is composed by the rails, the sleepers and the railpads. The ballast and soil layers are assumed to have horizontal stratification. Slopes are possible at one or either sides of the railtrack. The program may also consider a culvert box with approach slabs (not represented in the Figure).

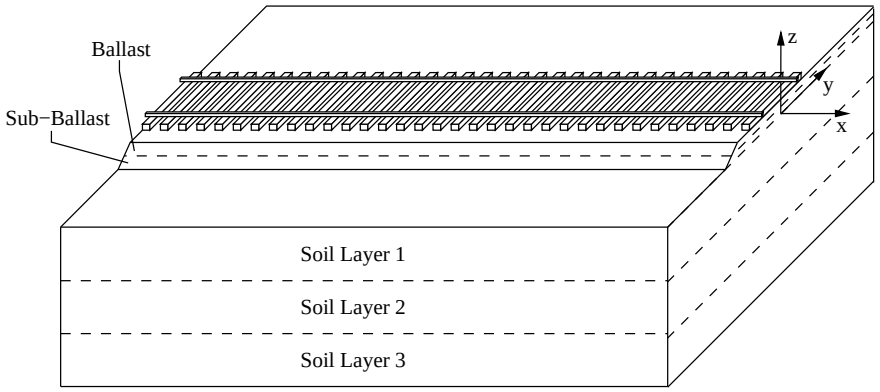

Figure 6.1: Overview of 3-D model

In Pegasus, the railtrack and the ballast/soil layers form two distinct structural systems, as represented in Figure 6.2. These two systems interact by means of interaction forces. The interaction forces between the sleepers and the underlying ballast are due to two distinct effects: (i) vertical contact between the sleeper's base and the ballast, and (ii) friction between the sleeper's lateral faces and the confining ballast. The definition of the interaction forces is non-linear due to the on/off contact distinction. This will be described further into the text.

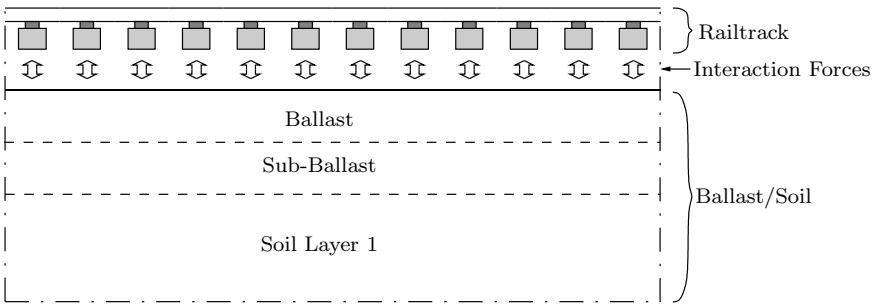

Figure 6.2: Railtrack system and ballast/soil system shown in the direction of the track

The railtrack system is built with Euler-Bernoulli beam elements representing the rails and the sleepers. Five degrees-of-freedom are considered per node, three translations and two rotations. The torsional rotation is neglected. The rails are connected to the sleepers with 3-D spring-damper elements, representing the railpads. Figure 6.3 gives a longitudinal and a transverse view of the railtrack model with a qualitative representation of the finite element discretization. The ballast-soil system is discretized with low-order eight-node solid hexahedral elements (Bathe, 1996; Hughes, 2003; Bhatti, 2005).

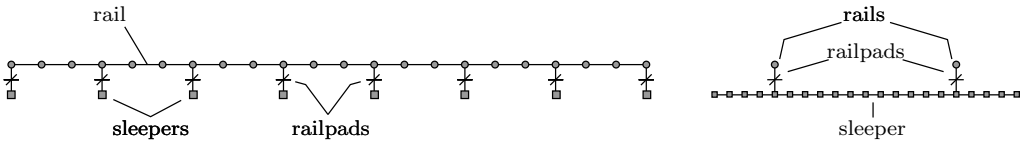

(a) - Longitudinal view (b) - Transversal view

Figure 6.3: Railtrack finite element model

The culvert, if existent, is considered by constraining the displacements of the nodes in contact with the (virtual) concrete surfaces of the culvert. Therefore, the culvert itself is not included in the model. It is here assumed that the culvert is founded on piles and that the motion of the culvert itself does not have an influence on the displacement field of the surrounding soil. The approach slabs are modelled with beam elements embedded in the soil, following the classical replacement of slabs with a grid of beams (Szilard, 2004). This procedure ensures that the support of the approach slabs in the culvert corresponds to a simple support, with no transmission of moments.

The coupled equations of motion of the railtrack and ballast-soil systems reads:

$$\begin{cases} \mathbf{K}_\mathrm{t}\mathbf{u}_\mathrm{t} + \mathbf{C}_\mathrm{t}\mathbf{v}_\mathrm{t} + \mathbf{M}_\mathrm{t}\mathbf{a}_\mathrm{t} = \mathbf{f}_\mathrm{g.t} + \mathbf{f}_\mathrm{train} + \mathbf{f}_\mathrm{a} \\ \mathbf{K}_\mathrm{s}\mathbf{u}_\mathrm{s} + \mathbf{C}_\mathrm{s}\mathbf{v}_\mathrm{s} + \mathbf{M}_\mathrm{s}\mathbf{a}_\mathrm{s} = \mathbf{f}_\mathrm{g.s} - \mathbf{f}_\mathrm{a} \end{cases} \tag{6.1}$$

where the subscripts t and s refer to the railtrack and ballast-soil systems, respectively.

Irrespective of the subscripts, $\mathbf{K}$, $\mathbf{C}$ and $\mathbf{M}$ are the global stiffness, damping and mass matrices of the structural systems, $\mathbf{u}$, $\mathbf{v}$ and $\mathbf{a}$ are, respectively, the vectors of nodal displacements, velocities and accelerations, $\mathbf{f}_{\mathrm{g}}$ is the vector of the gravity loads, $\mathbf{f}_{\mathrm{train}}$ is the vector of the wheel loads applied on the rails and $\mathbf{f}_{\mathrm{a}}$ is the vector of the interaction forces between the sleepers and the ballast.

All matrices are obtained by traditional finite element assembling procedure. The mass is lumped at the nodes of the finite elements, resulting in diagonal mass matrices. The railtrack system behaves linearly, but the ballast-soil system may include elements with non-linear behaviour. The stiffness matrix of the ballast/soil system ($\mathbf{K}_{\mathrm{s}}$) may thus be changing during the integration procedure, according to the non-linear stress-strain relationship. The damping matrices $\mathbf{C}_{\mathrm{t}}$ and $\mathbf{C}_{\mathrm{s}}$ represent the material damping of the railtrack and ballast/soil systems, respectively. These matrices were determined following the Rayleigh damping concept, as expressed in Eq. (4.7). For this, an equivalent constant stiffness matrix was assumed for the ballast/soil system ($\mathbf{K}_{\mathrm{s.lin}}$), resulting that both damping matrices are constant. The constant matrix $\mathbf{K}_{\mathrm{s.lin}}$ is built assuming typical values for the parameters defining the equivalent linear-elastic constitutive relations of the elements with non-linear behaviour.

The loading by the train is represented by an arbitrary number of moving forces acting on the rails. The speed of the loads may be constant or variable. The magnitude of the loads, defined in the three principal directions of the track, may also be constant or variable in time.

The method used to integrate the spatially discretized equations with respect to time (time integration) is the explicit predictor-corrector integration scheme (Zhai, 1996), already described in Chapter 4. This method is conditionally stable, and therefore the integration time step must be less than a critical value for convergence of the solution ($\Delta t \leq \Delta t_{\mathrm{crit}}$) (Hughes, 2003). This critical value is determined with (Hughes, 2003; Miller et al., 2007):

$$\Delta t_{\mathrm{crit}} = \min\left(\frac{L_{e.i}}{c_i}\right), \tag{6.2}$$

where $L_{e.i}$ is the smallest characteristic length of element i, and c_i is the corresponding dilatational wave speed of the element. For beam elements the characteristic length corresponds to the element length, and for eight-node hexahedral cuboid elements the smallest characteristic length corresponds to the minimum length of the cuboid faces. For beam elements, the velocity c is determined by:

$$c = \sqrt{\frac{E}{\rho}},$$

where E is the Young's modulus and ρ is the mass density. For solid elements, the velocity c is determined by:

$$c = \sqrt{\frac{M}{\rho}},$$

where M is the oedometer modulus, defined as:

$$M = \frac{E(1-\nu)}{(1+\nu)(1-2\nu)}, \tag{6.3}$$

where ν is the Poisson's ratio. This critical time-step value generally corresponds to a considerably small value (for the analyzed cases in the order of 1.25×10^{-5} s). As the frequencies of loading lies in a much lower frequency range, there are no accuracy improvements by using time steps smaller than the critical value. For large-scale problems, this explicit scheme is computationally faster than the Newmark implicit scheme, despite the fact that the time step required with the Newmark scheme might be one to two orders of magnitude bigger (Zhai, 1996).

The current version of Pegasus has some limitations. The train-track interaction is not explicitly accounted in the analyses. The consideration of the dynamic component of the train loading is significant when the track presents significant inhomogeneous characteristics (in terms of support stiffness, vertical level, etc), as was seen in Chapter 5, or when the simulation considers the short-wave irregularities of the rail, or the wheels out-of-roundness (Alves Costa et al., 2012).

The consideration of the train-track interaction can however be performed with Pegasus, using a two step calculation procedure (Kouroussis et al., 2011; Alves Costa et al., 2012). This procedure basically consists on using the one-dimensional model presented in Chapter 4 to estimate the train-track interaction forces, and then the program Pegasus to determine the corresponding response of the track/ballast/soil systems.

Another limitation of Pegasus is the fact that the program does not allow to consider the coupling between the soil skeleton and the groundwater flow, in case of saturated soils. According to (Kettil et al., 2008), the consideration of the two phase material in saturated media is important when the velocity of the train approaches the critical velocity of the track, and can be neglected for trains travelling at speeds significantly lower than the critical value.

6.2.2 Constitutive models for ballast and subgrade

In Pegasus there are currently two constitutive models available to represent the resilient nature of the granular materials forming the ballast/soil system: (i) the linear-elastic Hooke's Law and (ii) the nonlinear-elastic $K-\theta$ model.

Hooke's Law

The stress-strain relationship of the isotropic 3-D linear-elastic Hooke's Law in Cartesian coordinate system is written in matrix form as:

$$\sigma = \mathbf{D}\epsilon \tag{6.4}$$

where σ and ϵ are, respectively, the vector form of the stress and strain tensor, defined as:

$$\sigma = \begin{bmatrix} \sigma_{\mathrm{x}} \\ \sigma_{\mathrm{y}} \\ \sigma_{\mathrm{z}} \\ \tau_{\mathrm{xy}} \\ \tau_{\mathrm{yz}} \\ \tau_{\mathrm{zx}} \end{bmatrix}, \qquad \epsilon = \begin{bmatrix} \epsilon_{\mathrm{x}} \\ \epsilon_{\mathrm{y}} \\ \epsilon_{\mathrm{z}} \\ \gamma_{\mathrm{xy}} \\ \gamma_{\mathrm{yz}} \\ \gamma_{\mathrm{zx}} \end{bmatrix}, \tag{6.5}$$

and $\mathbf{D}$ is the constitutive stiffness matrix. The constitutive stiffness matrix is traditionally written in terms of the Young's modulus (E) and the Poisson's ratio (ν), as:

$$\mathbf{D} = \frac{E}{(1+\nu)(1-2\nu)} \begin{bmatrix} 1-\nu & \nu & \nu & 0 & 0 & 0 \\ \nu & 1-\nu & \nu & 0 & 0 & 0 \\ \nu & \nu & 1-\nu & 0 & 0 & 0 \\ 0 & 0 & 0 & \frac{1-2\nu}{2} & 0 & 0 \\ 0 & 0 & 0 & 0 & \frac{1-2\nu}{2} & 0 \\ 0 & 0 & 0 & 0 & 0 & \frac{1-2\nu}{2} \end{bmatrix}, \tag{6.6}$$

or in terms of the Bulk modulus (K) and the Shear modulus (G) as:

$$\mathbf{D} = \begin{bmatrix} K+\frac{4}{3}G & K-\frac{2}{3}G & K-\frac{2}{3}G & 0 & 0 & 0 \\ K-\frac{2}{3}G & K+\frac{4}{3}G & K-\frac{2}{3}G & 0 & 0 & 0 \\ K-\frac{2}{3}G & K-\frac{2}{3}G & K+\frac{4}{3}G & 0 & 0 & 0 \\ 0 & 0 & 0 & G & 0 & 0 \\ 0 & 0 & 0 & 0 & G & 0 \\ 0 & 0 & 0 & 0 & 0 & G \end{bmatrix}, \tag{6.7}$$

given the folowing relations between E, ν and K, G:

$$K = \frac{E}{3(1-2\nu)}$$
$$G = \frac{E}{2(1+\nu)}. \tag{6.8}$$

$K-\theta$ model

The non-linear $K-\theta$ model defines that the resilient modulus directly depends on the sum of the normal stresses (θ), defined positive for compression, according to Eq. (3.3), repeated here for convenience:

$$E_{\mathrm{r}} = K_1 \left(\frac{\theta}{\theta_0}\right)^{K_2}, \tag{6.9}$$

leaving the Poisson's ratio constant. This means that the full stiffness matrix $\mathbf{D}$ (Eq. (6.6)) is obtained by replacing the Young's modulus E with the resilient modulus E_{r}, which is a number that depends non-linearly on the sum of the normal stresses. The $K-\theta$ model is only defined under pressure conditions. During dynamic loading and particularly at the surface of the ballast layer, tensile stresses might occur. Therefore, the $E_{\mathrm{r}}-\theta$ relationship is here extended to the tension case by admitting a constant value for the resilient modulus, corresponding to its minimum value. This minimum value may be defined as low as necessary to maintain tensile stresses acceptably small (Allaart, 1992). Figure 6.4 depicts the corresponding adopted $E_{\mathrm{r}}-\theta$ relationship.

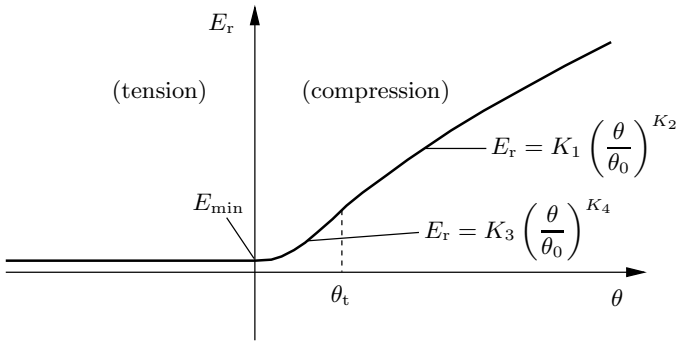

Figure 6.4: The $E_{\mathrm{r}}-\theta$ relationship

The corresponding mathematical expression of this $E_r - \theta$ relationship is:

$$E_r(\theta) = \begin{cases} E_{min}, \text{ if } \theta < 0 \\ E_{min} + K_3 \left(\frac{\theta}{\theta_0}\right)^{K_4}, \text{ if } 0 \leq \theta < \theta_t \\ K_1 \left(\frac{\theta}{\theta_0}\right)^{K_2}, \text{ if } \theta \geq \theta_t \end{cases} \tag{6.10}$$

The transition branch between $\theta = 0$ and $\theta = \theta_t$ assures a smooth transition between the constant branch of the tension side to the $K - \theta$ model assumed for $\theta \geq \theta_t$. This transition branch is defined by parameters K_3 and K_4. Knowing the parameters of the $K - \theta$ model (K_1 and K_2), the value for the minimum resilient modulus (E_{min}), and assuming a value for θ_t, which should be reasonably small (in the order of 10kPa) but meeting the requirement that:

$$K_1 \left(\frac{\theta_t}{\theta_0}\right)^{K_2} > E_{min},$$

the parameters K_3 and K_4 are determined to assure that the $E_r - \theta$ curve is of class C^1:

$$K_4 = \frac{K_1 K_2 \left(\frac{\theta_t}{\theta_0}\right)^{K_2}}{K_1 \left(\frac{\theta_t}{\theta_0}\right)^{K_2} - E_{min}}$$

$$K_3 = \frac{K_1 \left(\frac{\theta_t}{\theta_0}\right)^{K_2} - E_{min}}{\left(\frac{\theta_t}{\theta_0}\right)^{K_4}}$$

6.2.3 Sleeper-Ballast interaction

From the physical point of view, the interaction in vertical direction is due to normal pressure at the sleeper's base level, and friction between the sleepers lateral faces and the confining ballast. In horizontal directions, the interaction is mostly due to Coulomb friction at the sleeper's base level and to normal pressure between the sleeper's lateral faces and the confining ballast.

In the current version of Pegasus, the horizontal coupling is not accounted, only the vertical coupling is. The interaction forces between the railtrack system and the ballast/soil system are represented in Figure 6.5. The analyses are limited to vertical loading from

the trains, for which the horizontal interaction can be neglected. The horizontal motion of the railtrack is constrained with horizontal springs and dashpots, which do not affect the vertical coupling of the two systems, and are solely necessary to maintain the railtrack system in position.

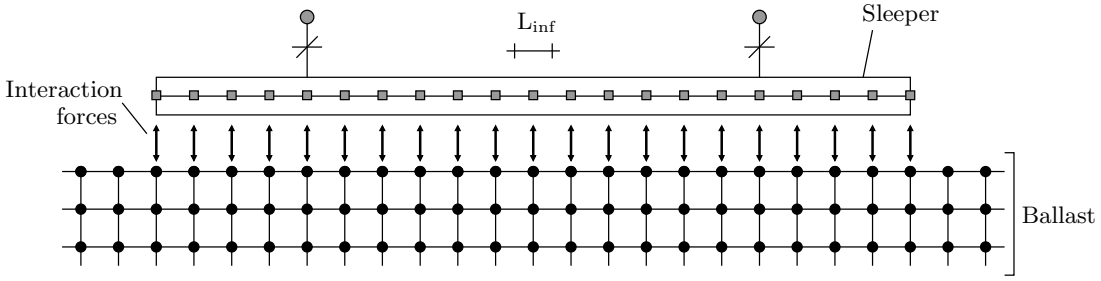

Figure 6.5: Sleeper-ballast interaction viewed in longitudinal direction of the sleeper

In vertical direction, the normal pressure between the sleepers and the ballast is assumed to be proportional to the difference in vertical displacement of the sleeper's bases and the ballast surface, following thus the penalty formulation for solving contact problems (Bhatti, 2006). The contact force is therefore determined by $K_{\mathrm{c}}\, d$, where K_{c} is a contact parameter, also referred to as a penalty parameter, and d is the aforementioned difference in vertical displacements, referred to in contact theory as the inter-penetration (Sneddon, 1965). On the other hand, the vertical friction between the sleepers lateral faces and the confining ballast was here assumed to be of the viscous type, being given by $C_{\mathrm{c}}\, \dot{d}$, where C_{c} is a friction parameter and $\dot{d}$ the relative velocity between the surfaces.

Given the above mentioned, the vertical interaction force between two superposed nodes, one belonging to the railtrack system and the other to the ballast/soil system, identified respectively by r.i and s.i, is determined (at each time step) with:

$$F_{\mathrm{a}.i} = \begin{cases} -k_{\mathrm{c}.i}\ (u_{\mathrm{t}.i} - u_{\mathrm{s}.i} + h_i) - c_{\mathrm{c}.i}\ (v_{\mathrm{t}.i} - v_{\mathrm{s}.i})\ , \text{ if } u_{\mathrm{t}.i} - u_{\mathrm{s}.i} + h_i < 0 \\ \\ -c_{\mathrm{c}.i}\ (v_{\mathrm{t}.i} - v_{\mathrm{s}.i})\ , \text{ if } u_{\mathrm{t}.i} - u_{\mathrm{s}.i} + h_i \geq 0 \end{cases} \tag{6.11}$$

where $F_{\mathrm{a}.i}$ is the vertical interaction force between nodes t.i and s.i, $k_{\mathrm{c}.i}$ and $c_{\mathrm{c}.i}$ the corresponding contact and friction parameters, respectively, $u_{\mathrm{t}.i}$ and $u_{\mathrm{s}.i}$ the corresponding vertical displacements, $v_{\mathrm{t}.i}$ and $v_{\mathrm{s}.i}$ the corresponding vertical velocities and h_i an eventual gap existing between these two nodes (for example, representing voids under the sleepers). Figure 6.6 represents the adopted axis system for the definition of the nodal displacements and the vertical gap.

Since the sleepers are modelled with beam elements, the width of the sleepers is not represented in the corresponding finite element mesh. Figure 6.7 shows a transverse view

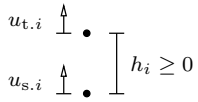

Figure 6.6: Axis system for vertical contact

of the sleeper-ballast interaction, where B is the width of the sleeper. As can be seen, in this example, for each sleeper's node ($t.i$) there are three nodes belonging to the ballast mesh located under the corresponding sleeper's width (nodes $s.i_1$ to $s.i_3$). In this regard, it is assumed that the sleepers have infinite stiffness in their transverse direction (direction of the width) and therefore it is possible to define interaction forces between node $t.i$ and each one of the underlying nodes ($s.i_1$ to $s.i_3$), as depicted in Figure 6.7.

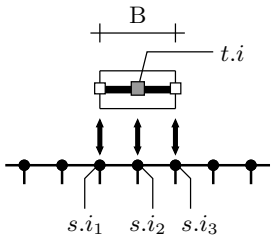

Figure 6.7: Sleeper-ballast interaction viewed in transverse direction of the sleeper

The value of the contact parameter (K_c) should be determined by testing. Here, in the absence of experimental results relative to this sleepers-ballast contact, it was assumed that the vertical inter-penetration between contacting sleepers and ballast during train loadings is in the order of 0.01 mm. This value is two orders of magnitude lower than the corresponding total displacements, assuring a very limited influence of the sleepers-ballast inter-penetration in the calculated total displacements. Considering a sleeper's width of 0.25 m and typical train loads, the resulting value assumed for K_c was 6.25 GN/m^2.

The value assumed for the friction parameter (C_c) is in accordance with the equivalent friction damping value defined and justified in Section 4.3.4, for the one-dimensional model. The resulting value for C_c was 2.5 kNs/m^2.

The transposition of these global contact and friction parameters (K_c and C_c) to their node-to-node equivalents ($k_{c.i}$ and $c_{c.i}$) is made with:

$$k_{c.i} = \frac{K_c \, L_{inf}}{n} \ , \quad c_{c.i} = \frac{C_c \, L_{inf}}{n} \tag{6.12}$$

where L_{inf} is the length of influence of the node i in longitudinal direction of the sleeper, as represented in Figure 6.5, and n is the number of nodes belonging to the corresponding ballast mesh along the sleeper's width (in the case of the example shown in Figure 6.7,

n=3).

6.2.4 Boundary conditions

Boundary conditions are necessary whenever the size of the finite element model is not big enough to contain the complete displacement field generated by the considered loading during the time period of the analysis. In case of analyses concerning train passages, the duration of the load is in the order of several seconds and the generated waves will propagate at speeds of several hundreds of meters per second. Therefore, inevitably the waves will reach the boundaries of the model, which will have usually less than 20-50 m in the vertical and transverse direction. Without absorbing boundaries, the impinging waves would be continuously reflected and kept inside the discretized domain, which would be an extraneous effect to the real physical event under study.

A number of methods have been employed to create absorbing boundaries. In order of increasing accuracy, these include local transmitting boundaries (Lysmer and Kuhlemeyer, 1969), the infinite element method (Bettess, 1980) and the boundary element method (Banerjee and Butterfield, 1981). The boundary element method, being the most exact approach, allows for boundaries very close to the loaded region (the track) (Galvín et al., 2010). However, with the boundary element method the sparsity nature of the finite element structure is destroyed, which in case of unavoidable large 3-D models may be very (calculation) time consuming.

In Pegasus, the adopted approach is the use of local transmitting boundaries, consisting of visco-elastic dampers (dashpots) and (eventually) springs placed at the nodes of the boundaries (Lysmer and Kuhlemeyer, 1969; Hall, 2003). Furthermore, when the stiff bedrock is deep under the railway level, it is possible to replace the deeper soil layer by a visco-elastic Winkler foundation. This procedure reduces the size of the finite element model and the calculation time. Figure 6.8 shows the referred method schematically, where the fourth layer of soil is replaced by a net of springs and dashpots at the bottom of the third layer.

This approach does not ensure a total energy absorption: the dashpots are tuned for a given wave velocity and for waves travelling in perpendicular direction with respect to the boundary surface of the model, only. It is thus important to build sufficiently large finite element models, where the local transmitting boundaries will be located sufficiently away from the loaded region.

Moreover, the replacement of a deeper layer of soil by a net of springs assumes a simplification: the horizontal strains inside the removed layer of soil and caused by the dynamic

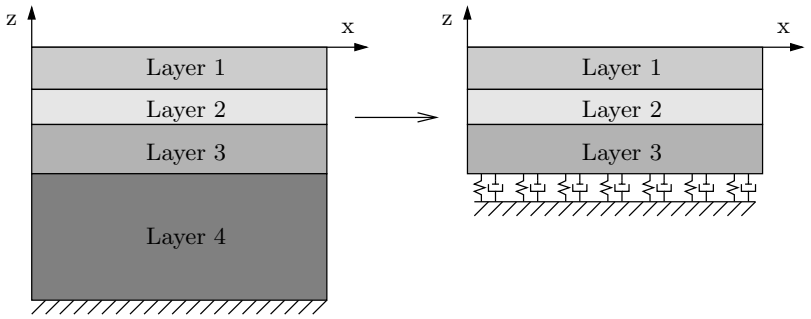

Figure 6.8: Replacing bottom layer with spring-damper system. 2D view

loading are negligible. Such simplification is only acceptable if the removed layer is deep under the loaded region. In this sense, for a given soil profile, it is necessary to perform preliminary verification studies before assuming the replacement of the deeper layer of soil by a net of springs and dampers.

The damping constants of the local absorbing dashpots, represented in Figure 6.9, are determined based on the wave velocities of the traversed media, according to (Lysmer and Kuhlemeyer, 1969):

$$\begin{aligned} c_{\mathrm{rd.p}} &= \rho\, v_{\mathrm{p}}\, A \\ c_{\mathrm{rd.s}} &= \rho\, v_{\mathrm{s}}\, A \end{aligned} \tag{6.13}$$

where $c_{\mathrm{rd.p}}$ and $c_{\mathrm{rd.s}}$ are the damping constants for the longitudinal and the transverse directions, respectively, ρ is the mass density, v_{p} and v_{s} are the velocities of the primary and secondary body waves of the traversed media and A is the area of influence of the node in the finite element mesh.

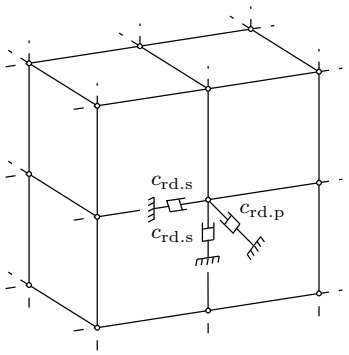

Figure 6.9: Transmitting boundaries with dashpots

The elastic constant of the springs replacing a deeper layer of soil are determined with:

$$k_p = \frac{M\,A}{H}$$
$$k_s = \frac{G\,A}{H} \tag{6.14}$$

where k_p and k_s are the elastic constants of the vertical and horizontal springs, respectively, M is the oedometer modulus of the removed layer, G is the corresponding shear modulus, A is the area of influence of the node in the finite element mesh and H is the height of the removed layer.

The consideration of springs at the nodes of the lateral boundaries of the model is also possible with Pegasus. The same Eq. (6.14) is used for the determination of the corresponding elastic parameters, although in this case the height (H) corresponds to an horizontal dimension, and it is not physically well defined.

6.2.5 Initial state

As performed with the one-dimensional model presented in Chapter 4, the initial state of the structural systems must be determined prior to the passage of the train's loads. This initial state designates the geometric configuration corresponding to the equilibrium of the two structural systems with the track/ballast/soil own weight, and considering the level of the track. This calculation step is necessary due to the non-linearities of the model (sleepers-ballast contact and the existence of elements with non-linear constitutive law) and to the fact that the dynamic stresses at the surface of the model are not negligible relative to the static component.

The weight of the constituting parts of the railtrack system and of the ballast/soil system can be derived from the corresponding mass matrices. As the crib and shoulder ballast (the ballast laterally surrounding the sleepers) is not explicitly included in the ballast/soil system, the corresponding weight must be applied as an external pressure at the ballast surface level (p_{bal} in Figure 6.10).

The initial horizontal stresses inside the ballast/soil system are in principle unknown. They mostly depend upon the materials, the geological history, the geometry of the system and the depth. In Pegasus, the initial horizontal stresses are estimated applying an external horizontal pressure at the lateral boundaries of the model, as represented in Figure 6.10.

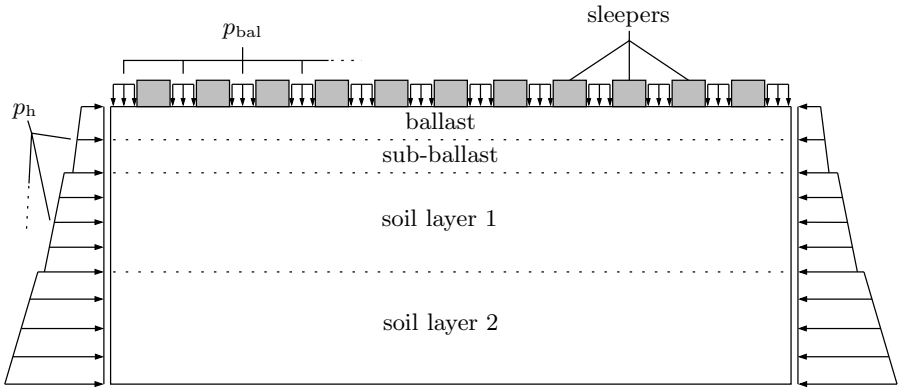

Figure 6.10: External weight applied in Pegasus. 2D view in longitudinal direction of the track

The value of the horizontal pressure is determined according to (Verruijt, 2006):

$$p_h = K_0 \gamma z \tag{6.15}$$

where K_0 is the coefficient of lateral earth pressure, γ is the volumetric weight of the material and z is the depth. The coefficient of lateral earth pressure was determined by:

$$K_0 = \frac{\nu}{1-\nu}, \tag{6.16}$$

derived assuming the Hooke's Law and that there can be no lateral deformations at the lateral boundaries of the models (Verruijt, 2006).

The calculation steps in Pegasus are organized in Figure 6.11. It can be seen that the initial state of the structural systems is attained in two steps: first the stress distribution due to ballast & soil weight is determined, after which the railtrack system and weight is introduced. The railtrack system can be positioned with a given prescribed level, by adjusting the vertical distance between the sleepers-ballast interacting nodes. This vertical distance is represented by h_i in Eq. (6.11). The algorithm is essentially the same used in the one-dimensional model, presented in Chapter 4.

6.3 Verification of results

The studies presented in this Section have a twofold purpose: (i) to verify the numerical results with an available analytical solution, valid for the three-dimensional case and (ii) to verify the necessary size of the finite elements to attain a good representation of the dynamic response. The description of the models used for these purposes is limited to the essential.

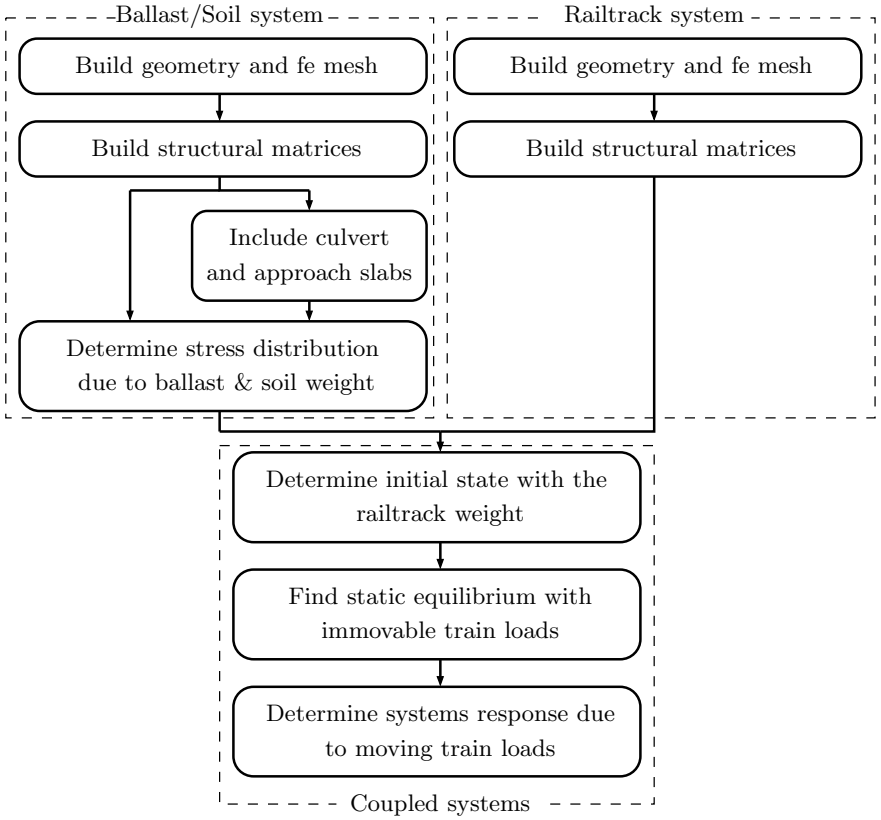

Figure 6.11: Calculation steps in Pegasus

A good representation of the dynamic motion is obtained with a minimum of ten (low-order) elements per wavelength (Kuhlemeyer and Lysmer, 1973; Wood, 2004). The maximum size of the finite elements is therefore given by $\ell_{\max} = \lambda/10$, where λ is the wavelength. The wavelength relates to the waves velocities and to the corresponding frequencies, according to $\lambda = v/f$. The maximum size of the finite elements is thus found with the minimum wave velocity of the materials (the shear wave velocity) and the maximum frequency of interest. The maximum frequency of interest depends on the phenomenon/loading to be described.

Table 6.1 lists the assumed maximum frequencies of interest, and the corresponding maximum element sizes for each of the materials/layers found at the culvert site and described in Chapter 2 (see Table 4.1). The assumed maximum frequencies of interest vary with the corresponding depth, in the sense that at the surface the frequencies may be relatively high, specially in case of hanging sleepers, whereas the deeper layers will perceive the passage of the bogie only, or even of the train as a unique load. It can be seen that the size of the finite elements shall not exceed 0.30 m at the ballast level and 0.50 m away from the loaded region.

Layer	v_s [m/s]	f [Hz]	ℓ_{max} [m]
Ballast	186	50	0.37
Sub-ballast	152	50	0.30
Sand emb.	140	15	0.93
Peat 1	50	10	0.50
Sand int.	150	10	1.50
Peat 2	80	10	0.80
Sand pleist.	180	10	1.80

Table 6.1: Maximum size of finite elements

The size of the finite elements also depends on geometrical and mesh constraints, e.g. dictated by the sleepers width and the sleepers spacing. Accordingly, Figure 6.12 represents three possible finite element meshes in a longitudinal view with respect to the track direction (x dir.). The fixed width of the sleepers is 0.25 m and the sleeper's spacing is 0.6 m. Basically, mesh 1 has two finite elements per sleeper in x direction, mesh 2 has four and mesh 3 has six. These three possibilities will be evaluated.

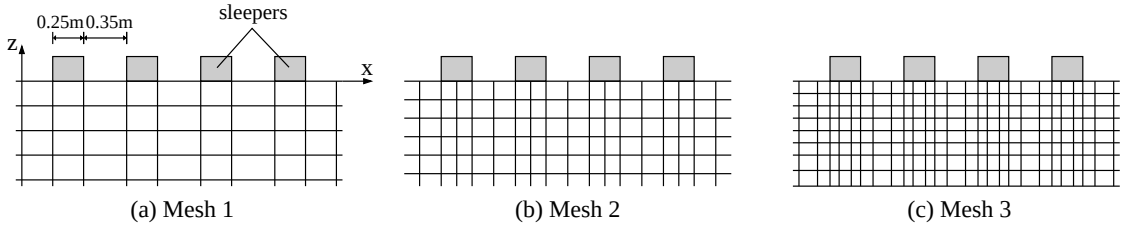

Figure 6.12: Finite element meshes 1, 2 and 3 in longitudinal view

Figure 6.13 shows the time history of stresses calculated with models having each of the meshes represented in Figure 6.12. The load corresponds to the passage of two axles of a bogie. The soil response is linear (elastic). The Figure compares these numerical results, represented with coloured lines, with the equivalent analytical solution due to Boussinesq, represented with thin black lines.* It can be seen that the numerical results follow with close agreement the analytical solution due to Boussinesq. Looking at the vertical stresses, it can also be seen that the two finner meshes are closer to the analytical solution, with negligible differences between the two.

The verification made above with the Boussinesq solution has shown that mesh 2 gives an adequate discretization of the ballast and sub-ballast layers in case of linear-elastic static calculations. Yet, it is important to verify if this is still valid for the case of non-linear

* Boussinesq obtained the static solution for the stresses and strains in a homogeneous isotropic linear elastic half space, loaded by a vertical point force at the surface. The stress field solution in cylindrical coordinates may be found in (Timoshenko and Goodier, 1970). The stress field resultant from pressure loads exerted by the sleepers was estimated using the principle of superposition.

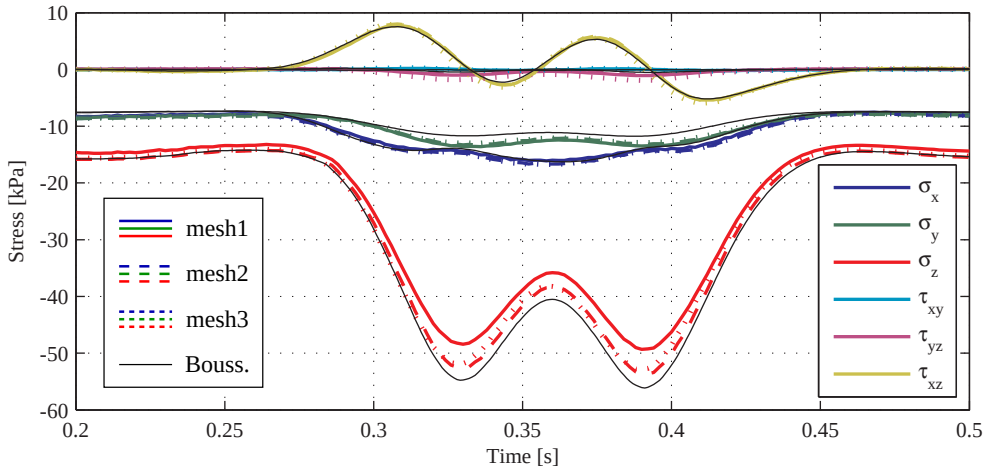

Figure 6.13: Stress history due to two axles passage at 40 m/s. Coloured lines are numerical results and black lines are analytical results (Boussinesq solution)

response. For this, two new identical non-linear models were created, one with a mesh-type 2 and the other with a mesh-type 3. The loading now consists of the self-weight of the track, ballast and soil, and of two vertical forces applied in each rail, linearly increasing from zero to 87 kN in 1 second, standing above the central sleeper of the model. The models comprise a ballast and a sub-ballast layer, having non-linear constitutive behaviour, and a sand layer having linear-elastic response. The corresponding adopted material properties are listed in Table 6.2.

Layer	H[m]	E [MPa]	ν	K_1 [MPa]	K_2
Ballast	0.4	-	0.2	110	0.6
Sub-ballast	0.4	-	0.2	110	0.6
Sand emb.	2.2	87	0.3	-	-

H - height of the layer
K_1, K_2 - parameters of the $K-\theta$ model

Table 6.2: Material properties of models with mesh-type 2 and 3

Figure 6.14 shows the finite element discretization adopted in the two models in a longitudinal view, giving also a qualitative representation of the corresponding final displacement fields. Figure 6.15 shows the displacement history of a node located at the surface of the ballast, under the loaded rail, determined with each of the models. As can be seen, the displacements obtained with the two models are approximately coincident, showing that mesh-type 2 and mesh-type 3 are equivalent for the calculation of the displacement field.

Figure 6.16 now shows the results obtained with the two models in terms of calculated

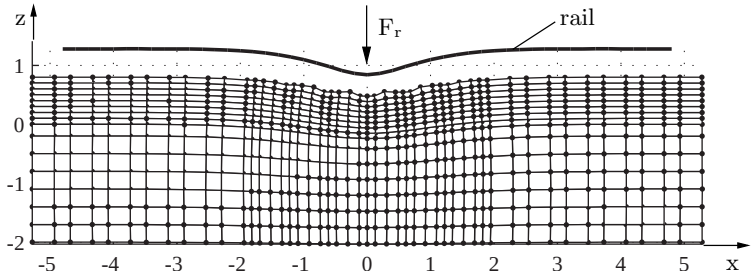

(a) Mesh 2

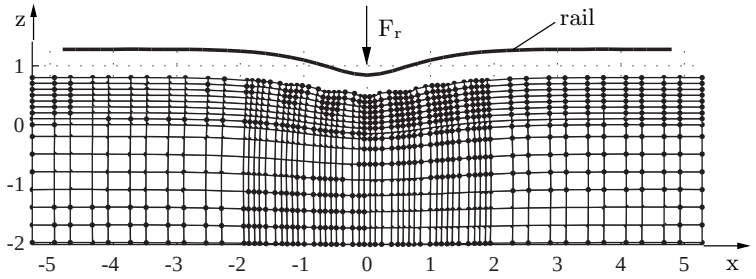

(b) Mesh 3

Figure 6.14: Qualitative representation of the displacement field in a longitudinal view

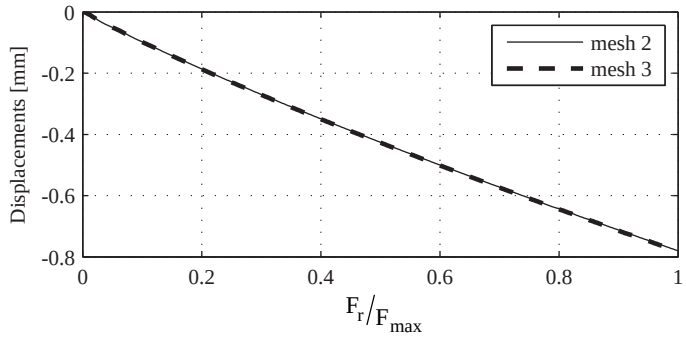

Figure 6.15: Displacements at surface of ballast under the rail

resilient modulus (E_r) in the ballast and the sub-ballast layers, for the same linearly increasing load. The resilient modulus was determined at points below the loaded sleeper. The solid lines are results from the mesh 2 model and the dashed lines from the mesh 3 model. Figure 6.17 depicts the locations of the three uppermost points: P1, P2, P3.

Figure 6.16 shows that the differences between the responses from the two models are only visible at the upper elements of ballast, specially at the two upper level of elements (z = 0.75 m and z = 0.65 m). These differences are already very small at a depth of 0.25 m, being negligible in the sub-ballast layer. It can also be seen that the response given by mesh 2 model at point P1 is in fact approximately an average value of the responses given by mesh 3 model at points P2 and P3.

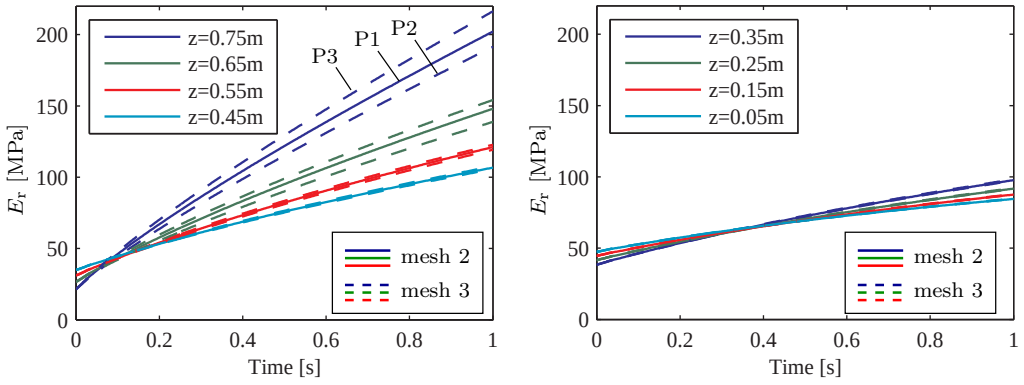

(a) Ballast layer (b) Sub-ballast layer

Figure 6.16: Time history of resilient modulus at the ballast and sub-ballast layers. Results obtained with mesh type 2 and mesh type 3

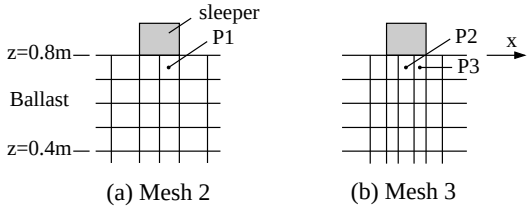

(a) Mesh 2 (b) Mesh 3

Figure 6.17: Location of points P1, P2 and P3 (longitudinal view)

From the results shown in this Section, it can be concluded that for static analyses (also) focused on the stress-strain response of the ballast and sub-ballast layers, a mesh with two elements under each sleeper in the longitudinal direction of the track (mesh type 2) corresponds to an adequate discretization, even considering their non-linear stress-strain relationship with the $K-\theta$ model. Other (not presented) results, have shown that the displacement field determined with a mesh type 1 is very close to the displacement field determined with a mesh type 2 or 3. Therefore, the following models will consider a mesh type 2 in the central region of study (for stress-strain observations) and a mesh type 1 for the non-central region, where the steady-state displacement field is expected to develop.

6.4 Linear vs. Non-linear analyses

The implications of considering the non-linear constitutive behaviour of the ballast and sub-ballast on the obtained dynamic response for moving loads is investigated next. For this, numerical results obtained with a model having non-linear elements and with a model having equivalent linear elements (and equal loading) will be compared. For the sake of simplicity, these models will hereafter be called non-linear and linear model, despite the

fact that the non-linear contact between the sleeper and the ballast is present in both models.

The model built for this analysis comprises 59 sleepers spaced 0.6 m. The model has a width of 14.5 m and a total depth of 4.3 m. Figure 6.18 shows a transverse view of the model and Figure 6.19 shows a longitudinal view of the model. The geometry adopted for the ballast embankment is originally based on the field tests, assuming that the railway track comprises several parallel tracks and that the track under study is the outer track, the closest to the slope of the embankment.

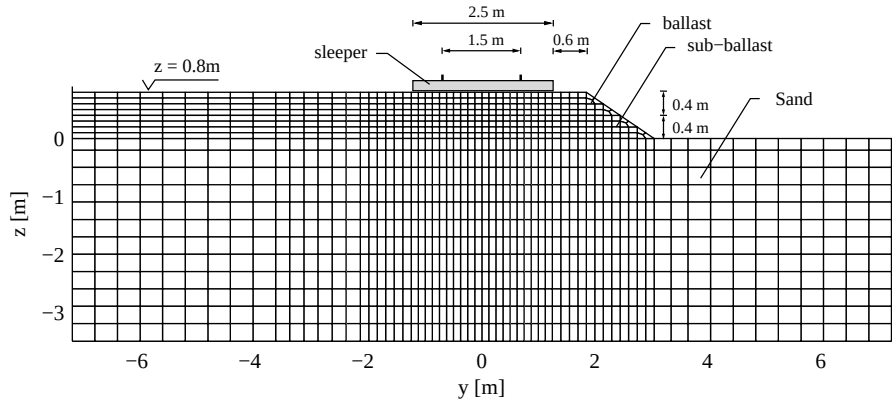

Figure 6.18: Transverse view of model with 59 sleepers

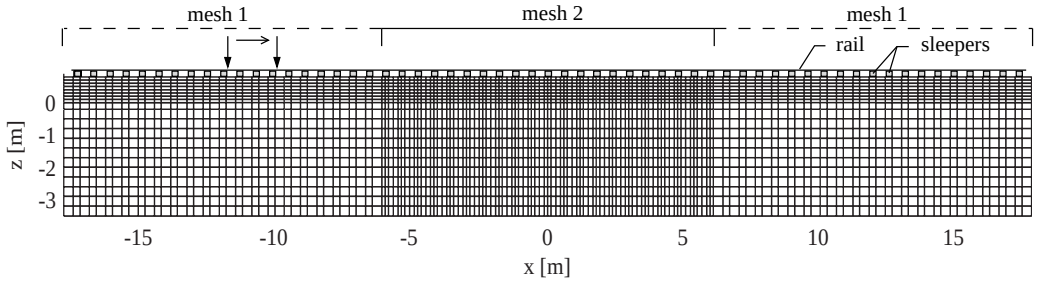

Figure 6.19: Longitudinal view of model with 59 sleepers

The adopted spatial reference system is the Cartesian coordinate system, based on Euclidean geometry. Figures 6.18 and 6.19 shows the coordinate system, and its origin. Hereafter, this coordinate system will be used to locate nodes and points. The top surface of the ballast, at the same level of the sleepers, is at $z = 0.8$ m. The origin of the longitudinal axis (x) is located at the center of the model. The origin of the transverse axis (y) is also located at the center of the model. The rails are spaced 1.5 m and therefore the rails have y coordinates -0.75 m and +0.75 m, each. The train moves from left to right in Figure 6.19, thus in positive x-direction.

The assumed soil profile has a ballast and a sub-ballast layer with 0.4 m height each, and one homogeneous sand layer with 5.5 m depth, on top of the rigid bedrock. The bottom 2 m of the sand layer were replaced in the model by a Winkler foundation, as described in Section 6.2.4. Absorbing dashpots were placed at the lateral boundaries to avoid reflections of impinging waves.

It was assumed that the sand layer has a linear-elastic behaviour. The adopted Young's modulus was 143 MPa, the Poisson's ratio was 0.3 and the mass density was 1.7 t/m^3. This sand layer may represent the Pleistocene sand layer found at the culvert site with a shear wave velocity of 180 m/s (see Table 4.1).

In the non-linear model, the parameters of the $K-\theta$ model defining the ballast and sub-ballast behaviour were derived from large-scale triaxial tests performed by Aursudkij et al. (2009). Accordingly, the values $K_1 = 110$ MPa and $K_2 = 0.6$ were adopted. The correspondent $E_\mathrm{r}-\theta$ curve is drawn in Figure 6.20. The minimum resilient modulus (E_min)

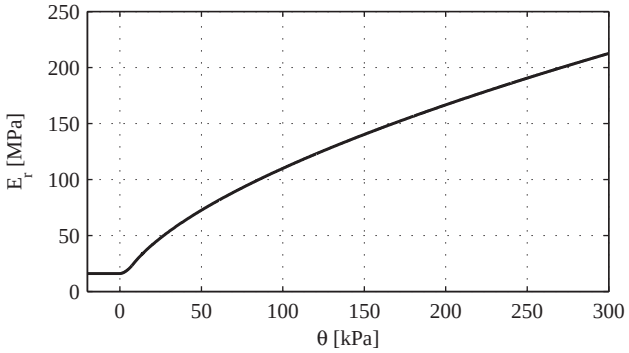

Figure 6.20: The $E_\mathrm{r}-\theta$ curve adopted for the ballast and sub-ballast layers

was assumed to be 16 MPa (Indraratna and Salim, 2005). The value of θ_t, figuring in Equation (6.10), was assumed to be 8 kPa. For the sub-ballast layer, the same $E_\mathrm{r}-\theta$ curve was adopted. The Poisson's ratio was assumed to be 0.2 and the mass density 1.8 t/m^3. In the equivalent linear model, the Young's modulus of the ballast and sub-ballast layers were assumed to be 150 MPa and 100 MPa, respectively. Table 6.3 summarizes these data.

			Linear model		Non-linear model			
Layer	H [m]	ρ [t/m^3]	E [MPa]	ν	K_1 [MPa]	K_2	E_min [MPa]	ν
Ballast	0.4	1.8	150	0.2	110	0.6	16	0.2
Sub-ballast	0.4	1.8	100	0.2	110	0.6	16	0.2
Sand	5.5	1.7	143	0.3	-	-	-	-

Table 6.3: Material properties of ballast, sub-ballast, and sand layers

The material damping was considered by means of the Rayleigh damping method. It was assumed a damping ratio of 2% at the frequency of 1 Hz and of 1.5% at the frequency of 30 Hz. The justification for the choice of these values will be given in the next Section.

The rails were assumed to have an UIC54 profile (vertical bending stiffness = 4910 kNm^2, transverse bending stiffness = 880 kNm^2 and mass = 54.77 kg/m). The sleeper were assumed to be made of wood (E = 10 GPa and ρ = 0.7 t/m^3), with 2.5 m length, 0.25 m width and 0.20 m height. The railpads were assumed to have a high stiffness value of 500 kN/mm (Teixeira, 2003), a damping constant of 15 kNs/m (Nielsen and Oscarsson, 2004) and a mass of 15 kg each.

The loading consists of two axle loads of 144 kN each, spaced 2.5 m, representing two axles of an ICM (motorcar) bogie, as defined in Table 4.4.

The model has around 600.000 dof and 186.000 solid elements. The required time step was 1.25×10^{-5} s. In the non-linear model, 34.000 elements present non-linear behaviour and the stiffness matrix was updated every 2.50×10^{-5} s (each two time steps). The corresponding calculation time on a i7 intel processor was 6 h per second of analysis with the linear model and 56 h per second of analysis with the non-linear model.

6.4.1 Slow moving loads

When the train loads are moving with a speed significantly smaller than the critical speed of the track, the participation of inertial forces in the dynamic equilibrium is limited and the displacement field is quasi-static. This condition is here analyzed considering loads moving with 130 km/h. Given the material properties of the homogeneous sand layer (E = 143 MPa, ν = 0.2 and ρ = 1.7 t/m^3), the Rayleigh wave velocity of an equivalent homogeneous half-space is around 600 km/h, which is approximately the value of the critical speed of this track model (Sheng et al., 1999). Therefore, the loads travel here with a speed only around 22% of the critical speed.

In the non-linear model, the resilient modulus of each finite element representing the ballast and the sub-ballast depends on the corresponding stress level, according to the $E_\mathrm{r} - \theta$ relationship shown in Figure 6.4. Figure 6.21 shows the distribution of the resilient modulus per (non-linear) element in the ballast and sub-ballast layers, in a transverse view, when the load is passing over the corresponding sleeper. It can be seen that the stiffness is higher at the higher level of the ballast, where the vertical stress will be also higher, and that it rapidly lowers in depth. The Figure also shows that the distribution of stiffness under the sleeper, along its length, is highly inhomogeneous, presenting a maximum (around 165 MPa) under the rails, and a minimum (around 92 MPa) at the

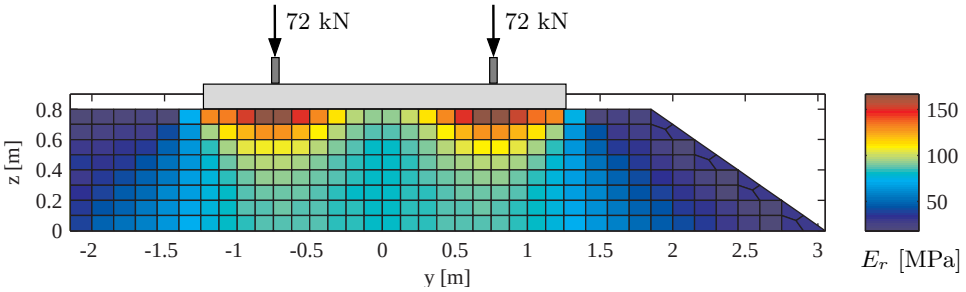

Figure 6.21: Distribution of the resilient modulus (E_r) in a transverse view, when the wheel loads are passing over the sleeper

center of the sleeper.

Figure 6.22 shows the distribution of E_r per element in a longitudinal view with respect to the track direction, when the first axle is passing over the central sleeper of the model. The longitudinal non-uniform distribution of stiffness is clear, with maximum values under the position of the train's axles.

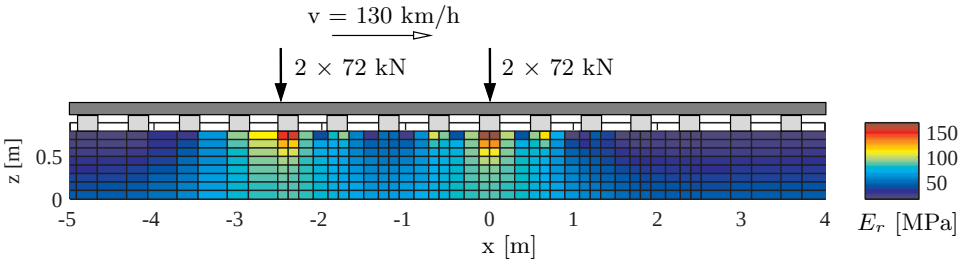

Figure 6.22: Distribution of the resilient modulus (E_r) in a longitudinal view, aligned with the rail ($y = -0.75$ m), when the first axle is passing over the central sleeper of the model ($t = 0.2$ s)

The dynamic vertical displacements calculated in the ballast layer are presented in Figure 6.23. The upper Figures 6.23(a) and 6.23(b) present the displacements calculated at the ballast surface ($z = 0.8$ m), under the inner and outer rails, respectively. The bottom Figures 6.23(c) and 6.23(d) present the displacements calculated inside the ballast layer ($z = 0.60$ m), at $y = -1.85$ m and $y = +1.85$ m, respectively. The point at $y = +1.85$ m is very close to the ballast embankment slope (see Figure 6.18). From the Figures, it is clear that the displacements response of both models are almost coincident, with a 3% difference in terms of maximum value. In fact, the Young's modulus of the ballast and sub-ballast layers of the linear model (150 MPa and 100 MPa, respectively) was tuned to give approximatelly the same displacement response as the non-linear model. The Figures also show that there are no significant differences between the inner and outer responses, both for linear and non-linear results.

A convenient way to represent results in terms of stresses is to use a *stress path* (Verruijt,

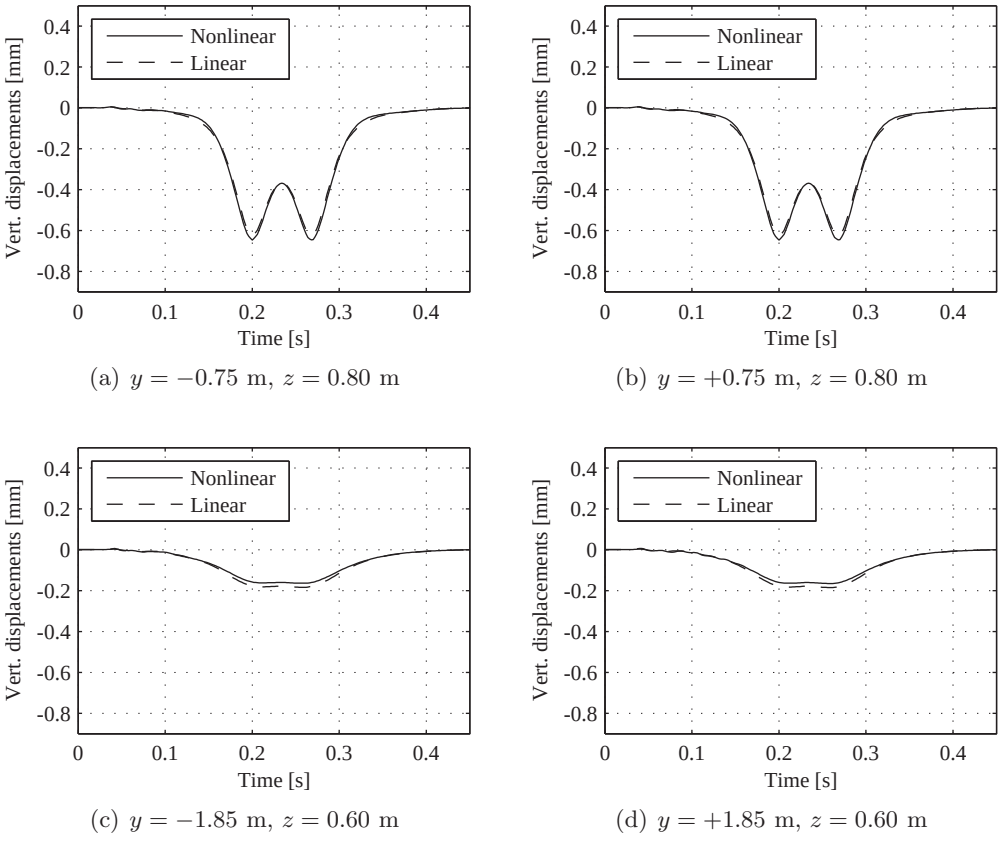

(a) $y = -0.75$ m, $z = 0.80$ m

(b) $y = +0.75$ m, $z = 0.80$ m

(c) $y = -1.85$ m, $z = 0.60$ m

(d) $y = +1.85$ m, $z = 0.60$ m

Figure 6.23: Vertical dynamic displacements obtained in the ballast for the slow moving load case. Comparison between linear and non-linear results

2006). In this representation, it is assumed that the state of stress in a point is characterized by two parameters: the mean normal stress (p) and the deviatoric stress (q). These parameters are represented in a diagram, called a *stress path*. The parameters p and q are determined with:

$$\begin{aligned} p &= \frac{\sigma_x + \sigma_y + \sigma_z}{3} \\ q &= \sqrt{\tfrac{1}{2}\left((\sigma_x - \sigma_y)^2 + (\sigma_y - \sigma_z)^2 + (\sigma_z - \sigma_x)^2\right) + 3(\tau_{xy}^2 + \tau_{yz}^2 + \tau_{zx}^2)}. \end{aligned} \tag{6.17}$$

with the mean normal stress defined positive in case of compression, following classical convention of soil mechanics.

Following Mohr-Coulomb failure criteria, the failure line in compression in the $p-q$ diagram is defined by an inclination angle (M_f), determined with (Atkinson, 2007):

$$M_f = \frac{6sin(\phi'_c)}{3 - sin(\phi'_c)} \tag{6.18}$$

where ϕ'_c is the critical state friction angle. According to Indraratna et al. (2006), it was here assumed that the friction angle of ballast (and sub-ballast) is 54 °.

Figure 6.24 shows the *stress paths* determined in the ballast and sub-ballast layers, at points located under the rail and under the loaded sleeper ($x = 0$ m, $y = 0.75$ m). The

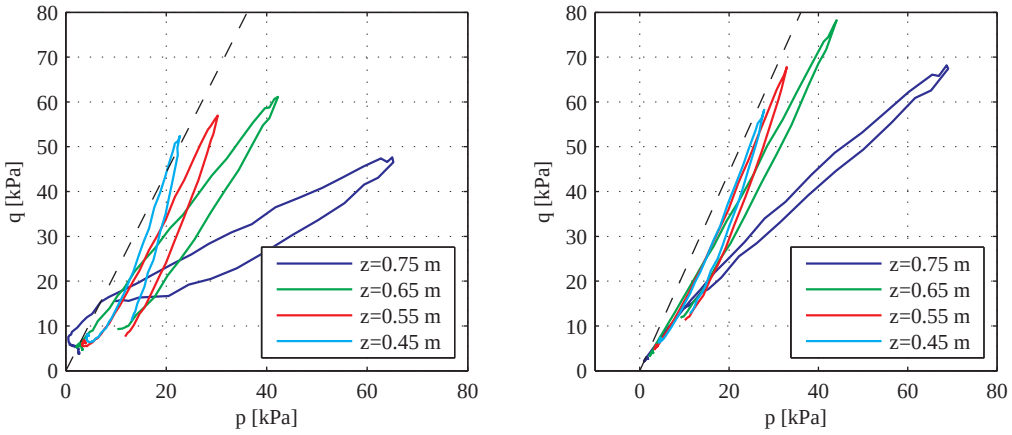

(a) **Linear elements** - Ballast (b) **Non-linear elements** - Ballast

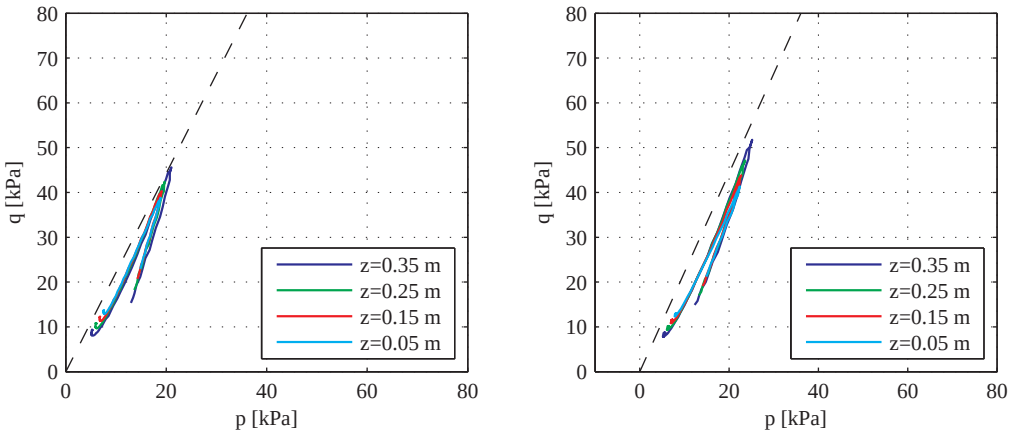

(c) **Linear elements** - Sub-ballast (d) **Non-linear elements** - Sub-ballast

Figure 6.24: Effect of the constitutive model on the *stress paths* at the ballast and sub-ballast layers. Results determined at points located under the rail and under the loaded sleeper ($x = 0$ m, $y = 0.75$ m), for the slow moving load case. The black dashed line is the failure line

stress paths are only shown for the first axle passage ($0 \leq t \leq 0.23$ s - see Figure 6.23). This facilitates the reading of the *stress paths* and eases the comparison between linear and non-linear results. The initial stresses due to ballast/railtrack weight are included in the *stress paths*.

By comparing results shown in Figures 6.24(a) and 6.24(b), it can be seen that the *stress paths* in the ballast layer (under the loaded sleeper) obtained considering linear behaviour

are significantly underestimated compared to the non-linear results. In terms of normal mean stress (p), the maximum value obtained with the non-linear elements exceeds by 8% the maximum value obtained with the linear elements, and in terms of deviatoric stress (q), this difference increases to 28%. In terms of *stress paths* calculated in the sub-ballast layer, shown in Figures 6.24(c) and 6.24(d), it can be seen that again the stresses determined with the non-linear elements are higher, but the differences are lower than those found at the ballast layer.

The *stress paths* at points located in the ballast, under the rail ($y = 0.75$ m), and between the loaded sleepers ($x = 0.212$ m), are shown in Figure 6.25. This Figure shows that during the passage of axle loads the stresses in the ballast layer and between the sleepers determined with the linear model are generally higher than those determined with the non-linear model. This is thus an opposite effect compared to what was found for the ballast response under the loaded sleeper.

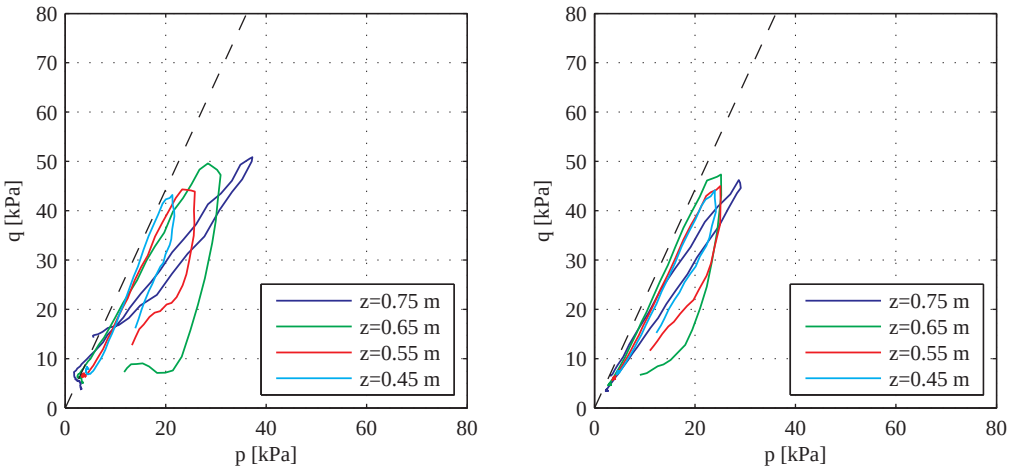

(a) **Linear elements** - Ballast (b) **Non-linear elements** - Ballast

Figure 6.25: Effect of the constitutive model on the *stress paths* at the ballast. Results determined at points located under the rail and between the sleepers ($x = 0.212$ m, $y = 0.75$ m), for the slow moving load case. The black dashed line is the failure line

Despite the differences between linear and non-linear results in terms of stresses, evidenced above, it was found that the contact stress between the sleeper and the ballast is here much less influenced by the adopted constitutive model. This can be seen in Figure 6.26, showing the contact stress distribution when the axle is passing over the corresponding sleeper. The contact stress is maximum under the rails, as expected, and the results obtained with the linear and non-linear elements are very close (4% difference in terms of maximum value).

The behaviour of soils during cyclic loading is highly influenced by the maximum induced shear strains. For very small strains (typically under 10^{-5} for sand) the shear modulus

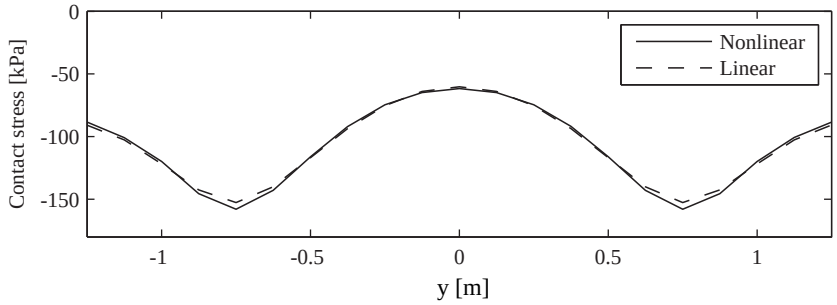

Figure 6.26: Maximum contact stress between the sleeper and the ballast

G has its maximum value and the behaviour can be approximately represented by a linear-elastic model. In the small strains regime (typically between 10^{-5} and 10^{-4} for sands) the shear modulus can be reduced by a factor 2, the soil exhibits a clear non-linear behaviour, but its properties remain unchanged with increasing number of load cycles. In the large strains regime, the shear modulus G can be reduced by a factor 100 from its initial maximum value and the soil presents non-linear and non-elastic behaviour.

In dynamic analyses considering the soil behaviour, it is thus important to look at the induced strain level. In three-dimensional problems, the octahedral shear strain gives a compact measure of the strain level in the soil. The octahedral shear strain is determined with:

$$\gamma_{\text{oct}}(t) = \frac{1}{3}\sqrt{(\epsilon_x - \epsilon_y)^2 + (\epsilon_y - \epsilon_z)^2 + (\epsilon_z - \epsilon_x)^2 + 6(\gamma_{xy}^2 + \gamma_{yz}^2 + \gamma_{zx}^2)} \tag{6.19}$$

Figure 6.27 shows the distribution of the octahedral shear strain on a longitudinal view, aligned with the rail ($y = -0.75$ m), when the front axle is passing over the central sleeper of the model ($t = 0.2$ s). According to these results, it is clear that the shear strains are higher on the elements located between the sleepers, rather than under the sleepers. The figure also shows that the shear strains obtained with the equivalent linear model are considerably underestimated, compared to the non-linear results.

Figure 6.28 shows the distribution of the octahedral shear strain on a transverse view at $x = 0.2125$ m, again when the front axle is passing over the central sleeper of the model ($t = 0.2$ s). This x location corresponds to the position of the centroids of the elements having maximum shear strains in Figure 6.27. Figure 6.28 shows again that the octahedral shear strains in the ballast and sub-ballast layers are significantly higher in the non-linear model, compared to the linear results. It can also be seen that the octahedral shear strains in the soil (under $z = 0.0$ m) can be as high as 1×10^{-4}, corresponding to the small strains regime limit for sands.

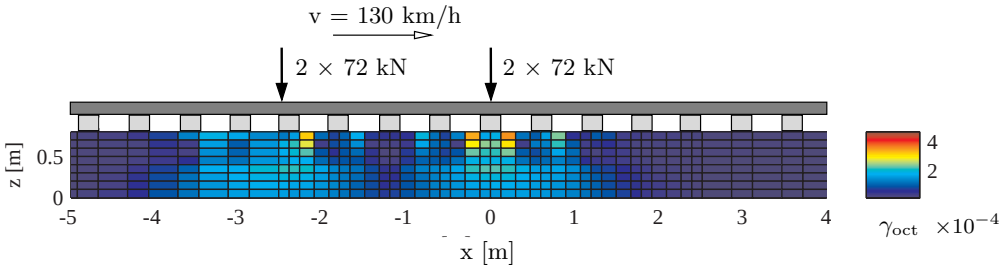

(a) Linear elements

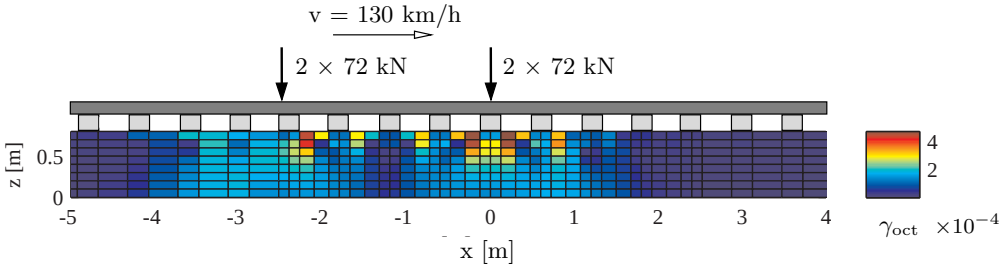

(b) Non-linear elements

Figure 6.27: Octahedral shear strain distribution in a longitudinal view, aligned with the rail, when the front axle is passing over the central sleeper of the model ($t = 0.2$ s)

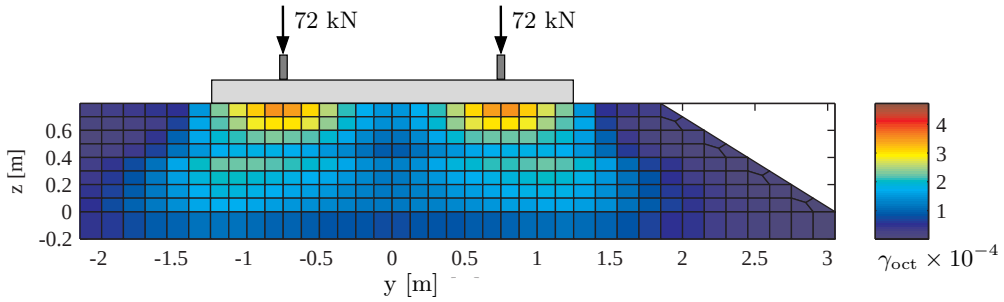

(a) Linear elements

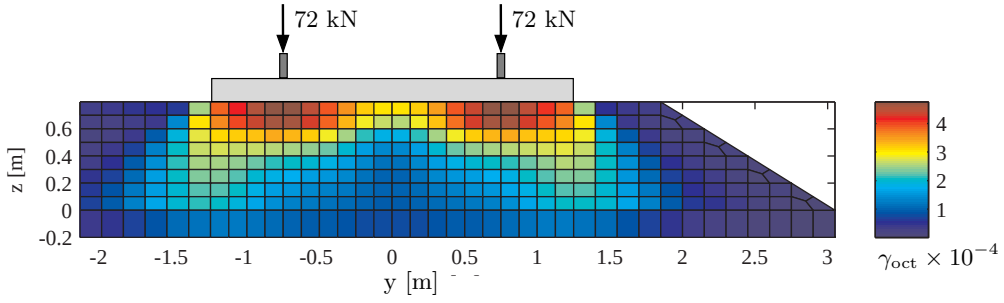

(b) Non-linear elements

Figure 6.28: Octahedral shear strain distribution in a transverse view, at $x = 0.2125$ m, when the front axle is passing over the central sleeper of the model ($t = 0.2$ s)

6.4.2 Fast moving load

In order to study the effect of the train speed on the results obtained with the linear model and with the non-linear model, the assumed velocity of the moving load is now raised to 450 km/h. This value corresponds to 75% of the critical speed. The velocity regime is thus still sub-critical, but the participation of the inertial forces in the dynamic equilibrium is considerably higher than in the previous case.

The vertical dynamic displacements calculated in the ballast layer for the fast moving load case are presented in Figure 6.29. Comparing Figure 6.29 with the equivalent result obtained for the slow moving load case, presented in Figure 6.23, it can be seen that the maximum downward displacements increase with the increase of the load velocity, and that an upward motion of the ballast, not seen in the slow moving load case, is now noticeable. Some significant differences between results obtained with the linear and the non-linear model can now be seen in Figure 6.29, namely, the non-linear response exhibits steady-state waves travelling behind the loads, not seen in the linear results. These steady-state waves are confined to the upper layers of ballast and sub-ballast, and they have a small impact on the maximum downward displacements caused by the axles loads. The displacements under the inner and outer rails (at $y = \pm 0.75$ m) are (again) approximately coincident, but Figures 6.29(c) and 6.29(d) reveal differences in the non-linear results between the two symmetrical points at $y = \pm 1.85$ m, not evidenced in the linear results.

Figure 6.30 shows the *stress paths* determined in the ballast layer, again at points located under the rail ($x = 0$ m, $y = 0.75$ m), for the fast moving load case. The crossing of the failure line can now be seen in both linear and non-linear results. The upward motion of the ballast before the passage of the first axle gives rise to the appearance of (unrealistic) tension stresses in the numerical results of the linear elements of ballast, which is not evidenced in the non-linear numerical results.

6.4.3 Discussion

The consideration of the non-linear constitutive behaviour of the ballast and sub-ballast layers has led to significant differences in terms of calculated numerical stresses. This was confirmed both for the case of high-speed and low-speed moving loads (Figure 6.24 and Figure 6.30). The inclination of the *stress paths* of the ballast under the loaded sleeper augments for the case of non-linear results, and so do the maximum mean stress (p) and deviatoric stress (q). On the contrary, between the sleepers, the obtained stress level is lower with the non-linear model. This indicates that by considering the non-linear constitutive behaviour of the ballast, the spreading of the loading with depth is less

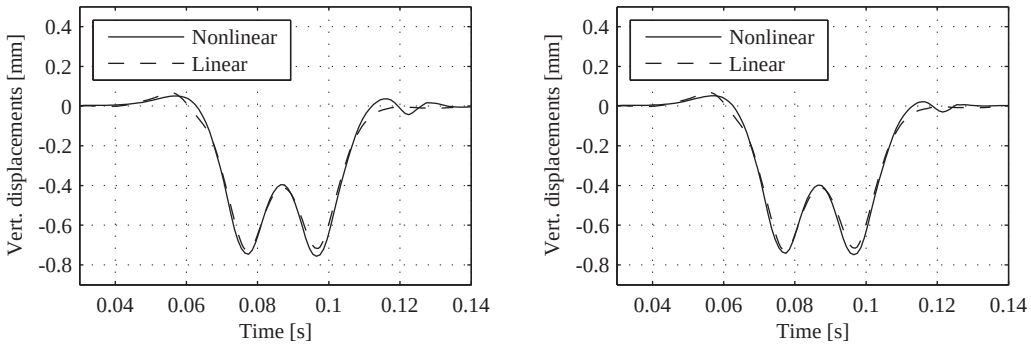

(a) $y = -0.75$ m, $z = 0.80$ m (b) $y = +0.75$ m, $z = 0.80$ m

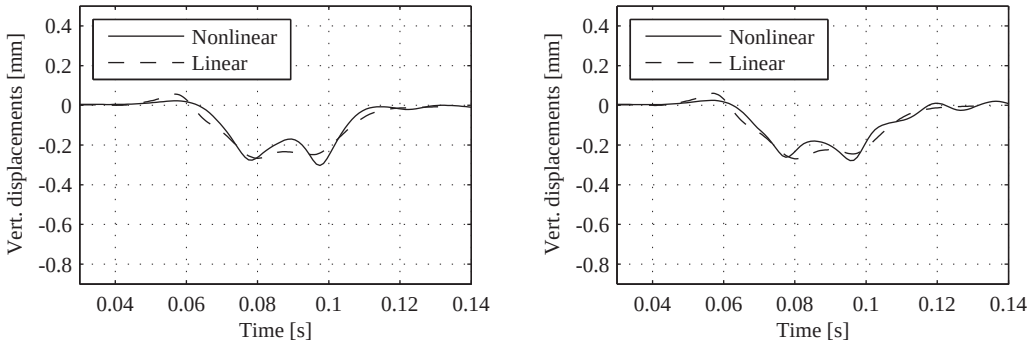

(c) $y = -1.85$ m, $z = 0.60$ m (d) $y = +1.85$ m, $z = 0.60$ m

Figure 6.29: Vertical dynamic displacements obtained in the ballast for the fast moving load case. Comparison between linear and non-linear results

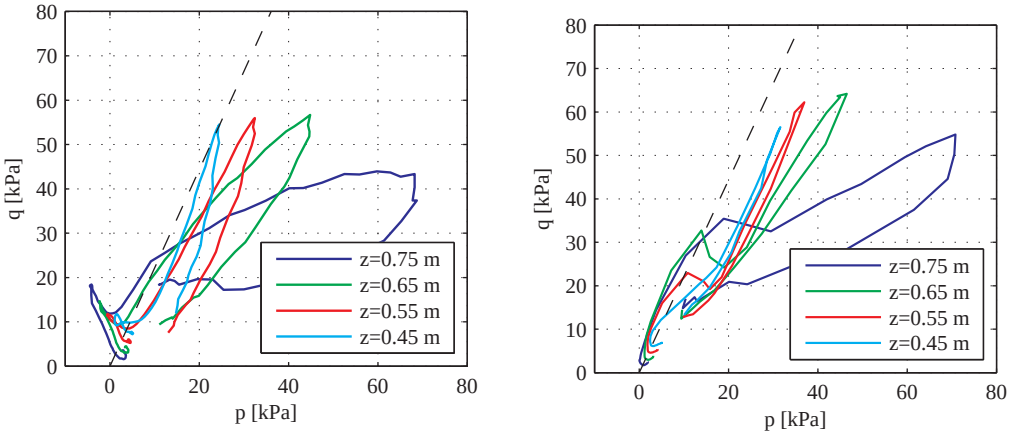

(a) **Linear elements** - Ballast (b) **Non-linear elements** - Ballast

Figure 6.30: Effect of the constitutive model on the *stress paths* at the ballast layer. Results determined at points located under the rail ($x = 0$ m, $y = 0.75$ m) for the fast moving load case. The black dashed line is the failure line

pronounced. This is in agreement with results found with the discrete element method, that show that the transmission of load in the ballast is made through a limited number of contact paths, essentially vertical right below the loaded sleeper (Lu and McDowell, 2007).

In Section 5.5.7, it was discussed that the consideration of the non-linear behaviour of the supporting material may lead to higher transmission of forces to the sleeper underneath the axle. The 3-D numerical results presented above do not, however, confirm this result, as depicted in Figure 6.26. A possible reason for this is the different force-displacement relation adopted in the one-dimensional and in the three-dimensional model. These force-displacement paths are represented in Figures 4.7 and 6.15, respectively, where it can be seen that in the three-dimensional case (Figure 6.15) the non-linear characteristic of the force-displacement path is significantly less pronounced.

The displacement response obtained with the non-linear and with the linear model are approximately coincident for the case of slow moving loads, but some differences arise on the fast moving load case. The non-linear response for the fast moving load case exhibits steady-state waves travelling behind the loads, not seen in the linear results. The existence of these elastic waves, associated to train speeds significantly below the critical regime, may contribute for increased degradation of the ballast layer by introducing additional vibration and the possibility of resonance effects associated to the trains axles configurations and speeds.

6.5 3-D dynamic simulation of a railway transition

The program Pegasus is here applied to model the ballast behaviour at transition zones. For this, the culvert case study is numerically represented by Pegasus, and the obtained dynamic response is analyzed to help interpret the measured long-term response, presented in Chapter 2. The specific aspects to be analyzed are: (i) the influence of decreased initial load on the ballast (due to hanging sleepers) and (ii) the influence of the motion of the approach slabs. At the end, the reasons for the magnitude of the voids existing under the sleepers located in the transition zones will be highlighted.

Recently, Coelho (2011) performed 3-D numerical simulations of the culvert case, using an available program. The model assumed linear-elastic behaviour for the ballast and the subgrade. Some important findings include the fact that the existence of hanging sleepers plays a major role on the behaviour of the track, the presence of the approach slabs causes a stress increase under the free ends of the slabs, and the dynamic response of the structure is (maximum) 20% higher than the equivalent static response. The studies here presented

constitute an extension of the work performed by Coelho, and are more focused on the short-term and long-term behaviour of the ballast layer.

6.5.1 Free track response

This Section introduces the 3-D simulation of the free track response at the culvert site, described in Chapter 2, so without the influence of the culvert box. The inclusion of the culvert and of the corresponding transition zones, will be made in the following Section.

Model parametrization

According to Figure 2.3, the soil profile at the culvert area is characterized by the existence of soft soils underlying a stiffer sand embankment that supports the railtrack itself. Table 4.1 presents the corresponding VSPT data. For these soil layers, the linear-elastic Hooke's Law was assumed. The corresponding shear modulus (G) were derived from the VSPT data, according to:

$$G = \rho\, v_S^2, \tag{6.20}$$

where ρ is the mass density and v_S is the shear wave velocity. The corresponding Young's modulus (E) were then determined using these values of G and estimated values of Poisson's ratio (ν). Table 6.4 presents the layering and the corresponding mechanical properties, in accordance with data presented in Table 4.1.

Layer	H [m]	E [MPa]	ν	ρ [t/m^3]
Sand embankment	4.2	87	0.3	1.7
Peat 1	3.2	12.8	0.495	1.7
Sand intermediate	1.2	100	0.3	1.7
Peat 2	2.4	32.6	0.495	1.7
Sand pleistocene	∞	143	0.3	1.7

Table 6.4: Material parameters of soil profile

The material damping of the soil layers was quantified with the VSPT data by Coelho (2011), following the procedure described in (Karl et al., 2006). According to these calculations, the damping ratio of the soil layers listed in Table 6.4 lies between 0.5% and 1%. In fact, the damping ratio depends on the induced shear strain in the soil: for low strains amplitudes typically lies in the range 1-2% and for the top soil layers, closer to the loading, in the range of 3-4% (Berggren et al., 2010). Here, the material damping was considered of Rayleigh type. It was assumed a damping ratio of 2% at the frequency of 1 Hz and of

1.5% at the frequency of 30 Hz, leading to the frequency-damping relationship shown in Figure 6.31. These adopted frequency-damping values assure that the material damping lies in an adequate range. However, it should be noted that in practice the damping in the system is governed by the radiation damping.

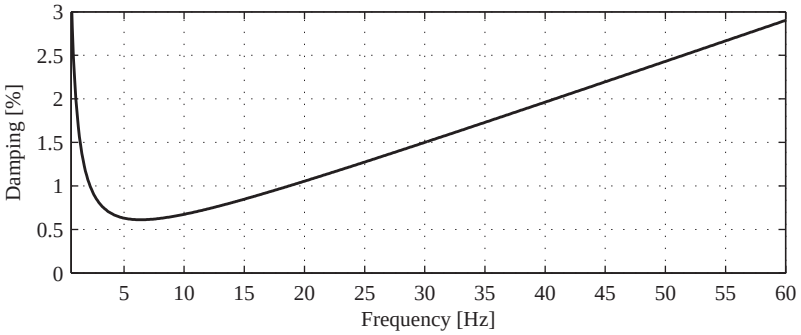

Figure 6.31: Damping ratio implemented with the Rayleigh Damping Method

For the ballast and sub-ballast layers the non-linear response will be considered using the $K-\theta$ model. The adopted parameters K_1 and K_2 were defined in Table 6.3, and the corresponding $E_\mathrm{r}-\theta$ curve was drawn in Figure 6.20.

The material damping of the ballast and sub-ballast layers was implemented with the same frequency-damping relationship shown in Figure 6.31. The damping matrix was determined with an equivalent linear (constant) stiffness matrix, obtained considering 150 MPa and 100 MPa for the Young's modulus of ballast and sub-ballast, respectively.

The railtrack system at the culvert site is (again) composed of rails with UIC54 profile (vertical bending stiffness = 4910 kNm^2, transverse bending stiffness = 880 kNm^2 and mass = 54.8 kg/m) and of wooden sleepers (E = 10 GPa and ρ = 0.7 t/m^3) with 2.5 m length, 0.25 m width and 0.20 m height. The railpads were assumed to have a high stiffness value of 500 kN/mm (Teixeira, 2003), a damping constant of 15 kNs/m (Nielsen and Oscarsson, 2004) and a mass of 15 kg each.

The considered train loading corresponds to the three vehicles described in Chapter 4, named as ICM (trailer), ICM (motorcar) and ICR carriage. The corresponding dead-weight load assumed per wheel was 54 kN, 72 kN and 87 kN, respectively, as listed in Table 4.4. The train loading will be represented by constant moving forces, only.

Total size of the model

The finite element model must have a total size that assures a good representation of the loaded domain, or, in other words, the size of the finite element model shall not influence the obtained response at the region of study.

At the culvert site, the existence of soft layers of soil that extend until approximately 11 m depth, cannot be omitted from the model, or otherwise replaced by a Winkler foundation (described in Section 6.2.4), because these soft layers of soil will have a very significant contribution to the surface response due to moving loads. In this regard, it was found that the consideration of a model with a total height of 13 m (thus including the soft layers and 1.2 m of the stiffer bottom layer of pleistocene sand) supported on a (stiff) Winkler foundation allowed for a good representation of the loaded region, in depth.

The verification of the necessary horizontal size of the model was made by comparing results obtained with two models, having different horizontal dimensions. For this specific study, it was assumed the linear-elastic behaviour for all finite elements of the models. Figures 6.32 and 6.33 shows two views of the models, identified as “small model” and “big model”. The “small model” has 59 sleepers length and 12.9 m in transverse direction, and the “big model” has 81 sleepers length and 19.3 m in transverse direction. The models have 1.0 million dof and 1.7 million dof, respectively. The results from the two models will be compared at their central region, where the finer mesh 2 was adopted.

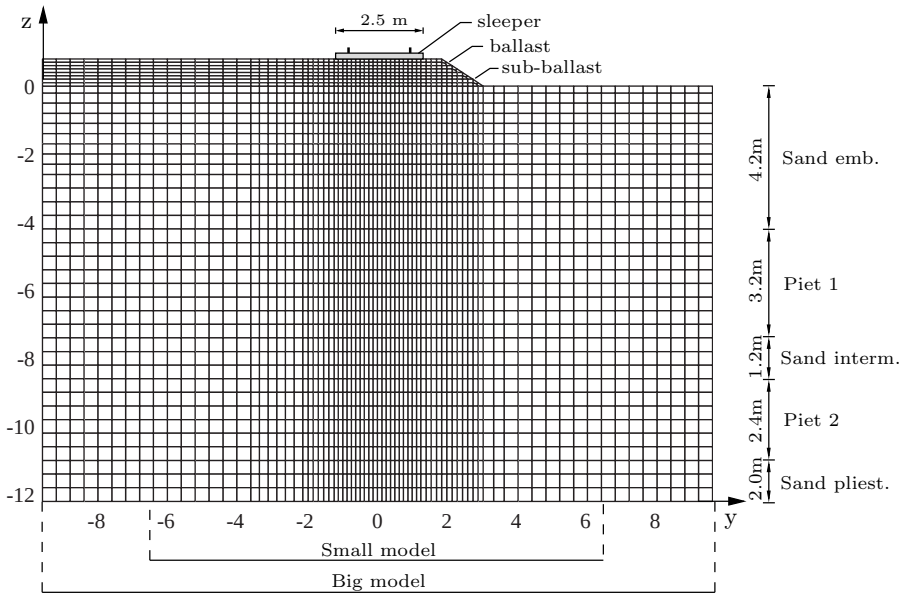

Figure 6.32: Transverse view of models used for total size verification

The loading consists of the self-weight of the soil and the track, and of four vertical moving

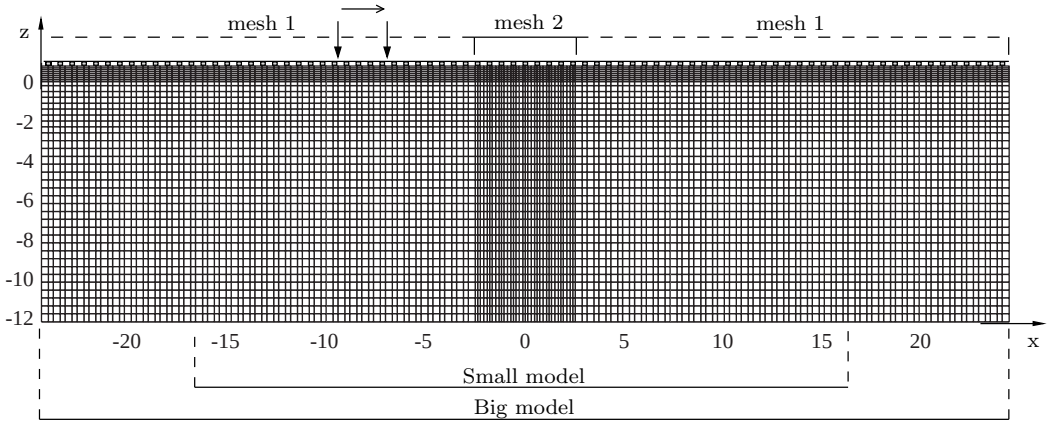

Figure 6.33: Longitudinal view of models used for total size verification

forces of 72 kN each, representing the dead-weight transmitted by four wheels of the same ICM (motorcar) bogie. The forces are initially positioned at $x = -9.7$ m and $x = -7.2$ m, as represented in Figure 6.33. After the static equilibrium for the loads at rest is found, the forces start moving with 130km/h and cross the central region of the model with a steady-state displacement field. The steady-state situation is verified by comparing results obtained a few seconds later.

The computational time of the analyses depends mainly on the time step required for convergence of the solution and of the number of degrees-of-freedom (dof) of the model. For the models under consideration, the required time step was 1.25×10^{-5} s. The corresponding calculation time on a i7 intel processor was 18 h per second of analysis and 24 h per second of analysis, for the small and big model, respectively.

Figure 6.34 shows vertical displacements and vertical stresses calculated with the two models described above. The displacements and stresses are relative to the initial state of the model. These results were determined at locations under the central sleeper of the models ($x = 0$ m), under the rail ($y = 0.75$ m), at the surface of the ballast ($z = 0.80$ m) and at the interface between the sand embankment and the peat layer ($z = -4.20$ m). As can be seen, the differences are small, negligible in terms of vertical stresses. Some differences (in the order of 2% maximum) can be seen in the vertical displacements, mainly due to differences on the response at the peat layers level. According to these results, it can be stated that the small model allows for a good representation of the loaded domain.

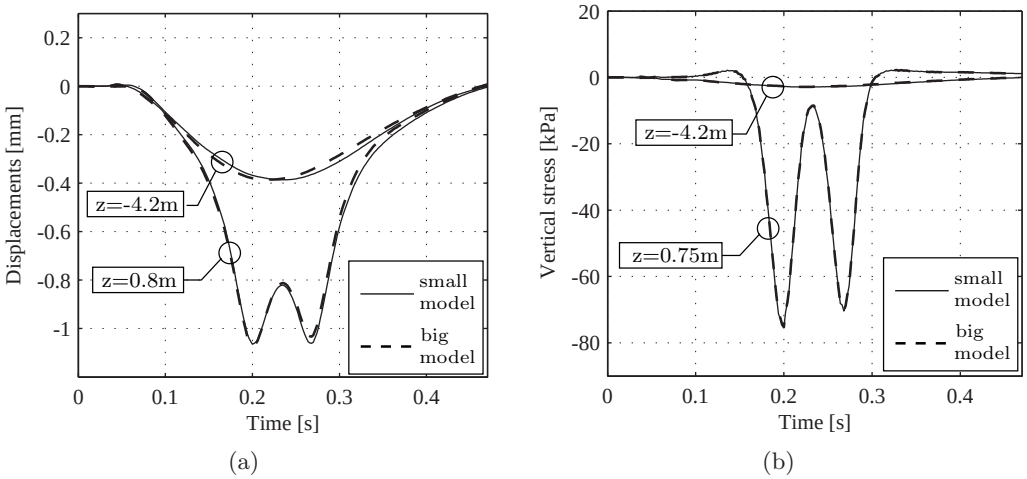

(a) (b)

Figure 6.34: Effect of model size on: (a) vertical displacements and (b) vertical stresses, calculated at surface of ballast and at interface between sand embankment and peat layer, under the rail at $x = 0$ m

Validation of the free track response

The validation of the numerical free track response was made for the values of maximum displacements measured with geophone G7, listed in Table 4.4. A model with the same finite element mesh of the above called "small model", represented in Figures 6.32 and 6.33, was used. However, the ballast and sub-ballast layers were now represented by non-linear elements, using parameters listed in Table 6.3. The model has 24.816 solid non-linear elements representing the ballast and sub-ballast layers, 316.272 solid linear elements representing the soil layers and 1646 beam elements representing the railtrack system, with a total of 1.1 million dof.

The loading consists of the soil/ballast weight, the railtrack weight and of the train loading, applied by this order, as indicated in Figure 6.11. The unloaded rail was assumed horizontal. The three vehicle types referred above were considered: the ICM (trailer), the ICM (motorcar) and the ICR carriage. For each vehicle type, the loading consisted on the application of four wheel forces, representing two axles spaced 2.5 m, belonging to the same bogie. As described in the previous Section, the static equilibrium for the train loads at rest was found, before these started to move with constant speed of 130 km/h.

The time step of the analyses was (again) 1.25×10^{-5} s. The stiffness matrix was updated every 2.50×10^{-5} s (each two time steps). The calculation time on a i7 intel processor was 67 h per second of analysis (factor 3.7 relative to the linear equivalent).

Figure 6.35 shows the time history of vertical displacements, relative to the initial state

of the track. Figure 6.35(a) shows displacements calculated at the central sleeper of the model ($x = 0$ m), at a transverse location approximately coincident to the position of the geophone ($y = 1$ m), for the passage of the three considered vehicles travelling at 130 km/h. Figure 6.35(b) shows displacements calculated at the top surface of the ballast under the central sleeper of the model ($x = 0$ m), at a transverse location under the rail ($y = 0.75$ m), for the passage of the ICM (motorcar) bogie (72 kN load).

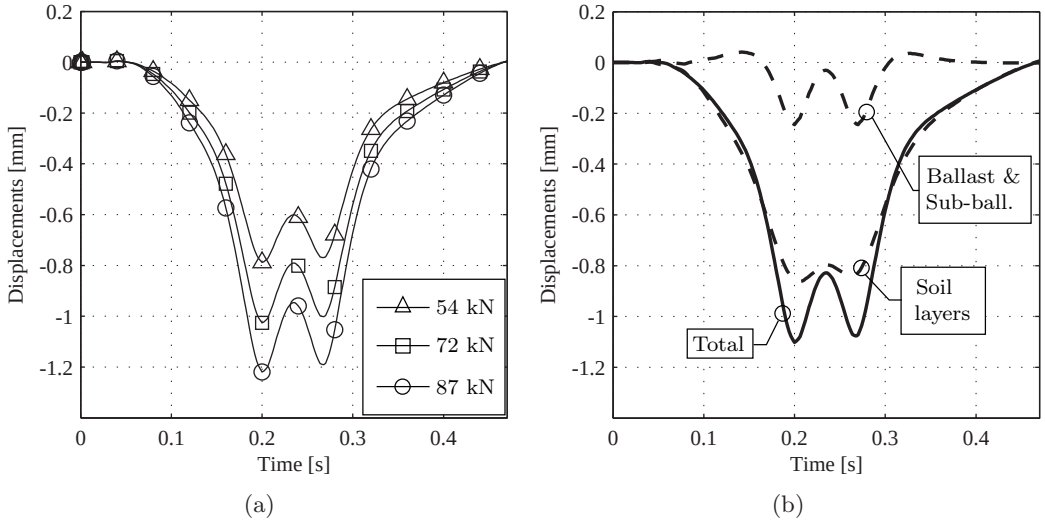

Figure 6.35: Vertical displacements calculated: (a) at the sleeper ($x = 0$ m, $y = 1$ m,$z = 0.8$ m) for three train loads travelling at 130 km/h and (b) at the ballast ($x = 0$ m, $y = 0.75$ m,$z = 0.8$ m) for the 72 kN wheel load, with decomposition of total displacements into part due to ballast & sub-ballast deformation and remaining part due to soil layers deformation

According to results shown in Figure 6.35(a), Table 6.5 lists the maximum vertical displacements measured and calculated for the three train loads considered. It can be seen that the agreement is good. However, the measured force-displacement relationship evidences a higher non-linear trend, compared to the numerical results. This may be due to the fact that the soil layers under the sub-ballast layer were assumed to behave linearly, having the soil layers a predominant contribution for the total displacements (around 78%), as can be seen in Figure 6.35(b).

Train	Static Load [kN]	Measured Displ. G7 [mm]	Numerical Displ. [mm]
ICM (trailer)	54	0.82	0.78
ICM (motorcar)	72	1.00	1.02
ICR	87	1.10	1.20

Table 6.5: Maximum vertical displacements measured at G7 and obtained with numerical model

6.5.2 The culvert transition

Model parametrization

For the 3-D simulation of the culvert transition, the stiff culvert and the corresponding approach slabs were included in the free track model described above. Figure 6.36 shows two longitudinal views of the culvert model. The model has now 79 sleepers length. Placed at the center of the model, the culvert box has a section of 2.65×2.10 m^2. The approach slabs have 4.1 m length. Under the approach slabs, it is assumed that there is a void with 2.9 m length. Therefore, the approach slabs have one side supported on the culvert and the other on 1.2 m of sand (elastic) support. The inclination of the approach slabs was not accounted considering that it plays a minor role on the dynamic response of the ballast/soil system (Coelho, 2011).

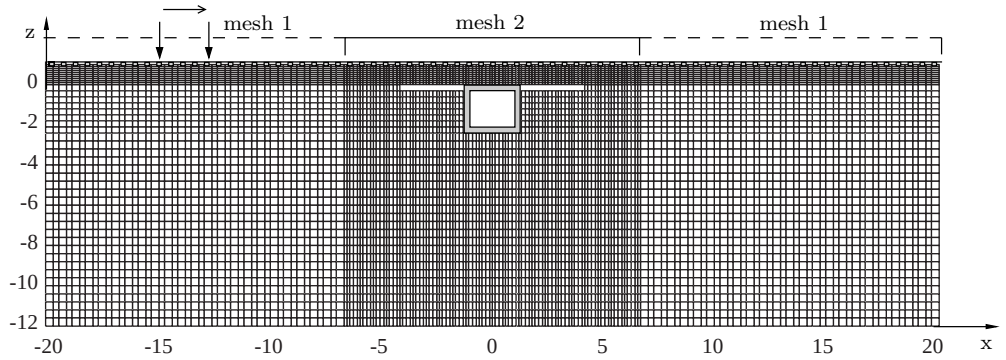

(a) Global view of the model

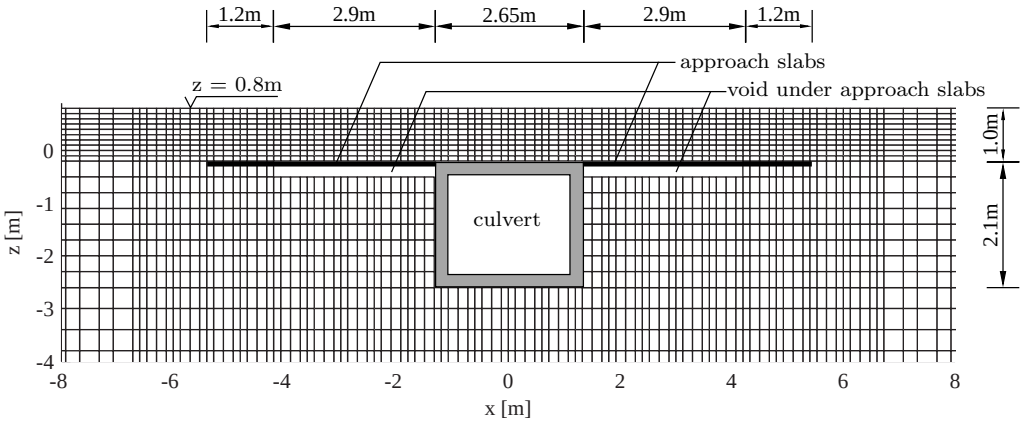

(b) Detail of the ballast/soil system in culvert region

Figure 6.36: The culvert model in longitudinal (xz) view

Figure 6.37 shows a transverse view of the culvert model. Here, it can be seen that the culvert crosses the model along its transverse length and that the approach slabs have the

width of the sleeper's length (2.5 m).

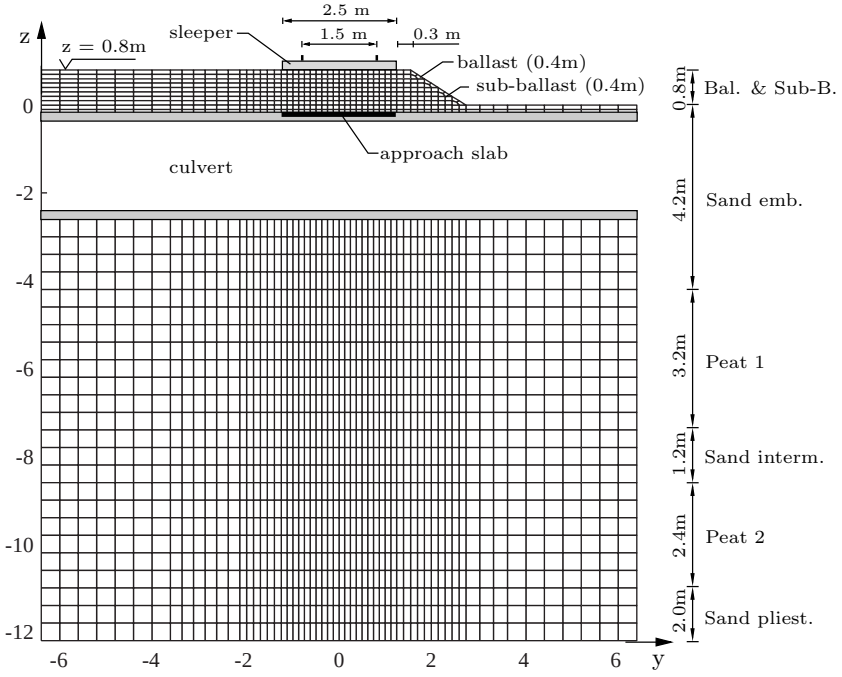

Figure 6.37: The culvert model in transverse (yz) view. Cut at $x = 0$ m

As already referred, the culvert box was not explicitly included in the model. The existence of the stiff culvert was accounted by constraining the displacements of the nodes in contact with its (virtual) concrete surfaces. A node in contact with the culvert is not allowed to move in the direction perpendicular to the culvert wall, but is allowed to move in coplanar directions. The friction between the soil and the culvert is neglected. The exception is made to the nodes contacting the culvert on its bottom surface (at $z = -2.3$ m) which are not constrained in any direction. In this respect, is was assumed that due to settlement of the underlayers, the soil in this region (immediately under the culvert) is not in touch with the concrete surface of the culvert, which is a structure founded on piles, and thus settlement free.

The approach slabs are modelled with a grid of beam elements. The properties of the beam elements were derived assuming a slab thickness of 0.3 m, a Young's modulus of 30 GPa, a Poisson's ratio of 0.2 and a mass density of 2.5 t/m^3.

The remaining properties given to the constituting elements of the model were given in Section 6.5.1, including the soil layering listed in Table 6.4.

Initial state

The initial state of the culvert model, prior to the passage of the trains, was determined considering the soil/ballast weight and the railtrack weight. The unloaded longitudinal level of the inner and outer rail was assumed equal. The assumed level is shown in Figure 4.8(b).

Figure 6.38 shows the distribution of the sleeper-ballast forces that support the railtrack system at rest. Each circle in the Figure represents one sleeper. The assumed level of the rail is also represented in the Figure. The results presented in Figure 6.38 are compa-

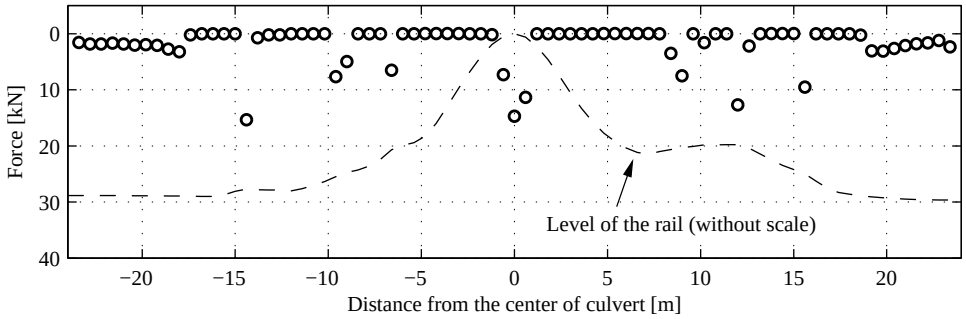

Figure 6.38: Sleeper-Ballast force distribution at rest

rable with the equivalent results obtained with the one-dimensional model, presented in Figure 4.9(b). However, a factor of 1.63 must be applied to the values presented in Figure 4.9(b) for quantitative comparison with values of Figure 6.38. This value results from the fact that the one-dimensional model comprises only one rail and half-sleeper (factor 2) and to the fact that the weight of the sleepers in the 3-D model are slightly lower (factor 0.815). Considering this factor, it can be seen the good agreement between 1-D and 3-D results.

The variation along the track of the sleeper-ballast force at rest has impact on the initial stress distribution on the ballast/sub-ballast layers. Figure 6.39 presents the vertical stress in the ballast/sub-ballast layers in a transverse view, obtained under an hanging sleeper (at $x = -1.80$ m) and under the central sleeper of the model (at $x = 0.00$ m). As can be seen, the initial vertical stress on the surface of the ballast under the central sleeper reaches a maximum value of -24 kPa, with a non-uniform distribution along the sleepers length, whereas under the hanging sleeper the superficial vertical stress is (obviously) approximately zero.

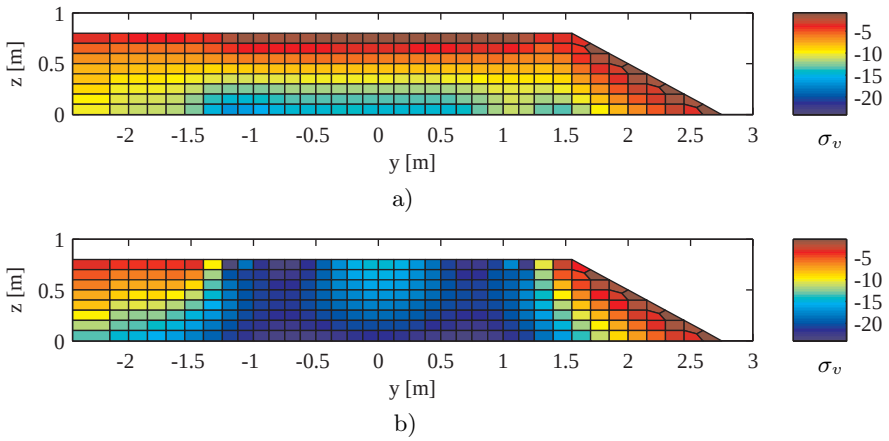

Figure 6.39: Initial vertical stress in the ballast/sub-ballast layers, (a) under the hanging sleeper at $x = -1.80$ m and (b) under the central sleeper at $x = 0.00$ m

Validation of the response at the transition

The validation of the results from the 3-D model was again based on the short-term measurements performed at the culvert site. The amount of voids introduced under the hanging sleepers surrounding the culvert were the same as those defined in the 1-D model (see Figure 4.10). The loading consists on four axles (eight wheel forces) belonging to two successive bogies of ICR carriages, with the configuration shown in Figure 6.40.

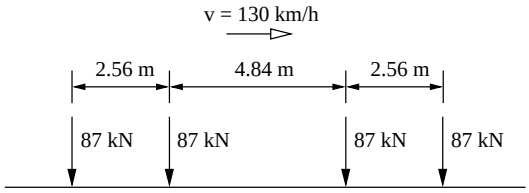

Figure 6.40: Load configuration of four successive wheels belonging to ICR carriages

Figure 6.41 presents the measured and calculated vertical displacements on six sleepers of the track, where the geophones were mounted. The corresponding positions are shown in Figure 6.42. It was assumed that the geophones were placed at $y = 1.0$ m, therefore 0.25 m distanced from the longitudinal axis of the outer rail, as shown in Figure 2.10.

The results in Figure 6.41 show that the 3-D numerical results are in good agreement with the measured displacements. This agreement is acchieved both in terms of downward displacements as in terms of upward displacements. Some overestimation of the upward motion of the central sleeper (G1) can, however, be seen.

As referred in Chapter 4, the downward displacements in the transition zone (geophones

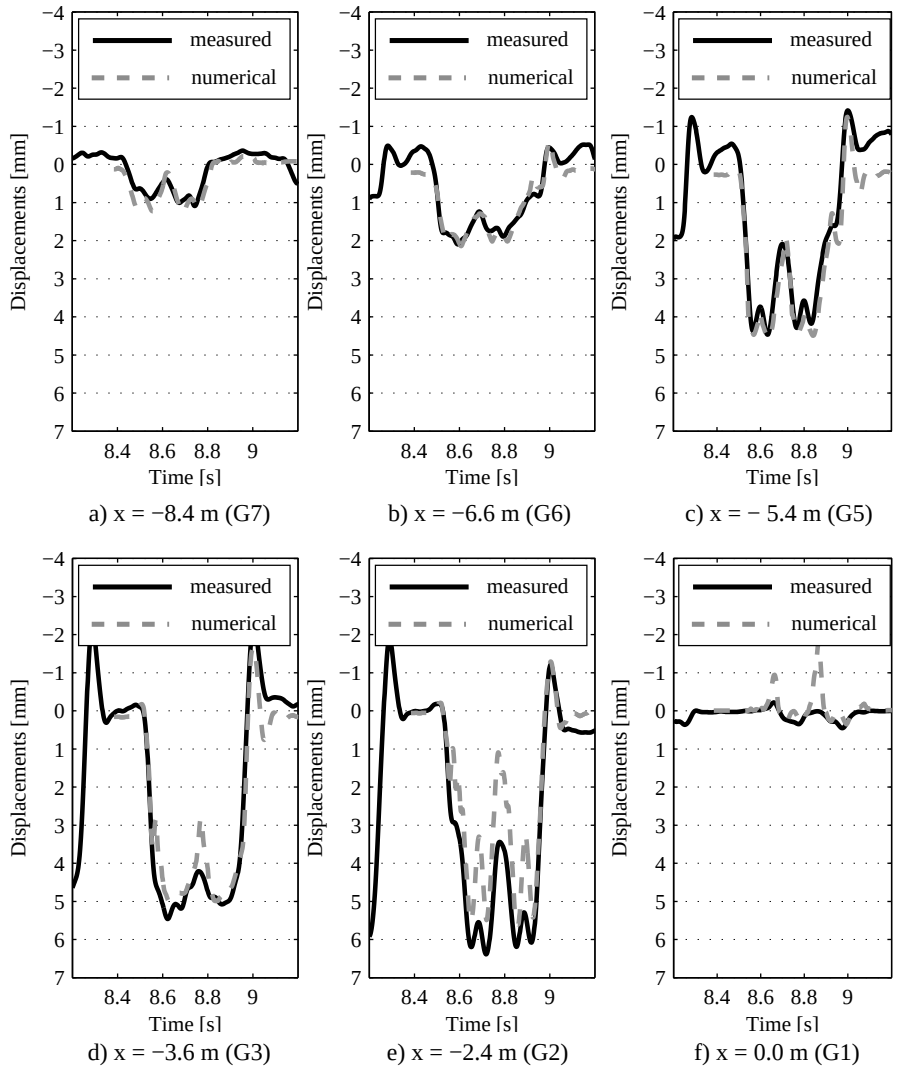

Figure 6.41: Vertical displacements of sleepers G7 to G1 due to an ICR passage at 130 km/h. Comparison between measured and calculated results

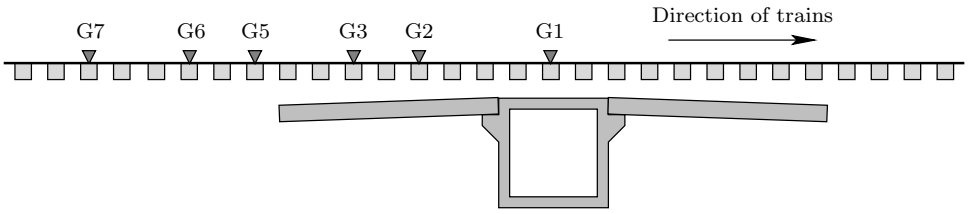

Figure 6.42: Position of geophones

G6, G5, G3 and G2) are highly influenced by the amount of voids under the sleepers. The good agreement between measured and calculated downward displacements at this region would therefore be expectable, since the amount of voids were previously calibrated in Chapter 4, with a 1-D model and the same measured data. The agreement attained in position G7, before the transition zone, coincides with the free track response validation described in Section 6.5.1.

The overall agreement in terms of upward motion of the sleepers was attained with a careful choice of the friction damping value, as explained in Chapter 4. The reduced measured upward motion of the central sleeper, compared to what was estimated by the numerical simulation, might be due to higher restriction of the upward motion of this sleeper compared to the hanging sleepers, due to possible higher confining pressures at its lateral faces.

Structural behaviour

In Chapter 5 it was seen that the voids under the sleepers estimated by the methodology for calculation of settlement, presented in Figure 5.11, were underestimated on locations above the approach slabs close to the box culvert. Figure 6.43 shows the voids profile estimated from calculations in Chapter 5 (profile 1) and the voids profile estimated from the dynamic measurements and confirmed with the direct measurements in the track (profile 2). As referred in Chapter 5, the increased settlement of the ballast in the regions $-3.0\text{m} \leq x \leq -1.8$ m and $1.8\text{m} \leq x \leq 3.0$ m, leading to the different voids profile evidenced in Figure 6.43, could not be explained directly from the 1-D results. The 3-D results and corresponding analyses presented next therefore seek to elucidate the reasons for this increased settlement of the ballast on the transition zones.

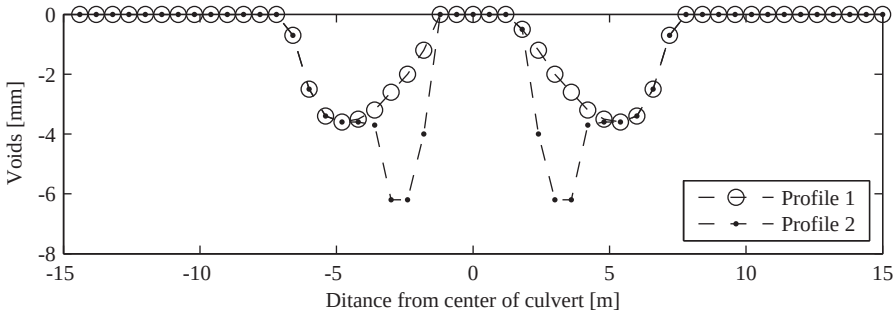

Figure 6.43: Voids under the sleepers around the culvert box. Profile 1 are voids calculated in Chapter 5 and profile 2 are voids determined from the dynamic measurements in Chapter 4

The transmissibility of the track, as defined in (4.16), was determined in Chapter 4 with the

1-D model for the ICR loading and the void profile 2, and shown in Figure 4.16. Figure 6.44 presents again the transmissibility obtained with the 1-D model, now together with the transmissibility determined with the 3-D simulation, considering the void profile 1 and 2 (correspondingly obtained with two different analyses). Comparing results obtained with the 1-D and 3-D models (with void profile 2) it can be seen that the agreement is good, although the transmissibility determined with the 1-D model is generally lower. Some differences are visible mainly past the center of the culvert, which are mostly caused by the fact that the 1-D model included the dynamic loading from the vehicles, not included in the 3-D simulation.

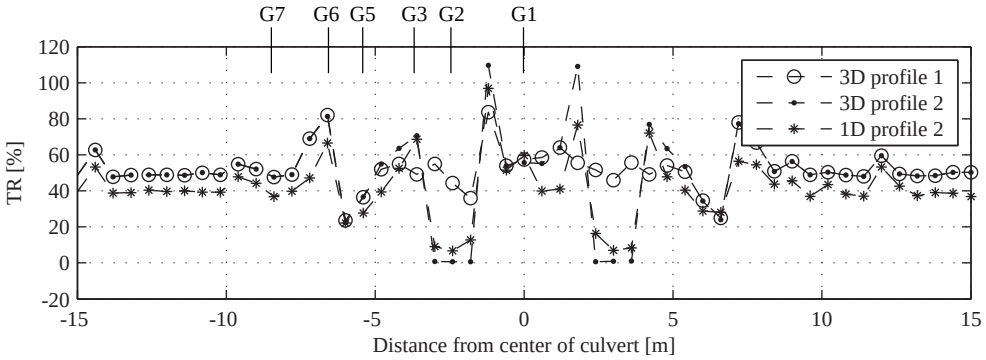

Figure 6.44: Transmissibility due to an ICR passage, obtained with the 3-D model considering the void profile 1 and 2, and with the 1-D model considering the void profile 2

Influence of decreased initial load on the ballast

Figure 6.45 shows the time history of dynamic vertical displacements and the p-q stresses (mean normal stress and deviatoric stress), at four points inside the ballast layer, considering the void profile 1. The points have coordinates $z = 0.65$ m and $y = -0.75$ m, therefore aligned with the inner rail. The x coordinate of the selected points are:

a) $x = -8.4$ m (G7), before the transition zone, corresponding to the displacements and stresses unaffected by the culvert transition;

b) $x = -3.6$ m (G3), in the transition zone but before the region with increased settlement of ballast;

c) $x = -1.8$ m, in the transition zone and in the region with increased settlement of ballast;

d) $x = -1.2$ m, the location of the highest transmissibility on top of the culvert structure.

Figure 6.45 shows that the stresses inside the ballast are significantly influenced by the existence of a transition. As can be seen, before the transition (at G7), the deviator stress

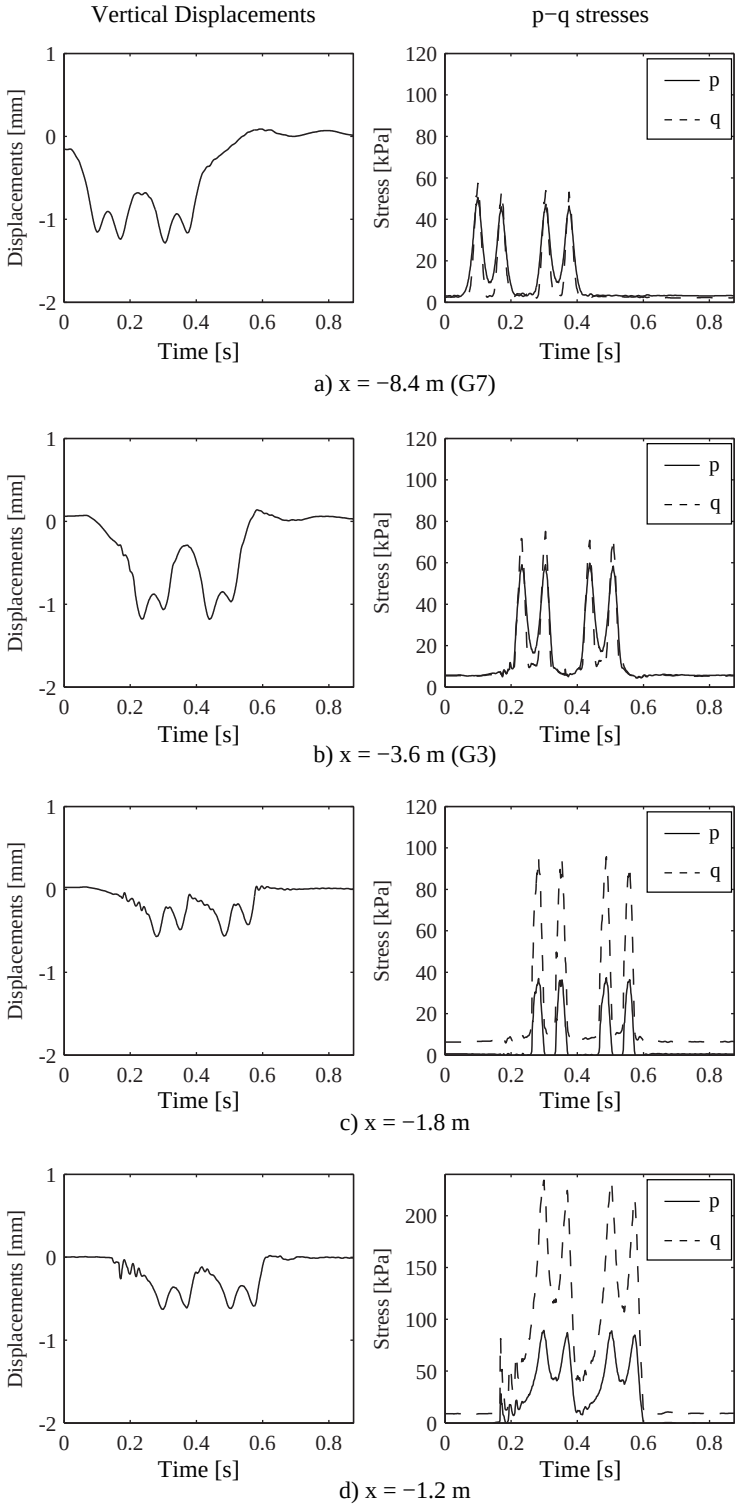

Figure 6.45: Vertical displacements and p-q stresses at four points inside the ballast layer (z = 0.65 m) and aligned with the inner rail ($y = -0.75$ m) considering the void profile 1

(q) reaches a maximum value slightly higher than the maximum normal stress (p), but in the transition zone the maximum q may be significantly higher than the maximum p.

Figure 6.46 shows the evolution of the normal stresses inside the ballast at $x = -8.4$ m before the transition and at $x = -1.8$ m. It can be seen that before the transition (at $x = -8.4$ m), the increase in vertical compression due to the axles passage goes together with an increase in the horizontal (confining) stresses. At $x = -1.8$ m, however, the increase in the horizontal stresses is only observed in terms of σ_{yy} (perpendicular to track), although significantly less pronounced, whereas in terms of σ_{xx} (parallel with track) the stresses decrease during the axles passage, instead of increasing. This gives a background explanation for the observed high deviator stress at $x = -1.8$ m, shown in Figure 6.45.

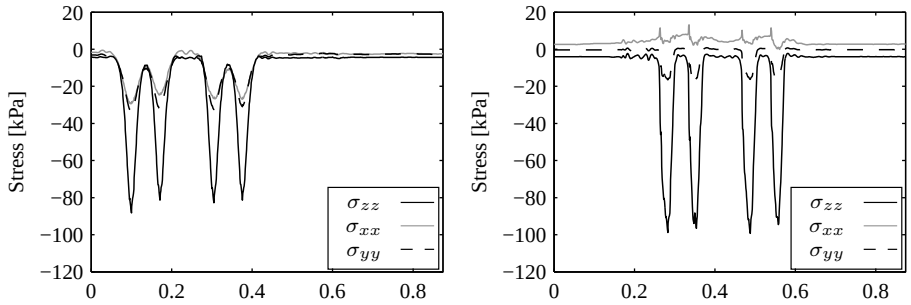

Figure 6.46: Normal stresses in the ballast inside the ballast layer ($z = 0.65$ m), aligned with the inner rail ($y = -0.75$ m) considering the void profile 1

Figure 6.45 d) also shows that the passage of the four axles at $x = -1.2$ m is preceded by an impact of the sleepers on the ballast (at $t \approx 0.2$ s). This impact originates the appearance of high-frequency elastic waves propagating in the ballast layer. These elastic waves rapidly decay in amplitude with distance from the source, as can be seen by looking at Figures 6.45 c) and b), where the amplitude of these waves is significantly smaller.

Influence of the motion of the approach slabs

As mentioned in Chapter 2, the current (unloaded) inclination of the approach slabs is 18.5% (corresponding to an angle of 10.5°). The level difference from the simple support at the culvert to the tip of the slabs is thus 0.74 m, considering the length of the slabs of 4.0 m. This initial inclination of the slabs was not considered in the 3-D model. During the loading from the trains, the slabs are pushed down and again released. The results presented next are aimed at proving that this motion will ease the roll and slip of ballast/soil particles located on top of the slabs.

Figure 6.47 shows the displacement field in a longitudinal view when the first slab is being pushed down due to the weight transmitted by two passing axles. The displacements

are magnified 400 times relative to the coordinate locations, in order to highlight the displacement field. It can be seen that the slabs are effectively bended during the train passage.

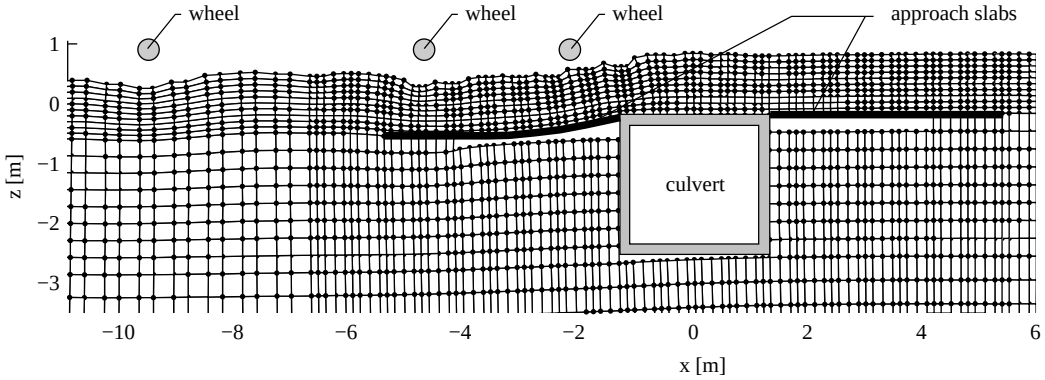

Figure 6.47: Displacement field (magnified 400 times) shown in a longitudinal view at $y = -0.75$ m and at $t = 0.273$ s, when the two front wheels are over the first approach slab

Figure 6.48 shows the displacements and stresses on three locations on top of the first approach slabs (at $z = 0.0$ m). Given the relatively small inclination angle of the slabs of 10.5 °, the normal contact stress with the plate will be a value close to σ_{zz}, shown in the Figure. Looking at σ_{zz} in Figure 6.48, it can be concluded that the motion of the slabs do not lead to a significant (absolute value) decrease of the normal contact stress from to the initial stress state (at $t = 0$). The results in terms of stresses also show that the impact of the sleepers on the ballast causes relatively high-frequency stress variations during minimum stress conditions.

The possible roll/slip of particles on top of the approach slabs will mostly depend on the relation between the contact shear stress and the contact normal stress, being essentially a friction mechanism. Given the fact that the initial inclination of the approach slabs was not considered in the 3-D model, these normal and shear stresses can only be estimated. For this, the stresses in a face coplanar with the inclined slabs were determined by rotation of the $x - z$ stresses. Figure 6.49 shows the corresponding time history of the normal contact stress ($\sigma_{zz'}$) and of the ratio between shear stress and normal stress ($\tau_{xz'}/\sigma_{zz'}$) of an element located on top of the center of the approach slab (at $x = -3.6$ m). Here it can be seen that the shear contact stress starts from an initial value of 16% of the normal contact stress, but during the upward motion of the slabs this relation reaches a maximum value of 40%.

Figure 6.50 now shows the *stress paths* determined at two points immediately above the approach slabs: one above the tip of the approach slabs (at $x = -5.4$ m) and the other above the center of the approach slabs (at $x = -3.6$ m). The dashed line represents the

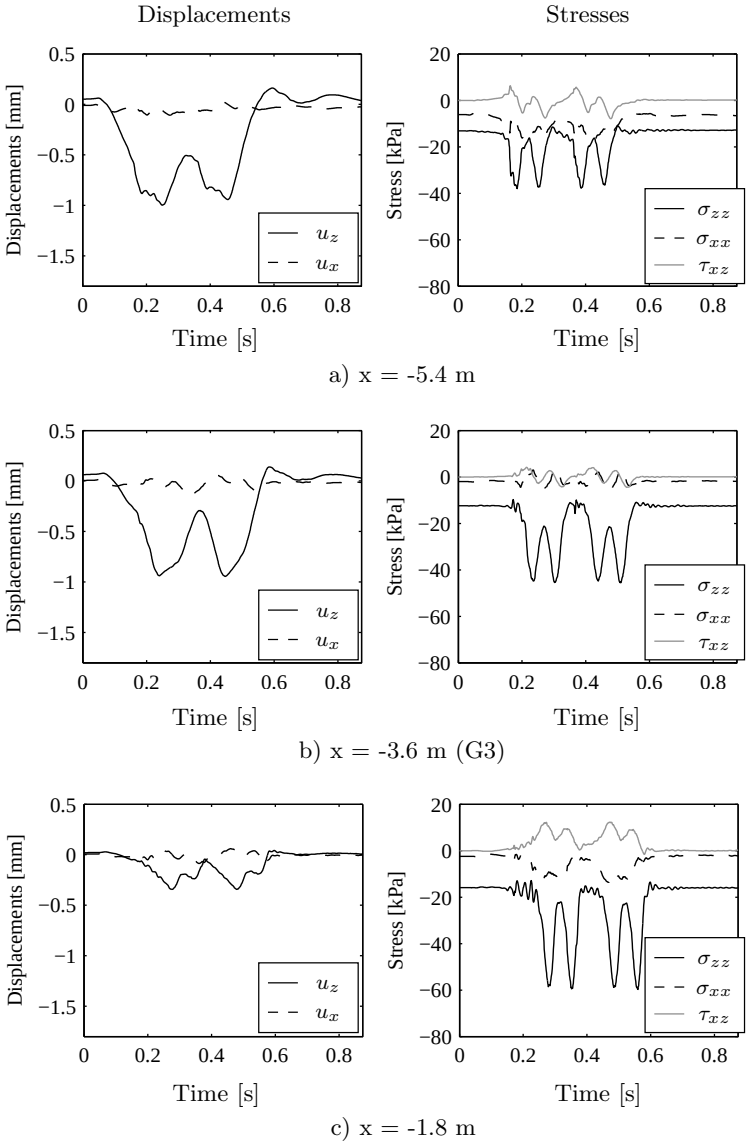

Figure 6.48: Dynamic displacements and stresses in $x-z$ plane on three locations on top of the approach slabs at $z = 0$ m, aligned with the inner rail at $y = -0.75$ m and considering the void profile 1

failure line, determined with Eq. (6.18), considering ϕ'_c=40°, corresponding to a high value of friction angle for sands (Atkinson, 2007). It can be seen that at $x = -3.6$ m the loading is well beyond the failure line.

The slabs not only bend in the $x-z$ plane due to trains passages, as depicted in Figure 6.47, but also rotate in the $y-z$ plane. This rotation is represented in Figure 6.51, showing the maximum dynamic vertical displacements in transverse alignments leveled with the approach slabs at $z = -0.2$ m, at three longitudinal locations: G7, G3 and G2. It can be seen that before the transition (at G7) the vertical displacement profile is approximately

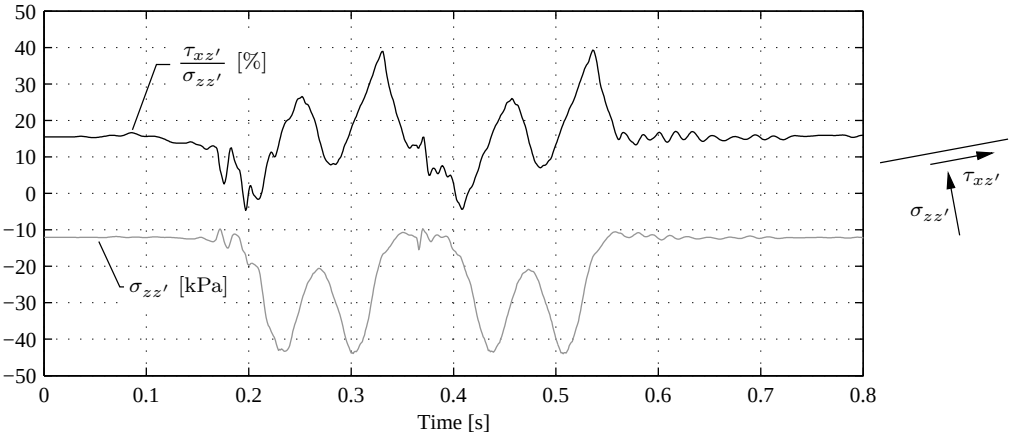

Figure 6.49: Time history of stresses in a face coplanar with the inclined slabs at $x = -3.6$ m, aligned with the inner rail at $y = -0.75$ m

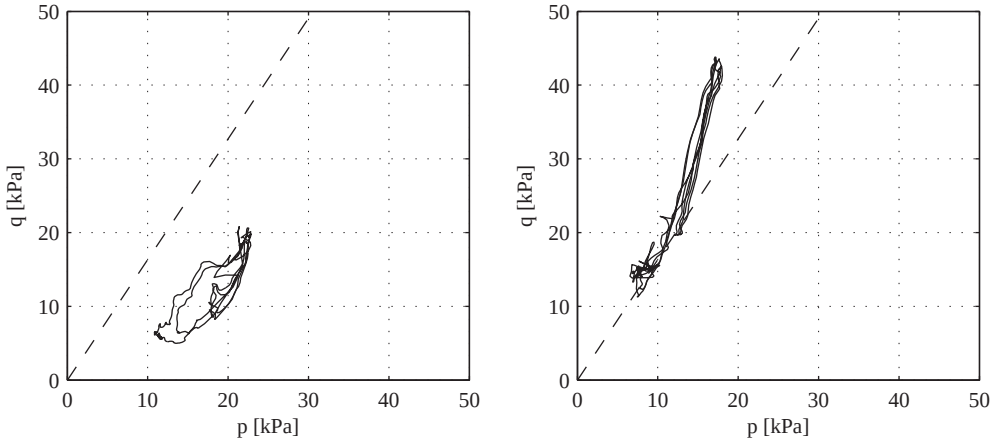

(a) $x = -5.4$ m (b) $x = -3.6$ m

Figure 6.50: *Stress paths* determined at points located under the inner rail ($y = -0.75$ m), immediately above the approach slabs at $z = -0.1$ m. The dashed line is the failure line determined with ϕ'_c=40°

symmetrical relative to the center of the sleeper, but at G3 and G2 a rotation towards the outer side occurs.

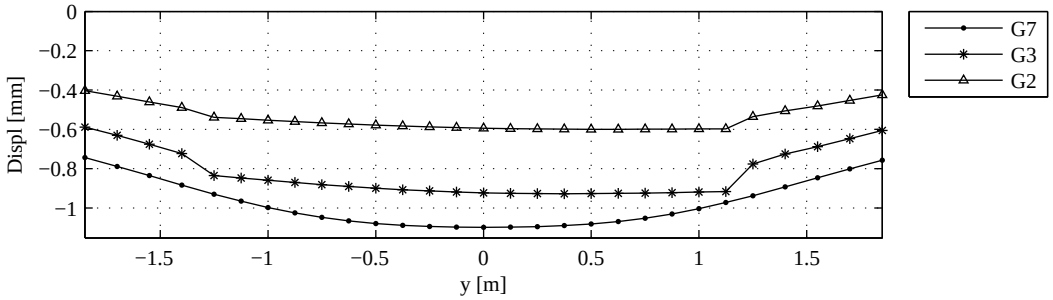

Figure 6.51: Maximum vertical displacements in transverse alignments leveled with the approach slabs ($z = -0.2$ m) at three longitudinal locations

The motion of the slabs will have a significant impact on the shear strains in the ballast/soil system. This can be seen in Figure 6.52, showing the octahedral shear strain (γ_{oct}), as defined in Section 6.4, in three transverse views. The instants of time selected for each of the transverse views correspond to the moment the front axle is passing over the corresponding sleeper. Figure 6.52 a) shows that before the transition, the maximum value of γ_{oct} is around 4.0×10^{-4}, occurring in the ballast layer, and lowering in depth. Figure 6.52 b) shows that at the tip of the approach slabs (position G5), the maximum values of γ_{oct} occur along all the depth of the ballast and sub-ballast layers, extending into the sand layer, with the maximum value of around 5.0×10^{-4}. Figure 6.52 c) shows that at the middle of the approach slabs (position G3), the maximum value of γ_{oct} occurs at the vicinity of the concrete slab, in the sand layer, reaching values above 10×10^{-4}, which is significantly beyond the small strains regime. The Figures also show that the shear strains are generally higher in the outer side, compared to the symmetrical position at the inner side.

6.5.3 Discussion

Figures 6.45 and 6.46 have shown that the deviatoric stress q significantly increases in the transition zone, compared to the case of the free track, not being followed by the mean normal stress p. This deviatoric stress increase is caused by decreased initial load on the ballast, in a region with hanging sleepers, where the confining pressure in the ballast during the axles passage is considerably smaller (see Figure 6.46). The consequence is that unrecoverable (plastic) deformations are more likely to occur, as failure of granular materials are determined by shear (Atkinson, 2007).

The existence of hanging sleepers on transition zones can lead to significant impact loads

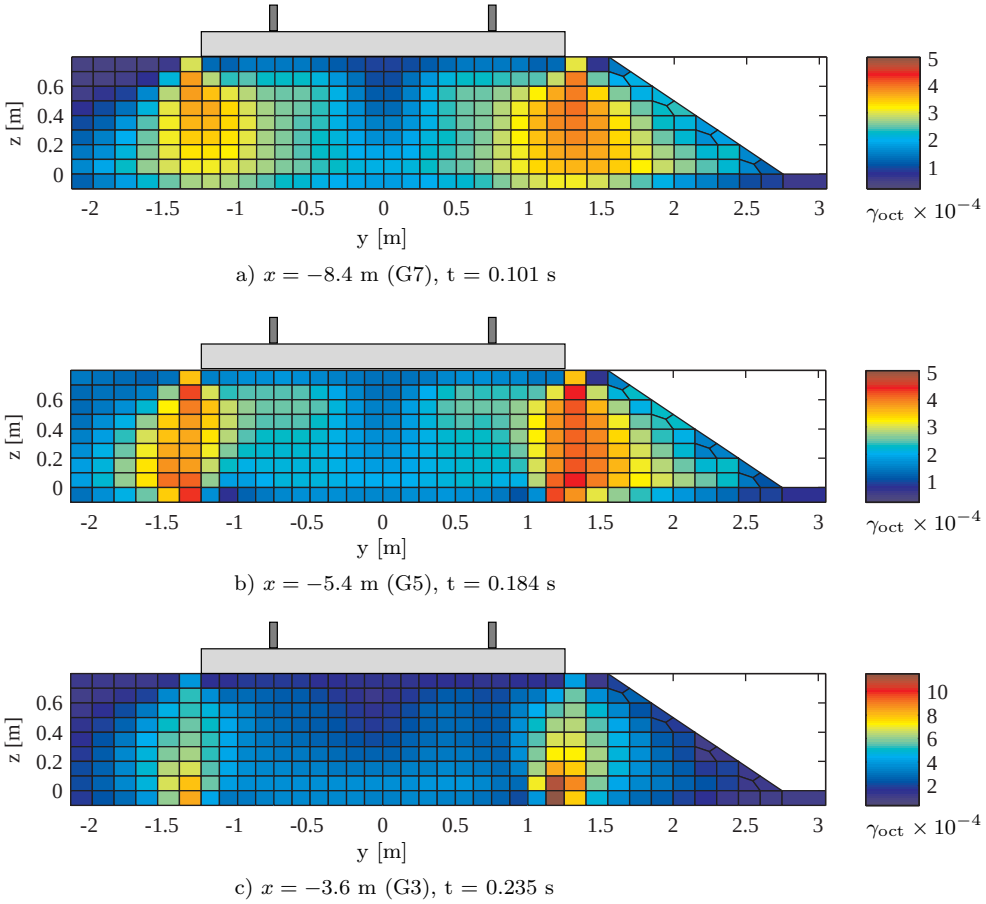

Figure 6.52: Three transverse views of the octahedral shear strain

on the ballast. The numerical evidence of these impacts are seen in Figures 6.45 and 6.48. As referred in Chapter 3, high impact forces in the ballast will produce higher degradation of the ballast particles, also leading to higher densification (Baessler and Ruecker, 2003). A consequence of this degradation mechanism will be an accelerated breakage of the ballast particles, as the particle size distribution of ballast samples collected from the culvert site, presented in Figure 2.9, clearly indicate.

The roll and slip of soil/ballast particles on top of the inclined approach slabs is significantly facilitated during dynamic loading from trains. From Figure 6.49, it is seen that the minimum coefficient of static friction preventing the particles in contact with the concrete from sliding is 0.40. Considering the design practice that assumes a coefficient of static friction between concrete surfaces and soils to be $\mu_s = \tan(\frac{2}{3}\phi'_c)$ (Atkinson, 2007), the corresponding value of critical state friction angle (ϕ'_c) is 34 °, which is already a considerably high value for soils (Atkinson, 2007). Considering the fact that the process occurs cyclicly, the rolling and slide of particles over the inclined approach slabs will likely occur (Suiker et al., 2005). Moreover, Figure 6.50 shows that the loading of the soil im-

mediately above the center of the approach slabs is well above the failure line, indicating failure, and therefore large plastic deformations, of this material.

Figure 6.52 shows that the deformation of the ballast and approach slabs system, during loading from trains, leads to a high concentration of shear strains on the lateral extremities of the slabs. This indicates that another mechanism will also contribute for the development of voids in the transition zones: the failure of the ballast-soil located over the approach slabs, on the x-z planes with $y = -1.25$ m and $y = +1.25$ m, with a possible flow of particles from the top of the approach slabs to the bottom.

Figure 6.52 also shows an asymmetrical inner/outer behaviour, with higher shear strains occurring in the outer side of the track, closer to the ballast slope. This is observed both before the transition (Figure 6.52 a)) as on the transition zone. These results may give an explanation for the higher settlements that were observed under the outer rail, compared to those observed under the inner rail, as referred in Chapters 2 and 5.

6.6 Conclusions

Using a newly developed finite element program (entitled Pegasus), the implications of considering the non-linear constitutive behaviour of the ballast and sub-ballast on the dynamic response for moving loads was investigated. The results obtained considering loads moving at a speed considerably below the critical speed of the track, have shown that the equivalent linear model gives essentially the same displacement field obtained with the non-linear model, but that the stress and strain response inside the ballast and sub-ballast layers is significantly different. For the case of loads moving at speeds approaching the critical speed of the track, not only the stress and strain fields are different, but also differences are seen in terms of dynamic displacements. Namely, the development of superficial steady-state waves travelling behind the loads can be seen in the results obtained with the non-linear model, not seen in the equivalent linear results.

The program Pegasus was applied to study the culvert case study presented in Chapter 2. The numerical results were analyzed in order to determine the reasons for the increased settlement of the ballast located over the approach slabs. From the 3-D simulations, it was found that:

- During the passage of an axle load the ballast in the transition zone is loaded above its theoretical strength, with q/p reaching 2.5 (Suiker et al., 2005; Indraratna et al., 2006), due to the low confinement stress under the hanging sleepers and the rotation of the approach slabs;

- The existence of hanging sleepers result in impact loads on the ballast, leading to high-frequency superficial waves;
- The ballast/soil above the approach slab has the tendency to start rolling/sliding;
- The dynamic motion of the slabs also leads to high shear strains on the lateral (transverse) extremities of the slabs.

According to these results, it can be concluded that both analyzed aspects, namely (i) the decreased initial load on the ballast (due to hanging sleepers) and (ii) the motion of the approach slabs, play a decisive role on the increased settlement of the ballast over the approach slabs.

Chapter 7

Improved Track Solutions for Transitions

7.1 Introduction

According to literature (see Chapter 2), increased degradation of transition zones in ballasted tracks is frequently caused by large and steep change in the stiffness of the track and foundation, due to structural discontinuities existing along the track. The proposed methods, referred in literature, to reduce problems at transitions are therefore generally intended to produce gradual stiffness profiles, also maintaining maximum and minimum values within acceptable limits (Li and Davis, 2005). The techniques for a gradual stiffness transition are usually separated between those based on smoothing the stiffness variation on the soft/embankment side, and those based on lowering the stiffness on the stiff/bridge side. The first type include the inclusion of a approach slabs, variable spaced sleepers, underlayments of hot-mix-asphalt or of geotextiles or of soil-cement, among others. The second type include the use of soft railpads, under sleeper pads, or ballast mats. If, however, the problem is caused mainly by geotechnical issues, other methods can be used to improve stability, including proper drainage, adequate compaction, stone column, and deep soil mix to strengthen the embankment (Briaud et al., 1997; Li and Davis, 2005).

In order to gain some insight into the adequacy and effectiveness of possible measures to overcome problems associated to transition zones, this Chapter analyses two cases: (i) the introduction of soft railpads on the stiff part of the transition (Section 7.4), and (ii) the possible replacement of the ballasted track by a slab track solution (Section 7.5).

7.2 Definition of track stiffness

The problems associated with transition zones are frequently closely related with large and steep change in the stiffness of the track and foundation. The vertical stiffness of a railway track is often measured or quantified with the "track modulus". This is defined as the supporting force per unit length of rail per unit vertical deflection under a vertical load (Li and Davis, 2005), and is determined with (Selig and Waters, 1994):

$$K_{\mathrm{m}} = \sqrt[3]{\frac{F^4}{64\,EI\,U^4}} \tag{7.1}$$

where K_{m} is the track modulus (in the unit of N/mm/mm), F is the vertical wheel load, U is the vertical deflection under the load, and EI is the bending stiffness of the rail. The track modulus is also designated in the literature with u (Selig and Waters, 1994; Teixeira, 2003), but here the usage of K_{m} is preferred, in order to avoid misidentification with u designating displacements.

According to Li and Davis (2005), the track modulus should be neither too low or too high, and the range of 14-69 N/mm/mm is referred as acceptable. Low track modulus is often associated with poor subgrade support, leading to the development of differential settlements, and high track modulus can lead to undesirably high dynamic vehicle/track interaction.

7.3 Standard case

In order to test the effectiveness of possible measures for transitions, it is necessary to have data and results relative to the standard case, in relation to which the improved solutions will be compared. This is here performed by means of a numerical simulation.

7.3.1 Numerical model

The model of the standard case is represented in Figure 7.1. This model basically corresponds to a simplification of the FEM model presented in Chapter 4. The loading from the train is now simplified to a constant moving force, and the railpads are now represented, by means of spring-dampers elements.

The support reaction of the sleepers is (again) given by spring-damper elements. The support takes place only if there is contact between the sleeper soffit and the ballast. The

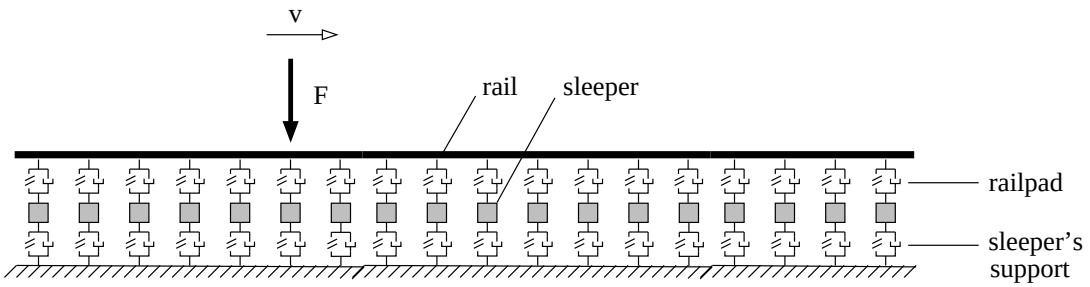

Figure 7.1: Model of the track used for the standard case

assumed force-displacement path of the springs follows a bi-linear model:

$$F_{\mathrm{sp}.i} = \begin{cases} k_{lin.i}\,(u_{\mathrm{t}.i} - u_{\mathrm{c}.i}) & \text{, if } u_{\mathrm{t}.i} \geq u_{\mathrm{c}.i}, \\ 0 & \text{, if } u_{\mathrm{t}.i} < u_{\mathrm{c}.i}. \end{cases} \tag{7.2}$$

where $F_{\mathrm{sp}.i}$ is the force passing through the spring i, $u_{\mathrm{t}.i}$ is the downward displacement of the sleeper i, $u_{\mathrm{c}.i}$ is the displacement at which sleeper i contacts the ballast, and $k_{lin.i}$ is the stiffness of the spring on the contact situation (compression). The assumed force-velocity relation of the dampers also follows a bi-linear model:

$$F_{\mathrm{d}.i} = \begin{cases} (c_{\mathrm{fr}.i} + c_{\mathrm{rd}.i})\,v_{\mathrm{s}.i} & \text{, if } u_{\mathrm{t}.i} \geq u_{\mathrm{c}.i}, \\ c_{\mathrm{fr}.i}\,v_{\mathrm{s}.i} & \text{, if } u_{\mathrm{t}.i} < u_{\mathrm{c}.i}. \end{cases} \tag{7.3}$$

where $F_{\mathrm{d}.i}$ is the force passing through damper i, $v_{\mathrm{s}.i}$ is the velocity of sleeper i, $c_{\mathrm{fr}.i}$ is the friction damping constant of sleeper i, and $c_{\mathrm{rd}.i}$ is the radiation damping constant, as was defined in Eq. (4.10).

7.3.2 Parametrization of the model

The values for the parameters of the model representing the standard case were derived from the culvert case, presented in Chapter 2. The standard case, however, corresponds to a single abrupt increase of the track stiffness, whereas the culvert case corresponds to a place where the stiffness increases rapidly, and then decreases after 1-2 m of track.

It is assumed symmetry along the longitudinal axis of the track and therefore the model represents only half railway track (one rail, half sleeper). The properties of the track are given in Table 7.1. The presented values are per rail seat, with exception for the rail properties.

The properties of the railpads were not measured for the culvert site. It is only known

Track component	Parameter	Value
Rail UIC54	Mass	54.7 kg/m
	Bending stiffness	4910 kNm^2
Sleeper	Mass (half-sleeper)	80 kg
	Sleeper distance	0.60 m
Railpads	Linear stiffness	500 kN/mm
	Linear viscous damping	15 kNs/m
Ballast/Soil	Linear stiffness (k_{lin}) of soft side	26 kN/mm
	Linear stiffness (k_{lin}) of stiff side	100 kN/mm
	Friction damping (c_{fr})	3.125 kNs/m
	Radiation damping (c_{rd})	112.9 kNs/m

Table 7.1: Track properties of the standard case model

that the stiffness of the railpads are relatively high, as the site is located above soft soils, and therefore no additional flexibility is required. From literature it was found that the stiffness of typical railpads in Europe can be as high as 500 kN/mm (Teixeira, 2003), and therefore this value was adopted. The damping constant of the railpads was taken from (Nielsen and Oscarsson, 2004).

The stiffness of the linear elastic foundation was defined based on the dynamic measurements on the culvert site, as given in Table 4.4. The selected train type for the spring stiffness calibration was the intercity ICM (motorcar unit), having 72 kN of static wheel load. The maximum downward displacements for the passage of this train at the sleepers is 1.0 mm on the soft side of the track, and 0.36 mm on the stiff side of the track.

7.3.3 Numerical results

Figure 7.2 superpose the rail and sleeper displacements, determined at three positions of the moving load: six meters before reaching the transition, on top of the transition (at $x = 0$), and six meters after the transition. It can be seen that the sleeper downward displacement, represented in the Figure with squares, is approximately 1.00 mm at the soft side of the track, and 0.36 mm at the stiff side. The displacements in the stiff zone are thus 2.8 times lowers than the displacements on the soft zone. The differences between the rail and sleepers displacements are small, because of the adopted high stiffness of the railpad.

Figure 7.3 presents the track modulus for this standard case transition, as was defined in Eq. (7.1). As can be seen, the track modulus changes abruptly within about three sleepers length by a factor of 3.4, from 40 N/mm/mm to 135 N/mm/mm. Futhermore, the track modulus on the stiff side of the track is considerably high, considering the maximum

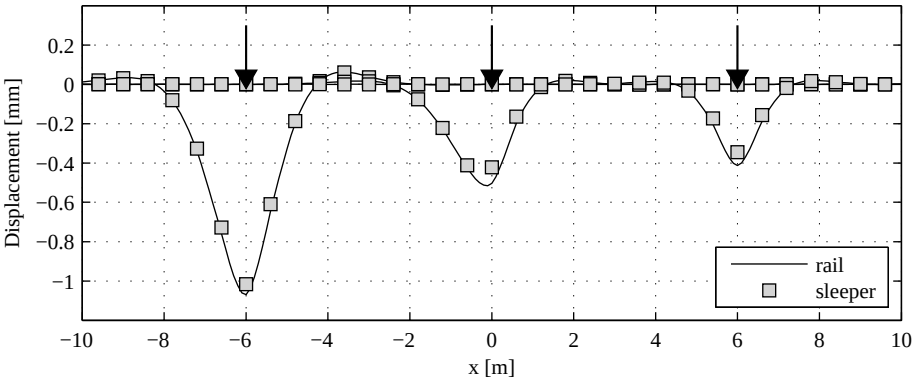

Figure 7.2: Rail and sleepers displacements in standard case model. Load of 72 kN moving at 120 km/h

referred acceptable limit of 69 N/mm/mm (Li and Davis, 2005).

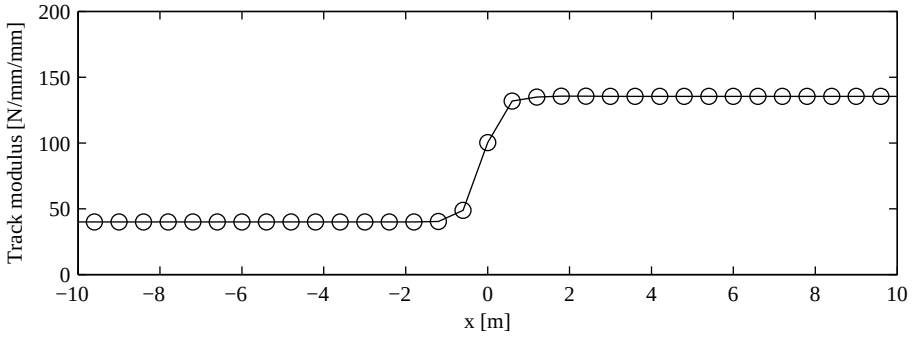

Figure 7.3: Track modulus of the standard case transition

The transmissibility of the track was defined in Eq. (4.16), and is repeated here for convenience:

$$\mathrm{TR}_i = \frac{\max|F_{\mathrm{tran}.i}(t)|}{F_{\mathrm{static}}}, \tag{7.4}$$

where TR_i is the transmissibility at sleeper i, $F_{\mathrm{tran}.i}$ is the force transmitted through sleeper i, and F_{static} is the static wheel load. Figure 7.4 shows the transmissibility of the standard case transition, where it can be seen that due to the steep track modulus variation (shown in Figure 7.3) a differential sleeper load on consecutive sleepers of more than 80% occurs (from 36% to 66% transmissibility), whereas Gardien (2005) states that this value may not be greater than 45%, in order to limit differential ballast degradation.

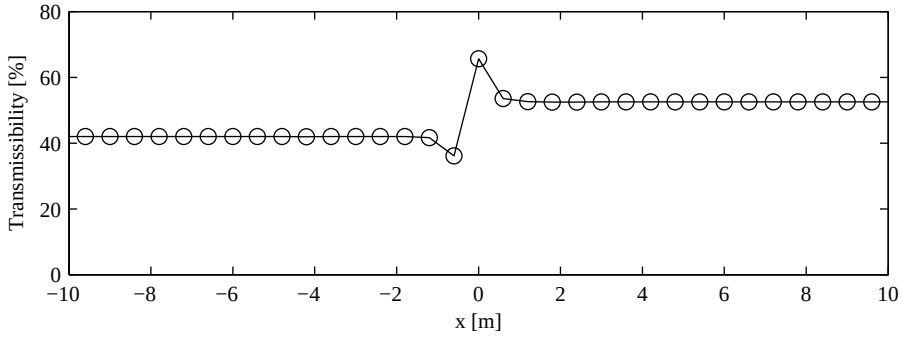

Figure 7.4: Transmissibility of the standard case transition

7.4 Soft pads under rails

As mentioned above, one possible measure to mitigate the problems at transition zones is to lower the stiffness of the railpads in the stiffer part of the track. In this sense, the railpad stiffness of the stiff side of the track was reduced from 500 kN/mm to 65 kN/mm, representing a soft railpad made with elastomere material (Esveld, 2001). The damping constant of the railpad is maintained from the standard case. The properties of the track and the loading, with exception for the railpad stiffness change, as well as the numerical model, are maintained from the previous standard case.

Figure 7.5 shows the displacement results obtained with the soft railpad case model. It can be seen that the sleeper deflection remains almost unchanged from the previous standard case, but that the rail deflections on the stiff side of the track are now considerably higher, and therefore the differential rail deflection is lower.

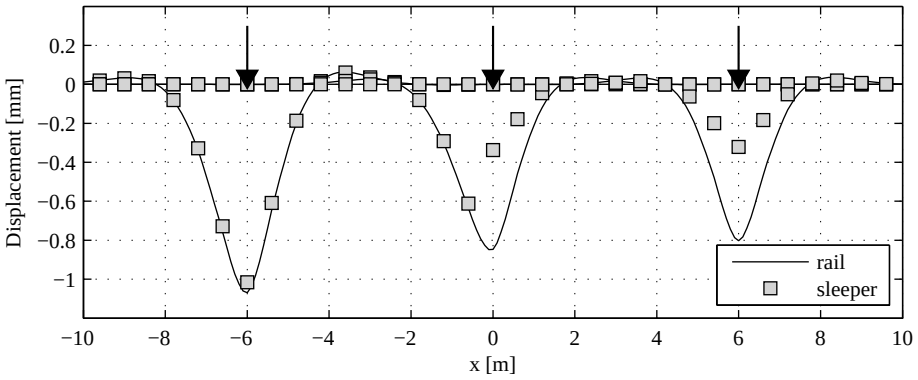

Figure 7.5: Rail and sleepers displacements for case with soft railpads. Load of 72 kN moving at 120 km/h

The track modulus for this soft railpad case is shown in Figure 7.6. Compared to the standard case (see Figure 7.3), the track modulus increase is significantly less pronounced, raising from 40 N/mm/mm to 56 N/mm/mm, therefore within the admissible limits referred above.

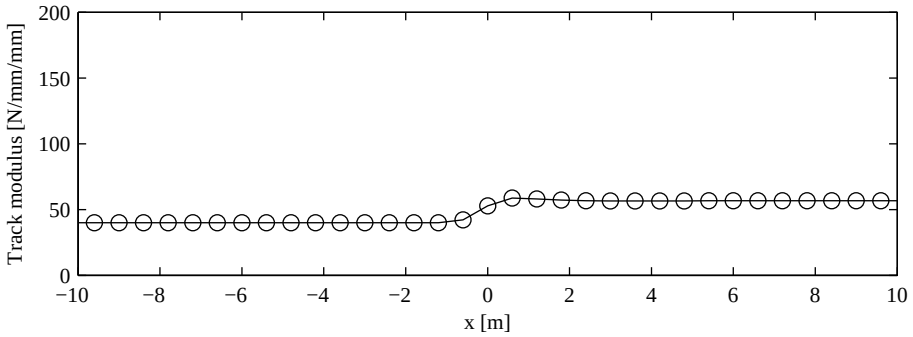

Figure 7.6: Track modulus of the case with soft railpads

Figure 7.7 shows the transmissibility determined for the soft railpads case transition. As can be seen, the differential sleeper load on consecutive sleepers does not exceeds 22%, therefore well below the admissible limit of 45%, referred by Gardien (2005).

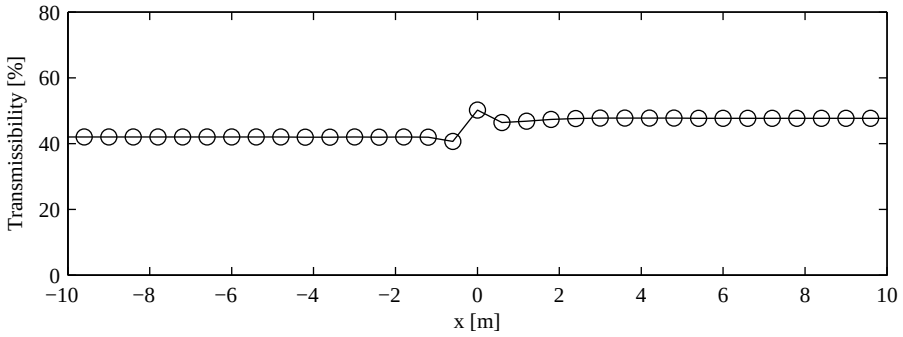

Figure 7.7: Transmissibility of the case with soft railpads

7.5 Slab track performance at railway transitions

Slab tracks, also called ballastless tracks, consists in an alternative to ballasted tracks. Slab tracks are common in Japanese high-speed lines, and have been progressively used in Europe, mainly in Germany and in the Netherlands. The slab track structure basically results from replacing the ballast/sub-ballast layers by a concrete slab, although there

are several specific structural solutions of slab tracks, of which Esveld (2003) gives a summarized description.

The slab track solution exists with rails discretely supported on sleepers, using railpads, or with rails continuously supported, embedded in a fill material. Figure 7.8 shows a transversal view of the slab track solution where the rails are embedded in Corkelast (polyurethane mixed with cork) (Shamalta and Metrikine, 2003). Typically, slab tracks are built using continuously reinforced concrete slabs (Schwartz and Taybji, 2002), although in Japan the solution with prefabricated slabs is common.

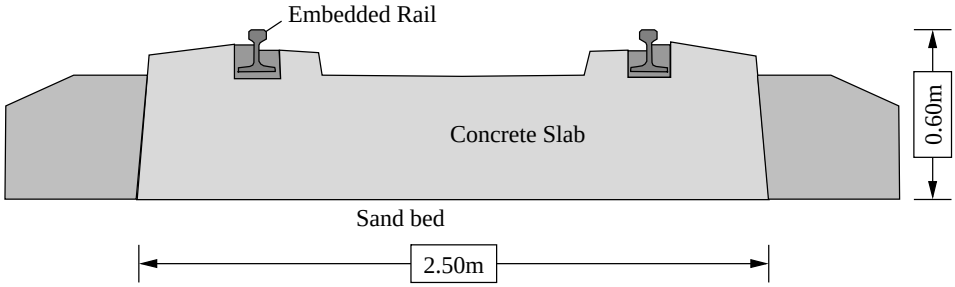

Figure 7.8: Embedded slab track. Modified from (Shamalta and Metrikine, 2003)

The main structural and operational advantages of slab tracks are their higher longitudinal and lateral permanent stability, reduced sensitivity to differential settlements, lower maintenance, prevention of churning up of ballast particles at high-speed, and an increase of passenger comfort due to better permanent alignment. Disadvantages are the initial cost of construction and a lower noise and vibration absorption, when compared with ballasted track, which may lead to accelerated damage of track components and rolling stock (Esveld, 2001, 2003; Steenbergen et al., 2007).

In this Section, the performance of slab tracks passing over regions with structural discontinuities is analyzed. For this, a model representing the structure of a slab track passing over an abrupt change of foundation stiffness is presented. The solution is obtained with analytical methods. As discussed in Chapter 3, solutions based on analytical methods representing transition zones of railways are scarce. This family of models add reliable and understandable results, besides its usefulness to verify discretized numerical models, e.g. based on the FEM.

7.5.1 Mathematical model

The model is composed of two Euler-Bernoulli beams, linked by visco-elastic elements, and supported by a visco-elastic foundation, representing the soil, as depicted in Figure 7.9.

The upper beam represents the rail and the lower one represents the concrete slab. The inter-connection visco-elastic elements represent either railpads, in case of rails supported on sleepers, or fill material, in case of rails embedded in the concrete slab. The model is fully linear. The stiffness of the (upper and lower) visco-elastic elements may change abruptly at section $x = 0$. The load consists of a uniformly moving constant force, which (generally) represents the weight of the vehicle load.

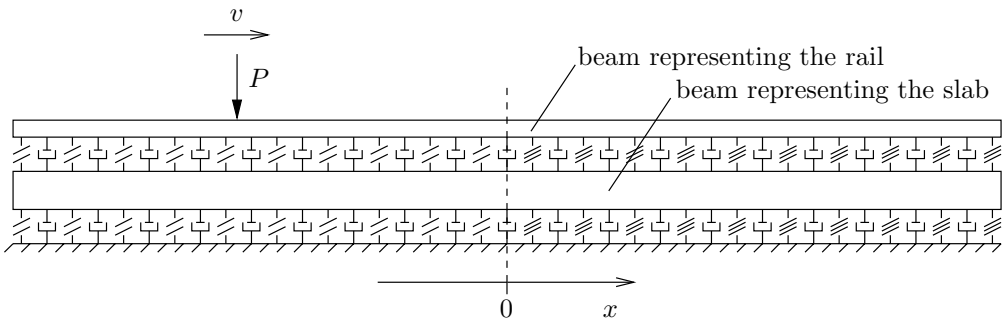

Figure 7.9: Model of double beam laid on inhomogeneous visco-elastic foundation

Response of the homogeneous foundation

Before presenting the solution for the inhomogeneous case, the response of the homogeneous case, as represented in Figure 7.10, is given here.

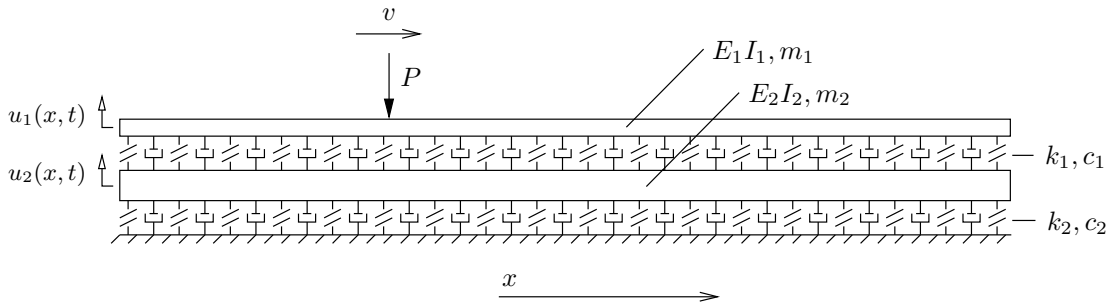

Figure 7.10: Model of double beam laid on homogeneous visco-elastic foundation

The equations of dynamic equilibrium for the vertical forced vibrations of the beams can

be written as (Shamalta and Metrikine, 2003):

$$\begin{aligned}
&\beta_1 \frac{\partial^4 u_1}{\partial x^4} + m_1 \frac{\partial^2 u_1}{\partial t^2} + k_1 (u_1 - u_2) + c_1 \left(\frac{\partial u_1}{\partial t} - \frac{\partial u_2}{\partial t} \right) = -P\delta (x - vt), \\
&\beta_2 \frac{\partial^4 u_2}{\partial x^4} + m_2 \frac{\partial^2 u_2}{\partial t^2} + k_1 (u_2 - u_1) + c_1 \left(\frac{\partial u_2}{\partial t} - \frac{\partial u_1}{\partial t} \right) + k_2 u_2 + c_2 \frac{\partial u_2}{\partial t} = 0,
\end{aligned} \tag{7.5}$$

with the radiation conditions expressed as:

$$\begin{aligned}
&\lim_{|x| \to \infty} \{|u_1|, |u_2|\} < \infty, \text{for } |t| \neq \infty, \\
&\lim_{(x - vt) \to -\infty} \{|u_1|, |u_2|\} < \infty, \text{for } t \to -\infty, \text{ and} \\
&\lim_{(x - vt) \to +\infty} \{|u_1|, |u_2|\} < \infty, \text{for } t \to +\infty.
\end{aligned} \tag{7.6}$$

In these equations the subscripts 1 and 2 refer to the upper and lower beam respectively. $u_i(x,t)$ is the vertical displacement of the beam i, as represented in Figure 7.10, β_i and m_i are, respectively, the flexural stiffness (EI) and the mass per unit length of the corresponding beams, k_i and c_i are, respectively, the stiffness and damping constants of the upper and lower visco-elastic elements per unit length, P is the constant value of the load, v is the velocity of the load and $\delta(...)$ is the Dirac delta function.

The solution of Equations (7.5) and (7.6) is here derived following the same method presented in (Shamalta and Metrikine, 2003). First, the Fourier transform with respect to time t is applied, and the initial system of partial differential Equations (7.5) is transformed into a system of ordinary differential equations. Then, the analytical solution of the transformed equations, with respect to frequency ω, is determined, and the inverse of the Fourier transform is applied. Finnaly, the closed-form solution is obtained using Jordan's lemma and the Residue theorem (Jeffrey and Dai, 2008).

The Fourier transform pair, with respect to time t, is written as:

$$\overline{u}(x, \omega) = \int_{-\infty}^{+\infty} u(x,t) \cdot e^{i\omega t} \, \mathrm{d}t, \tag{7.7}$$

$$u(x,t) = \frac{1}{2\pi} \int_{-\infty}^{+\infty} \overline{u}(x, \omega) \cdot e^{-i\omega t} \, \mathrm{d}\omega, \tag{7.8}$$

where the variable of integration ω represents frequency. Applying transformation (7.7)

to Equations (7.5), yields:

$$\begin{aligned}
&\beta_1 \frac{\partial^4 \overline{u}_1}{\partial x^4} - m_1\omega^2\overline{u}_1 + k_1\left(\overline{u}_1 - \overline{u}_2\right) + i\omega c_1\left(\overline{u}_1 - \overline{u}_2\right) = -\frac{P}{v}\exp(\frac{i\omega x}{v}),\\
&\beta_2 \frac{\partial^4 \overline{u}_2}{\partial x^4} - m_2\omega^2\overline{u}_2 + k_1\left(\overline{u}_2 - \overline{u}_1\right) + i\omega c_1\left(\overline{u}_2 - \overline{u}_1\right) + k_2\overline{u}_2 + i\omega c_2\overline{u}_2 = 0,
\end{aligned} \tag{7.9}$$

or by rearranging terms,

$$\begin{aligned}
&\beta_1 \frac{\partial^4 \overline{u}_1}{\partial x^4} + \left(k_1 - m_1\omega^2 + i\omega c_1\right)\overline{u}_1 + \left(-i\omega c_1 - k_1\right)\overline{u}_2 = -\frac{P}{v}\exp(\frac{i\omega x}{v}),\\
&\beta_2 \frac{\partial^4 \overline{u}_1}{\partial x^4} + \left(k_1 + k_2 - m_2\omega^2 + i\omega(c_1 + c_2)\right)\overline{u}_2 + \left(-i\omega c_1 - k_1\right)\overline{u}_1 = 0.
\end{aligned} \tag{7.10}$$

The solutions for $\overline{u}_1$ and $\overline{u}_2$ can be sought in the form:

$$\begin{bmatrix}\overline{u}_1(x,\omega)\\ \overline{u}_2(x,\omega)\end{bmatrix} = \begin{bmatrix}A_1^{st}(\omega)\\ A_2^{st}(\omega)\end{bmatrix}\exp\left(\frac{i\omega x}{v}\right). \tag{7.11}$$

where $A_i^{st}(\omega)$ are functions of complex numbers that define the steady-state solution in the frequency domain.

Substitution of Eq. (7.11) into Eq. (7.10) gives

$$\begin{bmatrix}h_1(\omega) & \eta(\omega)\\ \eta(\omega) & h_2(\omega)\end{bmatrix}\begin{bmatrix}A_1^{st}(\omega)\\ A_2^{st}(\omega)\end{bmatrix} = \begin{bmatrix}-\frac{P}{v}\\ 0\end{bmatrix}, \tag{7.12}$$

where

$$\begin{aligned}
h_1(\omega) &= \beta_1\frac{\omega^4}{v^4} + k_1 - m_1\omega^2 + i\omega c_1\\
h_2(\omega) &= \beta_2\frac{\omega^4}{v^4} + k_1 + k_2 - m_2\omega^2 + i\omega(c_1 + c_2)\\
\eta(\omega) &= -i\omega c_1 - k_1.
\end{aligned} \tag{7.13}$$

which when solved in terms of A_1^{st} and A_2^{st} results in

$$\begin{aligned}
A_1^{st}(\omega) &= -\frac{h_2(\omega)}{Q(\omega)}\cdot\frac{P}{v},\\
A_2^{st}(\omega) &= \frac{\eta(\omega)}{Q(\omega)}\cdot\frac{P}{v},
\end{aligned} \tag{7.14}$$

where

$$Q(\omega) = \left(\beta_1 \frac{\omega^4}{v^4} + k_1 - m_1\omega^2 + i\omega c_1\right)\left(\beta_2 \frac{\omega^4}{v^4} + k_1 + k_2 - m_2\omega^2 + i\omega(c_1 + c_2)\right) - (-i\omega c_1 - k_1)^2 \,. \tag{7.15}$$

The solution to the Equations (7.5) and (7.6) is thus obtained by applying the inverse Fourier transform, expressed in Eq. (7.8), which gives:

$$\begin{aligned} u_1(x,t) &= \frac{1}{2\pi}\frac{P}{v}\int_{-\infty}^{+\infty} \frac{-h_2(\omega)}{Q(\omega)} \cdot \exp\left(i\omega\left(\frac{x}{v} - t\right)\right) \mathrm{d}\omega, \\ u_2(x,t) &= \frac{1}{2\pi}\frac{P}{v}\int_{-\infty}^{+\infty} \frac{\eta(\omega)}{Q(\omega)} \cdot \exp\left(i\omega\left(\frac{x}{v} - t\right)\right) \mathrm{d}\omega. \end{aligned} \tag{7.16}$$

These integrals can be evaluated using Jordan's lemma and the Residue theorem (Jeffrey and Dai, 2008), which uses contour integration in the complex plane to state that having $g(x) = f(x) \cdot e^{iax}$ then

$$\int_{-\infty}^{+\infty} g(x)\,\mathrm{d}x = \begin{cases} 2\pi i \sum\limits_k \mathrm{Res}\left(g(x), z_k\right), & \text{if } a > 0 \\ -2\pi i \sum\limits_m \mathrm{Res}\left(g(x), z_m\right), & \text{if } a < 0 \end{cases} \tag{7.17}$$

where $\mathrm{Res}\left(g(x), z_k\right)$ denotes the residues of $g(x)$ at z_k, being z_k poles with positive imaginary part and $\mathrm{Res}\left(g(x), z_m\right)$ the residues of $g(x)$ at z_m, being z_m poles with negative imaginary part.

The poles of the integrands in Eqs. (7.16) are the roots of the denominator $Q(\omega)$, expressed in Eq. (7.15). Since this function is a polynomial of order eight with respect to the angular frequency ω, the roots of $Q(\omega)$ can be found using standard programs for finding roots of polynomials. Defining the poles that have a positive imaginary part as ω_n and those with negative imaginary part as ω_m, then application of the Jordan's lemma and the Residue

theorem to Eqs. (7.16) results in:

$$\begin{aligned}
u_1(x,t) &= +i\sum_n A_n \cdot \exp\left(i\omega_n\left(\tfrac{x}{v}-t\right)\right), \text{ for } x > vt \\
u_1(x,t) &= -i\sum_m A_m \cdot \exp\left(i\omega_m\left(\tfrac{x}{v}-t\right)\right), \text{ for } x < vt \\
u_2(x,t) &= +i\sum_n B_n \cdot \exp\left(i\omega_n\left(\tfrac{x}{v}-t\right)\right), \text{ for } x > vt \\
u_2(x,t) &= -i\sum_m B_m \cdot \exp\left(i\omega_m\left(\tfrac{x}{v}-t\right)\right), \text{ for } x < vt
\end{aligned} \tag{7.18}$$

where A_n, A_m, B_n, B_m are complex numbers determined by:

$$\begin{aligned}
A_n &= \frac{P}{v}\frac{h_2(\omega_n)}{\partial Q(\omega_n)/\partial\omega}, \qquad A_m = \frac{P}{v}\frac{h_2(\omega_m)}{\partial Q(\omega_m)/\partial\omega}, \\
B_n &= \frac{P}{v}\frac{-\eta(\omega_n)}{\partial Q(\omega_n)/\partial\omega}, \qquad B_m = \frac{P}{v}\frac{-\eta(\omega_m)}{\partial Q(\omega_m)/\partial\omega}.
\end{aligned} \tag{7.19}$$

Response of the inhomogeneous foundation

The response of the inhomogeneous model shown in Figure 7.9 is derived here. Figure 7.11 shows the parameters of the model. The left part of the model has visco-elastic elements with stiffness k_{11} and k_{21} for the upper and lower layers, respectively, which change to k_{12} and k_{22}, respectively, on the right part of the model. The vertical displacement field is defined by four functions $u_{ij}(x,t)$, as also identified in the Figure. It is assumed that the damping constant of the upper and lower visco-elastic elements does not change from left to right. It is also assumed that the force travels from left to right ($v > 0$), coming from "far away" before the discontinuity of the track.

The equations of dynamic equilibrium for the vertical forced vibrations of the beams, assuming that the moving force is on the left part of the model before reaching the discontinuity, is (for $x < 0$):

$$\begin{cases}
\beta_1\dfrac{\partial^4 u_{11}}{\partial x^4} + m_1\dfrac{\partial^2 u_{11}}{\partial t^2} + k_{11}\left(u_{11}-u_{21}\right) + c_1\left(\dfrac{\partial u_{11}}{\partial t} - \dfrac{\partial u_{21}}{\partial t}\right) = -P\delta\left(x-vt\right) \\
\beta_2\dfrac{\partial^4 u_{21}}{\partial x^4} + m_2\dfrac{\partial^2 u_{21}}{\partial t^2} + k_{11}\left(u_{21}-u_{11}\right) + c_1\left(\dfrac{\partial u_{21}}{\partial t} - \dfrac{\partial u_{11}}{\partial t}\right) + k_{21}u_{21} + c_2\dfrac{\partial u_{21}}{\partial t} = 0,
\end{cases} \tag{7.20}$$

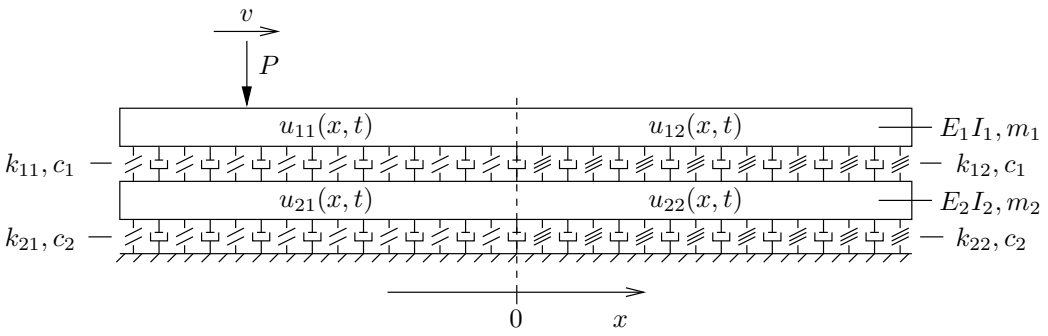

Figure 7.11: Parameters of the inhomogeneous model

and (for $x > 0$):

$$\begin{cases} \beta_1 \dfrac{\partial^4 u_{12}}{\partial x^4} + m_1 \dfrac{\partial^2 u_{12}}{\partial t^2} + k_{12}\left(u_{12} - u_{22}\right) + c_1 \left(\dfrac{\partial u_{12}}{\partial t} - \dfrac{\partial u_{22}}{\partial t} \right) = 0 \\ \\ \beta_2 \dfrac{\partial^4 u_{22}}{\partial x^4} + m_2 \dfrac{\partial^2 u_{22}}{\partial t^2} + k_{12}\left(u_{22} - u_{12}\right) + c_1 \left(\dfrac{\partial u_{22}}{\partial t} - \dfrac{\partial u_{12}}{\partial t} \right) + k_{22} u_{22} + c_2 \dfrac{\partial u_{22}}{\partial t} = 0, \end{cases} \tag{7.21}$$

where β_i denotes again the flexural stiffness (EI) of beam i. The radiation conditions are:

$$\begin{aligned} &\lim_{|x|\to\infty} \{|u_{11}|, |u_{12}|, |u_{21}|, |u_{22}|\} < \infty, \text{for } t \neq \infty, \\ &\lim_{(x-vt)\to-\infty} \{|u_{11}|, |u_{12}|, |u_{21}|, |u_{22}|\} < \infty, \text{for } t \to -\infty \text{ and} \\ &\lim_{(x-vt)\to+\infty} \{|u_{11}|, |u_{12}|, |u_{21}|, |u_{22}|\} < \infty, \text{for } t \to +\infty. \end{aligned} \tag{7.22}$$

and the interface conditions at $x = 0$ and $t \neq 0$ are:

$$\begin{aligned} &u_{11}\left(0,t\right) = u_{12}\left(0,t\right), && u_{21}\left(0,t\right) = u_{22}\left(0,t\right), \\ &u_{11,x}\left(0,t\right) = u_{12,x}\left(0,t\right), && u_{21,x}\left(0,t\right) = u_{22,x}\left(0,t\right), \\ &u_{11,xx}\left(0,t\right) = u_{12,xx}\left(0,t\right), && u_{21,xx}\left(0,t\right) = u_{22,xx}\left(0,t\right), \\ &u_{11,xxx}\left(0,t\right) = u_{12,xxx}\left(0,t\right), && u_{21,xxx}\left(0,t\right) = u_{22,xxx}\left(0,t\right). \end{aligned} \tag{7.23}$$

In Equations (7.23), the notation for derivative has changed from the traditional Leibniz's notation used above to a more compact form, where $f_{,x}$ denotes the derivative of function f with respect to x and $f_{,tt}$ denotes the second derivative of function f with respect to t, as examples.

The solution of Equations (7.20) to (7.23) is obtained following the method used by (van

Dalen, 2006), who has solved the problem of a single beam laid on an elastic foundation (no damping) subjected to a moving force.

Response for $t < 0$

When the load is far enough left from the transition, the displacement field is undisturbed by the existence of this transition, moving along stationary with the load. It is in fact the steady-state solution derived in the previous section. When the load approaches the transition, a transient response is added to this steady-state response, until the load reaches the section $x = 0$ at $t = 0$. The total displacement field on the left part of the model can then be separated in the steady-state response and the transient response, whereas on the right part the displacement field is given solely by the transient response:

$$\begin{aligned} u_{11}(x,t) &= u_{11}^{st}(x,t) + w_{11}(x,t) \\ u_{21}(x,t) &= u_{21}^{st}(x,t) + w_{21}(x,t) \\ u_{12}(x,t) &= w_{12}(x,t) \\ u_{22}(x,t) &= w_{22}(x,t) \end{aligned} \tag{7.24}$$

where $u_{11}^{st}(x,t)$ and $u_{21}^{st}(x,t)$ is the steady-state response and $w_{ij}(x,t)$ is the transient response. Since the steady-state solution is known (given in the previous section) the problem expressed in Equations (7.20) to (7.23) can be rewritten as:

$$\begin{cases} \beta_1 w_{11,xxxx} + m_1 w_{11,tt} + k_{11}\left(w_{11} - w_{21}\right) + c_1\left(w_{11,t} - w_{21,t}\right) = 0 \\ \\ \beta_2 w_{21,xxxx} + m_2 w_{21,tt} + k_{11}\left(w_{21} - w_{11}\right) + c_1\left(w_{21,t} - w_{11,t}\right) + k_{21} w_{21} + c_2 w_{21,t} = 0, \end{cases} \tag{7.25}$$

for $x < 0$, and:

$$\begin{cases} \beta_1 w_{12,xxxx} + m_1 w_{12,tt} + k_{12}\left(w_{12} - w_{22}\right) + c_1\left(w_{12,t} - w_{22,t}\right) = 0 \\ \\ \beta_2 w_{22,xxxx} + m_2 w_{22,tt} + k_{12}\left(w_{22} - w_{12}\right) + c_1\left(w_{22,t} - w_{12,t}\right) + k_{22} w_{22} + c_2 w_{22,t} = 0, \end{cases} \tag{7.26}$$

for $x > 0$. The radiation conditions are now:

$$\lim_{|x|\to\infty} \{w_{11}, w_{12}, w_{21}, w_{22}\} = 0, \tag{7.27}$$

and the interface conditions at $x = 0$ are:

$$\begin{aligned}
&[w_{12} - w_{11}]_{x=0} = i \sum A_n \exp(-i\omega_n t),\\
&[w_{21} - w_{22}]_{x=0} = i \sum B_n \exp(-i\omega_n t),\\
&\\
&[w_{12,x} - w_{11,x}]_{x=0} = -1/v \sum A_n \exp(-i\omega_n t),\\
&[w_{21,x} - w_{22,x}]_{x=0} = -1/v \sum B_n \exp(-i\omega_n t),\\
&\\
&[w_{12,xx} - w_{11,xx}]_{x=0} = -i/v^2 \sum A_n \exp(-i\omega_n t),\\
&[w_{21,xx} - w_{22,xx}]_{x=0} = -i/v^2 \sum B_n \exp(-i\omega_n t),\\
&\\
&[w_{12,xxx} - w_{11,xxx}]_{x=0} = 1/v^3 \sum A_n \exp(-i\omega_n t),\\
&[w_{21,xxx} - w_{22,xxx}]_{x=0} = 1/v^3 \sum B_n \exp(-i\omega_n t).
\end{aligned} \tag{7.28}$$

where A_n and B_n were given in Equations (7.19), and $[\ ]_{x=0}$ denotes the function (inside brackets) evaluated at $x = 0$.

The problem is now written in terms of homogeneous partial differential equations with homogeneous boundary conditions. Using separation of variables, the solution can be sought in the form:

$$\begin{aligned}
&w_{11}(x,t) = \sum_n W_{11n}(x) \cdot \exp(-i\omega_n t), \quad w_{12}(x,t) = \sum_n W_{12n}(x) \cdot \exp(-i\omega_n t),\\
&w_{21}(x,t) = \sum_n W_{21n}(x) \cdot \exp(-i\omega_n t), \quad w_{22}(x,t) = \sum_n W_{22n}(x) \cdot \exp(-i\omega_n t).
\end{aligned} \tag{7.29}$$

Substitution in Equations (7.25) and (7.26), gives after some rearrangements:

$$\begin{aligned}
&(\text{for } x < 0) \quad \begin{bmatrix} W_{11n,xxxx} \\ W_{21n,xxxx} \end{bmatrix} + \begin{bmatrix} h_{11n} & \eta_{11n} \\ \eta_{21n} & h_{21n} \end{bmatrix} \begin{bmatrix} W_{11n} \\ W_{21n} \end{bmatrix} = \begin{bmatrix} 0 \\ 0 \end{bmatrix},\\
&(\text{for } x > 0) \quad \begin{bmatrix} W_{12n,xxxx} \\ W_{22n,xxxx} \end{bmatrix} + \begin{bmatrix} h_{12n} & \eta_{12n} \\ \eta_{22n} & h_{22n} \end{bmatrix} \begin{bmatrix} W_{12n} \\ W_{22n} \end{bmatrix} = \begin{bmatrix} 0 \\ 0 \end{bmatrix},
\end{aligned} \tag{7.30}$$

being:

$$\begin{aligned}
h_{11n} &= \left(k_{11} - m_1\omega_n^2 - i\omega_n c_1\right)/\beta_1,\\
h_{21n} &= \left(k_{11} + k_{21} - m_2\omega_n^2 - i\omega_n(c_1 + c_2)\right)/\beta_2,\\
h_{12n} &= \left(k_{12} - m_1\omega_n^2 - i\omega_n c_1\right)/\beta_1,\\
h_{22n} &= \left(k_{12} + k_{22} - m_2\omega_n^2 - i\omega_n(c_1 + c_2)\right)/\beta_2,
\end{aligned} \tag{7.31}$$

and

$$\begin{aligned} \eta_{11n} &= (i\omega_n c_1 - k_{11})/\beta_1, \quad \eta_{21n} = (i\omega_n c_1 - k_{11})/\beta_2, \\ \eta_{12n} &= (i\omega_n c_1 - k_{12})/\beta_1, \quad \eta_{22n} = (i\omega_n c_1 - k_{12})/\beta_2. \end{aligned} \tag{7.32}$$

The solution of a system of homogeneous ordinary differential equations of order four, as those expressed in Eqs. (7.30), are found with the eigenvalues and the eigenvectors of the $[2 \times 2]$ central matrices in Eqs. (7.30). Deriving for the first system in (7.30):

$$\begin{bmatrix} h_{11n} & \eta_{11n} \\ \eta_{21n} & h_{21n} \end{bmatrix} \longrightarrow \underbrace{\begin{bmatrix} \Lambda_{11n} & \\ & \Lambda_{21n} \end{bmatrix}}_{\text{eigenvalues}} \text{ and } \underbrace{\begin{bmatrix} 1 & 1 \\ \phi_{11n} & \phi_{21n} \end{bmatrix}}_{\text{eigenvectors}}, \tag{7.33}$$

the general solution reads:

$$\begin{cases} W_{11n} = \sum_k C_k \exp(\lambda_{Ck} x) + D_k \exp(\lambda_{Dk} x) \\ W_{21n} = \sum_k C_k \phi_{11n} \exp(\lambda_{Ck} x) + D_k \phi_{21n} \exp(\lambda_{Dk} x) \end{cases} \tag{7.34}$$

where λ_{Ck} and λ_{Dk} are determined from Λ_{11n} and Λ_{21n} according to:

$$\begin{cases} \lambda_{C1} = \sqrt[4]{-\Lambda_{11n}} \\ \lambda_{C2} = -\sqrt[4]{-\Lambda_{11n}} \\ \lambda_{C3} = i\sqrt[4]{-\Lambda_{11n}} \\ \lambda_{C4} = -i\sqrt[4]{-\Lambda_{11n}} \end{cases} \qquad \begin{cases} \lambda_{D1} = \sqrt[4]{-\Lambda_{21n}} \\ \lambda_{D2} = -\sqrt[4]{-\Lambda_{21n}} \\ \lambda_{D3} = i\sqrt[4]{-\Lambda_{21n}} \\ \lambda_{D4} = -i\sqrt[4]{-\Lambda_{21n}} \end{cases}$$

As the functions W_{11n} and W_{21n} relate to the left part of the model (where $x < 0$), the radiation conditions expressed in Eq. (7.27) force the selection of those roots from λ_{Ck} and λ_{Dk} with positive real part, so that the solution vanishes for $x \to -\infty$. As these roots are given as pairs of complex conjugates, the solution for W_{11n} and W_{21n} has four components each, written as:

$$\begin{cases} W_{11n} = C_{11n} \exp(r_{C11n} x) + D_{11n} \exp(r_{D11n} x) + \\ \qquad + C_{21n} \exp(r_{C21n} x) + D_{21n} \exp(r_{D21n} x), \\ W_{21n} = C_{11n}\phi_{11n} \exp(r_{C11n} x) + D_{11n}\phi_{11n} \exp(r_{D11n} x) + \\ \qquad + C_{21n}\phi_{21n} \exp(r_{C21n} x) + D_{21n}\phi_{21n} \exp(r_{D21n} x), \end{cases} \tag{7.35}$$

where r_{C11n}, r_{C21n}, r_{D11n} and r_{D21n} are the values of λ_{Ck} and λ_{Dk} with positive real part.

The general solution for the second system in (7.30) is derived following the same proce-

dure, giving:

$$\begin{cases} W_{12n} &= C_{12n}\exp(r_{C12n}x) + D_{12n}\exp(r_{D12n}x) + \\ & \quad + C_{22n}\exp(r_{C22n}x) + D_{22n}\exp(r_{D22n}x), \\ W_{22n} &= C_{12n}\phi_{12n}\exp(r_{C12n}x) + D_{12n}\phi_{12n}\exp(r_{D12n}x) + \\ & \quad + C_{22n}\phi_{22n}\exp(r_{C22n}x) + D_{22n}\phi_{22n}\exp(r_{D22n}x). \end{cases} \tag{7.36}$$

As the functions W_{12n} and W_{22n} now relate to the right part of the model (where $x > 0$), the values selected for r_{C12n}, r_{C22n}, r_{D12n} and r_{D22n} now have negative real part, in order to vanish when $x \to +\infty$.

The eight unknowns left in Equations (7.35) and (7.36), the coefficients C_{ijn} and D_{ijn}, are determined from the interface conditions expressed in (7.28). Replacing Eq. (7.29) in Eq. (7.28) the interface conditions are condensed to:

$$\begin{cases} [W_{12n} - W_{11n}]_{x=0} = iA_n, \\ [W_{12n,x} - W_{11n,x}]_{x=0} = -\omega_n/vA_n, \\ [W_{12n,xx} - W_{11n,xx}]_{x=0} = -i\omega_n^2/v^2A_n, \\ [W_{12n,xxx} - W_{11n,xxx}]_{x=0} = \omega_n^3/v^3A_n, \end{cases} \quad \begin{cases} [W_{21n} - W_{22n}]_{x=0} = iB_n, \\ [W_{21n,x} - W_{22n,x}]_{x=0} = -\omega_n/vB_n, \\ [W_{21n,xx} - W_{22n,xx}]_{x=0} = -i\omega_n^2/v^2B_n, \\ [W_{21n,xxx} - W_{22n,xxx}]_{x=0} = \omega_n^3/v^3B_n, \end{cases} \tag{7.37}$$

Substitution of the solutions given for W_{11n}, W_{21n}, W_{12n} and W_{22n} in Eqs. (7.35) and (7.36) into Eqs. (7.37) results in a linear system of eight equations, which written in matrix form reads:

$$\mathbf{M}_n \cdot \begin{bmatrix} C_{12n} \\ D_{12n} \\ C_{22n} \\ D_{22n} \\ C_{11n} \\ D_{11n} \\ C_{21n} \\ D_{21n} \end{bmatrix} = \begin{bmatrix} iA_n \\ -\omega_n/vA_n \\ -i\omega_n^2/v^2A_n \\ \omega_n^3/v^3A_n \\ iB_n \\ -\omega_n/vB_n \\ -i\omega_n^2/v^2B_n \\ \omega_n^3/v^3B_n \end{bmatrix}, \tag{7.38}$$

where:

$$\mathbf{M}_n^{\mathrm{T}} = \begin{bmatrix} 1 & r_{C12n} & r_{C12n}^2 & r_{C12n}^3 & \phi_{12n} & \phi_{12n}r_{C12n} & \phi_{12n}r_{C12n}^2 & \phi_{12n}r_{C12n}^3 \\ 1 & r_{D12n} & r_{D12n}^2 & r_{D12n}^3 & \phi_{12n} & \phi_{12n}r_{D12n} & \phi_{12n}r_{D12n}^2 & \phi_{12n}r_{D12n}^3 \\ 1 & r_{C22n} & r_{C22n}^2 & r_{C22n}^3 & \phi_{22n} & \phi_{22n}r_{C22n} & \phi_{22n}r_{C22n}^2 & \phi_{22n}r_{C22n}^3 \\ 1 & r_{D22n} & r_{D22n}^2 & r_{D22n}^3 & \phi_{22n} & \phi_{22n}r_{D22n} & \phi_{22n}r_{D22n}^2 & \phi_{22n}r_{D22n}^3 \\ -1 & -r_{C11n} & -r_{C11n}^2 & -r_{C11n}^3 & -\phi_{11n} & -\phi_{11n}r_{C11n} & -\phi_{11n}r_{C11n}^2 & -\phi_{11n}r_{C11n}^3 \\ -1 & -r_{D11n} & -r_{D11n}^2 & -r_{D11n}^3 & -\phi_{11n} & -\phi_{11n}r_{D11n} & -\phi_{11n}r_{D11n}^2 & -\phi_{11n}r_{D11n}^3 \\ -1 & -r_{C21n} & -r_{C21n}^2 & -r_{C21n}^3 & -\phi_{21n} & -\phi_{21n}r_{C21n} & -\phi_{21n}r_{C21n}^2 & -\phi_{21n}r_{C21n}^3 \\ -1 & -r_{D21n} & -r_{D21n}^2 & -r_{D21n}^3 & -\phi_{21n} & -\phi_{21n}r_{D21n} & -\phi_{21n}r_{D21n}^2 & -\phi_{21n}r_{D21n}^3 \end{bmatrix},$$

from which the coefficients C_{ijn} and D_{ijn} may be determined.

With Equations (7.29), (7.35), (7.36), (7.38) and the steady-state solution given in the previous Section, the total reponse (7.24) for $t < 0$ is known analytically.

Response for $t > 0$

The displacement field $u_{ij}(x,t)$ is now sought for $t > 0$, thus after the passage of the load at the transition section. The initial conditions at $t = 0$ are known analytically, from the response obtained above for $t < 0$, as:

$$\begin{aligned} u_{11}(x,0) &= \sum_m -iA_m \exp\left(\tfrac{i\omega_m x}{v}\right) + \sum_n W_{11n}(x), \\ u_{21}(x,0) &= \sum_m -iB_m \exp\left(\tfrac{i\omega_m x}{v}\right) + \sum_n W_{21n}(x), \\ u_{11,t}(x,0) &= \sum_m -A_m\omega_m \exp\left(\tfrac{i\omega_m x}{v}\right) + \sum_n -i\omega_n W_{11n}(x), \\ u_{21,t}(x,0) &= \sum_m -B_m\omega_m \exp\left(\tfrac{i\omega_m x}{v}\right) + \sum_n -i\omega_n W_{21n}(x), \end{aligned} \tag{7.39}$$

for the left part of the model, and as:

$$\begin{aligned} u_{12}(x,0) &= \sum_n W_{12n}(x), & u_{22}(x,0) &= \sum_n W_{22n}(x), \\ u_{12,t}(x,0) &= \sum_n -i\omega_n W_{12n}(x), & u_{22,t}(x,0) &= \sum_n -i\omega_n W_{22n}(x), \end{aligned} \tag{7.40}$$

for the right part of the model. The equations of dynamic equilibrium for the vertical forced vibrations are:

$$\begin{cases} \beta_1 u_{11,xxxx} + m_1 u_{11,tt} + k_{11}\left(u_{11} - u_{21}\right) + c_1\left(u_{11,t} - u_{21,t}\right) = 0 \\ \\ \beta_2 u_{21,xxxx} + m_2 u_{21,tt} + k_{11}\left(u_{21} - u_{11}\right) + c_1\left(u_{21,t} - u_{11,t}\right) + k_{21}u_{21} + c_2 u_{21,t} = 0, \end{cases} \tag{7.41}$$

for $x < 0$, and:

$$\begin{cases} \beta_1 u_{12,xxxx} + m_1 u_{12,tt} + k_{12}\,(u_{12} - u_{22}) + c_1\,(u_{12,t} - u_{22,t}) = -P\delta\,(x - vt) \\ \\ \beta_2 u_{22,xxxx} + m_2 u_{22,tt} + k_{12}\,(u_{22} - u_{12}) + c_1\,(u_{22,t} - u_{12,t}) + k_{22} u_{22} + c_2 u_{22,t} = 0, \end{cases} \tag{7.42}$$

for $x > 0$. The radiation conditions are:

$$\begin{gathered} \lim_{|x|\to\infty} \{|u_{11}|, |u_{12}|, |u_{21}|, |u_{22}|\} < \infty, \text{for } t \neq \infty \ \text{ and} \\ \\ \lim_{(x-vt)\to\infty} \{|u_{11}|, |u_{12}|, |u_{21}|, |u_{22}|\} < \infty, \text{for } t \to \infty, \end{gathered} \tag{7.43}$$

and the interface conditions at $x = 0$ are the same as in Eq. (7.23).

The Laplace transform is now chosen to reduce the problem to a system of ordinary differential equations with respect to x. The Laplace transform is preferable to solve problems with given initial conditions, as is the case. The Laplace transform pair is written as:

$$\overline{u}_{ij}(x, s) = \int_0^\infty u_{ij}(x, t) \exp(-st)\,\mathrm{d}t, \tag{7.44}$$

$$u_{ij}(x, t) = \frac{1}{2\pi i} \int_{\sigma-i\infty}^{\sigma+i\infty} \overline{u}_{ij}(x, s) \exp(st)\,\mathrm{d}s, \tag{7.45}$$

where the variable of integration s is now a complex number ($s \in \mathbb{C}$). Applying transform (7.44) to Eqs. (7.41) and (7.42) gives:

$$\begin{cases} \beta_1 \overline{u}_{11,xxxx} + \left(k_{11} + c_1\, s + m_1\, s^2\right) \overline{u}_{11} - (k_{11} + c_1\, s)\, \overline{u}_{21} = \\ \\ \qquad = (m_1\, s + c_1)\, u_{11}(x, 0) + m_1\, u_{11,t}(x, 0) - c_1\, u_{21}(x, 0), \\ \\ \beta_2 \overline{u}_{21,xxxx} + \left(k_{11} + k_{21} + (c_1 + c_2)\, s + m_2\, s^2\right) \overline{u}_{21} - (k_{11} + c_1\, s)\, \overline{u}_{11} = \\ \\ \qquad = (m_2\, s + c_1 + c_2)\, u_{21}(x, 0) + m_2\, u_{21,t}(x, 0) - c_1\, u_{11}(x, 0), \end{cases} \tag{7.46}$$

for $x < 0$, and:

$$\begin{cases} \beta_1 \overline{u}_{12,xxxx} + \left(k_{12} + c_1\, s + m_1\, s^2\right) \overline{u}_{12} - \left(k_{12} + c_1\, s\right) \overline{u}_{22} = \\ \qquad = \left(m_1\, s + c_1\right) u_{12}(x,0) + m_1\, u_{12,t}(x,0) - c_1\, u_{22}(x,0) - \frac{P}{v} \exp\left(-\frac{s\, x}{v}\right), \\ \beta_2 \overline{u}_{22,xxxx} + \left(k_{12} + k_{22} + \left(c_1 + c_2\right) s + m_2\, s^2\right) \overline{u}_{22} - \left(k_{12} + c_1\, s\right) \overline{u}_{12} = \\ \qquad = \left(m_2\, s + c_1 + c_2\right) u_{22}(x,0) + m_2\, u_{22,t}(x,0) - c_1\, u_{12}(x,0), \end{cases} \tag{7.47}$$

for $x > 0$. Now the initial conditions expressed in Eqs. (7.39) and (7.40) are substituted in Eqs. (7.46) and (7.47) to give:

$$\begin{cases} \overline{u}_{11,xxxx} + h_{11s}\, \overline{u}_{11} + \eta_{11s}\, \overline{u}_{21} = \sum_m E_{1m} \exp\left(\frac{i\omega_m x}{v}\right) + \sum_n \Big[F_{C11n} \exp(r_{C11n}\, x) + \\ \qquad + F_{D11n} \exp(r_{D11n}\, x) + F_{C21n} \exp(r_{C21n}\, x) + F_{D21n} \exp(r_{D21n}\, x) \Big], \\ \overline{u}_{21,xxxx} + h_{21s}\, \overline{u}_{21} + \eta_{21s}\, \overline{u}_{11} = \sum_m E_{2m} \exp\left(\frac{i\omega_m x}{v}\right) + \sum_n \Big[G_{C11n} \exp(r_{C11n}\, x) + \\ \qquad + G_{D11n} \exp(r_{D11n}\, x) + G_{C21n} \exp(r_{C21n}\, x) + G_{D21n} \exp(r_{D21n}\, x) \Big], \end{cases} \tag{7.48}$$

$$\begin{cases} \overline{u}_{12,xxxx} + h_{12s}\, \overline{u}_{12} + \eta_{12s}\, \overline{u}_{22} = \sum_n \Big[F_{C12n} \exp(r_{C12n}\, x) + F_{D12n} \exp(r_{D12n}\, x) + \\ \qquad + F_{C22n} \exp(r_{C22n}\, x) + F_{D22n} \exp(r_{D22n}\, x) \Big] - \frac{P}{\beta_1\, v} \exp\left(-\frac{s\, x}{v}\right), \\ \overline{u}_{22,xxxx} + h_{22s}\, \overline{u}_{22} + \eta_{22s}\, \overline{u}_{12} = \sum_n \Big[G_{C12n} \exp(r_{C12n}\, x) + G_{D12n} \exp(r_{D12n}\, x) + \\ \qquad + G_{C22n} \exp(r_{C22n}\, x) + G_{D22n} \exp(r_{D22n}\, x) \Big], \end{cases} \tag{7.49}$$

for $x < 0$ (7.48) and $x > 0$ (7.49), respectively.

In these equations:

$$
\begin{aligned}
h_{11s} &= \tfrac{1}{\beta_1}\left(k_{11} + c_1 s + m_1 s^2\right), \quad h_{21s} = \tfrac{1}{\beta_2}\left(k_{11} + k_{21} + (c_1 + c_2)s + m_2 s^2\right), \\
h_{12s} &= \tfrac{1}{\beta_1}\left(k_{12} + c_1 s + m_1 s^2\right), \quad h_{22s} = \tfrac{1}{\beta_2}\left(k_{12} + k_{22} + (c_1 + c_2)s + m_2 s^2\right), \\
\eta_{11s} &= -\tfrac{1}{\beta_1}\left(k_{11} + c_1 s\right), \qquad \eta_{21s} = -\tfrac{1}{\beta_2}\left(k_{11} + c_1 s\right), \\
\eta_{12s} &= -\tfrac{1}{\beta_1}\left(k_{12} + c_1 s\right), \qquad \eta_{22s} = -\tfrac{1}{\beta_2}\left(k_{12} + c_1 s\right),
\end{aligned}
\tag{7.50}
$$

$$
\begin{aligned}
E_{1m} &= \tfrac{1}{\beta_1}\left(ic_1 B_m - (im_1 s + ic_1 + \omega_m m_1) A_m\right), \\
E_{2m} &= \tfrac{1}{\beta_2}\left(ic_1 A_m - (im_2 s + i(c_1 + c_2) + \omega_m m_2) B_m\right),
\end{aligned}
\tag{7.51}
$$

$$
\begin{aligned}
F_{Cijn} &= \epsilon_{1ijn}\, C_{ijn}, \quad F_{Dijn} = \epsilon_{1ijn}\, D_{ijn}, \\
G_{Cijn} &= \epsilon_{2ijn}\, C_{ijn}, \quad G_{Dijn} = \epsilon_{2ijn}\, D_{ijn},
\end{aligned}
\tag{7.52}
$$

$$
\begin{aligned}
\epsilon_{1ijn} &= \tfrac{1}{\beta_1}\left((s - i\omega_n)\, m_1 + (1 - \phi_{ijn})\, c_1\right), \\
\epsilon_{2ijn} &= \tfrac{1}{\beta_2}\left((s - i\omega_n)\, \phi_{ijn}\, m_2 + (\phi_{ijn} - 1)\, c_1 + \phi_{ijn}\, c_2\right).
\end{aligned}
\tag{7.53}
$$

Equations (7.48) and (7.49) are two systems of coupled non-homogeneous ordinary differential equations of order four with respect to x. The solution results from the sum of the homogeneous solution, as already given in Eqs. (7.34), and the particular solution for each exponential function on the right-hand side of the equations. The particular solution of a general case expressed by:

$$
\begin{bmatrix} u_{1,xxxx} \\ u_{2,xxxx} \end{bmatrix} + \begin{bmatrix} h_1 & \eta_1 \\ \eta_2 & h_2 \end{bmatrix} \begin{bmatrix} u_1 \\ u_2 \end{bmatrix} = \begin{bmatrix} C_1 \\ C_2 \end{bmatrix} \exp(\omega x), \tag{7.54}
$$

is given by:

$$
\begin{bmatrix} u_1 \\ u_2 \end{bmatrix} = \begin{bmatrix} D_1 \\ D_2 \end{bmatrix} \exp(\omega x), \tag{7.55}
$$

with:

$$
D_1 = \frac{C_1\left(\omega^4 + h_2\right) - \eta_1 C_2}{\left(\omega^4 + h_1\right)\left(\omega^4 + h_2\right) - \eta_1 \eta_2}, \qquad D_2 = \frac{C_2\left(\omega^4 + h_1\right) - \eta_2 C_1}{\left(\omega^4 + h_1\right)\left(\omega^4 + h_2\right) - \eta_1 \eta_2}. \tag{7.56}
$$

The solution for $\overline{u}_{ij}(x, s)$ thus have the same exponential functions as those listed on the right-hand side of above Eqs. (7.48) and (7.49), and additional four exponential functions

from the homogeneous solution, again respecting the boundary conditions of evanescence at infinity. The solutions are written as:

$$\begin{cases} \overline{u}_{11}(x,s) = \sum_m E'_{1m} \exp\left(\frac{i\omega_m x}{v}\right) + \sum_n F'_{in} \exp(r_{in}\, x) + H_{11} \exp(r_{H11}\, x) + \\ \qquad + J_{11} \exp(r_{J11}\, x) + H_{21} \exp(r_{H21}\, x) + J_{21} \exp(r_{J21}\, x), \\ \overline{u}_{21}(x,s) = \sum_m E'_{2m} \exp\left(\frac{i\omega_m x}{v}\right) + \sum_n G'_{in} \exp(r_{in}\, x) + H_{11}\phi_{11} \exp(r_{H11}\, x) + \\ \qquad + J_{11}\phi_{11} \exp(r_{J11}\, x) + H_{21}\phi_{21} \exp(r_{H21}\, x) + J_{21}\phi_{21} \exp(r_{J21}\, x), \end{cases} \tag{7.57}$$

$$\begin{cases} \overline{u}_{12}(x,s) = \sum_n F'_{jn} \exp(r_{jn}\, x) + P'_1 \exp(-\frac{sx}{v}) + H_{12} \exp(r_{H12}\, x) + \\ \qquad + J_{12} \exp(r_{J12}\, x) + H_{22} \exp(r_{H22}\, x) + J_{22} \exp(r_{J22}\, x), \\ \overline{u}_{22}(x,s) = \sum_n G'_{jn} \exp(r_{jn}\, x) + P'_2 \exp(-\frac{sx}{v}) + H_{12}\phi_{12} \exp(r_{H12}\, x) + \\ \qquad + J_{12}\phi_{12} \exp(r_{J12}\, x) + H_{22}\phi_{22} \exp(r_{H22}\, x) + J_{22}\phi_{22} \exp(r_{J22}\, x), \end{cases} \tag{7.58}$$

where the coefficients H_{ij} and J_{ij} compose the homogeneous solution for Eqs. (7.48) and (7.49) and the terms E', P', F' and G' are the coefficients of the particular solutions for each exponential function in the right-hand side of Eqs. (7.48) and (7.49). These coefficients are determined according to (7.56).

The eight unknowns in Eqs. (7.57) and (7.58), the coefficients H_{ij} and J_{ij}, are determined from the interface conditions expressed in terms of the functions $\overline{u}_{ij}$:

$$\begin{array}{ll} \overline{u}_{11}(0,s) = \overline{u}_{12}(0,s), & \overline{u}_{21}(0,s) = \overline{u}_{22}(0,s), \\ \overline{u}_{11,x}(0,s) = \overline{u}_{12,x}(0,s), & \overline{u}_{21,x}(0,s) = \overline{u}_{22,x}(0,s), \\ \overline{u}_{11,xx}(0,s) = \overline{u}_{12,xx}(0,s), & \overline{u}_{21,xx}(0,s) = \overline{u}_{22,xx}(0,s), \\ \overline{u}_{11,xxx}(0,s) = \overline{u}_{12,xxx}(0,s), & \overline{u}_{21,xxx}(0,s) = \overline{u}_{22,xxx}(0,s). \end{array} \tag{7.59}$$

which leads to a new linear system of eight equations:

$$\mathbf{M} \cdot \begin{bmatrix} H_{11} \\ J_{11} \\ H_{21} \\ J_{21} \\ H_{12} \\ J_{12} \\ H_{22} \\ J_{22} \end{bmatrix} = \begin{bmatrix} Z_{11} \\ Z_{12} \\ Z_{13} \\ Z_{14} \\ Z_{21} \\ Z_{22} \\ Z_{23} \\ Z_{24} \end{bmatrix}, \tag{7.60}$$

where:

$$\mathbf{M}^{\mathrm{T}} = \begin{bmatrix} 1 & r_{H11} & r_{H11}^2 & r_{H11}^3 & \phi_{11} & \phi_{11} r_{H11} & \phi_{11} r_{H11}^2 & \phi_{11} r_{H11}^3 \\ 1 & r_{J11} & r_{J11}^2 & r_{J11}^3 & \phi_{11} & \phi_{11} r_{J11} & \phi_{11} r_{J11}^2 & \phi_{11} r_{J11}^3 \\ 1 & r_{H21} & r_{H21}^2 & r_{H21}^3 & \phi_{21} & \phi_{21} r_{H21} & \phi_{21} r_{H21}^2 & \phi_{21} r_{H21}^3 \\ 1 & r_{J21} & r_{J21}^2 & r_{J21}^3 & \phi_{21} & \phi_{21} r_{J21} & \phi_{21} r_{J21}^2 & \phi_{21} r_{J21}^3 \\ -1 & -r_{H12} & -r_{H12}^2 & -r_{H12}^3 & -\phi_{12} & -\phi_{12} r_{H12} & -\phi_{12} r_{H12}^2 & -\phi_{12} r_{H12}^3 \\ -1 & -r_{J12} & -r_{J12}^2 & -r_{J12}^3 & -\phi_{12} & -\phi_{12} r_{J12} & -\phi_{12} r_{J12}^2 & -\phi_{12} r_{J12}^3 \\ -1 & -r_{H22} & -r_{H22}^2 & -r_{H22}^3 & -\phi_{22} & -\phi_{22} r_{H22} & -\phi_{22} r_{H22}^2 & -\phi_{22} r_{H22}^3 \\ -1 & -r_{J22} & -r_{J22}^2 & -r_{J22}^3 & -\phi_{22} & -\phi_{22} r_{J22} & -\phi_{22} r_{J22}^2 & -\phi_{22} r_{J22}^3 \end{bmatrix},$$

and

$$
\begin{aligned}
Z_{11} &= \sum_n \sum_{j=1}^{2} \left[F'_{Cj2n} + F'_{Dj2n} - F'_{Cj1n} - F'_{Dj1n}\right] + P'_1 - \sum_m E'_{1m} \\
Z_{12} &= \sum_n \sum_{j=1}^{2} \left[r_{Cj2n}F'_{Cj2n} + r_{Dj2n}F'_{Dj2n} - r_{Cj1n}F'_{Cj1n} - r_{Dj1n}F'_{Dj1n}\right] - \\
&\quad - \tfrac{s}{v}P'_1 - \sum_m \tfrac{i\omega_m}{v}E'_{1m}, \\
Z_{13} &= \sum_n \sum_{j=1}^{2} \left[r^2_{Cj2n}F'_{Cj2n} + r^2_{Dj2n}F'_{Dj2n} - r^2_{Cj1n}F'_{Cj1n} - r^2_{Dj1n}F'_{Dj1n}\right] + \\
&\quad + \left(\tfrac{s}{v}\right)^2 P'_1 + \sum_m \left(\tfrac{\omega_m}{v}\right)^2 E'_{1m}, \\
Z_{14} &= \sum_n \sum_{j=1}^{2} \left[r^3_{Cj2n}F'_{Cj2n} + r^3_{Dj2n}F'_{Dj2n} - r^3_{Cj1n}F'_{Cj1n} - r^3_{Dj1n}F'_{Dj1n}\right] - \\
&\quad - \left(\tfrac{s}{v}\right)^3 P'_1 + \sum_m \left(\tfrac{i\omega_m}{v}\right)^3 E'_{1m}, \\
Z_{21} &= \sum_n \sum_{j=1}^{2} \left[G'_{Cj2n} + G'_{Dj2n} - G'_{Cj1n} - G'_{Dj1n}\right] + P'_2 - \sum_m E'_{2m} \\
Z_{22} &= \sum_n \sum_{j=1}^{2} \left[r_{Cj2n}G'_{Cj2n} + r_{Dj2n}G'_{Dj2n} - r_{Cj1n}G'_{Cj1n} - r_{Dj1n}G'_{Dj1n}\right] - \\
&\quad - \tfrac{s}{v}P'_2 - \sum_m \tfrac{i\omega_m}{v}E'_{2m}, \\
Z_{23} &= \sum_n \sum_{j=1}^{2} \left[r^2_{Cj2n}G'_{Cj2n} + r^2_{Dj2n}G'_{Dj2n} - r^2_{Cj1n}G'_{Cj1n} - r^2_{Dj1n}G'_{Dj1n}\right] + \\
&\quad + \left(\tfrac{s}{v}\right)^2 P'_2 + \sum_m \left(\tfrac{\omega_m}{v}\right)^2 E'_{2m}, \\
Z_{24} &= \sum_n \sum_{j=1}^{2} \left[r^3_{Cj2n}G'_{Cj2n} + r^3_{Dj2n}G'_{Dj2n} - r^3_{Cj1n}G'_{Cj1n} - r^3_{Dj1n}G'_{Dj1n}\right] - \\
&\quad - \left(\tfrac{s}{v}\right)^3 P'_2 + \sum_m \left(\tfrac{i\omega_m}{v}\right)^3 E'_{2m}.
\end{aligned}
$$

With Eqs. (7.57), (7.58) and (7.60) the response in the frequency domain is known. The response in the time domain is obtained applying the following inverse Laplace transforms:

$$
u_{11}(x,t) = \frac{1}{2\pi}\int_{\sigma-i\infty}^{\sigma+i\infty} \mathrm{Re}\left[\overline{u}_{11}\exp(st)\right]\,\mathrm{d}s, \quad u_{12}(x,t) = \frac{1}{2\pi}\int_{\sigma-i\infty}^{\sigma+i\infty} \mathrm{Re}\left[\overline{u}_{12}\exp(st)\right]\,\mathrm{d}s,
$$

$$
u_{21}(x,t) = \frac{1}{2\pi}\int_{\sigma-i\infty}^{\sigma+i\infty} \mathrm{Re}\left[\overline{u}_{21}\exp(st)\right]\,\mathrm{d}s, \quad u_{22}(x,t) = \frac{1}{2\pi}\int_{\sigma-i\infty}^{\sigma+i\infty} \mathrm{Re}\left[\overline{u}_{22}\exp(st)\right]\,\mathrm{d}s.
$$

These integrations are carried out numerically, taking only the real part of the integrands, as the result in terms of displacements must be real, with $s = \sigma + i\omega$, being σ a small

positive and real value (van Dalen, 2006).

Limitations of the model

This linear one-dimensional model has several limitations. First, the adoption of an elastic foundation composed of distributed springs, representing the soil reaction, gives approximate results only if the load is travelling significantly below the critical velocity of the track (Vostroukhov, 2002). The soil equivalent stiffness depends on the frequency and wavelength of the waves travelling in the beams (Dieterman and Metrikine, 1996), and this fact is not represented in the adopted model. This one-dimensional model also disregards the lateral flexibility of the slab. According to Shamalta and Metrikine (2003), this is aceptable as long as the analysis is restricted to train velocities below the critical value and to the low-frequency regime, as is the case. Finally, the representation of the train load with a moving constant force, does not considers the train-track interaction. This interaction may be significant due to the transient response caused by the abrupt change of the foundation stiffness.

7.5.2 Parametrization of the model

The slab track is here assumed to be made with a continuously reinforced concrete slab, with rails embedded in a fill material, as in Figure 7.8. The effective area of the concrete slab is assumed to be 2.5×0.55 m^2. As in the standard case model, the model of the slab track represents half railway track (one rail, half slab). The properties of the track components are given in Table 7.2.

Track component	Parameter	Value
Rail UIC54	Mass	54.7 kg/m
	Bending stiffness	4910 kNm^2
Slab	Dimensions	2.5×0.55 m^2
	Mass (half-slab)	1.75 t/m
	Bending stiffness	520 000 kNm^2
Soil	Linear stiffness of soft side (k_{21})	43 300 kN/m^2
	Linear stiffness of stiff side (k_{22})	166 700 kN/m^2
	Radiation damping ($c_2 \equiv c_{rd}$)	460 kNs/m^2

Table 7.2: Properties of the slab track

The values of the stiffness of the soil/foundation were derived from the standard case values, presented in Table 7.1, dividing those values by 0.6 (the sleepers spacing), in order to obtain the distributed equivalents. Therefore, the abrupt stiffness jump of 3.85 (in

terms of spring stiffness values) is maintained. The radiation damping constant (c_2) was determined based on the Lysmer model, presented in Eq. (4.10).

The fill material (embedding the rails) was assumed to be constant along the track, but three different stiffness values were considered. Table 7.3 shows the properties addmitted for the fill materials. The fill 1 is the equivalent to the railpad considered in the standard case model (very stiff railpad used in soft soil sites), the fill 2 is the equivalent to the soft railpad considered in Section 7.4, and the fill 3 is Corkelast (polyurethane mixed with cork), as defined in (Shamalta and Metrikine, 2003).

Track component	Parameter	Value
Fill 1	Linear stiffness ($k_{11} = k_{12}$)	833 000 kN/m^2
Fill 2	Linear stiffness ($k_{11} = k_{12}$)	108 000 kN/m^2
Fill 3	Linear stiffness ($k_{11} = k_{12}$)	52 500 kN/m^2
Fill 1-3	Linear viscous damping (c_1)	25.0 kNs/m^2

Table 7.3: Properties of the fill material

7.5.3 Numerical results

Figure 7.12 shows the displacements in the rail and in the slab, (again) considering a wheel load of 72 kN moving at 120 km/h, and the fill material 1, for three positions of the load. Comparing this figure with the standard case equivalent, Figure 7.2, it can be seen that the slab displacements are significantly smaller than the sleepers displacements in the ballasted track. Furthermore, the length of the steady-state eigenfield moving with the load is higher, resulting in smaller dynamic stresses in the sand bed layer, since the wheel force will be transmitted to the sand bed layer over a bigger area.

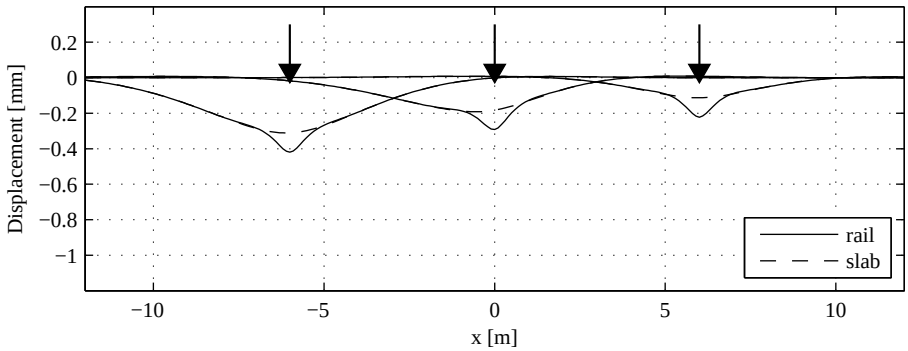

Figure 7.12: Rail and slab displacements in slab track model with fill material 1. Load of 72 kN moving at 120 km/h

Figure 7.13 presents the track modulus of the slab track transition with the fill material 1. It can be seen that, compared to the ballasted case, the track modulus changes more smoothly, within around 10 sleepers length. However, the track modulus values are very high, well above 69 N/mm/mm, which will lead to accelerated degradation of the track, due to dynamic vehicle/track interaction effects. The usage of soft railpads or soft fill materials is therefore mandatory for slab tracks.

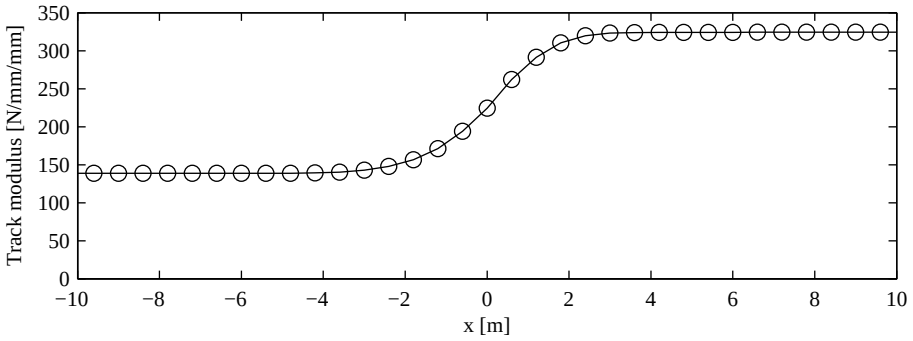

Figure 7.13: Track modulus of the slab track transition, with fill material 1

Figure 7.14 shows the displacements in the rail and in the slab, now considering the fill material 3, representing corkelast, embedding the rails. As can be seen, the rails displacements are considerably higher than those determined with the fill 1, and the differential rail displacements from soft to stiff side is considerably smaller (only 16% difference).

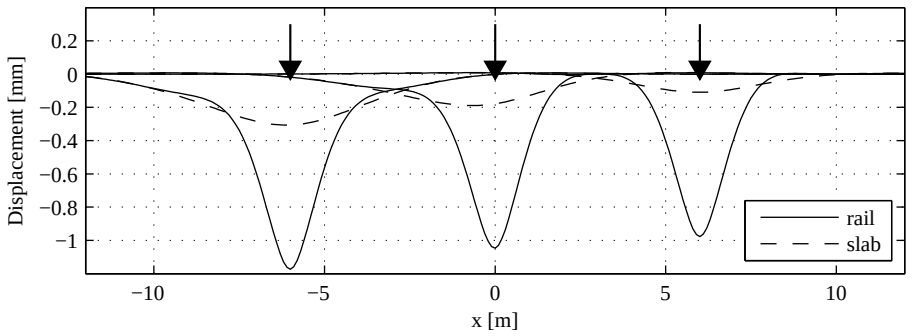

Figure 7.14: Rail and slab displacements in slab track model with fill material 3. Load of 72 kN moving at 120 km/h

The track modulus of the slab track transition with the fill material 2 and 3 is presented in Figure 7.15. As can be seen, the usage of soft fill materials significantly lowers the track modulus. Also, the effect caused by a support stiffness increase is much more attenuated using slab tracks with soft fill materials (or soft railpads). In the example presented with

fill material 3 (having a stiffness of 52 500 kN/m^2, equivalent to a railpad stiffness of 31.5 kN/mm), the slab support stiffness increases by a factor 3.85, but the track modulus increases only 28%.

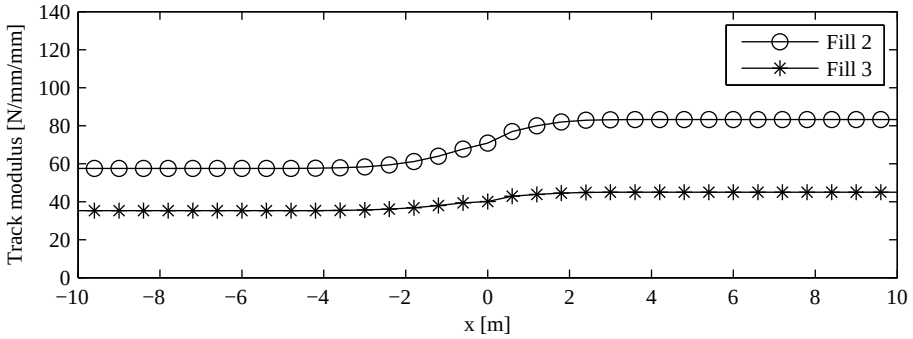

Figure 7.15: Track modulus of the slab track transition, with fill material 2 and 3

7.6 Conclusions

This Chapter analyzes the effects introduced by an abrupt change in the support stiffness of the track. For a ballasted track having stiff constant railpads, it was seen that an abrupt support stiffness variation results in a steep change of the track modulus, within about three sleepers length for the considered example. This also results in high differential sleeper loads on consecutive sleepers, of more than 80% for the considered example. This effect will trigger differential settlements in the ballast, leading to the development of hanging sleepers, and, consequently, to increased differential sleepers loads, and to increased degradation of the track.

One possible measure to improve the track behaviour at transitions corresponds to the introduction of soft railpads in the stiff side of the track. According to the example shown, this measure effectively reduces the track modulus variation, also maintaining the maximum values of track modulus within acceptable limits. As a consequence, the differential sleeper load is much less pronounced, and also kept under maximum admissible values, despite the steep variation of the stiffness of the support, by a factor of 3.85 for the considered example.

The behaviour of a slab track solution on a transition zone was also analyzed in this Chapter. Again, an abrupt change in the support stiffness of the track was considered. The numerical simulation has shown that with a concrete slab, the length of the eigenfield moving with the load is higher, resulting in higher soil stress ditribution, and also in

smoother track modulus variation, when passing over a sudden support stiffness change. In the example, a localized (steplike) variation of the stiffness of the support leads to a variation of the track modulus within about ten sleepers length, corresponding to 6 m of track.

In slab tracks, the inclusion of soft railpads, or soft fill materials (in case of embedded rails), is mandatory. The numerical example has shown that with stiff rail supports, the track modulus is extremely high, even in case of soft slab support. This leads to undesirably high dynamic vehicle/track interaction, and consequently to accelerated damage of track components and rolling stock.

When designed with soft railpads or soft fill materials, the dynamic response of a slab track is significantly less affected by support stiffness variations. The numerical simulation has shown that for a support stiffness abrupt change of factor 3.85, the track modulus increase can be as low as 28%, depending on the stiffness of the railpad (or fill material). Therefore, it can be concluded that the slab track solution has advantages over the ballasted track by allowing a better decoupling between the stiffness change of the track foundation and the rail displacements.

Chapter 8

Conclusions and Future Work

8.1 Conclusions

This thesis reports a study on the behaviour of railway transition zones, with special focus on the corresponding behaviour of ballast under dynamic loading. Numerical models for the simulation of dynamic and long-term behaviour of railway tracks are developed. These models are validated using field measurements performed at a passage over a culvert, in a region with soft soils, where the transition zones are made with approach slabs.

The one-dimensional models describe the coupled dynamic and long-term behaviour on transition zones quite well. Aspects represented in the models are the unloaded level of the track, the possibility of the existence of voids under the sleepers, and the characterization of the dynamics of the vehicles. It is shown that it is possible to obtain the distribution of the track weight over the sleepers (and thus determine the sleepers that are hanging) from a single levelling.

The importance of considering the inertia properties of the vehicles in terms of amplitudes of forces transmitted to the ballast versus results with constant moving forces reach 20%. The amplification from the vehicle dynamics is caused by long-wave uneveness of the track.

The distribution of the forces transmitted to the ballast varies considerably in transition zones. The force of the sleeper to the ballast may vary from zero and five times the average value, depending on the location of the sleeper, the existence of gaps, and the passing vehicle. It was found that the differences between the maximum load under consecutive sleepers are high.

The 1-D numerical simulations confirmed that the densification of ballast after tamping

plays an important role on the loss of quality of a transition. However, the 1-D model was unable to calculate the correct development of voids under the sleepers above the approach slabs. Another mechanism plays a role.

The 3-D calculations showed that the ballast is loaded beyond the elastic region and that the ballast/soil above the approach slab has the tendency to move by rolling/sliding. It is shown that this is caused by a combined effect of decreased initial load on the ballast and dynamic motion of the approach slabs. This explains the differences in voids between the measurements and the 1-D calculations.

On ballasted railway transitions where the problem is mostly caused by stiffness variations of the track support, the use of soft railpads on the stiff side of the transition is beneficial.

The slab track solution was also modeled and it was found that it has advantages over the ballasted track by showing much smaller differential rail displacements, for identical change of the track support stiffness.

8.2 Future work

There are issues and aspects related to the behaviour of ballast at transition zones that require further research. First of all, it was seen that factors, other than the loading amplitudes and loading history, may significantly influence the settlement of ballast. One of these factors is the existence of voids under the sleepers, which may develop and extend in several consecutive sleepers on transition zones. It is therefore believed that it is possible to improve the settlement model presented in this work, by incorporating this, and possibly other, factors. For this, additional research is necessary, which requires a significant experimental component. This experimental work shall also give additional information on the quantification of the parameters of the settlement model.

Along this work several tools of numerical modelling of railway tracks were developed. Although these models were validated, and proved to be adequate to study problems occurring at transition zones, there are still aspects that may be improved. For example, the consideration of the dynamics of the vehicles with the three-dimensional model of the track base system, the horizontal interaction between the sleepers and the ballast, the consideration of other non-linear constitutive models for the ballast besides the $K - \theta$ model, the definition of the material damping of ballast and soils with attention to high amplitudes response, or the improvement of the coding in order to decrease the required time of computation of three-dimensional non-linear analyses.

In the future, it is envisaged that the tools of numerical modelling developed in this work will be further applied to test and verify possible design solutions or mitigation measures to reduce problems at transition zones. In particular, it is important to analyze the behaviour of transition zones under high-speed trains, in order to reduce costs of construction of new high-speed railway lines. As seen along this work, the non-linearity cannot be ignored.

Bibliography

Achenbach, J.D. and Sun, C.T. Moving load on a flexible supported timoshenko beam. *International Journal of Solid and Structures*, 1:353–370, 1965.

Adif-Cedex. Improvement study of transition zone on conventional line. Technical Report D 2.2.6 GL, Innotrack, 2009.

Aki, K. and Richards, P.G. *Quantitative Seismology: Theory and Methods*. W.H. Freeman and Company, 1980.

Allaart, A.P. *Design principles for flexible pavements*. PhD thesis, TU Delft, 1992.

Allen, J.J. *The effects of non-constant lateral pressures on the resilient properties of granular materials*. PhD thesis, 1973.

Alva-Hurtado, J.E. and Selig, E.T. Permanent strain behavior of railroad ballast. In *10th International Conference on*, volume Vol. 1, pages 543–546, Stockholm, Sweden, 1981. A.A. Balkema, The Netherlands.

Alves Costa, P., Calçada, R. and Silva Cardoso, A. Influence of train dynamic modelling strategy on the prediction of trackground vibrations induced by railway traffic. *Proceedings of the Institution of Mechanical Engineers, Part F: Journal of Rail and Rapid Transit*, 2012. doi: 10.1177/0954409711433686.

Alves Ribeiro, A., Calçada, R. and Delgado, R. Dynamic effects induced by abrupt changes in track stiffness in high speed railway lines. In Sousa, Fernandes, Vargas and Azevedo, editors, *Applications of Computational Mechanics in Geotechnical Engineering*, pages 473–483, 2007.

Anderson, W.F. and Key, A.J. Model testing of Two-Layer railway track ballast. *Journal of Geotechnical and Geoenvironmental Engineering*, 126(4):317–323, Apr. 2000. doi: 10.1061/(ASCE)1090-0241(2000)126:4(317).

Atkinson, J. *The mechanics of soils and foundations*. Taylor & Francis, 2 edition, 2007.

Auersch, L. The excitation of ground vibration by rail traffic: theory of vehicle-track-soil interaction and measurements on high-speed lines. *Journal of Sound and Vibration*, 284 (1-2):103–132, June 2005. ISSN 0022-460X. doi: 10.1016/j.jsv.2004.06.017.

Augustin, S., Gudehus, G., Huber, G. and Schünemann, A. Numerical model and laboratory tests on settlement of ballast track. In *System Dynamics and Long-term Behaviour of Railway Vehicles, Track and Subgrade*. Springer, k. popp, w. schiehlen edition, 2003.

Aursudkij, B., McDowell, G.R. and Collop, A.C. Cyclic loading of railway ballast under triaxial conditions and in a railway test facility. *Granular Matter*, 11:391–401, 2009. doi: 10.1007/s10035-009-0144-4.

Baessler, M. and Ruecker, W. Track settlement due to cyclic loading with low minimum pressure and vibrations. In *System Dynamics and Long-term Behaviour of Railway Vehicles, Track and Subgrade*. Springer, k. popp, w. schielhen edition, 2003.

Banerjee, P. K. and Butterfield, R. *Boundary element methods in engineering science*. McGraw-Hill Book Co. (UK), 1981. ISBN 9780070841208.

Banimahd, M. and Woodward, P. 3-dimensional finite element modelling of railway transitions. In *Proceeding of the* 9^{th} *International Conference on Railway Engineering*, 2007.

Bathe, K.-J. *Finite Element Procedures*. Prentice Hall, 1996. ISBN 0-13-301458-4.

Berggren, Eric G., Kaynia, Amir M. and Dehlbom, Bjrn. Identification of substructure properties of railway tracks by dynamic stiffness measurements and simulations. *Journal of Sound and Vibration*, 329(19):3999 – 4016, 2010. ISSN 0022-460X. doi: 10.1016/j.jsv.2010.04.015.

Beskou, Niki D. and Theodorakopoulos, Dimitrios D. Dynamic effects of moving loads on road pavements: A review. *Soil Dynamics and Earthquake Engineering*, 31(4):547 – 567, 2011. ISSN 0267-7261. doi: 10.1016/j.soildyn.2010.11.002.

Bettess, P. More on infinite elements. *International Journal for Numerical Methods in Engineering*, 15(11):1613–1626, 1980. ISSN 1097-0207. doi: 10.1002/nme.1620151105.

Bhatti, M. Asghar. *Fundamental Finite Element Analysis and Applications: with Mathematica and Matlab Computations*. John Wiley & Sons, Inc, 1 edition, Feb. 2005. ISBN 0471648086.

Bhatti, M. Asghar. *Advanced Topics in Finite Element Analysis of Structures: with Mathematica and Matlab Computations*. John Wiley & Sons, Inc, 1 edition, 2006. ISBN 13 978-0-471-64807-9.

Bitzenbauer, J. and Dinkel, J. Dynamic interaction between a moving vehicle and an infinite structure excited by irregularities - fourier transforms solution. *Archive of Applied Mechanics*, 72(2):199–211, 2002. doi: 10.1007/s00419-001-0200-y.

Bowness, D., Lock, A., Powrie, W., Priest, J. and Richards, D. Monitoring the dynamic displacements of railway track. *Proceedings of the Institution of Mechanical Engineers, Part F: Journal of Rail and Rapid Transit*, 221(1):13–22, Jan. 2007. doi: 10.1243/0954409JRRT51.

Boyce, H.R. A non-linear model for the elastic behaviour of granular materials under repeated loading. In *Proc. Int. Symp. On Soils under Cyclic and Transient Loading*, pages 285–294, 1980.

Briaud, J.-L., James, R. W. and Hoffman, S. B. *Settlement of Bridge Approaches*. Transportation Research Board, (Washington, D.C), 1997. ISBN 0309060079, 9780309060073.

Brown, S.F. and Hyde, A.F.L. Significance of cyclic confining stress in repeated-load triaxial testing of granular material. *Transportation Research Record*, pages 49–58, 1975.

Brown, S.F. and Pappin, J.W. Analysis of pavements with granular bases. *Transportation Research Record*, pages 17–23, 1981.

Brown, S.F. and Pell, P.S. An experimental investigation of the stresses, strains and deflections in layered pavement structure subjected to dynamic loads. In *Proceedings of the 2nd Int. Conf. on Structural Design of Asphalt Pavements*, pages 487–504. Ann Arbor, 1967.

Budhu, M. *Soil Mechanics & Foundations*. John Wiley & Sons, Inc., 2000. ISBN 0-471-25231-X.

Burrow, M P N, Bowness, D and Ghataora, G S. A comparison of railway track foundation design methods. *Proceedings of the Institution of Mechanical Engineers, Part F: Journal of Rail and Rapid Transit*, 221(1):1–12, 2007. doi: 10.1243/09544097JRRT58.

Cai, Y., Sun, H. and Xu, C. Response of railway track system on poroelastic half-space soil medium subjected to a moving train load. *International Journal of Solids and Structures*, 45(18-19):5015 – 5034, 2008. ISSN 0020-7683. doi: 10.1016/j.ijsolstr.2008.05.002.

Chebli, H., Clouteau, D. and Schmitt, L. Dynamic response of high-speed ballasted railway tracks: 3d periodic model and in situ measurements. *Soil Dynamics and Earthquake Engineering*, 28(2):118 – 131, 2008. ISSN 0267-7261. doi: 10.1016/j.soildyn.2007.05.007.

Choros, H. and Adams, G.G. A steadily moving load on an elastic beam resting on a tensionless winkler foundation. *Journal of Applied Mechanics*, 46:175–180, 1979.

Clough, R.W. and Penzien, J. *Dynamics of Structures*. McGraw-Hill, Inc, 2nd edition, 2003. ISBN 0-07-113241-4.

Coelho, B. *Dynamics of railway transition zones in soft soils*. PhD thesis, TU Delft, 2011.

Coelho, B., Priest, J., Hölscher, P. and Powrie, W. Monitoring of transition zones in railways. University of Westminster, UK, 2009. Professor M.C. Forde, University of Edinburgh. ISBN 0-947644-64-4.

Coelho, B., Hölscher, P., Priest, J., Barends, F.B.J. and Powrie, W. An assessment of transition zone performance. *Proceedings of the Institution of Mechanical Engineers. Pt.F. Journal of Rail and Rapid Transit*, 225(2):129–139, 2011.

Correia, A.G., Hornych, P. and Akou, Y. Review of models and modelling of unbound granular materials. In Correia, A.G., editor, *Proc. Int. Workshop on Modelling and Advanced Testing for Unbound Granular Materials*. A. A. Balkema/Roterdam, 1999.

Costa, P. Alves, Calçada, R., Cardoso, A. Silva and Bodare, A. Influence of soil non-linearity on the dynamic response of high-speed railway tracks. *Soil Dynamics and Earthquake Engineering*, 30(4):221–235, 2010. ISSN 0267-7261. doi: 10.1016/j.soildyn.2009.11.002.

Dahlberg, T. Some railroad settlement models - a critical review. *Proceedings of the Institution of Mechanical Engineers, Part F: Journal of Rail and Rapid Transit*, 215(4): 289–300, 2001. ISSN 0954-4097. doi: 10.1243/0954409011531585.

Dahlberg, T. Railway track dynamics - a survey. Technical report, Linkoping University, 2003.

Dieterman, H.A. and Metrikine, A.V. The equivalent stiffness of a half-space interacting with a beam. critical velocities of a moving load along the beam. *European Journal of Mechanics A/Solids*, 15(1):67–90, 1996.

Dieterman, H.A. and Metrikine, A.V. Critical velocities of a harmonic load moving uniformly along an elastic layer. *Trans. ASME Journal of Applied Mechanics*, 64:596–600, 1997.

Dimitrovová, Z. and Varandas, J.N. Critical velocity of a load moving on a beam with a sudden change of foundation stiffness: Applications to high-speed trains. *Computers & Structures*, 87:1224 – 1232, 2009. ISSN 0045-7949. doi: 10.1016/j.compstruc.2008.12.005.

Diyaljee, V.A. Effects of stress history on ballast deformation. *Journal of Geotechnical Engineering*, 113(8):909–914, 1987. doi: 10.1061/(ASCE)0733-9410(1987)113:8(909).

EN 13450. *Aggregates for railway ballast*, 2002.

EN 933-1. *Tests for geometrical properties of aggregates - Part 1: Determination of particle size distribution*, 1997.

Esveld, C. Eindrapport trillingshinder (final report on vibration hinderance, in Dutch). Technical Report CUR/COB commission L40, Gouda, The Netherlands, 2000.

Esveld, C. *Modern Railway Track*. MRT-Productions, Zaltbommel, The Netherlands, 2nd ed. edition, 2001. ISBN 90-800-324-3-3.

Esveld, C. Developments in High-Speed track design. *IABSE Symposium Report*, 87(12): 37–45, 2003. doi: 10.2749/222137803796328782.

EU. White paper - european transport policy for 2010: time to decide, 2001.

Faure, M. Compactage par vibration des enrobs pour couche de roulement. *Bull. liaison Labo. Ponts et Ch.*, 119:73–77, 1982.

Fillipov, A.P. Steady-state vibrations of an infinite beam on an elastic half-space subjected to a moving load. *Izvestija Akademii Nauk SSSR Mehanika I Mashinostroenie*, 6:97–105, 1961.

Ford, R. Differential ballast settlement, and consequent undulations in track, caused by Vehicle-Track interaction. *Vehicle System Dynamics: International Journal of Vehicle Mechanics and Mobility*, 24(1 supp 1):222 – 233, 1995.

Fortunato, E. *Renewal of Railway Platforms. Studies about Bearing Capacity. (In Portuguese)*. PhD thesis, FEUP, 2005.

Galvín, P. and Domínguez, J. High-speed train-induced ground motion and interaction with structures. *Journal of Sound and Vibration*, 307(3-5):755 – 777, 2007. ISSN 0022-460X. doi: 10.1016/j.jsv.2007.07.017.

Galvín, P., Romero, A. and Domínguez, J. Fully three-dimensional analysis of high-speed traintracksoil-structure dynamic interaction. *Journal of Sound and Vibration*, 329(24): 5147 – 5163, 2010. ISSN 0022-460X. doi: 10.1016/j.jsv.2010.06.016.

Gardien, W. Transitions from rheda track to ballast track. Technical Report GMV-WG-040029300, Holland Railconsult, Utrecht, 2005.

Hall, Lars. Simulations and analyses of train-induced ground vibrations in finite element models. *Soil Dynamics and Earthquake Engineering*, 23(5):403 – 413, 2003. ISSN 0267-7261. doi: DOI: 10.1016/S0267-7261(02)00209-9.

Hicks, R.G. *Factors influencing the resilient properties of granular materials*. PhD thesis, 1970.

Hicks, R.G. and Monismith, C.L. Prediction of the resilient response of pavements containing granular layers using non-linear elastic theory. In *Proc. 3rd Int. Conf. on Asphalt Pavements*, pages 410–429, 1972.

Hölscher, P. and Meijers, P. Literature study of knowledge and experience of transition zones. Technical Report 415990-0011 v02, GeoDelft, Delft, Nov. 2007.

Hölscher, P. and Meijers, P. Analysis of track and soil behaviour at transition zones. Technical Report 1001069-000-GEO-0006-sr, Deltares, 2009.

Hughes, T.J.R. *The Finite Element Method, Linear Static and Dynamic Finite Element Analysis*. Prentice-Hall, Inc., 1987. ISBN 0-13-317025-X.

Hughes, T. J .R. *The Finite Element Method*. Dover Publications Inc., mar 2003. ISBN 0486411818.

Hunt, H.E.M. Settlement of railway track near bridge abutments. *Proceedings of the ICE - Transport*, 123(1):68–73, Feb. 1997. ISSN 0965-092X.

Ilias, H. The influence of railpad stiffness on wheelset/track interaction and corrugation growth. *Journal of Sound and Vibration*, 227(5):935–948, Nov. 1999. doi: 10.1006/jsvi.1999.2059.

Indraratna, B. and Salim, W. *Mechanics of ballasted rail tracks: a geotechnical perspective*. Taylor & Francis, 2005. ISBN 9780415383295.

Indraratna, B., Ionescu, D., Christie, D. and Chowdhury, R. Compression and degradation of railway ballast under One-Dimensional loading. *Australian Geomechanics Journal*, pages 48–61, Dec. 1997.

Indraratna, B., Ionescu, D. and Christie, H. D. Shear behavior of railway ballast based on large-scale triaxial tests. *J. Geotech. and Geoenvir. Engrg*, 124(5):439–449, May 1998. ISSN 1090-0241. doi: 10.1061/(ASCE)1090-0241(1998)124:5(439).

Indraratna, B., Khabbaz, H., Salim, W. and Christie, D. Geotechnical properties of ballast and the role of geosynthetics. *Journal of Ground Improvement*, 10(3):91 – 102, 2006.

Ionescu, D. *Evaluation of the engineering behaviour of railway ballast*. PhD thesis, University of Wollongong, 2004.

Jeffrey, A. and Dai, H.-H. *Handbook of Mathematical Formulas and Integrals*. Academic Press of Elsevier, 2008.

Jezequel, L. Analysis of critical speeds of a moving load on an infinite periodically supported beam. *Journal of Sound and Vibration*, 73:606–610, 1980.

Karl, L., Haegeman, W. and Degrande, G. Determination of the material damping ratio and the shear wave velocity with the seismic cone penetration test. *Soil Dynamics and Earthquake Engineering*, 26(12):1111 – 1126, 2006. ISSN 0267-7261. doi: 10.1016/j.soildyn.2006.03.001.

Kausel, E. and Rosset, J.M. Stiffness matrices for layered soils. *Bulletin of the Seismological Society of America*, 71(6):1743–1761, 1981.

Kaynia, A.M., Madshus, C. and Zackrisson, P. Ground vibration from high-speed trains : Prediction and countermeasure. *Journal of Geotechnical and Geoenvironmental Engineering*, 126(6):531–537, 2000.

Kedhr, S. *Transportation Research Record*, 1043:131–138, 1985.

Kempfert, H.G. and Hu, Y. Prediction on the long-term behavior of subsoils under high-speed railways. In *Geotechnical Engineering for Transportation Infraestructure*, Amsterdam, 1999. Balkema. ISBN 90 5809 047 7.

Kenney, J.T. Steady-state vibrations of beam on elastic foundation for moving load. *Journal of Applied Mechanics*, 21:359–364, 1954.

Kerr, A. D. and Bathurst, L. A. A method for upgrading the performance at track transitions for high-speed service. Technical Report DOT/FRA/RDV-02/05, U. S. Department of Transportation. Federal Railroad Administration, 2001.

Kerr, A. D. and Moroney, B. E. track transition problems and remedies. *American Railway Engineering Association - Bulletin 742*, pages 267–298, 1993. ISSN 0003-0694.

Kettil, P., Lenhof, B., Runesson, K. and Wiberg, N.-E. Coupled simulation of wave propagation and water flow in soil induced by high-speed trains. *International Journal for Numerical and Analytical Methods in Geomechanics*, 32(11):1311–1319, 2008. ISSN 1096-9853. doi: 10.1002/nag.670.

Kolisoja, P. *Resilient deformation characteristics of granular materials*. PhD thesis, Tampere University of Technology, 1997.

Kouroussis, G., Verlinden, O. and Conti, C. Free field vibrations caused by high-speed lines: Measurement and time domain simulation. *Soil Dynamics and Earthquake Engineering*, 31(4):692 – 707, 2011. ISSN 0267-7261. doi: 10.1016/j.soildyn.2010.11.012.

Krylov, V. V. Generation of ground vibrations by superfast trains. *Applied Acoustics*, 44 (2):149 – 164, 1995. ISSN 0003-682X. doi: 10.1016/0003-682X(95)91370-I.

Kuhlemeyer, R.L. and Lysmer, J. Finite element method accuracy for wave propagation problems. *Journal of the Soil Mechanics and Foundations Division*, 99(5):421–427, 1973.

Labra, J.J. An axially stressed railroad track on an elastic continuum subjected to a moving load. *Acta Mechanica*, 22:113–129, 1975.

Lackenby, J., Indraratna, B., McDowell, G. and Christie, D. Effect of confining pressure on ballast degradation and deformation under cyclic triaxial loading. *Geotechnique*, 57 (6):527–536, 2007. ISSN 0016-8505.

Lane, H., Ekevid, T., Kettil, P., Ching, C.Y. and Wiberg, N.-E. Vehicle-track-underground modeling of rail induced wave propagation. *Computers & Structures*, 85(15-16):1215 – 1229, 2007. ISSN 0045-7949. doi: 10.1016/j.compstruc.2006.11.032.

Lei, X and Zhang, B. Influence of track stiffness distribution on vehicle and track interactions in track transition. *Proceedings of the Institution of Mechanical Engineers, Part F: Journal of Rail and Rapid Transit*, 224(6):592–604, 2010. doi: 10.1243/09544097JRRT318.

Lekarp, Fredrick, Isacsson, Ulf and Dawson, Andrew. State of the art. II: permanent strain response of unbound aggregates. *Journal of Transportation Engineering*, 126(1):76–83, 2000. doi: 10.1061/(ASCE)0733-947X(2000)126:1(76).

Li, D. and Davis, D. Transition of railroad bridge approaches. *Journal of Geotechnical and Geoenvironmental Engineering*, 131(11):1392–1398, Nov. 2005. doi: 10.1061/(ASCE)1090-0241(2005)131:11(1392).

Li, D., Otter, D. and Carr, G. Railway bridge approaches under heavy axle load traffic: Problems, causes, and remedies. *Proceedings of the Institution of Mechanical Engineers, Part F: Journal of Rail and Rapid Transit*, 224(5):383–390, 2010. doi: 10.1243/09544097JRRT345.

Lim, W.L. *Mechanics of Railway Ballast Behaviour*. PhD, The University of Nottingham, May 2004.

Lombaert, G., Degrande, G., Kogut, J. and Franois, S. The experimental validation of a numerical model for the prediction of railway induced vibrations. *Journal of Sound and Vibration*, 297(3-5):512 – 535, 2006. ISSN 0022-460X. doi: 10.1016/j.jsv.2006.03.048.

López-Pita, A., Teixeira, P.F., Casas, C., Ubalde, L. and Robusté, F. Evolution of track geometric quality in high-speed lines: Ten years experience of the Madrid-Seville line. *Proceedings of the Institution of Mechanical Engineers, Part F: Journal of Rail and Rapid Transit*, 221(2):147 –155, Mar. 2007. doi: 10.1243/0954409JRRT62.

Lu, M. and McDowell, G. The importance of modelling ballast particle shape in the discrete element method. *Granular Matter*, 9:69–80, 2007. ISSN 1434-5021. 10.1007/s10035-006-0021-3.

Lundqvist, A. and Dahlberg, T. Dynamic train/track interaction including model for track settlement evolvement. *Vehicle System Dynamics*, 41 (Supplement):667–676, 2004.

Lundqvist, A. and Dahlberg, T. Load impact on railway track due to unsupported sleepers. *Proceedings of the Institution of Mechanical Engineers – Part F – Journal of Rail & Rapid Transit (Professional Engineering Publishing)*, 219(2):67 – 77, 2005. ISSN 09544097.

Lundqvist, A., Larsson, R. and Dahlberg, T. Influence of railway track stiffness variations on wheel/rail contact forces. Porto, Portugal, 2006.

Lysmer, J. and Kuhlemeyer, R.L. Finite dynamic model for infinite media. *Journal of the Engineering Mechanics Division*, 95(EM4):859–877, 1969.

Mathews, P.M. Vibrations of a beam on elastic foundation. *Zeitschrift für Angewandte Mathematik und Mechanik*, 38:105–115, 1958.

MathWorks Inc. *Release R2009b documentation for MATLAB*, 2009.

Mauer, L. An interactive Track-Train dynamic model for calculation of track error growth. *Vehicle System Dynamics: International Journal of Vehicle Mechanics and Mobility*, 24 (1 supp 1):209, 1995. ISSN 0042-3114. doi: 10.1080/00423119508969626.

Metrikine, A.V. and Popp, K. Vibration of a periodically supported beam on an elastic half-space. *European Journal of Mechanics - A/Solids*, 18(4):679 – 701, 1999. ISSN 0997-7538. doi: 10.1016/S0997-7538(99)00141-2.

Metrikine, A.V., Wolfert, A.R.M. and Dieterman, H.A. Transition radiation in an elastically supported string. abrupt and smooth variations of the support stiffness. *Wave Motion*, 27(4):291 – 305, 1998. ISSN 0165-2125. doi: 10.1016/S0165-2125(97)00055-3.

Metrikine, A.V., Verichev, S.N. and Blaauwendraad, J. Stability of a two-mass oscillator moving on a beam supported by a visco-elastic half-space. *International Journal of Solids and Structures*, 42(34):1187 – 1207, 2005. ISSN 0020-7683. doi: 10.1016/j.ijsolstr.2004.03.006.

Miller, Karol, Joldes, Grand, Lance, Dane and Wittek, Adam. Total lagrangian explicit dynamics finite element algorithm for computing soft tissue deformation. *Communications in Numerical Methods in Engineering*, 23(2):121–134, 2007. ISSN 1099-0887. doi: 10.1002/cnm.887.

Mylonakis, G., Nikolaou, S. and Gazetas, G. Footings under seismic loading: Analysis and design issues with emphasis on bridge foundations. *Soil Dynamics and Earthquake Engineering*, 26(9):824–853, 2006. ISSN 0267-7261. doi: 10.1016/j.soildyn.2005.12.005.

Nielsen, J. C. O. and Oscarsson, J. Simulation of dynamic train-track interaction with state-dependent track properties. *Journal of Sound and Vibration*, 275(3-5):515–532, Aug. 2004. doi: 10.1016/j.jsv.2003.06.033.

Okada, H. High-speed railways in china. *Japan Railway and Transport Review*, 48:22–29, 2007.

ORE. Stresses in the rails, the ballast and the formation resulting from traffic loads. Technical Report D71/RP 13/E, International Union of Railways, Office of Research and Experiments, Utrecht, The Netherlands, 1970.

Plotkin, D. and Davis, D. Bridge approaches and track stiffness. Technical Report DOT/FRA/ORD08/01, U. S. Department of Transportation. Federal Railroad Administration, 2008.

Powrie, W., Yang, L. and Clayton, C. Stress changes in the ground below ballasted railway track during train passage. *Proceedings of the Institution of Mechanical Engineers, Part F: Journal of Rail and Rapid Transit*, 221(2):247–262, Jan. 2007. doi: 10.1243/0954409JRRT95.

Priest, J.A. and Powrie, W. Determination of dynamic track modulus from measurement of track velocity during train passage. *Journal of Geotechnical and Geoenvironmental Engineering*, 135(11):1732, 2009. ISSN 10900241. doi: 10.1061/(ASCE)GT.1943-5606.0000130.

Priest, J.A., Powrie, W., Grabe, P.J., Clayton, C.R.I. and Yang, L. Measurements of transient ground movements below a ballasted railway line. *Géotechnique*, 60:667–677, Jan. 2010. ISSN 0016-8505, 1751-7656. doi: 10.1680/geot.7.00172.

Read, D. and Li, D. Design of track transitions. Technical Report 79, Transportation Research Board of the National Academies, Pueblo, Colorado, 2006.

Recuero, A.M, Escalona, J.L. and Shabana, A.A. Finite-element analysis of unsupported sleepers using three-dimensional wheelrail contact formulation. *Proceedings of the Institution of Mechanical Engineers, Part K: Journal of Multi-body Dynamics*, 225(2): 153–165, 2011. doi: 10.1177/2041306810394971.

Ribeiro, A.C., Calçada, R. and Delgado, R. Track-train dynamic behaviour on transition zones of high speed railway lines. In Topping, B.H.V., editor, *Proceedings of the Eleventh International Conference on Civil, Structural and Environmental Engineering Computing*, 2007. doi: 10.4203/ccp.86.48.

Sasaoka, C. D. and Davis, D. D. Implementing track transition solutions for heavy axle load service. In *Proceedings of AREMA 2005 Annual Conference*, 2005.

Sato, Y. Japanese studies on deterioration of ballasted track. *Vehicle System Dynamics: International Journal of Vehicle Mechanics and Mobility*, 24(1 supp 1):197, 1995. ISSN 0042-3114. doi: 10.1080/00423119508969625.

Saussine, G., Cholet, C., Gautier, P.E., Dubois, F., Bohatier, C. and Moreau, J.J. Modelling ballast behaviour under dynamic loading. part 1: A 2D polygonal discrete element method approach. *Computer Methods in Applied Mechanics and Engineering*, 195(19-22):2841–2859, 2006. ISSN 0045-7825. doi: 10.1016/j.cma.2005.07.006.

Schmitt, L. Recent sncf research on ballasted high speed track. fatigue behaviour. In *Track for High-Speed Railways*, Porto, Portugal, 2006.

Schooleman, R. B. Overgang kunstwerk-aardebaan voor de hoge-snelheidslijn. Technical Report 7-96-110-10, T.U.Delft, 1996.

Schwartz, C.W. and Taybji, S.D. Analysis of concrete slab track system. In *Proceedings of the 3rd International Symposium on 3D Finite Element for Pavement Analysis, Design, and Research*, pages 159–178, 2002.

Sekine, E., Kono, A. and Kito, A. Strength and deformation characteristics of railroad ballast in ballast particle abrasion process. *Quarterly Report of RTRI*, 46(4):256–261, 2005.

Selig, E.T. and Waters, J.M. *Track geotechnology and substructure management*. Thomas Telford, Oct. 1994. ISBN 9780727720139.

Shamalta, M. and Metrikine, A. V. Analytical study of the dynamic response of an embedded railway track to a moving load. *Archive of Applied Mechanics*, 73:131–146, 2003. ISSN 0939-1533.

Sheng, X., Jones, C.J.C. and Petyt, M. Ground vibration generated by a load moving along a railway track. *Journal of Sound and Vibration*, 228(1):129 – 156, 1999. ISSN 0022-460X. doi: 10.1006/jsvi.1999.2406.

Sheng, X., Jones, C.J.C. and Thompson, D.J. A theoretical model for ground vibration from trains generated by vertical track irregularities. *Journal of Sound and Vibration*, 272(3-5):937 – 965, 2004. ISSN 0022-460X. doi: 10.1016/S0022-460X(03)00782-X.

Sheng, X., Jones, C.J.C. and Thompson, D.J. Prediction of ground vibration from trains using the wavenumber finite and boundary element methods. *Journal of Sound and Vibration*, 293(3-5):575 – 586, 2006. ISSN 0022-460X. doi: 10.1016/j.jsv.2005.08.040.

Shenton, M.J. Ballast deformation and track deterioration. In *Track Technology*, pages 253–265. Thomas Telford Ltd, London, 1985.

Sneddon, I. N. The relation between load and penetration in the axisymmetric boussinesq problem for a punch of arbitrary profile. *International Journal of Engineering Science*, 3(1):47 – 57, 1965. ISSN 0020-7225. doi: 10.1016/0020-7225(65)90019-4.

Steenbergen, M.J.M.M., Metrikine, A.V. and Esveld, C. Assessment of design parameters of a slab track railway system from a dynamic viewpoint. *Journal of Sound and Vibration*, 306(1-2):361–371, Sept. 2007. ISSN 0022-460X. doi: 16/j.jsv.2007.05.034.

Stewart, H.E. Permanent strains from cyclic Variable-Amplitude loadings. *Journal of Geotechnical Engineering*, 112(6):646–660, June 1986. doi: 10.1061/(ASCE)0733-9410(1986)112:6(646).

Suiker, A.S.J. *The mechanical behaviour of ballasted railway tracks*. PhD thesis, TU Delft, 2002.

Suiker, A.S.J. and de Borst, R. A numerical model for the cyclic deterioration of railway tracks. *International Journal for Numerical Methods in Engineering*, 57(4):441–470, 2003. doi: 10.1002/nme.683.

Suiker, A.S.J., Selig, E.T. and Frenkel, R. Static and cyclic triaxial testing of ballast and subballast. *Journal of Geotechnical and Geoenvironmental Engineering*, 131(6):771–782, June 2005. doi: 10.1061/(ASCE)1090-0241(2005)131:6(771).

Sun, H., Cai, Y. and Xu, C. Three-dimensional simulation of track on poroelastic half-space vibrations due to a moving point load. *Soil Dynamics and Earthquake Engineering*, 30(10):958 – 967, 2010. ISSN 0267-7261. doi: 10.1016/j.soildyn.2010.04.007.

Sweere, G.T.H. *Unbound granular bases for roads*. PhD thesis, TU Delft, 1990.

Szilard, R. *Theories and Applications of Plate Analysis: Classical Numerical and Engineering Methods*. Wiley, 2004.

Takatsu, T. The history and future of high-speed railways in japan. *Japan Railway and Transport Review*, 48:6–21, 2007.

Teixeira, P.F. *Contribution to the reduction of track maintenance costs by optimizing its vertical stiffness* (in Spanish). PhD thesis, Technical University of Catalonia, 2003.

Timoshenko, S. Stresses in rails. *Transactions of the Institute of Ways of Communications*, 1915.

Timoshenko, S.P. and Goodier, J.N. *Theory of Elasticity*. McGraw-Hill Higher Education, 3rd edition, Oct. 1970. ISBN 0070858055.

Uzan, J. Characterization of granular material. *Transportation Research Record*, pages 52–59, 1985.

van Dalen, K. Ground vibrations induced by a high-speed train running over inhomogeneous subsoil. transition radiation in two-dimensional inhomogeneous elastic systems. Master's thesis, Delft University of Technology, 2006.

van Dalen, K.N. and Metrikine, A.V. Transition radiation of elastic waves at the interface of two elastic half-planes. *Journal of Sound and Vibration*, 310(3):702–717, 2008. ISSN 0022-460X. doi: 10.1016/j.jsv.2007.06.007.

Varandas, J.N. Modelling subsoil wave propagation generated by superficial dynamic excitation. Application to spectral analysis of surface waves (in Portuguese), 2005.

Varandas, J.N., Hölscher, P. and Silva, M.A.G. Dynamic behaviour of railway tracks on transitions zones. *Computers & Structures*, 89(13-14):1468–1479, July 2011. ISSN 0045-7949. doi: 16/j.compstruc.2011.02.013.

Varandas, J.N., Silva, R., Silva, M.A.G., Lopes, N. and Hölscher, P. The impact of rail corrugation on the degradation of ballast. In Pombo, J., editor, *Proceedings of the First International Conference on Railway Technology: Research, Development and Maintenance*, pages 543–546. Civil-Comp Press, 2012. doi: 10.4203/ccp.98.42.

Varandas, J.N., Hölscher, P. and Silva, M.A.G. Settlement of ballasted track under traffic loading. Application to transition zones. *Proceedings of the Institution of Mechanical Engineers, Part F: Journal of Rail and Rapid Transit*, In Press, 2013. ISSN 0954-4097.

Verruijt, A. *Soil Mechanics*. Delft University of Technology, 2006.

Vesnitskii, A.I. and Metrikine, A.V. Transient radiation in a periodically non-uniform elastic guide. *Izv. RAN. Mekhanika Tverdogo Tela*, 28(6):164 – 168, 1993.

Vestnitskii, A. I. and Metrikine, A. V. Transient radiation in a periodically non-uniform guide. *Mechanics of Solids*, 28:158–162, 1993.

Vortok International. www.vortok.com, 2007.

Vostroukhov, A.V. *Three-dimensional Dynamic Models of a Railway Track for High-speed Trains*. PhD thesis, T. U. Delft, 2002.

Wood, D.M. *Geotechnical Modelling*. Spon Press, 1 edition, 2004. ISBN 0-415-34304-6.

Yang, L. A, Powrie, W. and Priest, J. A. Dynamic stress analysis of a ballasted railway track bed during train passage. *Journal of Geotechnical and Geoenvironmental Engineering*, 135(5):680, May 2009. ISSN 10900241. doi: 10.1061/(ASCE)GT.1943-5606.0000032.

Zhai, W.M. Two simple fast integration methods for Large-Scale dynamic problems in engineering. *International Journal for Numerical Methods in Engineering*, 39(24):4199–4214, 1996. ISSN 1097-0207.

Zhai, W. and Cai, Z. Dynamic interaction between a lumped mass vehicle and a discretely supported continuous rail track. *Computers & Structures*, 63(5):987–997, June 1997. doi: 10.1016/S0045-7949(96)00401-4.

Zhai, W.M., Wang, K.Y. and Lin, J.H. Modelling and experiment of railway ballast vibrations. *Journal of Sound and Vibration*, 270(4-5):673–683, Mar. 2004. ISSN 0022-460X. doi: 10.1016/S0022-460X(03)00186-X.

Zhang, Shuguang, Xiao, Xinbiao, Wen, Zefeng and Jin, Xuesong. Effect of unsupported sleepers on wheel/rail normal load. *Soil Dynamics and Earthquake Engineering*, 28(8): 662–673, 2008. ISSN 0267-7261. doi: 10.1016/j.soildyn.2007.08.006.